Exploring the Optical Properties of Anticancer Drugs/Metal Nanoclusters inside the Confined Environments and on the Graphene Oxide Surface

A Thesis

Submitted in partial fulfillment of the requirements

for the degree of

Doctor of Philosophy

by

K Raj Kumar

ID: 20123155

Indian Institute of Science Education and Research (IISER), Pune

2018

Dedicated

to

My Parents

Indian Institute of Science Education and Research (IISER), Pune

Certificate

Certified that the work incorporated in this thesis entitled "**Exploring the Optical Properties of Anticancer Drugs/Metal Nanoclusters inside the Confined Environments and on the Graphene Oxide Surface**" submitted by **Mr. K Raj Kumar** was carried out by the candidate, under my supervision. The work presented here or any part of it has not been included in any other thesis submitted previously for the award of any degree or diploma from any other university or institution.

Partha Hazra

Date: 10th January 2018

Dr. Partha Hazra
Research Supervisor

Email: p.hazra@iiserpune.ac.in | Contact no: +91 (20) 25908077

Declaration

I declare that this written submission represents my ideas in my own words, and wherever other's ideas have been included, I have adequately cited and referenced the original sources. I also declare that I have adhered to all principles of academic honesty and integrity and have not misrepresented or fabricated or falsified any idea/data/fact/source in my submission. I understand that violation of the above will cause for disciplinary action by the Institute and can also evoke penal action from the sources, which have thus not been properly cited or from whom proper permission has not been taken when needed.

Date: 10th January 2018

K Raj Kumar

ID: 20123155

Acknowledgement

First and foremost, I would like to express my heartfelt thanks to my thesis advisor, Dr. **Partha Hazra** for his constant encouragement, support, and guidance throughout my research. His expertise in fluorescence spectroscopy improved my research skills and prepared me for future challenges. His diligent effort and training was the reason behind every success achieved by me and undoubtedly is the asset for my future research. This thesis would not have been possible without his valuable support. I acknowledge Indian Institute of Science Education and Research (IISER), Pune for providing excellent research facilities and an outstanding research environment.

I am grateful to the Research Advisory Committee (RAC) members Dr. S. K. Asha (NCL Pune) and Dr. Nirmalya Ballav for their suggestions and comments during RAC meetings. The critical examination of my research work and valuable comments by all of the RAC members were always very useful. Because of their guidance and suggestions I gained experience to work in diverse fields of research which was indeed very helpful. I am grateful to our collaborators, Dr. N. Ballav and Dr. Sudipta Basu for giving me the opportunity to work with them in different collaborative research projects.

I wish to express my sincere thanks to Prof. M. Jayakannan, Chair Chemistry. I specially thank Prof. B. S. M. Rao, past dean of doctoral studies at IISER-Pune for their generous support and encouragement. I am thankful to every faculty of IISER-Pune who was always ready to share their knowledge and experience with me. It was indeed a pleasure to work in such an ambiance.

I thank IISER Pune librarians, IT staff and administrative staff especially Mayuresh, Tushar and Yathish for their kind support. I am thankful to University Grants Commission (UGC), Department of Science and Technology (DST), Government of India, for my research scholarship the financial support during the course of Ph.D. I would like to thank to DST-SERB and Infosys foundation for financial Support to attend an international conference.

It's my pleasure to thank all the members of the team, I belong to; Dr. Abhigyan, Dr. Krishna, Sagar, Konoya, Bibhisan, Hrishikesh, Aslam, Joy and Dr. imitayaz as they always maintained a very lively environment in lab. An all time running discussion and sharing of experiences helped me to expand the horizon of knowledge. Special thanks are due to Mr. Sagar and Konoya for the many insightful discussions and critical assessment of my work

and during my thesis writing. I would also like to thank Subrahmanyam (from Dr. Prasenjit Ghosh and group) and Sandeep Palvai (from Dr. Sudipta Basu and group) for giving me the opportunity to work with them and contributing significantly in the publications of mine.

I thank all my friends, seniors and juniors for their help and support during my research tenure.

No words can ever convey my sense of gratitude for my parents. It is due to their unconditional trust, timely encouragement, endless patience and unstinting sacrifice; I am able to reach this position. I dedicate this thesis to my parents who unremittingly supported me during my years of study.

IISER Pune **K Raj Kumar**

Table of Contents

Contents i

List of Abbreviations iii

Synopsis v

List of Publications xi

1. Introduction 1

1.1. Motivation of the Thesis 2
1.2. Working Systems 3
1.2.1. Graphene and Graphene Oxide 3
1.2.2. Mesoporous Silica Nanochannels 7
1.2.3. Reverse Micelles 9
1.2.4. Fluorescent Metal Clusters 12
1.3. References 19

2. Experimental: Materials and Methods 27

2.1. Materials 28
2.1.1 Synthesis and Sample Preparations 29
2.2. Experimental Methods 32
2.2.1. Absorption Measurements 32
2.2.2. Steady State Fluorescence Measurements 32
2.2.3. Time Resolved Fluorescence Measurements 33
2.2.3a. Time Correlated Single Photon Counting Technique 33
2.2.3a.1. Analysis of Fluorescence Decays 35
2.2.3a.2. Time Resolved Fluorescence Anisotropy Measurements 36
2.2.3b. Femtosecond Time Resolved Fluorescence Upconversion 38
2.2.4. Circular Dichroism 41
2.3. References 42

3. Loading of an Anticancer Drug into/on to the Material and Subsequent Release to Biomolecules 44

3a. **Loading of an Anticancer Drug onto Graphene Oxide Surface and Subsequent Release by Biomolecules** 45
3a.1. Introduction and Motivation of the Work 45
3a.2. Results and Discussion 46
3a.2a. Characterizations of Graphene Oxide (GO) 46
3a.2b. Steady State Fluorescence Spectroscopy Results 47

3a.2c. Fluorescence Lifetime Measurements 51
3a.2d. Scanning and Transmission Electron Microscopy Results 54
3a.2e. Powder X-Ray Diffraction and Raman Spectroscopy Results 56
3a.3. Conclusion 58
3a.4. References 59
3a.5. Appendix 61

3b. **Loading of an Anticancer Drug into Mesoporous Silica Nanochannel and Subsequent Release to Cellular DNA** 69
3b.1. Introduction and Motivation of the Work 69
3b.2. Results and Discussion 70
3b.2a. Steady State Fluorescence and Circular Dichroism Measurements 70
3b.2b. Time Resolved Fluorescence Results 78
3b.2c. Confocal Microscopy and Field-emission Scanning Electron Microscopy (FE-SEM) 80
3b.2d. *In vitro* assay 83
3b.3. Conclusion 84
3b.4. References 85

4. Excited State Proton Transfer Dynamics of Topotecan inside Bio-mimicking Nano-cavity 87
4.1. Introduction 88
4.2. Results and Discussion 89
4.2a. Steady State Measurements 89
4.2b. Fluorescence Lifetime Measurements 92
4.2c. Time Resolved Fluorescence Anisotropy Measurements 97
4.3. Conclusion 99
4.4. References 100

5. Excited State Fluorescence Dynamics of Highly Stable Copper Nanoclusters Synthesized inside the Aqueous Nanopool of Reverse Micelles 102
5.1. Introduction and Motivation of the Work 103
5.2. Results and Discussion 104
5.2a. Characterizations 104
5.2b. Steady State Emission Results 106
5.2c. Excitation Dependent Emission and Emission Dependent Excitation Spectra 108
5.2d. Fluorescence Dynamics 112
5.3. Conclusion 120
5.4. References 120

List of Abbreviations

ACN	Acetonitrile
ADC	Analog to digital converter
AgNCs	Silver nanoclusters
AOM	Acousto-optic modulator
AOT	aerosol OT, dioctyl sodium sulfosuccinate
av	Average
AuNCs	Gold nanoclusters
CD	Circular dichroism
CFD	Constant fraction discriminator
CMC	Critical micellar concentration
CPT	Camptothecin
CuNCs	Copper nanoclusters
CTAB	Cetyl trimethylammonium bromide
DCM	Dichloromethane
DMSO	Dimethyl sulfoxide
DNA	Deoxyribonucleic acid
Em	Emission
EPT	Ellipticine
ESPT	Excited state proton transfer
EtOH	Ethanol
Ex	Excitation
fs	Femtosecond
FWHM	Full width at half maximum
GO	Graphene Oxide
HOMO	Highest energy occupied molecular orbital
HPTS	8-Hydroxypyrene-1,3,6-trisulfonic acid
HSA	Human serum albumin
IC	Internal conversion
ISC	Inter system crossing
LBO	Lithium triborate
LED	Light emitting diode
LUMO	Lowest energy unoccupied molecular orbital
Lys	Lysozyme
MCM-41	Mesoporous silica nanochannels
MeCN	Acetonitrile
MeOH	Methanol
mM	Milli molar

NCs	Nanocluster
ns	Nanosecond
ps	Picosecond
RM	Reverse micelle
SDS	Sodium dodecyl sulphate
Ref	Reference
TAC	Time to amplitude converter
TCSPC	Time correlated single photon counting
TPT	Topotecan
TRES	Time-resolved emission spectra
TRANES	Time resolved area normalized emission spectra
TX-100	Triton X-100
μL	Micro liter
μM	Micro molar
UV-Vis	Ultraviolet-visible

Synopsis

Fluorescence spectroscopy is a sensitive tool compared to any other spectroscopic techniques to probe the micro-environments of any system by observing the modulation in the optical properties of fluorophores. For designing novel drug carriers, it is very essential to establish the influence of the carrier environments on the photophysical properties of fluorescent drugs during its transportation to the active sites. Consequently, many research works are invested to understand the changes in photophysical properties of drug/fluorophore during loading into the nano-carriers and subsequent *in vitro* release from the delivery vehicle.[1] Delivery of anticancer drug becomes even more challenging due to their water insoluble nature and poor cellular uptake. In this regard, graphene derivatives, i.e., graphene oxide (GO) and mesoporous silica nanochannels (MCM-41) are excellent choice of delivery media owing to their large surface area and biocompatible nature, which improves the drug efficacy compared to free drug.[1b,2] The focus in chapter 3 is to probe the loading of an anticancer drug (ellipticine) into these nanomaterials (GO and MCM-41) and its subsequent release to biomolecules (DNA/RNA). These processes have been monitored with help of intrinsic fluorescence switching of drug, which circumvents the utilization of any complex or sophisticated technique.

Chemotherapeutic agents have received tremendous attention due to their potential pharmaceutical applications towards cancer treatment. Among various chemotherapeutic agents, topotecan (TPT) is found to be a potential inhibitor for growth of the tumour cells by inhibiting the human topoisomerase I (Top1) enzyme activity though the Top1-DNA cleavable complex formation.[3] Moreover, the entire biological activity of TPT depends on the formation of Top1-TPT-DNA complex, the stability of which may be influenced by the light driven electronic perturbation of the drug.[3] Interestingly, TPT undergoes efficient proton release upon photo-irradiation owing to its strong photo-acidity in the excited state.[4] Thus, it would be intriguing to understand the nano-confinement effect on the photophysical properties of TPT inside biological nano-cavities, considering the presence of confined water in a small membrane pocket. Hence, we have explored (in Chapter 4) the excited state proton transfer dynamics of topotecan (TPT) inside bio-mimicking nano-cavities of aqueous reverse micelles (RM) using steady-state and time-resolved fluorescence spectroscopic techniques.

We believe that our results might provide a new insight towards the understanding of fluorescence properties of TPT inside a cell-like environment.

Fluorescent metal nanoclusters (NCs) have attracted a special attention due to their unique optical properties arising from the quantum confinement effect.[5] They have been considered as ideal replacement materials for organic fluorophores and semiconducting quantum dots in the applications of optoelectronics, bioimaging, catalysis, and sensing due to their ultrafine size, excellent photo-stability and low toxicity.[5] Among the metal NCs, gold and silver have been well explored compared to copper despite the latter being more biocompatible, extremely cheap and commonly used in daily life. Keeping these aspects in mind, we have designed a simple and effective strategy for the synthesis of highly stable and ultrabright fluorescent CuNCs within the water 'nanopool' of reverse micelles without using any toxic reducing agents (Chapter 5). To unravel the fundamental origins and mechanism of fluorescence properties of CuNCs, understanding the carrier dynamics is important, which is still lacking in literature. Thus, the origin and mechanism behind the multi-fluorescence and spectral broadening behaviors of CuNCs have been demonstrated (Chapter 5).

Chapter 1 (**Introduction**) This chapter gives a brief overview about the different working systems (graphene oxide, mesoporous silica nanochannels, reverse micelles and copper nanoclusters), which are used to explore the research works.

Chapter 2 (**Experimental: Materials and Methods**) This chapter describes the sample preparation protocols, experimental methods, different techniques (absorption, steady state fluorescence, time correlated single photon counting (TCSPC), fluorescence upconversion and circular dichroism (CD)) and analysis procedures (for different instrumentations), which are majorly utilized during the research.

Chapter 3 (**Loading of an Anticancer Drug into/onto the Material Surface and Subsequent Release to Biomolecules**) This chapter deals with loading and subsequent release of an anticancer drug, ellipticine. Using the unique fluorescence switching properties of ellipticine, we have successfully monitored its loading in/on to materials such as graphene oxide (GO) and mesoporous silica nanochannels (MCM-41) subsequent release to

biomolecules. This chapter is divided into two sections, one is devoted for graphene oxide and second section deals with the MCM-41. Both the sections are discussed as follows;

3a. Loading of an Anticancer Drug onto Graphene Oxide and Subsequent Release to DNA/RNA: a Direct Optical Detection: In this sub-section, we have synthesized graphene oxide (GO) from graphite flakes and thoroughly characterized by various techniques such as powder X-ray diffraction (XRD), Raman spectroscopy, FT-IR, AFM, FE-SEM and HR-TEM. We have demonstrated fluorescence-switching of ellipticine (EPT), during its loading onto GO and subsequent release to specific intra-cellular biomolecules (DNA and RNA) at physiological pH. The green fluorescence of EPT switches to blue in presence of GO upon loading and switches back to green in presence of polynucleotides (DNA/RNA). The intensified blue emission of the ellipticine-GO (EPT-GO) complex with human serum albumin (HSA), switches to bluish green upon addition of dsDNA (**Figure 1**). Finally, we have shown that EPT can also be released to DNA even from the EPT-GO-HSA composite. Electron microscopy, XRD and Raman spectroscopy reveals the formation of distinctive 3D assemblies involving GO and biomolecule(s) probably through non-covalent interactions and is primarily responsible for the biomolcule(s) assisted fluorescence-switching of EPT. To our knowledge, such morphological patterns of the composited systems are very unusual, reported here the first time and could find applications in the fabrication of biomedical devices. Moreover, our approach of direct optical detection of drug loading and releasing is very cheap, appealing and will be useful for clinical trial experiments once the cytotoxicity of GO is duly taken care. Moreover, our work is expected to stimulate future experiments across physical chemistry, bio-chemistry, computational chemistry and material science, for the development of various GO-based self-assembled structures with important biomolecules.

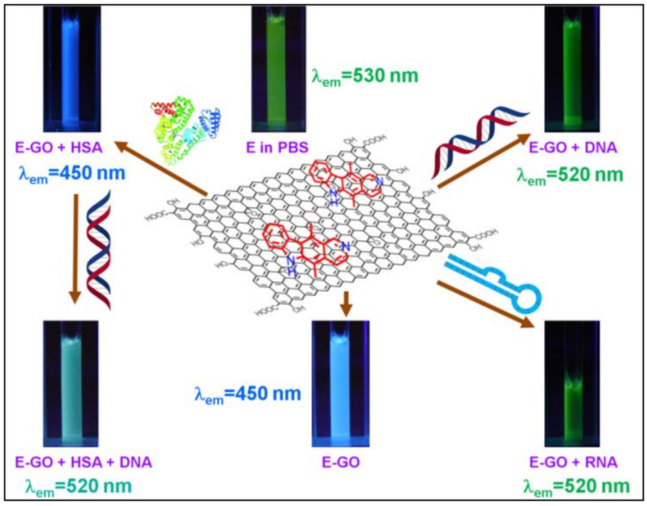

Figure 1. Fluorescence switching of ellipticine in presence of GO with various bio-macromolecules (HSA/dsDNA/RNA).

3b. Loading of an Anticancer Drug into Mesoporous Silica Nanochannels and its Subsequent Release to Cellular DNA: Herein, mesoporous silica nanochannels (MCM-41) based molecular switching of a biologically important anticancer drug, namely, ellipticine (EPT) has been utilized to probe its efficient loading onto MCM-41, and subsequent release to intra-cellular biomolecule, like, DNA. Exploiting various spectroscopic techniques (like, steady state fluorescence, time-resolved fluorescence and circular dichroism), it has been shown that EPT can be easily translocated from MCM-41 to DNA without using any external stimulant. Blue emission of EPT in polar aprotic solvent i.e., dichloromethane (DCM) completely switches to green upon loading inside MCM-41 due to the conversion from neutral to protonated form of the drug inside nano-pores. Powder X-ray diffraction (PXRD), N_2 gas adsorption and confocal fluorescence microscopy results confirm the adsorption of EPT inside the nano-pores of MCM-41. Here, lysozyme (Lyz) protein has been utilized as a pore blocker of MCM-41 in order to prevent premature drug release. Interestingly, EPT is released to DNA even from the EPT-MCM-Lyz composite system, and results in intensification of green fluorescence. Electron microscopy results reveal the formation of distinctive garland kind of morphology involving MCM-41 and DNA probably through non-covalent interactions, and this is believed to be responsible for the DNA assisted release of drug molecules from silica nano-pores. Confocal laser scanning microscopy (CLSM) imaging revealed that EPT-MCM successfully internalized into the HeLa cervical cancer cells and localized into the nucleus (**Figure 2**). Cell viability assay results infer that EPT-MCM and Lyz-EPT-MCM showed much improved efficacy in HeLa cancer cells compared to free ellipticine.

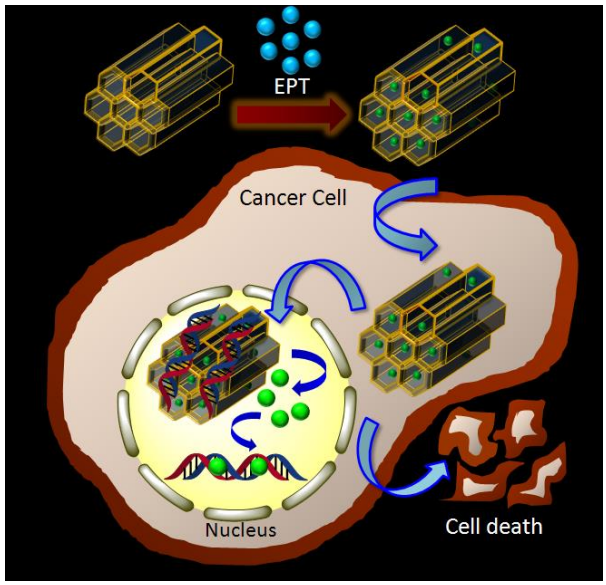

Figure 2. Internalization of anticancer drug, ellipticine loaded MCM-41 into cancerous cells and localizing into the nucleus to specifically target to nuclear DNA.

Chapter 4 (Excited State Proton Transfer Dynamics of Topotecan inside Bio-mimicking Nano-cavity) This chapter deals with understanding an important excited state

phenomenon, i.e., excited state proton transfer (ESPT) process, of a potentially important anticancer drug, Topotecan (TPT) inside bio-mimicking nano-confined environment known as reverse micelles (RM). The ESPT dynamics of TPT has been explored in aqueous reverse micelle using steady state and time-resolved fluorescence measurements. In bulk water, TPT exhibits single emission, which is believed to be originated from zwitterionic (Z^*) form of the drug, as an outcome of ESPT process from excited state cationic form (C^*) of TPT to the nearby water molecule. In AOT/n-heptane RM, the drug shows dual emission attributed to the simultaneous existence of both C^* and Z^* forms of the drug. The presence of single iso-emissive point in time-resolved area normalized emission spectrum (TRANES) further confirms the co-existence of two species (C^* and Z^*) in the excited state. Both the time-resolved emission spectrum (TRES) and TRANES infer the generation of excited state zwitterionic form (Z^*) of TPT from the excited state cationic form (C^*) of TPT, as a result of ESPT process from the –OH group of TPT to the nearby water molecule (**Figure 3**). Interestingly, ESPT dynamics was found to be severely retarded within the polar nano-cavity of RM, exhibiting time constant of 250 ps to 1 ns, which is significantly slower than the dynamics obtained in bulk water (32 ps).The observed slow ESPT dynamics in RM compared to bulk water is mainly attributed to the sluggish hydrogen bonded network dynamics of water molecules inside the nano-cavity of RM and the screening of the sodium ions present at the interface.

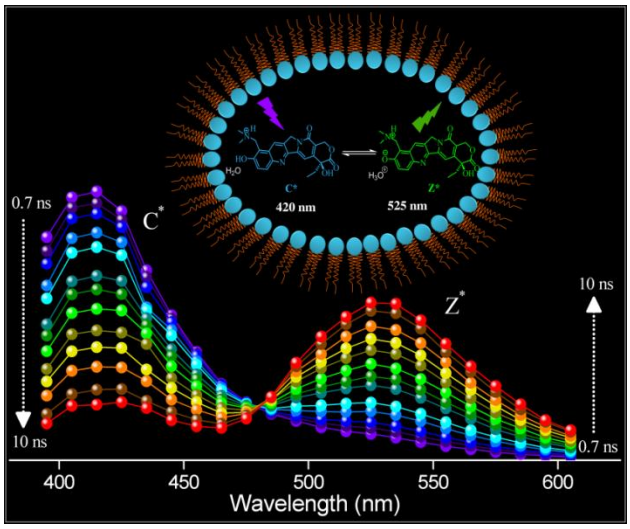

Figure 3. Time-resolved area normalized emission spectra (TRANES) of TPT in aqueous reverse micelle (λ_{ex} = 375 nm) at w_0 = 10.

Chapter 5 (**Ultrafast Fluorescence Dynamics of Highly Stable Copper Nanoclusters Synthesized inside the Nanopool of Reverse Micelles**) Herein, we have reported a new strategy for the synthesis of highly stable fluorescent copper nanoclusters (CuNCs) with L-cysteine (Cys) as a protecting ligand within the water nano-pool of reverse micelles (RMs) (**Figure 4**). In the present work, efforts are also given to address the origin of excitation-dependent fluorescence spectral shift of CuNCs. From our experiments, we have

elucidated that the broad fluorescence from CuNCs in RM consists of two spectrally overlapped bands corresponding to the metal-core and surface states of CuNCs. The intrinsic emission of CuNCs distributed in shorter wavelength regions (<470 nm) is mainly originated from metal-core. On the other hand, extrinsic fluorescence band (>470 nm) is caused by surface states and consists of a much broader emission due to the presence of numerous surface states. The trapping of excited electrons in the various surface states leads to the emission in the longer wavelength regions and is believed to be responsible for excitation dependent emission of CuNCs in RM. Excited state dynamics, which controls the optical properties of CuNCs, have also been investigated by TCSPC and femtosecond fluorescence up-conversion techniques. Femto-second fluorescence up-conversion and TCPSC decay profiles of CuNCs comprise of multitude of lifetime components spanning from <1 ps to few nano-second time scale (**Figure 4**). We have rationalized the dynamics on the basis of several competing deactivation pathways and a broad distribution of radiative electron-hole recombination dynamics originating from core and surface states.

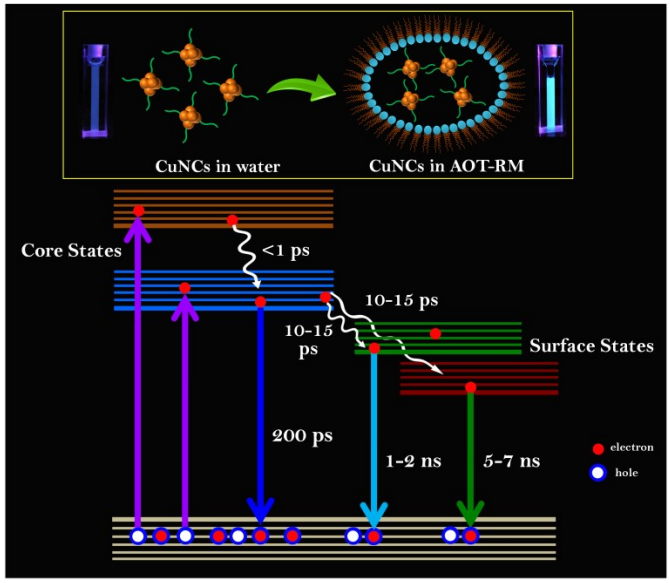

Figure 4. Schematic illustration showing all the excited state relaxation dynamics of CuNCs.

References

1. (a) N. Alarcos, B. Cohen, M. Ziółek and A. Douhal, Chem. Rev., 2017, 117, 13639-13720; (b) V. Georgakilas, J. N. Tiwari, K. C. Kemp, J. A. Perman, A. B. Bourlinos, K. S. Kim and R. Zboril, Chem. Rev., 2016, 116, 5464-5519.
2. (a) C. Chung, Y.-K. Kim, D. Shin, S.-R. Ryoo, B. H. Hong and D.-H. Min, Acc. Chem. Res., 2013, 46, 2211-2224; (b) Y. Wang, Z. Li, J. Wang, J. Li and Y. Lin, Trends Biotechnol., 2011, 29, 205-212; (c) B. G. Trewyn, I. I. Slowing, S. Giri, H.-T. Chen and V. S. Y. Lin, Acc. Chem. Res., 2007, 40, 846-853.
3. C. Kollmannsberger, K. Mross, A. Jakob, L. Kanz and C. Bokemeyer, Oncology, 1999, 56, 1-12.
4. (a) M. R. di Nunzio, Y. Wang and A. Douhal, J. Phys. Chem. B, 2012, 116, 7522-7530;
5. (a) H. Qian, M. Zhu, Z. Wu and R. Jin, Acc. Chem. Res., 2012, 45, 1470-1479; (b) P. Yu, X. Wen, Y.-R. Toh, X. Ma and J. Tang, Part. Part. Syst. Charact., 2015, 32, 142-163.

List of Publications

No.	Publications (Included in Thesis)
01	Loading of an anti-cancer drug into mesoporous silica nano-channels and its subsequent release to DNA. **R. K. Koninti**, S. Palvai, S. Satpathi, S. Basu and P. Hazra*. ***Nanoscale,*** 2016, 8, 18436–18445.
02	Excited State Proton Transfer Dynamics of Topotecan inside Bio-mimicking Nano-cavity. **R. K. Koninti**, K. Gavvala, A. Sengupta and P. Hazra*. ***The Journal of Physical Chemistry B***, 2014, 119, 2363–2371.
03	Loading of an Anti-cancer Drug onto Graphene Oxide and Subsequent Release to DNA/RNA: A Direct Optical Detection. **R. K. Koninti**, A. Sengupta, K. Gavvala, N. Ballav* and P. Hazra*. ***Nanoscale***, 2014, 6, 2937–2944.
04	Ultrafast fluorescence dynamics of highly stable copper nanoclusters synthesized inside the nanopool of reverse micelles. **R. K. Koninti**, S. Satpathi and P. Hazra*. ***The Journal of Physical Chemistry C***, 2018, 122, 5742–5752.

No.	Publications (Not Included in Thesis)
05	Spectroscopy and dynamics of cryptolepine in the nano-cavity of cucurbit[7]uril and DNA. **R. K. Koninti**, S. Satpathi, K. Gavvala and P. Hazra*. ***ChemPhysChem***, 2016, 17, 506–515.
06	Solvation Dynamics in Different Phases of the Lyotropic Liquid Crystalline System. B. Roy, S. Satpathi, K. Gavvala, **R. K. Koninti** and P. Hazra*. ***The Journal of Physical Chemistry B***, 2015, 119, 11721–11731.
07	Excited State Proton Transfer Dynamics of an Eminent Anticancer Drug, Ellipticine, in Octyl Glucoside Micelle. K. Gavvala, **R. K. Koninti**, A. Sengupta and P. Hazra*. ***Physical Chemistry Chemical Physics***, 2014, 16, 14953–14960.
08	Cucurbit[7]uril assisted ultra-violet to visible fluorescence switch of a heart medicine. K. Gavvala, **R. K. Koninti**, A. Sengupta and P. Hazra*. ***Physical Chemistry Chemical Physics***, 2014, 16, 2823–2826.
09	An anticancer drug to probe non-specific protein-DNA interactions. A. Sengupta, **R. K. Koninti**, K. Gavvala, N. Ballav and P. Hazra*. ***Physical Chemistry Chemical Physics***, 2014, 16, 3914–917.
10	Femtosecond to Nanosecond Dynamics of 2,2-Bipyridine-3,3-diol inside the Nano-

Cavities of Molecular Containers.
K. Gavvala, A. Sengupta, **R. K. Koninti** and P. Hazra*.
Physical Chemistry Chemical Physics, 2014, 16, 933–939.

11 Urea induced unfolding dynamics of flavinadenine dinucleotide (FAD): Spectroscopic and molecular dynamics simulation studies from femto-second to nano-second regime.
A. Sengupta, R. K. Singh, K. Gavvala, **R. K. Koninti**, A. Mukherjee* and P. Hazra*.
The Journal of Physical Chemistry B, 2014, 118, 1881–1890.

12 Spectroscopic and Thermodynamic Insights into the Interaction between Proflavine and Human Telomeric G-Quadruplex DNA.
V. Kumar, A. Sengupta, K. Gavvala, **R. K. Koninti** and P. Hazra*.
The Journal of Physical Chemistry B, 2014, 118, 11090–11099.

13 Role of Mg^{2+} Ions in Flavin Recognition by RNA Aptamer.
A. Sengupta, K. Gavvala, **R. K. Koninti** and P. Hazra*.
Journal of Photochemistry and Photobiology B: Biology, 2014, 140, 240–248.

14 A green solvent induced DNA package.
S. Satpathi, A. Sengupta, V. M. Hridya, K. Gavvala, **R. K. Koninti**, B. Roy, P. Hazra *.
Scientific Reports, 2014, 5:09137.

15 Folding dynamics of flavin adenine dinucleotide (FAD) inside non-aqueous and aqueous reverse micelles.
A. Sengupta*, K. Gavvala, **R. K. Koninti**, H. Chaudhuri, P. Hazra*.
Chemical Physics Letters, 2013, 584, 67-70.

16 Supramolecular Host Inhibited Excited State Proton Transfer and Fluorescence Switch of an Anti-cancer Drug, Topotecan.
K. Gavvala, A. Sengupta, **R. K. Koninti** and P. Hazra*.
ChemPhysChem, 2013, 14, 3375–3383.

17 Prototropical and photophysical properties of ellipticine inside the nanocavities of molecular containers.
K. Gavvala, A. Sengupta, **R. K. Koninti** and P. Hazra*.
The Journal of Physical Chemistry B, 2013, 117, 14099–14107.

18 Double-Proton transfer dynamics of 2,2'-bipyridine-3,3'-diol within the mesoporous silica nano-channels.
R. K. Koninti and P. Hazra*.
Manuscript under Preparation.

19 Excited State Proton Transfer Dynamics of a Firefly's Chromophore D-Luciferin in Protein Nano-Cavity.
R. K. Koninti and P. Hazra*.
Manuscript under Preparation.

20 Spectroscopy and Dynamics of Cryptolepine in bile Salt Aggregates.
R. K. Koninti and P. Hazra*.
Manuscript under Preparation.

Chapter 1

Introduction

The present chapter provides a brief introduction about different working systems, such as graphene oxide, mesoporous silica nanochannels (MCM-41), reverse micelles (RM) and fluorescent copper nanoclusters, which are used in different projects depicted in the thesis. Motivation behind this thesis work has also been discussed in this chapter.

1. Introduction

1.1. Motivation of the Thesis

Fluorescence spectroscopy is a sensitive tool compared to any other spectroscopic techniques to probe the micro-environments of any system by observing the modulation in the optical properties of fluorophores. For designing novel drug carriers, it is very essential to establish the influence of the carrier environments on the photophysical properties of fluorescent drugs during its transportation to the active sites. Consequently, many research works are invested to understand the changes in photophysical properties of drug/fluorophore during loading into the nano-carriers and subsequent *in vitro* release from the delivery vehicle.[1] Delivery of anticancer drug becomes even more challenging due to their water insoluble nature and poor cellular uptake. In this regard, graphene derivatives, i.e., graphene oxide (GO) and mesoporous silica nanochannels (MCM-41) are excellent choice of delivery media owing to their large surface area and biocompatible nature, which improves the drug efficacy compared to free drug.[1b,2] The focus in chapter 3 is to probe the loading of an anticancer drug (ellipticine) into these nanomaterials (GO and MCM-41) and its subsequent release to biomolecules (DNA/RNA). These processes have been monitored with help of intrinsic fluorescence switching of drug, which circumvents the utilization of any complex or sophisticated techniques.

Chemotherapeutic agents have received tremendous attention due to their potential pharmaceutical applications towards cancer treatment. Among various chemotherapeutic agents, topotecan (TPT) is found to be a potential inhibitor for growth of the tumour cells by inhibiting the human topoisomerase I (Top1) enzyme activity though the Top1-DNA cleavable complex formation.[3] Moreover, the entire biological activity of TPT depends on the formation of Top1-TPT-DNA complex, the stability of which may be influenced by the light driven electronic perturbation of the drug.[3] Interestingly, TPT undergoes efficient proton release upon photo-irradiation owing to its strong photo-acidity in the excited state.[4] Thus, it would be intriguing to understand the nano-confinement effect on the photophysical properties of TPT inside biological nano-cavities, considering the presence of confined water in a small membrane pocket. Hence, we have explored (in Chapter 4) the excited state proton transfer dynamics of topotecan (TPT) inside bio-mimicking nano-cavities of aqueous reverse micelles (RM) using steady-state and time-resolved fluorescence spectroscopic techniques. We believe that our results might provide a new insight towards the understanding of fluorescence properties of TPT inside a cell-like environment.

Fluorescent metal nanoclusters (NCs) have attracted a special attention due to their unique optical properties arising from the quantum confinement effect.[5] They have been considered as ideal replacement materials for organic fluorophores and semiconducting quantum dots in the applications of optoelectronics, bioimaging, catalysis, and sensing due to their ultrafine size, excellent photo-stability and low toxicity.[5] Among the metal NCs, gold and silver have been well explored compared to copper despite the latter being more biocompatible, extremely cheap and commonly used in daily life. Keeping these aspects in mind, we have designed a simple and effective strategy for the synthesis of highly stable and ultrabright fluorescent CuNCs within the water 'nanopool' of reverse micelles without using any toxic reducing agents (Chapter 5). To unravel the fundamental origins and mechanism of fluorescence properties of CuNCs, understanding the carrier dynamics is important, which is still lacking in literature. Thus, the origin and mechanism behind the multi-fluorescence and spectral broadening behaviors of CuNCs have been demonstrated (Chapter 5).

1.2. Working Systems

This part in chapter 1, describes brief introduction about different working systems, such as graphene oxide (GO), mesoporous silica nanochannels (MCM-41), reverse micelles (RMs) and fluorescent copper nanoclusters (NCs), which are used in different projects depicted in the thesis.

1.2.1. Graphene and Graphene Oxide

Graphene, a two dimensional (2D) planar sheet with one atom thick monolayer, has become one of the popular and engrossing topics in the fields of materials science, physics, chemistry, and nanotechnology.[6] Graphene consisting of densely packed sp^2 carbon atoms in regular hexagonal pattern (like honeycomb network), is generally considered as the basic building block of other carbon allotropes, such as 0D fullerenes, 1D carbon nanotubes, and 3D graphite (**Scheme 1.1**).[7] Each sp^2 carbon atom in graphene forms three σ-bonds with neighboring carbon atoms and the strength of these covalent C-C bonds are nearly equivalent to the bonds involved in diamond providing similar mechanical and thermal strength to graphene.[6] The remaining electron in $2p_z$ orbital forms a conducting π bond, which is responsible for its graphitic nature.[6,8] Graphene was first prepared in 2004, by peeling a single layer of graphene sheet using a sticky tape and a pencil.[9] Notably, the Nobel Prize in Physics for 2010 was awarded to A. K. Geim and K. Novoselov for "groundbreaking experiments regarding the two-dimensional material graphene". Extensive studies on graphene have been focused on a wide range of potential applications, including field-effect transistors,[10] lithium-

ion batteries,[11] supercapacitors,[12] solar cells,[13] and fuel cells[14] due to its exceptional properties such as, high current density, ballistic transport, chemical inertness, high thermal conductivity (>5000 W/m/K), optical transmittance, large surface area (~2630 m^2/g), long-range π conjugation and high carrier transport mobility (experimentally reported electron mobility value at room temperature >15,000 $cm^2V^{-1}s^{-1}$).[2a,9,15] Most of the interesting applications require growth of single-layer graphene on a suitable substrate, which is very difficult to control by physical methods, and is yet to be achieved. Large-scale production of graphene involves techniques, such as, exfoliation from graphite by chemical derivatization, thermal expansion, use of surfactants, along with the popular oxidation-reduction process.[7,16]

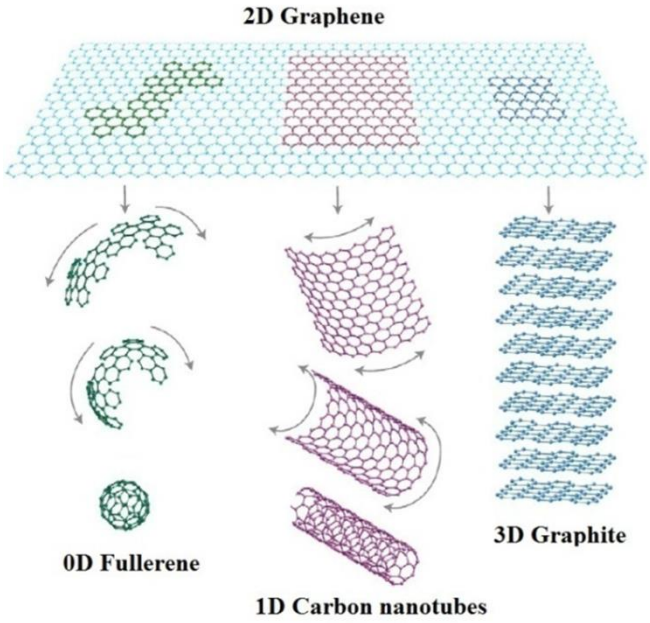

Scheme 1.1. (a) Graphene structure of single two-dimensional hexagonal sheet of carbon atoms; (Reprinted with permission from ref. 16g; Copyright 2018 Springer Nature).

Hydrophobic graphene sheets tend to agglomerate to graphite because of the favorable Van der Waals and strong π-π stacking interactions between the individual layers. Such aggregation behavior of graphene significantly restricts its potential in biological applications due to the inefficient coupling with biomolecules, limited cellular uptake, and diminished delivery efficiency.[2b,17] Therefore, it was necessary to develop novel biocompatible graphene with high solubility and stability in physiological environments. So, researchers have started using modified graphene such as, graphene oxide (GO), which has very similar structural features to that of graphene but having a better water solubility due to presence of functional groups such as, epoxide (1,2-ether), hydroxyl, carbonyls and carboxyl (**Scheme 1.2**).

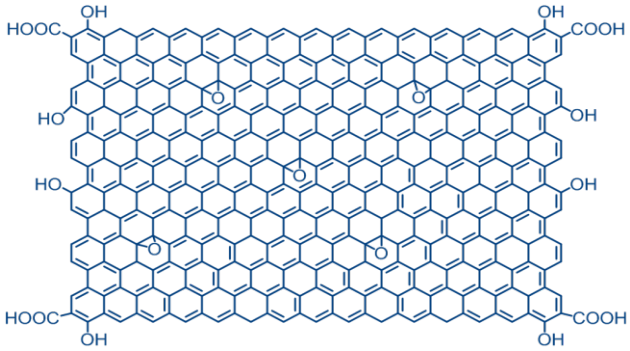

Scheme 1.2. Schematic representation of graphene oxide structure.

In 1958, Hummers reported the widely popular method of GO synthesis involving the oxidation of graphite by $KMnO_4$ and $NaNO_3$ in concentrated H_2SO_4.[18] The continuous aromatic lattice structure of graphene is disturbed by different functionalization such as, epoxide (1,2-ether), hydroxyl, carbonyls and carboxyl (**Scheme 1.2**) due to this oxidation process.[16d,19] Due to the presence of aromatic domains and various functional groups, GO undergoes a complex interplay of ionic and non-ionic interactions with various types of molecules in solution.[13,16e,20] GO and its derivatives have been used as a supporting material for a variety of metal and metal oxide nanoparticles (such as Pt, Au, TiO_2 etc.), and fluorescent molecules for their improved applications.[16a,16c,16f,19,21] GO exhibits superior biological applications than graphene due to its high specific surface area (2630 m^2/g), planar sp^2 hybridized carbon domain (π-π conjugation), enriched oxygen-containing functional groups and intrinsic bio-compatibility, low cost and scalable production, and facile biological/chemical functionalization.[8,22] Moreover, the -COOH and -OH groups of GO facilitate the conjugation with various systems, such as polymers, biomolecules (bio-targeting ligand), DNA, protein, quantum dots, nanoparticles and others imparting GO with multi-functionalities and multi-modalities for diverse biological and medical applications.[1b,23]

Inspired by the idea of carbon nanotube-based drug delivery, Dai et al., in 2008 first explored GO as a novel and efficient nano-carrier for the delivery of water insoluble aromatic anticancer drugs into cells.[24] In their approach, GO was first conjugated with an amine-terminated six armed polyethylene glycol (PEG) molecule, followed by the loading of a water insoluble anticancer drug, SN38 (a derivative of camptothecin) onto GO surface by simple non-covalent adsorption via π-π stacking. The PEG-functionalized SN38 loaded NGO exhibits high cytotoxicity for the cancerous HCT-116 cells, which is 1000 times more potent than camptothecin (CPT). Since then, GO has been utilized in many biomedical applications such as, drug/gene delivery, bio-sensing, bio-imaging, antibacterial materials and

biocompatible scaffold for cell culture. Zhang et al., reported that modified GO could be efficiently utilized for targeted drug delivery and controlled release in the tumortherapy.[25] In another work, Dai group has demonstrated the pH dependent drug release from GO surface,[23b] which later expedited pH controlled GO-based drug delivery systems by many groups, Chen et al.,[26] Bai et al.,[27] Misra et al.,[28] and Shen et al.[29]. Apart from pH-activated drug release, recently Pan and coworkers[30] have developed a thermo-responsive drug delivery cargo based on poly(N-isopropyl acryl amide) grafted graphene sheets. Moreover, folic acid and -SO_3H groups modified GO has been employed for the combined loading of two drugs, doxorubicin (DOX) and CPT. This approach exhibits enhanced specific targeting and higher cytotoxicity to MCF-7 and human breast cancer cells. Recently, Rana et al.[31] reported the delivery of an anti-inflammatory drug, Ibuprofen, by using a chitosan-grafted GO. Yang and coworkers[32] have designed a magnetic and bio-dual targeting drug delivery cargo based on GO-Fe_3O_4 nanoparticle hybrid to enhance the anticancer effect. Recently Liu et al.[33] and Sheng group[34] have studied gene delivery using modified GO, which shows improved protection for the genes from enzymatic cleavage. Apart from these, GO have been extensively studied for their widespread applications in bio-sensing and detection such as thrombin, ATP, oligonucleotide, amino acids and dopamine etc.[35]

Notably, in most of the cases, the fluorescence of the dye molecules is drastically quenched in presence of GO due to the efficient excited state electron transfer from GO surface to dyes.[36] Based on this quenching phenomenon, graphene-based biosensors were employed for developing many applications including molecular diagnostics, industrial and environmental monitoring and civil defence.[37] Wang et al., reported the drastic fluorescence quenching of rhodamine 6G (R6G) upon formation of $R6G^+GO^-$ nano-composite, which can act as a simplistic, label-free sensor (detection limit 0.2 nM to 10 nM) towards DNA among other macromolecules in biological fluids by means of recovering the R6G emission.[38] Huang et al. developed a GO-acridine orange conjugate for reversible fluorescence nano-switch based selective detection of toxic heavy metal ion, such as, Hg^{2+} by molecular logic gate operation.[39] In order to diagnose pathogenic or genetic diseases, the super-quenching ability of GO was utilized for selective detection of DNA and proteins.[40] Fluorophore labelled single stranded DNA adsorbed on GO surface exhibits drastic quenching of the fluorescent dye, which had been regained by the "turn-on" method upon addition of perfect complimentary sequence (targeted sequence). This method has been used to determine the concentration of the targeted sequence detection with very high sensitivity (pM to nM range).[38,40b,41]

1.2.2. Mesoporous Silica Nanochannels

Mesoporous silica nanoparticles (MSNs) are chemically and thermally stable nanomaterials with ordered porous structure containing numerous empty channels (meso-pores).[42] Since the first discovery of mesoporous silica nanoparticles (MSNs) in 1992 by Beck and coworkers, it has gained enormous interest among the scientific community,[43] principally due to its large surface area (900–1500 cm^2g^{-1}), pore volume (0.5–1.5 cm^3g^{-1}), and adjustable pore size (1 to 30 nm).[44] Additional features of silica nanoparticles, such as, water dispersibility, versatile surface modification, high drug binding affinity, low toxicity,[2c,44a,45] cell penetrating ability[46] and chemical stability, make it suitable for biological and biomedical applications, including drug delivery,[44a,45b,47] protein adsorption,[48] enzyme immobilization,[48c, 49] and bio-separation.[44b,44d,47c,50] Among the various mesoporous silica materials, Mobil crystalline material (MCM-41) has garnered popularity due to its highly ordered -Si-O framework, and hexagonal channels (*P6mm* symmetry) of relatively uniform diameter with a large surface area (up to 1200 m^2g^{-1}).[51] The synthesis of MCM-41 is performed by sol-gel method (**Scheme 1.3**), involving the polymerization of orthosilicates on the rod-shaped micelle template followed by calcinations to remove the surfactants.[2c,43,52] Interestingly, the pore diameter (ranging from 1.5 to 20 nm) of MCM-41 can be easily controlled through the hydrocarbon chain length of the surfactant used during the synthesis.[52a,53]

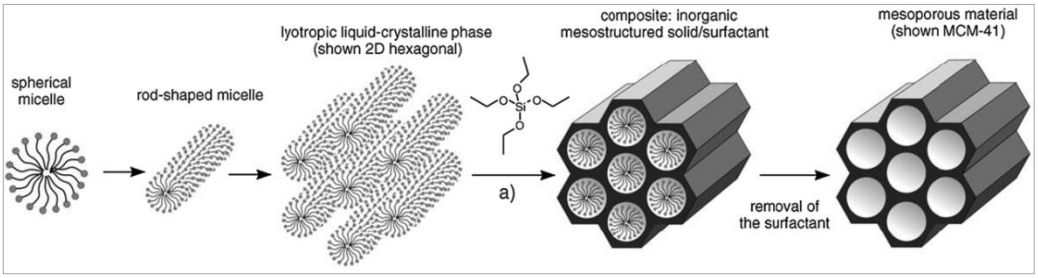

Scheme 1.3. Possible mechanistic pathway for the synthesis of MCM-41 following surfactant template method. Reprinted with permission from ref. 52b; Copyright 2018 John Wiley and Sons.

The porous and large accessible surface area of MCM-41, renders it in a variety of important industrial applications, such as adsorption of gases and metal ions,[54] loading of catalysts[42,55] and nanoparticles.[2c] In Presence of silanol (-Si-OH) groups (**Scheme 1.4**) on the MCM-41 surface favors the conjugation of various essential molecules such as pharmaceutical drugs, proteins, and other biomolecules etc., making it as a suitable cargo for biological applications.[2d,56] The solubility and bio-compatibility of this material have been

enhanced by the surface modification/conjugation with different biomolecules, dendrimers and polymers.[46a,56a] Furthermore, the abundant silanol (-Si-OH) groups and the large surface area also help in the physisorption of several guest molecules through H-bonding and surface adsorption by hydrophobic interactions.[45b,47a,47c,56c,57] Large pore volume and ordered network of MCM-41 accommodates a maximum loading of guest/drug molecules, which undergoes a controlled release to its targeted area making it advantageous over other MSNs.[47c,57a,58] Moreover, it shows high cellular uptake due to its nano-sized structure,[42,44d,59] thus several therapeutic hydrophobic drugs, enzymes and aptamers, which are not easily transferable through membrane can be incorporated into the nanochannels of MCM-41 for delivery into targeted cells.[2d,44d]

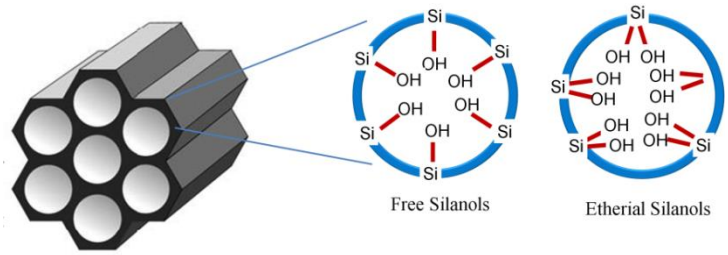

Scheme 1.4. Schematic structure of MCM-41 framework. Reprinted with permission from ref. 57c; Copyright 2018 Royal Society of Chemistry.

MCM-41 materials as successful drug delivery agents was first reported in 2001, where Vallet-Regi et al.,[58a] showed the loading and subsequent release of model drug ibuprofen (IBF) from the nanochannels.[53b] This resulted in increased efforts by researchers to explore the use of MCM-41in widespread biomedical applications, ranging from drug/gene delivery, bio-sensing and bio-imaging.[60] MCM-41 materials have shown efficiency in the loading and release of different guest molecules such as camptothecin, propidium iodide, paclitaxel, doxorubicin, curcumin and different fluorophores.[47a,56c,59-61]

To have an effective therapeutic effect, silica nanoparticles must release their drugs in the cytoplasm to minimize the possibility of undesirable side effects to normal cells and organs.[2d] To ensure the delivery of drugs in the cytoplasm, prevention of their premature release from silica nanoparticles is necessary before reaching its targeted sites.[2d] In order to achieve this, nanoparticles, quantum dots, dendrimers, supramolecular assemblies, polymers, peptides, proteins, enzymes and DNA aptamers etc.,[44a,45b,61d,61e,62] used as gatekeepers to these nanochannels. The removal of these gatekeepers (capping agents) by either intracellular or external agents like temperature,[62m,63] pH,[56b,62j,64] chemical reactions,[65] light,[66] enzymatic

activity,[67] and ultrasound,[68] etc., triggers the release of the drug/guest molecules from the silica nanochannels.

Modulation in the photophysical properties of fluorescent guests/drugs have been commonly observed upon the encapsulation in MCM-41 nanochannels.[1a,69] This modulation in the spectral properties can be utilized in many applications such as, sensing, imaging, lasing, stabilizing, and other purposes.[1a] Recently, photophysical properties of many guest molecules (fluorophores) confined in MCM-41 have been extensively studied by Douhal research group and few other research groups.[1a,69] Interaction of hemicyanine dye (DY-630-MI) with MCM-41, resulted in improved photostability and significant decrement in the blinking behaviour in fluorescence traces.[69a] This behaviour is a result of the rigid environment of silica material, which restricts the cis-trans isomerization of dye and protects it from solute-solvent interaction.[69a] The proton transfer rate of HPTS, a famous photoacid molecule, decreases in presence of MCM-41, due to the partially loss of electronic charge of SO^{3-} by H-bonding interactions with MCM-41 framework and the restricted diffusion space available.[69g] On the contrary, when intramolecular proton transfer probe 2-[5′-N-(3-triethoxysilyl)propylurea-2′-hydroxyphenyl]-benzothiazole ($HBTNH_2$) the interacts with these MCM41 frameworks, leads to greater yield of anion emission, i.e., create more favorable condition of excited state intramolecular proton transfer (ESIPT) process.[69c] The understanding of the interactions between the guest molecules and MCM-41 materials, thus helps to determine the key processes that governs their adsorption, and therefore, provides insight to the reaction mechanisms involved in this nano-confined environment. In this respect, fluorescence spectroscopic techniques have been proved to be advantageous to explore various properties of MCM-41, such as acidity, polarity, porosity, or surface charge as a function of the changes in the spectral and dynamical properties of the fluorescent guest molecules.

1.2.3. Reverse Micelles

Reverse micelle (RM) is a nanometer-sized water or polar solvent droplet surrounded by a layer of surfactant molecules immersed in a non-polar solvent (**Scheme 1.5**). Nanometer sized “water pool” which is surrounded by surfactants in such a way that the polar head groups are oriented toward the ‘water pool’ and non-polar tails are projected out toward the bulk non-polar organic phase (**Scheme 1.5**). The unique confinement effect of RMs has been used as a model system of various biological environments, such as, protein pockets and cell membranes.[70] AOT (aerosol OT, dioctyl sodium sulfosuccinate, **Scheme 1.6**), a well known

anionic surfactant, easily forms RM in non-polar solvents by the addition of water/polar solvents. Although AOT extensively used for formation of RMs, but other surfactants such as SDS, CTAB and TX-100 (**Scheme 1.6**) etc. also form stable RMs in hydrocarbon solvents with the support of a co-surfactant.[70c-f,71] However, short chain length alcohols or amines are required as co-surfactants for the formation of the above mentioned RMs.[70c-f] Enormous studies have been performed to reveal the structure as well as the biological importance of the confined water in the reverse micelle pool. Studies like, dynamics light scattering (DLS), time-resolved IR spectroscopy, small angle neutron scattering (SANS), small angle X-ray scattering (SAXS), fluorescence correlation spectroscopy (FCS) and molecular dynamics simulations have been extensively used to understanding the formation, and structure of reverse micelle.[72] A generalization of several characterization methods show that the size of a water reverse micelle is usually governed by the following equation;[73]

$$R_H(nm) = 2.3w_0 \qquad (1.1)$$

where, R_H is the hydrodynamic radius of the water RM, and w_0 stand for water to surfactant concentration ratio (w_0 = [water]/[AOT])[70d,73]. The water molecules confined inside reverse micelle "water pool" are drastically different in structure, dynamics and several other physical properties (like polarity and viscosity) compared to the bulk water.[70b-d,71] In the confined water of reverse micelles having relative dielectric constants (ε) of 30-40, which are very close to ε of methanol (33) and much smaller than ε of bulk water (78).[70c,70e] Using photoacid (2-naphthol-6,8- disulfonate), it has been reported that RMs with r_{max} >16 Å, the dielectric constant of the aqueous phase is ~70 and for smaller micelles, it is as low as 60.[73] Compared to the bulk water, the micro-viscosity of water in AOT reverse micelles is reported to be very large at low w_0 (40 cP at w_0 = 4).[74] Micro-viscosity decreases with increase in w_0 and at higher w_0 becomes constant (near ~15 cP).[74a] Probing the interior water pool of AOT reverse micelles with a highly charged decavanadate (V_{10}) oligomer using ^{51}V NMR spectroscopy indicate that a proton gradient exists inside the reverse micelles, leaving the interior neutral while the interfacial region is acidic.[70f,75] Notably, water molecules, which are confined in nanopool of RM, is classified into two types: '*bound water*' and '*free water*'. '*Bound water*' molecules in the interfacial peripheries of water nanopools are regarded as immobile with low dielectric property because of strong binding to the head groups of AOT, while *free water* molecules in the core of water pools have been reported to be mobile and polar almost like water in bulk.[70a-f,71,76] Water nanopool of RMs have been used for wide range of applications such as nano-reactor for synthesis of nanoparticles,[77] controlling the

reaction kinetics,[78] trapping of hydrogen bonded dry urea (without any intervening water molecules),[79] etc. RMs have also been extensively used in enzymatic reactions and chemical catalysis.[80] Encapsulation of biomolecules such as enzymes, proteins and nucleic acids (DNA and RNA) within the nanopool of RMs are also reported in literature.[81]

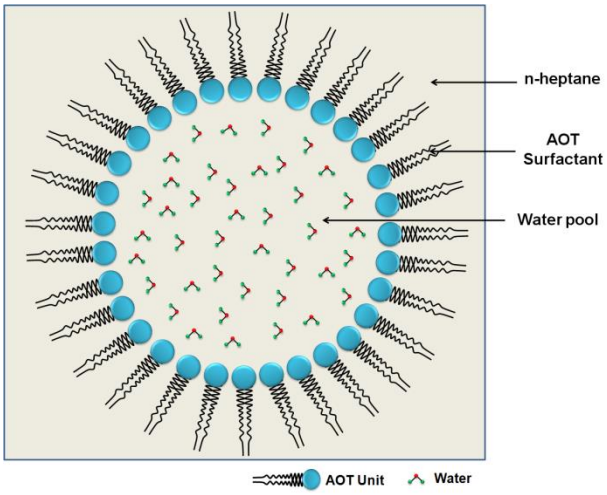

Scheme 1.5. Schematic representation of reverse micelle.

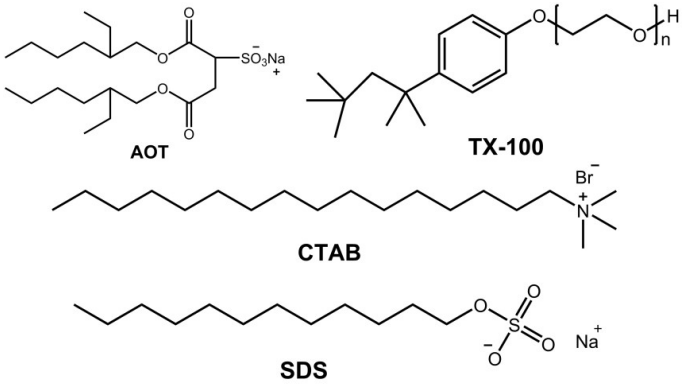

Scheme 1.6. Chemical structures of surfactants.

The water core of RM is similar to water pockets present in the bio-aggregates. To understand the dynamics of proton transfer processes in biological water, many group studied ESPT in reverse micellar environments. Excited state double proton transfer dynamics of 7-azaindole in 'water pool' has been investigated and the retardation of proton transfer was attributed to the increased free energy of prerequisite solvation to form a cyclically H-bonded 1:1 7-azaindole/water complex.[82] Using complementary techniques, such as ultrafast time-resolved transient absorption and 2D NMR, Levinger et al. demonstrated a comprehensive picture of the environmental effect inside the RM on the proton transfer dynamics of 8-Hydroxypyrene-1,3,6-trisulfonic acid (HPTS).[83] ESPT behavior of 7-hydroxy-4-

methylcoumarin has been explored to differentiate confined 'water pools' of the various reverse micelles using steady-state and time-resolved fluorescence measurements.[84] ESPT dynamics of 2-(2′-pyridyl)benzimidazole in reverse micelle was investigated by Datta and coworkers, and the observed rise time in the tautomer emission was explained by consideration of slowing down of the ESPT process and slow solvation of the more polar excited state of the tautomeric form in the restricted environment of the micro-emulsion.[85] Douhal and coworkers observed slower proton transfer dynamics of 7-hydroxyquinoline (7HQ) inside AOT reverse micelles. The lower fluidity of confined water within the RM with respect to normal bulk water alters the related H-bond network dynamics and, therefore, was believed to be responsible for the slower proton transfer dynamics.[86] Fayer group probed proton transfer kinetics of the fluorescent photoacid 8-hydroxypyrene-1,3,6-trisulfonate (HPTS) in both ionic and neutral reverse micelles by time-correlated single-photon counting technique. They observed that the nature of interfaces, ionic versus neutral, results in major differences in the location of the photoacid and in the proton transfer dynamics.[87] Very recently, Sarkar and coworkers showed that it is possible to control the intramolecular proton transfer (ESIPT) process of curcumin by simply changing AOT reverse micellar interfacial properties by choosing appropriate polar solvents.[88] They also reported that proton transfer of firefly's chromophore (D-luciferin) in nanometer size 'water pool' of RM increases with increasing w_0 values.[89] However, the ESPT of D-luciferin is inhibited in non-aqueous reverse micelles with DMF and DMSO as a polar core.[89]

1.2.4. Fluorescent Metal Clusters

Metal nanoclusters (NCs) consisting of few to several tens of atoms (size <2 nm) have recently received a special attention among researchers due to their unique optical and electronic properties.[5,90] As the size of NCs approaches close to the Fermi wavelength of electron, it possesses discrete energy levels due to quantum confinement effect.[5,90] This quantum confinement is majorly responsible for their molecule-like optical properties, and greatly inspires researchers to develop NCs as an alternative to conventional fluorophores.[5,90] Moreover, the properties of NCs are believed to be in between the nanoparticles and individual molecules, and are considered as an ideal replacement towards the semiconducting quantum dots and organic fluorophore for many technical applications due to their ultrafine size, excellent photo-stability and low toxicity.[5b,90b,91]

Because of these unique properties, NCs have been actively utilized in many applications like, optoelectronics, bioimaging, catalysis, biological labeling, and sensing.[91b,92] In order to

improve their applications in bioimaging and photonics, understanding the mechanism of their fluorescence behavior is of primary importance, which has been investigated in recent reports.[93] The exact origin behind the luminescence behaviour of metal nanoclusters still remains unclear. Jin has proposed the optical properties of metal NCs,[94] based on the free-electron model theory. According to this theory, free electrons on the nanoparticle surface give rise to the polarization in an electronic field which in turn depends on the number of electrons. However, when the free electron number significantly decreases, (so that nanoparticle size approaches to the Fermi wavelength) the continuous band structure breaks up into discrete energy levels (**Scheme 1.7**). The luminescence of metal NCs is the outcome of electronic transition from *sp* bands (above the Fermi level) to *d* bands or the electronic transitions between lowest unoccupied orbital to the highest occupied orbital (HOMO–LUMO).[95] The emission energy (E_δ) of NC depend on the number of atoms, N, in each nanocluster and is simply represented in Jellium model (eqn. 1.2),[90a]

$$E_\delta = \frac{E_f}{N^{1/3}} \qquad (1.2)$$

where, E_f is the Fermi energy of metal atom and E_δ is the luminescence energy of NCs.

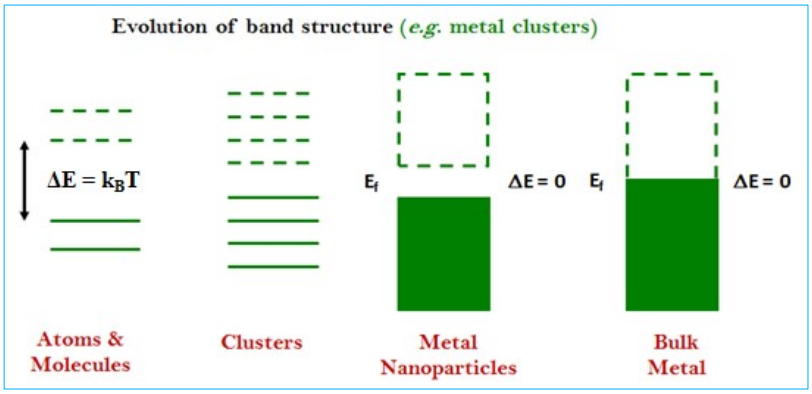

Scheme 1.7. Evolution of band structure in the metal nanoclusters.

Other mechanisms are also proposed to explain the luminescence properties of ultrasmall metal nanoclusters. Huang et al.,[95a] proposed that visible luminescence (high energy) band of AuNCs is corresponding to the radiative electron-hole (e-h) recombination of excited electron from higher energy *sp*-band to *d*-band (interband transition, **Scheme 1.8**), while, Whetten et al.,[96] suggested that infrared luminescence (lower energy) band of AuNCs is attributed to the radiative e-h recombination of excited electron within the *sp*-conduction band across the HOMO-LUMO gap (intraband transition, **Scheme 1.8**).

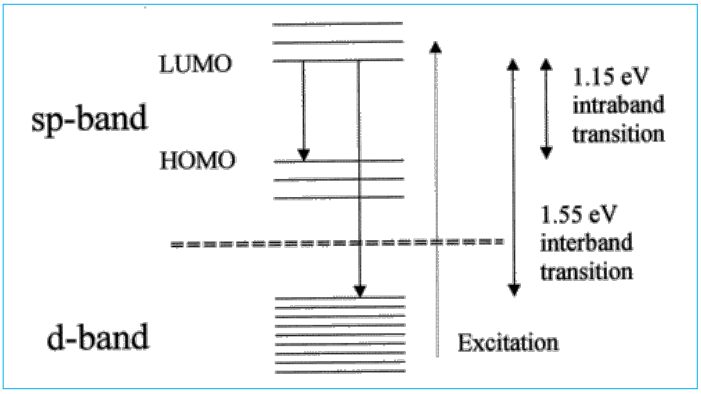

Scheme 1.8. Schematic representation of energy level diagram for the origin of two luminescence bands in the AuNCs. (i) High energy (visible) luminescence band correspond to the radiative electron-hole (e-h) recombination of excited electron from *sp*-band to *d*-band (interband transition); (ii) low energy (infrared) luminescence band corresponds to the radiative e-h recombination of excited electron within the *sp*-conduction band across the HOMO-LUMO gap (intraband transition). Reprinted with permission from ref. 96; Copyright 2018 American Chemical Society.

Like semiconducting quantum dots, metal NCs also exhibit size-dependent fluorescence behavior. In this regard, Dickson's group have synthesized a series of AuNCs with various atom numbers and observed sized-dependent fluorescence behaviour of NCs (Au_5 (385 nm), Au_8 (455 nm), Au_{13} (510 nm), Au_{23} (760 nm), and Au_{31} (866 nm)).[97] However, the emission energy of larger AuNCs is slightly deviated from this spherical Jellium model due to the electron screening effects and the distortion of the harmonic potential well, suggesting the presence of other emission mechanisms.[98] In addition to the size and structure, optical properties of metal NCs are also highly sensitive to the oxidation state of the metal atoms.[5]

Ligands used for NCs synthesis play very important role in the cluster formation, and they are referred to as protective agents/ligands, which can prevent the further aggregation between these super atoms keeping the size dependent fluorescence property intact. Protecting ligands do not only act as capping agents but also largely influence the optical properties of NCs, such as, the peak position and spectrum shape.[93,99] Several research groups have used different kinds of protective ligands for AuNCs synthesis, and interestingly, different luminescence maxima of Au_{25} NCs was observed in all these cases. For example, luminescence maximum of Au_{25} NCs is at 640 nm (bovine serum albumin),[100] 750 nm (phenyl ethane thiol),[99a] 700 nm (glutathione),[101] 700 nm (human serum albumin),[102] 670 nm (pepsin),[103] and 684 nm (dihydrolipoic acid).[104] These observations imply that the ligands on the surface of the NCs influence the emission energy due to additional emission mechanism. Jin et al. investigated the effect of surface-protected ligands of AuNCs and concluded that the

electron transfer from the surface ligands to the metal core can significantly affect the luminescence quantum efficiency.[99a] Thus, strong electron donating surface ligands enhance the fluorescence quantum yield of NCs, majorly in two different ways, (i) charge transfer from the ligands to the metal core through direct bonding (ii) direct donation of delocalized electrons of electron-rich atoms or groups of the ligands to the metal core.[99a,105] Hence, the selection of protecting ligands (such as, choosing electron-rich ligands) may improve the luminescence quantum yield of NCs.[99a]

Furthermore, emission properties of NCs also depend on the synthetic procedure. For example, two research groups have reported the different emission behaviors for same glutathione-protected Au_{25} NCs. Shibu et al.[102] observed two emission bands (500 and 700 nm), while Negishi et al.[106] observed only one emission band at 827 nm for the same glutathione-protected Au_{25} NCs. Apart from these conditions, other environmental parameters such as temperature and pH of the medium also affect the luminescence properties of nanoclusters.[107] Temperature dependent luminescence measurements of NCs confirm that the dominating electron-electron scattering process relaxes the hot electrons, which results in very broad luminescence band. Here it is necessary to mention that unlike bulk and nanoparticles, electron-phonon scattering process is very weak in nanocluster due to small size or enhanced quantum confinement effect.[5b,93,108]

Fluorescent NCs have complicated arrangement of metal atoms and surface ligands resulting in complex carrier dynamics and fluorescence mechanism. Ultrafast spectroscopic techniques have been employed to decipher the carrier dynamics and fluorescence mechanism of metal NCs, which have provided valuable insights towards their respective fluorescence mechanism.[5b,109] Ramakrishna and coworkers have observed two emission bands in different sized gold nanoclusters (Au_{25} and Au_{38}); a weak visible luminescence band (low quantum yield) and a near-infrared (NIR) luminescence bands, and the origin of these bands along with their dynamics has been probed using transient absorption and fluorescence up-conversion measurements.[107b,110] The luminescence of AuNCs in the visible region is attributed to the ultrafast electron relaxation (200 fs) within the Au core states and the NIR emission band results from the radiative electron-hole recombination (ns to μs) from Au shell to ground electronic state.[107b,110] Pyo et al. obtained ultrabright luminescent Au_{22} NCs by rigidifying the thiolate shell and observed dual luminescence bands (visible and NIR).[111] Visible luminescence decay of this Au_{22} NCs comprised of two relaxation time components, one in ultrafast timescale (200 fs) from core to shell, which then undergoes intersystem

crossing to populate the triplet states of the gold, and another in picosecond time scale due to radiative e-h recombination within the core states. NIR luminescence decay profile of the same Au_{22} NCs shows multi-exponential behaviour with several slow components (ns to μs) attributed to the luminescence from gold shell states, where ligands have significant contribution.[111] The effect of protecting ligands on the carrier dynamics of AuNCs have been observed in hexanethiol (C6S)- and glutathione (GS)-protected Au_{25} nanoclusters, which exhibit a luminescence wavelength dependent growth (180 fs to 300 fs) and a decay (240 fs to 980 fs) component, suggesting the relaxation of core-gold to shell-gold states.[101] Goodson's group reported the dendrimer protected Au_{25} NCs emission in the visible region is associated with the metal core, and is short-lived (~250 fs); whereas the NIR luminescence (longer lifetime, ns to μs) is related to the surface states arising from the ligand interaction.[112] Influence of structural morphology on the luminescence dynamics of Au_{25} NCs have been noticed in rod and sphere structures. The Au_{25}-sphere shows wavelength dependent luminescence growth (150 fs to 200 fs) and decay (>200 fs to 600 fs) whereas, Au_{25}-rod show only decay (>200 fs to 600 fs) components. Observed growth components in Au_{25}-sphere NCs corresponds to relaxation of core-gold to shell-gold states and this type of shell structure is absent in Au_{25}-rod morphology.[107c] Miller et al., have demonstrated using transient absorption measurements that core-gold to shell-gold decay dominates at the early time of excited-state relaxation of Au_{25} clusters.[113] Miller et al., proposed a core-shell relaxation model to explain the excited-state relaxation of $[Au_{25}(SCH_2CH_2Ph)_{18}]$. They have observed that ultrafast (<200 fs) relaxation within multilevel electronic states of the Au_{13} core and slightly slower lifetime (1.2 ps) component arise from the relaxation of electron from core to the semi-ring.[113] Pyo et al., monitored ultrafast dynamics of glutathione protected Au_{22} NCs ($Au_{22}(SG)_{18}$) and surface modified with pyrene (Py).[114] The fluorescence decay profile consisting of lifetime time constants 160 fs, 1.6 ps, 16 ps and >1 ns. The decay component of 160 fs was assigned as the core to shell-gold relaxation of the Au_{22} cluster, whereas 1.6 ps and 16 ps decay components assigned to the time scale of the electron/energy transfer deactivation process occurring in the Au_{22}-Py cluster. The last long lived (>1 ns) component was assigned to the surface state arising from the surface ligands or the ligand/metal interface.[114] Meng et al.,[115] reported that rod shaped Au_{25} and Ag doped (Ag_xAu_{25-x}) nanoclusters fluorescence dynamics. The excited state relaxation in Ag_xAu_{25-x} is comprised with an ultrafast (~0.58 ps), fast (~20.7 ps) followed by ultraslow (7.4 μs) correspond to the internal conversion, nuclear relaxation and electron relaxation back to the ground state,

respectively. Interestingly, the nuclear relaxation timescale is much slower in un-doped Au_{25} (~52 ps) compared to Ag_xAu_{25-x} (~20.7 ps).[115] Jin and coworkers observed ultrafast dynamics in mono atom doped M_1Au_{24} nanocluster and assigned an ultrafast relaxation of electron within the core states in the time constant of 0.6 ps, electron transfer from Au core to shell relaxation with a timescale of 3-5 ps and very slow (>1 ns) electron relaxation to the ground states.[116]

The dual fluorescence of Au_{25} NCs is a result of spectral broadening due to their specific core-semi ring structures,[108b,117] whereas, small AuNCs (Au_8 and Au_{10}) doesn't have any dual fluorescence characteristics due to absence of any core-semi ring structure, which is generally present in neutral gold atoms.[107d] In the case of ultrasmall sized clusters (Au_8), emission energy solely depends on the number of atoms composed in the NCs, on the other hand, for slightly larger clusters (Au_{25}) both the number of atoms and surface ligands protecting the NCs are responsible.[97a,108b] It has been experimentally confirmed that the ultrasmall AuNCs, such as Au_{10} and Au_8, exhibit excitation wavelength dependent fluorescence,[93,108a] and the fluorescence band was found to be red-shifted upon increasing the excitation wavelength. Recently, Tang and coworker reported, broad fluorescence of Au_8 nanocluster consists of two spectrally overlapped emission bands, intrinsic and extrinsic, corresponding to the metal core and surface ligands respectively.[93] The reason behind this unusual phenomenon is not fully understood yet. However, there is a growing evidence in favor of the argument that the emission arises from the radiative recombination of excitons located on surface states of NCs.[93] They proposed that two spectrally overlapped bands, fluorescence band-I intrinsically arise from the Au_8 core and band-II arises extrinsically originates from the localized surface trap states, which are interface between Au core and protecting ligands. Femto second time-resolved fluorescence dynamics of Au_8 NCs suggested that 1.28 ps corresponds to the excited electrons in the metal core state that are trapped into the surface sates; slow component 11.6 ps was attributed to electron-acoustic phonon scattering and the slowest component (100-150 ps) was ascribed to e-h recombination process.[93] The effective trapping of excited electrons into massive surface states is responsible for the excitation wavelength dependent fluorescence; this kind of surface trapping was observed in various colloidal nanoparticles. Recently, Díez et al., represented the three types of emitting regions in the AgNCs, which are responsible for their excitation dependent emission energies and *vice versa*.[118] Tang and coworkers have demonstrated that bandwidth of fluorescence doesn't depend on the temperature (even at cryogenic temperatures) because of weak phonon coupling in ultrasmall

NCs.[108] Bigioni and coworkers, explored the ultrafast dynamics of glutathione (SG) protected silver NCs, the photoluminescence decay consisting of two components (3 ps and 130 ps) for $Ag_{15}(SG)_{11}$ and 480 fs and 130 ps for $Ag_{32}(SG)_{19}$. The ultrafast lifetime components 3 ps (Ag_{15}) and 480 fs (Ag_{32}) in both NCs, is correspond to a fast relaxation from metal core emissive states, similar to gold core states. The longer lifetime component 130 ps (both Ag_{15} and Ag_{32}) in AgNCs are due to relaxation of excited electrons from metal-ligand state.[119] Unlike gold and silver nanoclusters, optical properties of copper nanocluster (CuNCs) have not been explored at all in the literature.

Among noble metal nanoclusters, gold nanoclusters (AuNCs) and some extent of silver nanoclusters (AgNCs) are significantly explored in terms of synthesis,[100,105,120] stabilization[105,111,121] and physical properties[105] in comparison with copper nanocluster (CuNCs) which is relatively unstable due to the low redox potential ($E^0_{Cu(II)/Cu(0)}$ = 0.34 V) of copper (Ag ($E^0_{Ag(I)/Ag(0)}$ = 0.80 V) and Au ($E^0_{Au(III)/Au(0)}$ = 1.50 V)).[122] Stabilization of CuNCs remains the primary challenge in their syntheses and applications.[5c,90a,123] In absence of stabilization, CuNCs would strongly interact with each other and aggregate irreversibly in order to reduce their surface energy.[5c,90a,123] Thus, a proper stabilizing scaffold is indispensable without which they tend to agglomerate and form non-fluorescent nanoparticles.[5a,5b,90a] Organic scaffolds are found to be advantageous, which can modulate the spectroscopic properties of the CuNCs depending on their interaction between the ligands and metals. Recently, dendrimer, thiols, polymers, various bio-molecules such as DNA oligomers, peptides, and serum albumin (bovine, human and lysozyme, etc.) have been efficiently utilized as scaffolds for the synthesis CuNCs emitting from blue to near-infrared region.[122,124] However, most of these methods generate low quantum yield CuNCs. Moreover, the syntheses involve toxic reducing agents, multiple steps, and high cost scaffolds such as protein/DNA. Recently, CuNCs are emerging as a very promising analytical platform for diverse sensing applications, especially for metal ions, biomolecules (proteins, nucleic acids etc.), small molecules and pH.[124i] Similar to that of AuNCs and AgNCs, the fluorescence properties of CuNCs are dependent on their chemical environments, including the cluster size, solvent and surface capping ligands or CuNCs prepared from different synthetic strategies etc.[124b,124d,124h,124i,125] Wu et al. demonstrated that the significant luminescence intensity enhancement of 1-dodecanethiol-capped CuNCs via self-assembly strategy.[126] Understanding the origin and mechanism behind the multi-fluorescence and spectral broadening behaviors of CuNCs are fundamentally important for their applications in

bioimaging and photonics. Dynamics studies of CuNCs are not available in the literature and its fundamental understanding of the fluorescence mechanism is still lacking.

1.3. References

1. (a) N. Alarcos, B. Cohen, M. Ziółek and A. Douhal, *Chem. Rev.*, 2017, **117**, 13639-13720; (b) V. Georgakilas, J. N. Tiwari, K. C. Kemp, J. A. Perman, A. B. Bourlinos, K. S. Kim and R. Zboril, *Chem. Rev.*, 2016, **116**, 5464-5519.
2. (a) C. Chung, Y.-K. Kim, D. Shin, S.-R. Ryoo, B. H. Hong and D.-H. Min, *Acc. Chem. Res.*, 2013, **46**, 2211-2224; (b) Y. Wang, Z. Li, J. Wang, J. Li and Y. Lin, *Trends Biotechnol.*, 2011, **29**, 205-212; (c) B. G. Trewyn, I. I. Slowing, S. Giri, H.-T. Chen and V. S. Y. Lin, *Acc. Chem. Res.*, 2007, **40**, 846-853; (d) J. M. Rosenholm, C. Sahlgren and M. Linden, *Nanoscale*, 2010, **2**, 1870-1883.
3. C. Kollmannsberger, K. Mross, A. Jakob, L. Kanz and C. Bokemeyer, *Oncology*, 1999, **56**, 1-12.
4. (a) M. R. di Nunzio, Y. Wang and A. Douhal, *J. Phys. Chem. B*, 2012, **116**, 7522-7530; (b) M. R. di Nunzio, Y. Wang and A. Douhal, *J. Phys. Chem. B*, 2012, **116**, 8182-8190; (c) K. Gavvala, A. Sengupta, R. K. Koninti and P. Hazra, *ChemPhysChem*, 2013, **14**, 3375-3383.
5. (a) H. Qian, M. Zhu, Z. Wu and R. Jin, *Acc. Chem. Res.*, 2012, **45**, 1470-1479; (b) P. Yu, X. Wen, Y.-R. Toh, X. Ma and J. Tang, *Part. Part. Syst. Charact.*, 2015, **32**, 142-163; (c) J. Li, J.-J. Zhu and K. Xu, *Trends Anal. Chem.*, 2014, **58**, 90-98.
6. A. K. Geim, *Science*, 2009, **324**, 1530.
7. C. N. R. Rao, A. K. Sood, K. S. Subrahmanyam and A. Govindaraj, *Angew. Chem. Int. Ed.*, 2009, **48**, 7752-7777.
8. S. Guo and S. Dong, *Chem. Soc. Rev.*, 2011, **40**, 2644-2672.
9. K. S. Novoselov, A. K. Geim, S. V. Morozov, D. Jiang, Y. Zhang, S. V. Dubonos, I. V. Grigorieva and A. A. Firsov, *Science*, 2004, **306**, 666.
10. X. Wang, X. Li, L. Zhang, Y. Yoon, P. K. Weber, H. Wang, J. Guo and H. Dai, *Science*, 2009, **324**, 768.
11. (a) E. Yoo, J. Kim, E. Hosono, H.-s. Zhou, T. Kudo and I. Honma, *Nano Lett.*, 2008, **8**, 2277-2282; (b) C. Wang, D. Li, C. O. Too and G. G. Wallace, *Chem. Mater.*, 2009, **21**, 2604-2606.
12. M. D. Stoller, S. Park, Y. Zhu, J. An and R. S. Ruoff, *Nano Lett.*, 2008, **8**, 3498-3502.
13. X. Li, G. Zhang, X. Bai, X. Sun, X. Wang, E. Wang and H. Dai, *Nat. Nanotechnol.*, 2008, **3**, 538.
14. L. Qu, Y. Liu, J.-B. Baek and L. Dai, *ACS Nano*, 2010, **4**, 1321-1326.
15. (a) J.-H. Chen, C. Jang, S. Xiao, M. Ishigami and M. S. Fuhrer, *Nat. Nanotechnol.*, 2008, **3**, 206; (b) V. Georgakilas, M. Otyepka, A. B. Bourlinos, V. Chandra, N. Kim, K. C. Kemp, P. Hobza, R. Zboril and K. S. Kim, *Chem. Rev.*, 2012, **112**, 6156-6214; (c) K. S. Novoselov, Z. Jiang, Y. Zhang, S. V. Morozov, H. L. Stormer, U. Zeitler, J. C. Maan, G. S. Boebinger, P. Kim and A. K. Geim, *Science*, 2007, **315**, 1379.
16. (a) Y. Kopelevich and P. Esquinazi, *Adv. Mater.*, 2007, **19**, 4559-4563; (b) S. Yang, X. Feng, L. Wang, K. Tang, J. Maier and K. Müllen, *Angew. Chem. Int. Ed.*, 2010, **49**, 4795-4799; (c) D. R. Dreyer, S. Park, C. W. Bielawski and R. S. Ruoff, *Chem. Soc. Rev.*, 2010, **39**, 228-240; (d) K. P. Loh, Q. Bao, P. K. Ang and J. Yang, *J. Mater. Chem.*, 2010, **20**, 2277-2289; (e) S. Niyogi, E. Bekyarova, M. E. Itkis, J. L. McWilliams, M. A. Hamon and R. C. Haddon, *J. Am. Chem. Soc.*, 2006, **128**, 7720-7721; (f) S. Stankovich, D. A. Dikin, G. H. B. Dommett, K. M. Kohlhaas, E. J. Zimney, E. A. Stach, R. D. Piner,

S. T. Nguyen and R. S. Ruoff, *Nature*, 2006, **442**, 282; (g) A. K. Geim and K. S. Novoselov, *Nat. Mater.*, 2007, **6**, 183.
17. K. Liu, J.-J. Zhang, F.-F. Cheng, T.-T. Zheng, C. Wang and J.-J. Zhu, *J. Mater. Chem.*, 2011, **21**, 12034-12040.
18. W. S. Hummers and R. E. Offeman, *J. Am. Chem. Soc.*, 1958, **80**, 1339-1339.
19. D. A. Dikin, S. Stankovich, E. J. Zimney, R. D. Piner, G. H. B. Dommett, G. Evmenenko, S. T. Nguyen and R. S. Ruoff, *Nature*, 2007, **448**, 457.
20. (a) Y. Liang, D. Wu, X. Feng and K. Müllen, *Adv. Mater.*, 2009, **21**, 1679-1683; (b) Y. Xu, H. Bai, G. Lu, C. Li and G. Shi, *J. Am. Chem. Soc.*, 2008, **130**, 5856-5857; (c) Y. Si and E. T. Samulski, *Nano Lett.*, 2008, **8**, 1679-1682.
21. (a) X. Li, X. Wang, L. Zhang, S. Lee and H. Dai, *Science*, 2008, **319**, 1229; (b) D. Li, M. B. Müller, S. Gilje, R. B. Kaner and G. G. Wallace, *Nat. Nanotechnol.*, 2008, **3**, 101; (c) E. Yoo, T. Okata, T. Akita, M. Kohyama, J. Nakamura and I. Honma, *Nano Lett.*, 2009, **9**, 2255-2259; (d) G. Williams, B. Seger and P. V. Kamat, *ACS Nano*, 2008, **2**, 1487-1491; (e) J. Huang, L. Zhang, B. Chen, N. Ji, F. Chen, Y. Zhang and Z. Zhang, *Nanoscale*, 2010, **2**, 2733-2738.
22. H. Jiang, *Small*, 2011, **7**, 2413-2427.
23. (a) H. Lei, L. Mi, X. Zhou, J. Chen, J. Hu, S. Guo and Y. Zhang, *Nanoscale*, 2011, **3**, 3888-3892; (b) X. Sun, Z. Liu, K. Welsher, J. T. Robinson, A. Goodwin, S. Zaric and H. Dai, *Nano Res.*, 2008, **1**, 203-212; (c) J. Zhang, F. Zhang, H. Yang, X. Huang, H. Liu, J. Zhang and S. Guo, *Langmuir*, 2010, **26**, 6083-6085; (d) F. Zhang, B. Zheng, J. Zhang, X. Huang, H. Liu, S. Guo and J. Zhang, *J. Phys. Chem. C*, 2010, **114**, 8469-8473; (e) D. Y. Lee, Z. Khatun, J.-H. Lee, Y.-k. Lee and I. In, *Biomacromolecules*, 2011, **12**, 336-341; (f) H. Dong, W. Gao, F. Yan, H. Ji and H. Ju, *Anal. Chem.*, 2010, **82**, 5511-5517; (g) W. Chen, P. Yi, Y. Zhang, L. Zhang, Z. Deng and Z. Zhang, *ACS Appl. Mater. Interfaces*, 2011, **3**, 4085-4091; (h) J. Shen, M. Shi, N. Li, B. Yan, H. Ma, Y. Hu and M. Ye, *Nano Res.*, 2010, **3**, 339-349.
24. Z. Liu, J. T. Robinson, X. Sun and H. Dai, *J. Am. Chem. Soc.*, 2008, **130**, 10876-10877.
25. W. Zhang, Z. Guo, D. Huang, Z. Liu, X. Guo and H. Zhong, *Biomaterials*, 2011, **32**, 8555-8561.
26. X. Yang, X. Zhang, Z. Liu, Y. Ma, Y. Huang and Y. Chen, *J. Phys. Chem. C*, 2008, **112**, 17554-17558.
27. H. Bai, C. Li, X. Wang and G. Shi, *Chem. Commun.*, 2010, **46**, 2376-2378.
28. D. Depan, J. Shah and R. D. K. Misra, *Mater. Sci. Eng. C*, 2011, **31**, 1305-1312.
29. L. Zhang, J. Xia, Q. Zhao, L. Liu and Z. Zhang, *Small*, 2010, **6**, 537-544.
30. Y. Pan, H. Bao, N. G. Sahoo, T. Wu and L. Li, *Adv. Funct. Mater.*, 2011, **21**, 2754-2763.
31. V. K. Rana, M.-C. Choi, J.-Y. Kong, G. Y. Kim, M. J. Kim, S.-H. Kim, S. Mishra, R. P. Singh and C.-S. Ha, *Macromol Mater. Eng.*, 2011, **296**, 131-140.
32. X. Yang, Y. Wang, X. Huang, Y. Ma, Y. Huang, R. Yang, H. Duan and Y. Chen, *J. Mater. Chem.*, 2011, **21**, 3448-3454.
33. L. Feng, S. Zhang and Z. Liu, *Nanoscale*, 2011, **3**, 1252-1257.
34. B. Chen, M. Liu, L. Zhang, J. Huang, J. Yao and Z. Zhang, *J. Mater. Chem.*, 2011, **21**, 7736-7741.
35. (a) H. Chang, L. Tang, Y. Wang, J. Jiang and J. Li, *Anal. Chem.*, 2010, **82**, 2341-2346; (b) Y. Wang, Z. Li, D. Hu, C.-T. Lin, J. Li and Y. Lin, *J. Am. Chem. Soc.*, 2010, **132**, 9274-9276; (c) L. Tang, Y. Wang, Y. Liu and J. Li, *ACS Nano*, 2011, **5**, 3817-3822; (d) X. Dong, J. Cheng, J. Li and Y. Wang, *Anal. Chem.*, 2010, **82**, 6208-6214; (e) Y. Wang, Y. Li, L. Tang, J. Lu and J. Li, *Electrochem. Commun.*, 2009, **11**, 889-892.
36. X.-H. Zhao, R.-M. Kong, X.-B. Zhang, H.-M. Meng, W.-N. Liu, W. Tan, G.-L. Shen and R.-Q. Yu, *Anal. Chem.*, 2011, **83**, 5062-5066.

37. S. Kochmann, T. Hirsch and O. S. Wolfbeis, *Trends Anal. Chem.*, 2012, **39**, 87-113.
38. X. Wang, S. Zhong, Y. He and G. Song, *Anal. Methods*, 2012, **4**, 360-362.
39. W. T. Huang, Y. Shi, W. Y. Xie, H. Q. Luo and N. B. Li, *Chem. Commun.*, 2011, **47**, 7800-7802.
40. (a) C.-H. Lu, H.-H. Yang, C.-L. Zhu, X. Chen and G.-N. Chen, *Angew. Chem. Int. Ed.*, 2009, **48**, 4785-4787; (b) X. Liu, F. Wang, R. Aizen, O. Yehezkeli and I. Willner, *J. Am. Chem. Soc.*, 2013, **135**, 11832-11839.
41. (a) C. Lu, P.-J. J. Huang, B. Liu, Y. Ying and J. Liu, *Langmuir*, 2016, **32**, 10776-10783; (b) B. Liu, Z. Sun, X. Zhang and J. Liu, *Anal. Chem.*, 2013, **85**, 7987-7993; (c) L. Gao, C. Lian, Y. Zhou, L. Yan, Q. Li, C. Zhang, L. Chen and K. Chen, *Biosens. Bioelectron.*, 2014, **60**, 22-29.
42. D. E. De Vos, M. Dams, B. F. Sels and P. A. Jacobs, *Chem. Rev.*, 2002, **102**, 3615-3640.
43. C. T. Kresge, M. E. Leonowicz, W. J. Roth, J. C. Vartuli and J. S. Beck, *Nature*, 1992, **359**, 710.
44. (a) J. L. Vivero-Escoto, I. I. Slowing, B. G. Trewyn and V. S. Y. Lin, *Small*, 2010, **6**, 1952-1967; (b) I. I. Slowing, B. G. Trewyn, S. Giri and V. S. Y. Lin, *Adv. Funct. Mater.*, 2007, **17**, 1225-1236; (c) F. Tang, L. Li and D. Chen, *Adv. Mater.*, 2012, **24**, 1504-1534; (d) C.-H. Lee, L.-W. Lo, C.-Y. Mou and C.-S. Yang, *Adv. Funct. Mater.*, 2008, **18**, 3283-3292.
45. (a) A. B. Descalzo, R. Martínez-Máñez, F. Sancenón, K. Hoffmann and K. Rurack, *Angew. Chem. Int. Ed.*, 2006, **45**, 5924-5948; (b) D. R. Radu, C.-Y. Lai, K. Jeftinija, E. W. Rowe, S. Jeftinija and V. S. Y. Lin, *J. Am. Chem. Soc.*, 2004, **126**, 13216-13217.
46. (a) I. Slowing, B. G. Trewyn and V. S. Y. Lin, *J. Am. Chem. Soc.*, 2006, **128**, 14792-14793; (b) D.-M. Huang, Y. Hung, B.-S. Ko, S.-C. Hsu, W.-H. Chen, C.-L. Chien, C.-P. Tsai, C.-T. Kuo, J.-C. Kang, C.-S. Yang, C.-Y. Mou and Y.-C. Chen, *FASEB J.*, 2005, **19**, 2014-2016; (c) T.-H. Chung, S.-H. Wu, M. Yao, C.-W. Lu, Y.-S. Lin, Y. Hung, C.-Y. Mou, Y.-C. Chen and D.-M. Huang, *Biomaterials*, 2007, **28**, 2959-2966; (d) J. Lu, M. Liong, S. Sherman, T. Xia, M. Kovochich, A. E. Nel, J. I. Zink and F. Tamanoi, *NanoBiotechnology*, 2007, **3**, 89-95; (e) S. Mayor and R. E. Pagano, *Nat. Rev. Mol. Cell Biol.*, 2007, **8**, 603.
47. (a) R. Kotcherlakota, A. K. Barui, S. Prashar, M. Fajardo, D. Briones, A. Rodriguez-Dieguez, C. R. Patra and S. Gomez-Ruiz, *Biomater. Sci.*, 2016, **4**, 448-459; (b) I. I. Slowing, J. L. Vivero-Escoto, C.-W. Wu and V. S. Y. Lin, *Adv. Drug Delivery Rev.*, 2008, **60**, 1278-1288; (c) Q. He and J. Shi, *J. Mater. Chem.*, 2011, **21**, 5845-5855.
48. (a) A. Vinu, V. Murugesan and M. Hartmann, *J. Phys. Chem. B*, 2004, **108**, 7323-7330; (b) M. Xue and G. H. Findenegg, *Langmuir*, 2012, **28**, 17578-17584; (c) S. Hudson, J. Cooney and E. Magner, *Angew. Chem. Int. Ed.*, 2008, **47**, 8582-8594.
49. (a) K. Yasutaka, Y. Takato, K. Takashi, M. Kohsuke and Y. Hiromi, *J. Phys. Chem. B*, 2011, **115**, 10335-10345; (b) M. M. Lynch, J. Liu, M. Nigra and M.-O. Coppens, *Langmuir*, 2016, **32**, 9604-9610.
50. Z. Ma, J. Bai, Y. Wang and X. Jiang, *ACS Appl. Mater. Interfaces*, 2014, **6**, 2431-2438.
51. J. S. Beck, J. C. Vartuli, W. J. Roth, M. E. Leonowicz, C. T. Kresge, K. D. Schmitt, C. T. W. Chu, D. H. Olson, E. W. Sheppard, S. B. McCullen, J. B. Higgins and J. L. Schlenker, *J. Am. Chem. Soc.*, 1992, **114**, 10834-10843.
52. (a) Y. Liu, J. Goebl and Y. Yin, *Chem. Soc. Rev.*, 2013, **42**, 2610-2653; (b) F. Hoffmann, M. Cornelius, J. Morell and M. Fröba, *Angew. Chem. Int. Ed.*, 2006, **45**, 3216-3251.
53. (a) M. Kruk, M. Jaroniec and A. Sayari, *J. Phys. Chem. B*, 1997, **101**, 583-589; (b) P. Horcajada, A. Rámila, J. Pérez-Pariente, R. Vallet, x and M., *Micropor. Mesopor. Mat.*, 2004, **68**, 105-109; (c) F. Letellier, J. Blanchard, K. Fajerwerg, C. Louis, M. Breysse, D. Guillaume and D. Uzio, *Catal. Lett.*, 2006, **110**, 115-124.

54. (a) A. Benhamou, M. Baudu, Z. Derriche and J. P. Basly, *J. Hazard. Mater.*, 2009, **171**, 1001-1008; (b) B. Coasne, F. R. Hung, R. J. M. Pellenq, F. R. Siperstein and K. E. Gubbins, *Langmuir*, 2006, **22**, 194-202.
55. P. Van Der Voort, M. Baltes and E. F. Vansant, *J. Phys. Chem. B*, 1999, **103**, 10102-10108.
56. (a) Z. Li, J. C. Barnes, A. Bosoy, J. F. Stoddart and J. I. Zink, *Chem. Soc. Rev.*, 2012, **41**, 2590-2605; (b) M. W. Ambrogio, C. R. Thomas, Y.-L. Zhao, J. I. Zink and J. F. Stoddart, *Acc. Chem. Res.*, 2011, **44**, 903-913; (c) S. Jambhrunkar, S. Karmakar, A. Popat, M. Yu and C. Yu, *RSC Adv.*, 2014, **4**, 709-712.
57. (a) D. Tarn, C. E. Ashley, M. Xue, E. C. Carnes, J. I. Zink and C. J. Brinker, *Acc. Chem. Res.*, 2013, **46**, 792-801; (b) A. Mathew, S. Parambadath, S. S. Park and C.-S. Ha, *Micropor. Mesopor. Mat.*, 2014, **200**, 124-131; (c) F. Raji, A. Saraeian, M. Pakizeh and F. Attarzadeh, *RSC Adv.*, 2015, **5**, 37066-37077.
58. (a) M. Vallet-Regi, A. Rámila, R. P. del Real and J. Pérez-Pariente, *Chem. Mater.*, 2001, **13**, 308-311; (b) J. Salonen, L. Laitinen, A. M. Kaukonen, J. Tuura, M. Björkqvist, T. Heikkilä, K. Vähä-Heikkilä, J. Hirvonen and V. P. Lehto, *J. Control. Release*, 2005, **108**, 362-374; (c) M. Arruebo, M. Galán, N. Navascués, C. Téllez, C. Marquina, M. R. Ibarra and J. Santamaría, *Chem. Mater.*, 2006, **18**, 1911-1919; (d) J. Andersson, J. Rosenholm, S. Areva and M. Lindén, *Chem. Mater.*, 2004, **16**, 4160-4167.
59. A. Demortière, S. Buathong, B. P. Pichon, P. Panissod, D. Guillon, S. Bégin-Colin and B. Donnio, *Small*, 2010, **6**, 1341-1346.
60. T. Lebold, C. Jung, J. Michaelis and C. Bräuchle, *Nano Lett.*, 2009, **9**, 2877-2883.
61. (a) M. Liong, J. Lu, M. Kovochich, T. Xia, S. G. Ruehm, A. E. Nel, F. Tamanoi and J. I. Zink, *ACS Nano*, 2008, **2**, 889-896; (b) J. Lu, E. Choi, F. Tamanoi and J. I. Zink, *Small*, 2008, **4**, 421-426; (c) T. Xia, M. Kovochich, M. Liong, H. Meng, S. Kabehie, S. George, J. I. Zink and A. E. Nel, *ACS Nano*, 2009, **3**, 3273-3286; (d) J. L. Vivero-Escoto, I. I. Slowing, C.-W. Wu and V. S. Y. Lin, *J. Am. Chem. Soc.*, 2009, **131**, 3462-3463; (e) F. Muhammad, M. Guo, W. Qi, F. Sun, A. Wang, Y. Guo and G. Zhu, *J. Am. Chem. Soc.*, 2011, **133**, 8778-8781; (f) J. Kim, J. E. Lee, J. Lee, J. H. Yu, B. C. Kim, K. An, Y. Hwang, C.-H. Shin, J.-G. Park, J. Kim and T. Hyeon, *J. Am. Chem. Soc.*, 2006, **128**, 688-689; (g) C.-L. Zhu, X.-Y. Song, W.-H. Zhou, H.-H. Yang, Y.-H. Wen and X.-R. Wang, *J. Mater. Chem.*, 2009, **19**, 7765-7770; (h) J. M. Rosenholm, E. Peuhu, J. E. Eriksson, C. Sahlgren and M. Lindén, *Nano Lett.*, 2009, **9**, 3308-3311.
62. (a) F. Torney, B. G. Trewyn, V. S. Y. Lin and K. Wang, *Nat. Nanotechnol.*, 2007, **2**, 295; (b) R. Liu, Y. Zhang, X. Zhao, A. Agarwal, L. J. Mueller and P. Feng, *J. Am. Chem. Soc.*, 2010, **132**, 1500-1501; (c) S. Giri, B. G. Trewyn, M. P. Stellmaker and V. S. Y. Lin, *Angew. Chem. Int. Ed.*, 2005, **44**, 5038-5044; (d) J. E. Lee, N. Lee, H. Kim, J. Kim, S. H. Choi, J. H. Kim, T. Kim, I. C. Song, S. P. Park, W. K. Moon and T. Hyeon, *J. Am. Chem. Soc.*, 2010, **132**, 552-557; (e) C.-Y. Lai, B. G. Trewyn, D. M. Jeftinija, K. Jeftinija, S. Xu, S. Jeftinija and V. S. Y. Lin, *J. Am. Chem. Soc.*, 2003, **125**, 4451-4459; (f) L. Tan, H.-X. Wu, M.-Y. Yang, C.-J. Liu and R.-X. Zhuo, *RSC Adv.*, 2015, **5**, 10393-10399; (g) M. Chen, X. He, K. Wang, D. He, S. Yang, P. Qiu and S. Chen, *J. Mater. Chem. B*, 2014, **2**, 428-436; (h) J. Lee, H. Kim, S. Han, E. Hong, K.-H. Lee and C. Kim, *J. Am. Chem. Soc.*, 2014, **136**, 12880-12883; (i) Y. Zhao, B. G. Trewyn, I. I. Slowing and V. S. Y. Lin, *J. Am. Chem. Soc.*, 2009, **131**, 8398-8400; (j) S. Wu, X. Huang and X. Du, *Angew. Chem. Int. Ed.*, 2013, **52**, 5580-5584; (k) S. Zhou, H. Sha, B. Liu and X. Du, *Chem. Sci.*, 2014, **5**, 4424-4433; (l) P. Zhang, F. Cheng, R. Zhou, J. Cao, J. Li, C. Burda, Q. Min and J.-J. Zhu, *Angew. Chem. Int. Ed.*, 2014, **53**, 2371-2375; (m) Z. Yu, N. Li, P. Zheng, W. Pan and B. Tang, *Chem. Commun.*, 2014, **50**, 3494-3497.

63. (a) Y.-Z. You, K. K. Kalebaila, S. L. Brock and D. Oupický, *Chem. Mater.*, 2008, **20**, 3354-3359; (b) Q. Fu, G. V. Rama Rao, T. L. Ward, Y. Lu and G. P. Lopez, *Langmuir*, 2007, **23**, 170-174.
64. (a) C. Park, K. Oh, S. C. Lee and C. Kim, *Angew. Chem. Int. Ed.*, 2007, **46**, 1455-1457; (b) J.-T. Sun, C.-Y. Hong and C.-Y. Pan, *J. Phys. Chem. C*, 2010, **114**, 12481-12486; (c) H. Meng, M. Xue, T. Xia, Y.-L. Zhao, F. Tamanoi, J. F. Stoddart, J. I. Zink and A. E. Nel, *J. Am. Chem. Soc.*, 2010, **132**, 12690-12697; (d) F. Muhammad, A. Wang, M. Guo, J. Zhao, W. Qi, G. Yingjie, J. Gu and G. Zhu, *ACS Appl. Mater. Interfaces*, 2013, **5**, 11828-11835.
65. (a) R. Liu, X. Zhao, T. Wu and P. Feng, *J. Am. Chem. Soc.*, 2008, **130**, 14418-14419; (b) R. Liu, Y. Zhang and P. Feng, *J. Am. Chem. Soc.*, 2009, **131**, 15128-15129.
66. (a) N. K. Mal, M. Fujiwara and Y. Tanaka, *Nature*, 2003, **421**, 350; (b) S. Angelos, E. Choi, F. Vögtle, L. De Cola and J. I. Zink, *J. Phys. Chem. C*, 2007, **111**, 6589-6592; (c) Y. Yang, W. Song, A. Wang, P. Zhu, J. Fei and J. Li, *Phys. Chem. Chem. Phys.*, 2010, **12**, 4418-4422; (d) A. Schlossbauer, S. Warncke, P. M. E. Gramlich, J. Kecht, A. Manetto, T. Carell and T. Bein, *Angew. Chem. Int. Ed.*, 2010, **49**, 4734-4737; (e) M. Li, H. Yan, C. Teh, V. Korzh and Y. Zhao, *Chem. Commun.*, 2014, **50**, 9745-9748.
67. (a) A. Schlossbauer, J. Kecht and T. Bein, *Angew. Chem. Int. Ed.*, 2009, **48**, 3092-3095; (b) A. Schlossbauer, D. Schaffert, J. Kecht, E. Wagner and T. Bein, *J. Am. Chem. Soc.*, 2008, **130**, 12558-12559; (c) K. Patel, S. Angelos, W. R. Dichtel, A. Coskun, Y.-W. Yang, J. I. Zink and J. F. Stoddart, *J. Am. Chem. Soc.*, 2008, **130**, 2382-2383; (d) A. Bernardos, E. Aznar, M. D. Marcos, R. Martínez-Máñez, F. Sancenón, J. Soto, J. M. Barat and P. Amorós, *Angew. Chem. Int. Ed.*, 2009, **48**, 5884-5887; (e) C. Park, H. Kim, S. Kim and C. Kim, *J. Am. Chem. Soc.*, 2009, **131**, 16614-16615; (f) L. Mondragón, N. Mas, V. Ferragud, C. de la Torre, A. Agostini, R. Martínez-Máñez, F. Sancenón, P. Amorós, E. Pérez-Payá and M. Orzáez, *Chem. Eur. J.*, 2014, **20**, 5271-5281.
68. H. J. Kim, H. Matsuda, H. Zhou and I. Honma, *Adv. Mater.*, 2006, **18**, 3083-3088.
69. (a) B. Cohen, C. M. Alvarez, N. A. Carmona, J. A. Organero and A. Douhal, *Phys. Chem. Chem. Phys.*, 2011, **13**, 1819-1826; (b) M. Gil, C. Martin, J. A. Organero, M. T. Navarro, A. Corma and A. Douhal, *J. Phys. Chem. C*, 2010, **114**, 6311-6317; (c) B. Cohen, S. Wang, J. A. Organero, L. F. Campo, F. Sanchez and A. Douhal, *J. Phys. Chem. C*, 2010, **114**, 6281-6289; (d) C. Martín, P. Piatkowski, B. Cohen, M. Gil, M. T. Navarro, A. Corma and A. Douhal, *J. Phys. Chem. C*, 2015, **119**, 13283-13296; (e) N. Alarcos, B. Cohen and A. Douhal, *J. Phys. Chem. C*, 2014, **118**, 19431-19443; (f) B. Cohen, F. Sanchez and A. Douhal, *J. Am. Chem. Soc.*, 2010, **132**, 5507-5514; (g) N. Alarcos, B. Cohen and A. Douhal, *Phys. Chem. Chem. Phys.*, 2016, **18**, 2658-2671.
70. (a) N. E. Levinger, *Science*, 2002, **298**, 1722; (b) P. L. Luisi and B. E. Straub, *Reverse Micelles*, 1 edn., Springer, New York, U.S.A., 1984; (c) N. Nandi, K. Bhattacharyya and B. Bagchi, *Chem. Rev.*, 2000, **100**, 2013-2046; (d) N. M. Correa, J. J. Silber, R. E. Riter and N. E. Levinger, *Chem. Rev.*, 2012, **112**, 4569-4602; (e) K. Bhattacharyya, *Acc. Chem. Res.*, 2003, **36**, 95-101; (f) D. C. Crans and N. E. Levinger, *Acc. Chem. Res.*, 2012, **45**, 1637-1645; (g) K. Bhattacharyya and B. Bagchi, *J. Phys. Chem. A*, 2000, **104**, 10603-10613.
71. N. E. Levinger and L. A. Swafford, *Annu. Rev. Phys. Chem.*, 2009, **60**, 385-406.
72. (a) H. B. Bohidar and M. Behboudnia, *Colloids Surf. A*, 2001, **178**, 313-323; (b) V. R. Vasquez, B. C. Williams and O. A. Graeve, *J. Phys. Chem. B*, 2011, **115**, 2979-2987; (c) D. E. Moilanen, E. E. Fenn, D. Wong and M. D. Fayer, *J. Phys. Chem. B*, 2009, **113**, 8560-8568; (d) R. Costard and T. Elsaesser, *J. Phys. Chem. B*, 2013, **117**, 15338-15345; (e) I. R. Piletic, H.-S. Tan and M. D. Fayer, *J. Phys. Chem. B*, 2005, **109**, 21273-21284; (f) S. H. Chen, *Annu. Rev. Phys. Chem.*, 1986, **37**, 351-399; (g) M. R. Harpham, B. M.

Ladanyi, N. E. Levinger and K. W. Herwig, *J. Chem. Phys.*, 2004, **121**, 7855-7868; (h) B. A. Simmons, C. E. Taylor, F. A. Landis, V. T. John, G. L. McPherson, D. K. Schwartz and R. Moore, *J. Am. Chem. Soc.*, 2001, **123**, 2414-2421; (i) A. Orte, M. J. Ruedas-Rama, J. M. Paredes, L. Crovetto and J. M. Alvarez-Pez, *Langmuir*, 2011, **27**, 12792-12799; (j) J. Chowdhary and B. M. Ladanyi, *J. Phys. Chem. B*, 2009, **113**, 15029-15039.

73. B. Cohen, D. Huppert, K. M. Solntsev, Y. Tsfadia, E. Nachliel and M. Gutman, *J. Am. Chem. Soc.*, 2002, **124**, 7539-7547.
74. (a) M. Hasegawa, T. Sugimura, Y. Suzaki, Y. Shindo and A. Kitahara, *J. Phys. Chem.*, 1994, **98**, 2120-2124; (b) S.-Y. Park, O.-H. Kwon, T. G. Kim and D.-J. Jang, *J. Phys. Chem. C*, 2009, **113**, 16110-16115.
75. B. Baruah, J. M. Roden, M. Sedgwick, N. M. Correa, D. C. Crans and N. E. Levinger, *J. Am. Chem. Soc.*, 2006, **128**, 12758-12765.
76. (a) I. R. Piletic, D. E. Moilanen, D. B. Spry, N. E. Levinger and M. D. Fayer, *J. Phys. Chem. A*, 2006, **110**, 4985-4999; (b) R. Biswas, J. Furtado and B. Bagchi, *J. Chem. Phys.*, 2013, **139**, 144906; (c) D. B. Spry, A. Goun, K. Glusac, D. E. Moilanen and M. D. Fayer, *J. Am. Chem. Soc.*, 2007, **129**, 8122-8130.
77. (a) M. P. Pileni, *J. Phys. Chem.*, 1993, **97**, 6961-6973; (b) M. P. Pileni, *Langmuir*, 1997, **13**, 3266-3276; (c) M.-P. Pileni, *Nat. Mater.*, 2003, **2**, 145; (d) D. Singha, N. Barman and K. Sahu, *J. Colloid Interface Sci.*, 2014, **413**, 37-42; (e) P. Setua, A. Chakraborty, D. Seth, M. U. Bhatta, P. V. Satyam and N. Sarkar, *J. Phys. Chem. C*, 2007, **111**, 3901-3907.
78. (a) C. M. L. Carvalho and J. M. S. Cabral, *Biochimie*, 2000, **82**, 1063-1085; (b) K. Holmberg, *Curr. Opin. Colloid Interface Sci.*, 2003, **8**, 187-196; (c) N. L. Klyachko and A. V. Levashov, *Curr. Opin. Colloid Interface Sci.*, 2003, **8**, 179-186.
79. (a) E. Caponetti, D. Chillura-Martino, F. Ferrante, L. Pedone, A. Ruggirello and V. Turco Liveri, *Langmuir*, 2003, **19**, 4913-4922; (b) A. Sengupta, R. V. Khade and P. Hazra, *J. Phys. Chem. A*, 2011, **115**, 10398-10407.
80. A. Küchler, M. Yoshimoto, S. Luginbühl, F. Mavelli and P. Walde, *Nat. Nanotechnol.*, 2016, **11**, 409–420.
81. (a) K. G. Valentine, R. W. Peterson, J. S. Saad, M. F. Summers, X. Xu, J. B. Ames and A. J. Wand, *Structure*, **18**, 9-16; (b) K. Das, S. Maiti and P. K. Das, *Langmuir*, 2014, **30**, 2448-2459; (c) K. G. Valentine, G. Mathies, S. Bédard, N. V. Nucci, I. Dodevski, M. A. Stetz, T. V. Can, R. G. Griffin and A. J. Wand, *J. Am. Chem. Soc.*, 2014, **136**, 2800-2807; (d) M. G. Pawar and S. G. Srivatsan, *J. Phys. Chem. B*, 2013, **117**, 14273-14282; (e) I. Dodevski, N. V. Nucci, K. G. Valentine, G. K. Sidhu, E. S. O'Brien, A. Pardi and A. J. Wand, *J. Am. Chem. Soc.*, 2014, **136**, 3465-3474; (f) H. Workman and P. F. Flynn, *J. Am. Chem. Soc.*, 2009, **131**, 3806-3807.
82. O.-H. Kwon and D.-J. Jang, *J. Phys. Chem. B*, 2005, **109**, 20479-20484.
83. M. Sedgwick, R. L. Cole, C. D. Rithner, D. C. Crans and N. E. Levinger, *J. Am. Chem. Soc.*, 2012, **134**, 11904-11907.
84. S. D. Choudhury and H. Pal, *J. Phys. Chem. B*, 2009, **113**, 6736-6744.
85. T. K. Mukherjee, D. Panda and A. Datta, *J. Phys. Chem. B*, 2005, **109**, 18895-18901.
86. G. Angulo, J. A. Organero, M. A. Carranza and A. Douhal, *J. Phys. Chem. B*, 2006, **110**, 24231-24237.
87. C. Lawler and M. D. Fayer, *J. Phys. Chem. B*, 2015, **119**, 6024-6034.
88. C. Banerjee, C. Ghatak, S. Mandal, S. Ghosh, J. Kuchlyan and N. Sarkar, *J. Phys. Chem. B*, 2013, **117**, 6906-6916.
89. J. Kuchlyan, D. Banik, N. Kundu, S. Ghosh, C. Banerjee and N. Sarkar, *J. Phys. Chem. B*, 2014, **118**, 3401-3408.

90. (a) J. Zheng, P. R. Nicovich and R. M. Dickson, *Annu. Rev. Phys. Chem.*, 2007, **58**, 409-431; (b) S. Choi, R. M. Dickson and J. Yu, *Chem. Soc. Rev.*, 2012, **41**, 1867-1891.
91. (a) Z. Luo, K. Zheng and J. Xie, *Chem. Commun.*, 2014, **50**, 5143-5155; (b) C.-A. J. Lin, T.-Y. Yang, C.-H. Lee, S. H. Huang, R. A. Sperling, M. Zanella, J. K. Li, J.-L. Shen, H.-H. Wang, H.-I. Yeh, W. J. Parak and W. H. Chang, *ACS Nano*, 2009, **3**, 395-401.
92. (a) T.-H. Lee and R. M. Dickson, *Opt. Photonics News*, 2004, **15**; (b) H. Chen, S. Li, B. Li, X. Ren, S. Li, D. M. Mahounga, S. Cui, Y. Gu and S. Achilefu, *Nanoscale*, 2012, **4**, 6050-6064; (c) X. Jia, J. Li, L. Han, J. Ren, X. Yang and E. Wang, *ACS Nano*, 2012, **6**, 3311-3317; (d) S. Chattoraj and K. Bhattacharyya, *J. Phys. Chem. C*, 2014, **118**, 22339-22346; (e) X. Wu, X. He, K. Wang, C. Xie, B. Zhou and Z. Qing, *Nanoscale*, 2010, **2**, 2244-2249; (f) W. Feng, T. Wee Beng, Z. Yong, F. Xianping and W. Minquan, *Nanotechnology*, 2006, **17**, R1; (g) Y. Liu, K. Ai, X. Cheng, L. Huo and L. Lu, *Adv. Funct. Mater.*, 2010, **20**, 951-956; (h) J. Sun, J. Zhang and Y. Jin, *J. Mater. Chem. C*, 2013, **1**, 138-143; (i) X. Yuan, T. J. Yeow, Q. Zhang, J. Y. Lee and J. Xie, *Nanoscale*, 2012, **4**, 1968-1971.
93. X. Wen, P. Yu, Y.-R. Toh, X. Ma, S. Huang and J. Tang, *Nanoscale*, 2013, **5**, 10251-10257.
94. S. Wang, X. Meng, A. Das, T. Li, Y. Song, T. Cao, X. Zhu, M. Zhu and R. Jin, *Angew. Chem. Int. Ed.*, 2014, **53**, 2376-2380.
95. (a) T. Huang and R. W. Murray, *J. Phys. Chem. B*, 2001, **105**, 12498-12502; (b) T. P. Bigioni, R. L. Whetten and Ö. Dag, *J. Phys. Chem. B*, 2000, **104**, 6983-6986.
96. S. Link, A. Beeby, S. FitzGerald, M. A. El-Sayed, T. G. Schaaff and R. L. Whetten, *J. Phys. Chem. B*, 2002, **106**, 3410-3415.
97. (a) J. Zheng, C. Zhang and R. M. Dickson, *Phys. Rev. Lett.*, 2004, **93**, 077402; (b) J. Zheng, J. T. Petty and R. M. Dickson, *J. Am. Chem. Soc.*, 2003, **125**, 7780-7781.
98. (a) C.-C. Huang, Z. Yang, K.-H. Lee and H.-T. Chang, *Angew. Chem.*, 2007, **119**, 6948-6952; (b) M. Yu, C. Zhou, J. Liu, J. D. Hankins and J. Zheng, *J. Am. Chem. Soc.*, 2011, **133**, 11014-11017.
99. (a) Z. Wu and R. Jin, *Nano Lett.*, 2010, **10**, 2568-2573; (b) F. Dufour, B. Fresch, O. Durupthy, C. Chaneac and F. Remacle, *J. Phys. Chem. C*, 2014, **118**, 4362-4376.
100. J. Xie, Y. Zheng and J. Y. Ying, *J. Am. Chem. Soc.*, 2009, **131**, 888-889.
101. M. S. Devadas, J. Kim, E. Sinn, D. Lee, T. Goodson and G. Ramakrishna, *J. Phys. Chem. C*, 2010, **114**, 22417-22423.
102. E. S. Shibu, M. A. H. Muhammed, T. Tsukuda and T. Pradeep, *J. Phys. Chem. C*, 2008, **112**, 12168-12176.
103. H. Kawasaki, K. Hamaguchi, I. Osaka and R. Arakawa, *Adv. Funct. Mater.*, 2011, **21**, 3508-3515.
104. L. Shang, S. Brandholt, F. Stockmar, V. Trouillet, M. Bruns and G. U. Nienhaus, *Small*, 2012, **8**, 661-665.
105. I. Diez and R. H. A. Ras, *Nanoscale*, 2011, **3**, 1963-1970.
106. Y. Negishi, Y. Takasugi, S. Sato, H. Yao, K. Kimura and T. Tsukuda, *J. Am. Chem. Soc.*, 2004, **126**, 6518-6519.
107. (a) J. T. van Wijngaarden, O. Toikkanen, P. Liljeroth, B. M. Quinn and A. Meijerink, *J. Phys. Chem. C*, 2010, **114**, 16025-16028; (b) M. S. Devadas, S. Bairu, H. Qian, E. Sinn, R. Jin and G. Ramakrishna, *J. Phys. Chem. Lett.*, 2011, **2**, 2752-2758; (c) M. S. Devadas, V. D. Thanthirige, S. Bairu, E. Sinn and G. Ramakrishna, *J. Phys. Chem. C*, 2013, **117**, 23155-23161; (d) X. Le Guével, B. Hötzer, G. Jung, K. Hollemeyer, V. Trouillet and M. Schneider, *J. Phys. Chem. C*, 2011, **115**, 10955-10963.
108. (a) P. Yu, X. Wen, Y.-R. Toh and J. Tang, *J. Phys. Chem. C*, 2012, **116**, 6567-6571; (b) X. Wen, P. Yu, Y.-R. Toh and J. Tang, *J. Phys. Chem. C*, 2012, **116**, 11830-11836.

109. S. H. Yau, O. Varnavski and T. Goodson, *Acc. Chem. Res.*, 2013, **46**, 1506-1516.
110. M. S. Devadas, K. Kwak, J.-W. Park, J.-H. Choi, C.-H. Jun, E. Sinn, G. Ramakrishna and D. Lee, *J. Phys. Chem. Lett.*, 2010, **1**, 1497-1503.
111. K. Pyo, V. D. Thanthirige, K. Kwak, P. Pandurangan, G. Ramakrishna and D. Lee, *J. Am. Chem. Soc.*, 2015, **137**, 8244-8250.
112. S. H. Yau, O. Varnavski, J. D. Gilbertson, B. Chandler, G. Ramakrishna and T. Goodson, *J. Phys. Chem. C*, 2010, **114**, 15979-15985.
113. (a) S. A. Miller, J. M. Womick, J. F. Parker, R. W. Murray and A. M. Moran, *J. Phys. Chem. C*, 2009, **113**, 9440-9444; (b) S. A. Miller, C. A. Fields-Zinna, R. W. Murray and A. M. Moran, *J. Phys. Chem. Lett.*, 2010, **1**, 1383-1387.
114. K. Pyo, V. D. Thanthirige, S. Y. Yoon, G. Ramakrishna and D. Lee, *Nanoscale*, 2016, **8**, 20008-20016.
115. M. Zhou, J. Zhong, S. Wang, Q. Guo, M. Zhu, Y. Pei and A. Xia, *J. Phys. Chem. C*, 2015, **119**, 18790-18797.
116. M. Zhou, H. Qian, M. Y. Sfeir, K. Nobusada and R. Jin, *Nanoscale*, 2016, **8**, 7163-7171.
117. (a) X. Wen, P. Yu, Y.-R. Toh, A.-C. Hsu, Y.-C. Lee and J. Tang, *J. Phys. Chem. C*, 2012, **116**, 19032-19038; (b) M. Zhu, C. M. Aikens, F. J. Hollander, G. C. Schatz and R. Jin, *J. Am. Chem. Soc.*, 2008, **130**, 5883-5885.
118. I. Diez, R. H. A. Ras, M. I. Kanyuk and A. P. Demchenko, *Phys. Chem. Chem. Phys.*, 2013, **15**, 979-985.
119. B. A. Ashenfelter, A. Desireddy, S. H. Yau, T. Goodson and T. P. Bigioni, *J. Phys. Chem. C*, 2015, **119**, 20728-20734.
120. (a) D. Thompson, J. P. Hermes, A. J. Quinn and M. Mayor, *ACS Nano*, 2012, **6**, 3007-3017; (b) Z. Shen, H. Duan and H. Frey, *Adv. Mater.*, 2007, **19**, 349-352; (c) J. T. Petty, J. Zheng, N. V. Hud and R. M. Dickson, *J. Am. Chem. Soc.*, 2004, **126**, 5207-5212.
121. (a) C. I. Richards, S. Choi, J.-C. Hsiang, Y. Antoku, T. Vosch, A. Bongiorno, Y.-L. Tzeng and R. M. Dickson, *J. Am. Chem. Soc.*, 2008, **130**, 5038-5039; (b) N. Goswami, F. Lin, Y. Liu, D. T. Leong and J. Xie, *Chem. Mater.*, 2016, **28**, 4009-4016.
122. R. Ghosh, A. K. Sahoo, S. S. Ghosh, A. Paul and A. Chattopadhyay, *ACS Appl. Mater. Interfaces*, 2014, **6**, 3822-3828.
123. Y. Hu, W. Guo and H. Wei, *Isr. J. Chem.*, 2015, **55**, 682-697.
124. (a) M. Zhao, L. Sun and R. M. Crooks, *J. Am. Chem. Soc.*, 1998, **120**, 4877-4878; (b) N. K. Das, S. Ghosh, A. Priya, S. Datta and S. Mukherjee, *J. Phys. Chem. C*, 2015, **119**, 24657-24664; (c) X. Yang, Y. Feng, S. Zhu, Y. Luo, Y. Zhuo and Y. Dou, *Anal. Chim. Acta*, 2014, **847**, 49-54; (d) Z. Qing, X. He, D. He, K. Wang, F. Xu, T. Qing and X. Yang, *Angew. Chem. Int. Ed.*, 2013, **52**, 9719-9722; (e) A. Rotaru, S. Dutta, E. Jentzsch, K. Gothelf and A. Mokhir, *Angew. Chem. Int. Ed.*, 2010, **49**, 5665-5667; (f) Z. Zhou, Y. Du and S. Dong, *Anal. Chem.*, 2011, **83**, 5122-5127; (g) H. Huang, H. Li, A.-J. Wang, S.-X. Zhong, K.-M. Fang and J.-J. Feng, *Analyst*, 2014, **139**, 6536-6541; (h) N. Goswami, A. Giri, M. S. Bootharaju, P. L. Xavier, T. Pradeep and S. K. Pal, *Anal. Chem.*, 2011, **83**, 9676-9680; (i) X. Hu, T. Liu, Y. Zhuang, W. Wang, Y. Li, W. Fan and Y. Huang, *Trends Anal. Chem.*, 2016, **77**, 66-75.
125. (a) Y. Ling, J. J. Wu, Z. F. Gao, N. B. Li and H. Q. Luo, *J. Phys. Chem. C*, 2015, **119**, 27173-27177; (b) Z. Wang, B. Chen, A. S. Susha, W. Wang, C. J. Reckmeier, R. Chen, H. Zhong and A. L. Rogach, *Adv. Sci.*, 2016, **3**, 1600182-n/a.
126. Z. Wu, J. Liu, Y. Gao, H. Liu, T. Li, H. Zou, Z. Wang, K. Zhang, Y. Wang, H. Zhang and B. Yang, *J. Am. Chem. Soc.*, 2015, **137**, 12906-12913.

Chapter 2

Experimental: Materials and Methods

In the present chapter we discuss the detail description of materials and chemicals, synthetic procedures, sample preparations and various experimental techniques that are used for different studies. This chapter is divided into two sections. In first section, the full list materials, synthesis and sample preparations are discussed; whereas in second section we discuss about different experimental techniques and analysis.

2. Experimental: Materials and Methods

2.1. Materials

The present section contains the list of several fluorescent anticancer drugs, organic molecules, organic solvents and various salts that are used in different experiments.

Table 2.1. Materials, its source and purity along with the chapter number.

Name	Source	Grade (Purity)	Ch.
Graphite flakes	Sigma-Aldrich	98%	2
Ellipticine	Sigma-Aldrich	High purity > 99%	2
Topotecan	Sigma-Aldrich	Purity ≥ 99%	3
Mesoporous silica (MCM-41)	Sigma-Aldrich	Purity ≥ 99%	2
Human serum albumin (HSA)	Sigma-Aldrich	Molecular Biology	2
Hen egg white lysozyme	Sigma-Aldrich	Purity >90%	2
Salmon sperm DNA (2000 bp long)	Sigma-Aldrich	Molecular Biology	2
Calf thymus DNA Na salt (1000 bp long)	Sigma-Aldrich	Molecular Biology	2
Glucose	Sigma-Aldrich	Purity ≥ 99%	2
Hydrogen peroxide (H_2O_2)	Sigma-Aldrich	ISO	2
Sulphuric Acid (H_2SO_4)	SRL, India	Purity 98%	2
Potassium persulfate ($K_2S_2O_8$)	SRL, India	Purity 99%	2
Phosphorus pentoxide (P_2O_5)	SRL, India	Purity 99%	2
Sodium nitrate ($NaNO_3$)	SRL, India	Purity 98%	2
Potassium permanganate ($KMnO_4$)	SRL, India	Purity 98%	2
Hydrochloric acid (HCl)	Merck, India	Purity 99.5%	2
Sodium phosphate dibasic (NaH_2PO_4)	SRL, India	Purity 99.5%	2
Sodium phosphate dibasic (Na_2HPO_4)	SRL, India	Purity 99.5%	2
Sodium chloride (NaCl)	SRL, India	BioXtra≥ 99.5%	2
Sodium hydroxide (NaOH)	SRL, India	Purity 98%	2,3,4
n-heptane	Spectrochem	Spectroscopy	3,4
Dioctyl sulfosuccinate sodium salt (AOT)	Sigma-Aldrich	Ultra >99.0%	3,4
CTAB	Sigma-Aldrich	Purity ≥ 99%	4
Triton-X	Sigma-Aldrich	Purity ≥ 99%	4
DMSO	Merck, India	Spectroscopy	2
Copper (II) chloride ($CuCl_2$)	Sigma-Aldrich	Purity, 98%	3
L-Cysteine	Sigma-Aldrich	Purity, 97%	3
1-heptanol	Sigma-Aldrich	Purity, 97%	3

2.1.1. Synthesis and Sample Preparations

Detailed description of synthesis, preparation of samples and experimental methods in each chapter is given below.

Chapter 3a: Synthesis of Graphene Oxide (GO) GO was synthesized using modified Hummers method[1] from graphite flakes. 2 g of graphite flakes was added in 97 wt% H_2SO_4 (20mL), 1.6 g $K_2S_2O_8$ and 1.6 g P_2O_5 mixture. The mixture was kept at 80 °C for 8 hrs, cooled at room temperature, diluted with 0.5 L of de-ionized water and left for overnight. Then the mixture was filtered, washed several times with de-ionized water for removal of residual acids, and dried in vacuum oven overnight at 60 °C. Finally, we obtained 1.3 g of pre-oxidized graphite. The pre-oxidized graphite was further subjected to oxidation process for synthesizing GO. 1 g of pre-oxidized graphite powder and sodium nitrate ($NaNO_3$; 0.5 g, 0.5 eql.) mixture was taken in a flask kept in ice-water bath. Then, concentrated H_2SO_4 (97 wt%, 40 ml) was added with stirring. After that potassium permanganate ($KMnO_4$; 3 g, 2 eql.) added very slowly over ~1 hr, and continued the stirring for 2 hrs in ice-water bath. After removing from the ice water bath, the stirring was continued vigorously for 2 days at room temperature, and after that aqueous H_2SO_4 (5 wt%, 100 ml) was added very slowly up to ~1 hr with constant stirring. The temperature was automatically raised up to 60 °C, and then the final temperature of the reaction mixture was kept above 90 °C by supplying external heat. The resultant mixture was further stirred for 2 hrs at 98 °C, and the temperature was then reduced to 60 °C. Then H_2O_2 aqueous solution (30wt%, 10 ml) was added and the mixture was stirred for 2 hrs at room temperature. The product was repeatedly washed with aqueous HCl solution (10 wt%) and then rinsed with de-ionized water repeatedly up to neutral pH obtained. Then mixture was washed with ethanol solution for three times and finally oxidized compound was dried at ambient conditions overnight.

Chapter 3a: As ellipticine (C17H14N2) (EPT) is not soluble in water, we have used DMSO stock solution for all experiments. Concentrated ellipticine (EPT) stock solution was prepared in DMSO solvent. 4 µl of this stock solution was added into 4 ml of aqueous buffer solution (pH 7) and strongly sonicated to obtain a homogeneous solution in PBS. For all the experiments, the concentration of EPT was kept ~7µM. GO (0.16 mg/ml) stock solution was prepared in aqueous solution by strong sonication about 2 hrs, centrifuged ~14,000 rpm to remove large sized GO sheets and supernant solution was used for titration to the EPT containing PBS solution. DNA, RNA samples are properly annealed at ~90 °C and gradually allowed to cool at room temperature. Concentration of salmon sperm DNA was estimated by

its absorbance at 260 nm using extinction coefficient 13,800 $M^{-1}cm^{-1}$ per base pair,[2] and TAR-RNA concentration was measured by its absorbance at 260 nm with using molar extinction coefficient 2,73,800 $M^{-1}cm^{-1}$ generated by IDT SciTools. The molar extinction coefficient of human serum albumin (HSA) used for concentration calculation is 36,500 $M^{-1}cm^{-1}$ at 280 nm[3]. All the experiments were performed at room temperature in aqueous buffer.

Chapter 3b: Mesoporous silica (MCM-41) with pore diameter of 20-30 Å is dried in vacuum oven at 200 ºC in order to remove trace amount of encapsulated water molecules. 2 mg of EPT dissolved in dichloromethane (DCM) solvent (30 ml) and 10 mg of dried MCM-41 was introduced to the EPT containing DCM solvent. Then the dispersed solution was allowed for stirring at room temperature in nitrogen gas environment for overnight to avoid moisture absorption. Loading of drug into MCM-41 was verified by fluorescence spectra. Drug loaded MCM-41 particles were extracted from DCM solvent by centrifugation (10000 rpm). EPT-MCM was repetitively washed with DCM solvent to remove the unbound or weakly bounded drug molecules from MCM-41, and finally the compound was dried overnight at inert conditions. Extracted EPT loaded MCM-41 (EPT-MCM) sample was dispersed in 10 mM phosphate buffer saline (PBS) containing 100 mM NaCl for bio-molecular interactions. DNA samples are properly annealed at 90-95 ºC and gradually allowed to cool at room temperature. Concentration of calf thymus DNA was estimated by its absorbance at 260 nm using extinction coefficient 6,600 $M^{-1}cm^{-1}$ per base pair.[4] The molar extinction coefficient of lysozyme used for concentration calculation was 37,970 M^{-1} cm^{-1} at 280 nm.[5]

Cell Viability Assay: Five thousand HeLa cells were seeded per well in 96-well microliter plate and incubated overnight in a 5% CO_2 incubator at 37 °C for attachment. Cells were then treated with EPT-MCM (ellipticine loaded MCM-41), EPT-MCM-Lys (Lysozyme protected EPT-MCM) and free ellipticine in different concentrations (0.097, 0.19, 0.39, 0.78, 1.59, 3.12, 6.25, 12.5, 25, 50 μM) for 24h. Free EPT was dissolved in DMSO to make a stock solution of 5 mM concentration. Serial dilutions of free drugs in DMSO were made from this stock solution and 2 μL of each free drug solution was added to cells to obtain desired final concentrations. 20 μL of MTT reagent (5 mg/ml) was added to each well and incubated for 4 h at 37 °C. Formazan crystals were then solubilised in 100 μL of the solubilization buffer (10% SDS in 0.01 M HCl) and incubated overnight. Absorbance was measured with spectrophotometer at 300 nm. The percent cell viability was calculated considering the untreated cells as 100% viability and the effectiveness of EPT-MCM and EPT-MCM-Lys were compared with the free drug.

Cellular Internalization through Confocal Laser Scanning Microscopy (CLSM) Studies: 1×10^5 HeLa cells were seeded on a cover slip in a 6 well plate and incubated overnight in a 5% CO_2 incubator at 37 °C for attachment. Cells were then treated with EPT-MCM and EPT-MCM-Lys systems (at a concentration equivalent to 2 μg/mL of ellipticine) for 1, 3, 6 and 12h. Cells were then washed twice with PBS and fixed with 500 μL of paraformaldehyde (3.7% in PBS, pH = 6.9) by incubating for 10 min at 4 °C. The paraformaldehyde was aspirated and cells are washed trice with PBS, followed by staining the cells for nuclei with 2 μg/ml Hoechst by incubating at 37 °C for 5 min. Then cells were washed thrice with PBS and mounted on a glass slide using 5 μL Slow Fade Gold Antifade Reagent. The slides were subjected to fluorescence imaging using a CLSM (Zeiss LSM 710).

Chapter 4: Dioctyl sulfosuccinate sodium salt (AOT) was properly dried under vacuum pump about 48 hrs before preparing RM. Topotecan (TPT) was directly added to n-heptane solvent and sonicated for 15 minutes for uniform distribution of drug molecules. After that AOT (0.1 M) was added to the above mentioned solution, and a clear transparent solution was observed. The concentration of AOT was kept at 0.1 M for all measurements. The size of confined 'nanopool' depends on the w_0 value, where w_0 = [water]/[AOT].[6] RM of various w_0 values were prepared by the addition of appropriate amount of Milli-Q water to the AOT/n-heptane system.

Chapter 5: AOT, CTAB and TX-100 were properly dried under vacuum pump about 48 hrs before preparing reverse micelles. RM of various w_0 values were prepared by the addition of appropriate amount of Milli-Q water to the AOT/CTAB/TX-100-n-heptane system. In the case of CTAB and TX-100 reverse micelles systems 1-heptanol was used as a co-surfactant.

Synthesis of CuNCs in the Aqueous Phase: CuNCs in bulk water were synthesised similar to the recently reported synthetic procedure with slight modification.[7] Typically, 1 mM of $CuCl_2$ was added into 35 mM of L-cysteine solution. After vigorous stirring of this solution, NaOH (0.1 M) was added slowly to adjust the pH around 10-11. This mixture was then stirred continuously at 50-55 °C in water bath for 4-5 hours. The colour of the reaction mixture changes from transparent to light brown colour indicating the formation of CuNCs. The formation of CuNCs was confirmed by the appearance of blue emission under UV light. CuNCs obtained were stored at 4 °C in a dark place.

Synthesis of CuNCs inside Reverse Micelles: AOT (0.2 M) was dissolved in 10 mL n-heptane solvent and divided into two 5 mL parts each. Aqueous solutions of $CuCl_2$ (20 mM) and L-cysteine (240 mM) were prepared in separate vials. In one part of AOT/n-heptane solution $CuCl_2$ (180 μL for w_0 = 20) was added to maintain fixed w_0 value. In another part of

AOT/n-heptane solution, aqueous L-cysteine solution (180 μL for w_0 = 20) was added. In both the cases same molar ratio (w_0) i.e., w_0 = [H_2O]/[AOT] was maintained and the solutions were vigorously stirred for 2 hrs at room temperature. Subsequently, both the solutions were mixed together and the resultant mixture was heated at 50 °C under stirring conditions. By the addition of very small amount (10 μl) of 0.1 M NaOH, the colour of solution turned to light violet from colorless, indicating the initiation of reaction due to activation of L-cysteine. After 5 hrs of stirring at 50 °C, the reaction mixture was tested under UV-lamp to confirm the formation of fluorescent CuNCs inside the reverse micelles. CuNCs synthesis in other two reverse micelles, such as positive charged surfactant CTAB and neutral surfactant TX-100, also followed similar method, as AOT. In these procedures (CTAB and TX-100 reverse micelles) 1-heptanol used as co-surfactant. Importantly, in this synthetic procedure we have not used any toxic reducing agent. Notably, L-cysteine acts as both reducing as well as protecting ligand for CuNCs.

2.2. Experimental Methods

In this section we have provided detailed description of experimental methods used for various experiments done in this thesis.

2.2.1. Absorption Measurements

The absorption spectroscopy is a well known technique; hence, we are not providing instrumental setup for absorption measurements here. Briefly, all the absorption measurements were recorded on a double beam, ultraviolet-visible (UV-Vis) spectrophotometer (Shimadzu-2450). In all experimental conditions chromophore concentrations were kept in micro molar (μM) range to avoid molecular aggregations. Path length of the cuvette was kept fixed at 1 cm for all the measurements. Moreover, all the absorption measurements were carried out at room temperature (25 ºC) unless otherwise specified.

2.2.2. Steady State Fluorescence Measurements

Steady state fluorescence spectra and quantum yield measurements were carried out on a Jobin Yvon Fluoromax-4 spectrofluorometer. The schematic diagram of spectrofluorometer is shown in **Figure 2.1**. In generally, the light source is a xenon arc lamp (power 150 watt), which emits a continuous emission from ~250 nm to ~800 nm. Monochromator (MC1) is used to select a particular excitation wavelength of light. Fluorescence is collected at right angle to the incident light beam to avoid transmitted light coming from the light source and

detected through a monochromator (MC2) and a photomultiplier tube (PMT). PMT is the detection device which works based on principle of photoelectric current generation. When a photon emitted from sample falls over metal array kept in vacuum and high voltage (950 V), it immediately generates electrons. The flow of electron along the voltage bias generates the signal. This method minimizes the inherent background noise (dark count ~1000 counts/sec) in detector (compared to traditional voltage detection module) and results much sensitive detection. Polarizers (P1 and P2) on both excitation and emission sides are used to filter the light for specific polarized light, which are used to measure anisotropy. Monochromators (MC1 and MC2) and polarizers (P1 and P2) controlling the direction and wavelengths of excitation and emission light are automated and computer controlled.

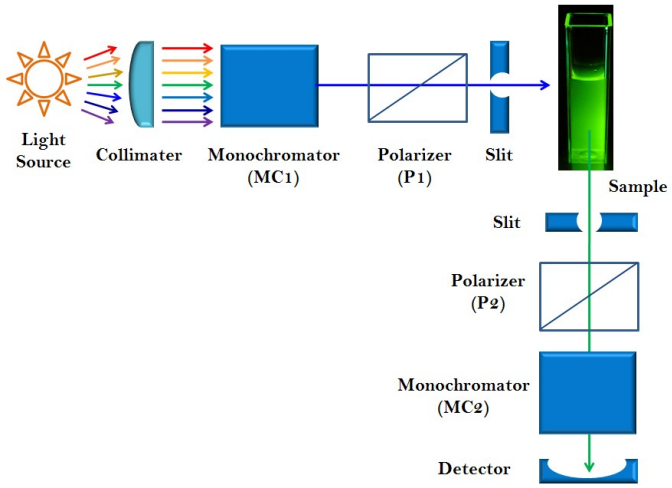

Figure 2.1. Schematic representation of spectrofluorimeter set up.

2.2.3. Time Resolved Fluorescence Measurements

2.2.3a. Time Correlated Single Photon Counting Technique (TCSPC)

After the excitation samples with a pulsed laser the excited fluorophore relaxes to ground state with an emission, which is the characteristic of emissive state. In this cases the change in the fluorescence intensity decay exponential with the time

$$I(t) = I(0)\exp(-{}^{t}/_{\tau}) \qquad (2.1)$$

where I(t) and I(0) are the fluorescence intensities at time t and 0 respectively, and τ is the fluorescence lifetime. Average time spent by the fluorophore in the excited state before coming to the ground state is called the fluorescence lifetime (τ). The time-correlated single photon counting (TCSPC) is the most popular technique for the determination of fluorescence lifetime. The basic principle of TCSPC is the probability of a single emitted photon to be

detected at a time (t) after the pulsed laser excitation, which is directly proportional to the fluorescence intensity at that time (t).[8] **Figure 2.2** shows the schematic representation of conventional TCSPC instrument set-up. In our TCSPC setup, we have used excitation sources as diode lasers (pico-LED). The full width at half maximum (FWHM) of a laser diode is ~100 ps and the repetition rate is 1 MHz. In general TCSPC can work in two different modes, forward and reverse modes. In forward mode, excitation pulse resulting from the diode laser acts as start pulse. In reverse mode, emission photon resulting from the sample excitation acts as starts pulse. In case of high repetition-rate laser sources (nano-LED/pico-LED/fs LASER), the time-to amplitude convertor (TAC) is overloaded due to continuous excitation pulses, when diode laser acts as a start pulse. Since LASER with high repetition rate (1 MHz) used as an excitation source, the reverse timing mode, which is effective to minimize the dead time caused by too many TAC reset events, has been employed for the measurements. So, avoiding the overloading in TAC, in recently most of TCSPC instruments mainly work in reverse mode.

After the pulsed excitation, single emitted photon signal from fluorophore reach to an electronics called constant fraction discriminator (CFD). The arrival times of particular photon was accurately recorded by CFD. After passing through CFD, the emitted photon signal reaches to TAC and immediately starts charging the capacitor inside TAC. Charging of the TAC capacitor generates a voltage ramp linearly with time. This is called as the START signal. TCSPC electronics is set in such a way that after the excitation only one stop photon from the sample is detected for every 100-200 excitation pulses. Arrival of an excitation pulse through synchroniser (SYNC) meanwhile reaches to TAC and stops the charging of TAC capacitor. This is called as the STOP signal. TAC is the most important component of the TCSPC system and acts as a stopwatch and measures the time gap between the start (fluorescence) and stop (excitation) pulses. The amplitude of this pulse is proportional to the charge in the capacitor, and hence to the time difference between the start and stop pulses. TAC output pulse gives a numerical value within the analog-to-digital converter (ADC) and a count is stored in the data storage corresponding to that number. This process is repeated several times to generate a histogram corresponding to the lifetime decay of the sample. The so called decay result from TCSPC instrument can be either deconvoluted considering the effect of the pulse or can be analyzed by graph plotting software by neglecting the effect of the excitation pulse. Majorly three LEDs have been used for sample excitation, namely, 375 nm (FWHM <100 ps), 402 nm (FWHM <100 ps) and 444 nm (FWHM <120 ps). Instrument response of our TCSPC set-up using the above mentioned diode lasers is ~100 ps, and with

the help of deconvolution method (discussed next section) we could able to detect lifetime of ~40 ps. The detector used in this TCSPC set-up was a MCP-PMT. In comparison to simple dynode chains in PMT, MCP-PMT consists of numerous small holes. The holes in these plates are micro-channels, and the generated photoelectrons are proximity focused into the MCP. As here electrons travel short distances, this type of PMT shows fastest time response compare to conventional PMT.

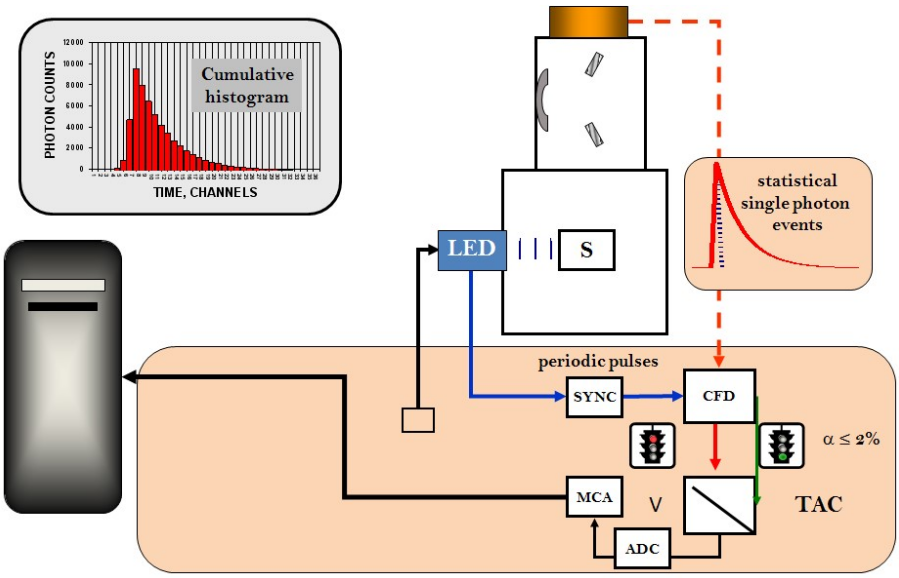

Figure 2.2. Schematic representation of spectrofluorimeter set up.

2.2.3a.1. Analysis of Fluorescence Decays

The measured decay profile is a convolution of the measured instrumental prompt response P(t) and the theoretical fluorescence response function F(t). The net result (R(t)) obtained for δ function excitation will be;[8-9]

$$R(t) = \int_0^t P(t') \times F(t - t')\, dt' \qquad (2.2)$$

where, t′ is the variable time delays (in practice, channel numbers) of the infinitesimally small widths dt′ (i.e., channel widths) of which P(t′) is composed. By measuring P(t) experimentally over 'i' channels of data, the convoluted form of R(t) can be obtained from eqn. 2.2. Here one has to assume a functional form of F(t), for example one, two or three exponentials. By iterating the values of the decay components until good agreement is obtained, the best fit values are determined.

$$F(t) = \sum_i \alpha_i\, e^{-t/\tau_i} \qquad (2.3)$$

where τ_i and α_i are the lifetime and the corresponding pre-exponential factor (amplitude) of the i^{th} component. The standard statistical procedure to confirm goodness of fit is the χ^2 test. The χ^2 is given by;

$$\chi^2 = \sum_{i=1}^{n} \omega_i [R(t) - R_c(t)]^2 \qquad (2.4)$$

where, $R_c(t)$ is calculated by assuming functional form of F(t) and $\omega_i = 1/R(t)$. The χ^2 value ~1 indicates good fit.

The analysis of fluorescence decays were performed using the commercially available lifetime analysis software (DAS 6.5) from IBH (UK). Error in all lifetime measurements is ~5%.

2.2.3a.2. Time Resolved Fluorescence Anisotropy Measurements

In fluorescence anisotropy measurement, the sample is excited with a polarized light and the time dependent parallel [$I_{\parallel}(t)$] and perpendicular [$I_{\perp}(t)$] components of the fluorescence are used to calculate the time-resolved fluorescence anisotropy, r(t), by following equation,[8b, 9]

$$r(t) = \frac{I_{\parallel}(t) - I_{\perp}(t)}{I_{\parallel}(t) + 2I_{\perp}(t)} \qquad (2.5)$$

To compensate the polarization biased of the detection system and monochromator efficiency, the above equation is modified to;

$$r(t) = \frac{I_{\parallel}(t) - GI_{\perp}(t)}{I_{\parallel}(t) + 2GI_{\perp}(t)} \qquad (2.6)$$

where "*G"* is the instrumental correction factor for detector sensitivity and monochromator efficiency to the polarization direction of the emission.

The time-resolved anisotropy measurements were done by automated toggling method using time-correlated single photon counting set-up and exciting the sample by different diode lasers (375 nm (IBH, UK, Nano LED, FWHM ~100 ps)), 405 nm (IBH, UK, FWHM ~100 ps) and 444 nm (IBH, UK, Nano LED, FWHM ~120 ps) for different systems. In toggling method, a movable polarizer was used in the emission side, whereas the excitation polarizer was kept fixed at vertical position. This polarizer rotates between parallel and perpendicular orientations and the emission intensities at parallel [$I_{\parallel}(t)$] and perpendicular [$I_{\perp}(t)$] polarization were collected alternatively for 60 seconds until a certain peak difference between parallel [$I_{\parallel}(t)$] and perpendicular [$I_{\perp}(t)$] decay is reached. For typical anisotropy decay the difference between the peak counts at parallel and perpendicular polarization were kept at 10000. The *G*-factor was measured by taking two additional decay measurements

[$I_{HV}(t)$ and $I_{HH}(t)$] of the same sample with the excitation polarizer toggling between perpendicular or horizontal positions. Value of *G*-factor is given by, $G = I_{HV}(t)/I_{HH}(t)$, where $I_{HV}(t)$ and $I_{HH}(t)$ denotes the fluorescence decay profiles of the sample measured using horizontally or perpendicularly (H) polarized excitation light and detecting the emission components polarized vertically (V) and horizontally (H), respectively. For a simple isotropic rotor, r(t) decays with a single rotational correlation time[8-9] (τ_r) represented by the following equation;

$$r(t) = r_0 \exp(-t/\tau_r) \qquad (2.7)$$

For more complicated systems, r(t) takes the form of a sum of exponentials;

$$r(t) = r_0 \sum \beta_i \exp(-t/\tau_{r_i}) \qquad (2.8)$$

where β_i and τ_{ri} are the fractional contribution of total depolarization and rotational correlation times of the i^{th} component, respectively. r_0 represents the fundamental anisotropy.

Wobbling-in-a-Cone Model

The restricted rotational diffusion of a fluorophore in supramolecular assemblies (micelles and reverse micelles etc.) can be explained in terms of the "wobbling-in-cone model", which can reveal structural and dynamical properties of the fluorophore inside restricted reverse micellar environment.[10] According to the wobbling-in-a-cone model, the decay of anisotropy can be described by the following eqn. 2.9[10b]

$$r(t) = r_0 \left[S^2 \exp\left(\frac{-t}{\tau_{slow}}\right) + (1 - S^2) \exp\left(\frac{-t}{\tau_{fast}}\right)\right] \qquad (2.9)$$

where S^2 is the order parameter, which can be used for understanding the location of the probe inside the reverse micelle. τ_{slow} and τ_{fast} are slow and fast rotational relaxation of the probe molecule inside the reverse micelle, respectively, and r_0 is the limiting anisotropy. The order parameter (S^2) describes the equilibrium orientational distribution of the probe inside the reverse micelle and follows the relation:

$$0 \leq S^2 \leq 1$$

where S = 0 indicates the motion is completely free and S = 1 corresponds to the completely restricted environment.

The wobbling semicone angle θ° for the probe to execute the wobbling in cone motion, and the semicone angle θ° can be defined by the following equation,

$$\theta^{\circ} = Cos^{-1}\left[\frac{1}{2}\left(\left(\sqrt{(1+8S)}\right)-1\right)\right] \qquad (2.10)$$

The semicone angle (θ°) is considered as a magnitude of spatial restriction of the probe, has values in range of 0^0 to 90°, corresponding to the unrestricted and completely restriction rotation of the probe, respectively.

2.2.3b. Femtosecond Time Resolved Fluorescence Upconversion

With the TCSPC set-up, it is impossible to resolve the lifetime components, which appears less than tens of pico-seconds due to time response of the electronics involved in TCSPC set-up. In such situation femtosecond fluorescence upconversion set-up can detect the ultrafast dynamics taking place in less than 1 ps time-scale. In this fluorescence upconversion system, a tunable femto-second laser source, Mai Tai HP (Spectra Physics, USA) is used for excitation. Mai Tai is one box Ti-Sapphire oscillator, which provides <100 fs pulse width, and therefore, helps to resolve lifetime components of pico-seconds to sub pico-seconds time-scale. The broad range tunability (690-1040 nm) of Mai Tai laser is appropriate to excite various kinds of fluorophores. In additionally, high quality, stable, horizontally polarized (>500:1 horizontal), Gaussian pulses (TEM_{00}, M2 <1.1) with stable average power (>2.5 W) and high peak power (>300 kW) offers minimal fluctuation in the laser pulses. The greatest advantage of Mai Tai is that it provides excellent beam pointing stability, minimal average power fluctuations, as well as it eliminates wavelength drift. Mai Tai uses the output from the high power fiber coupled diode laser model to end-pump Nd^{3+} ion doped Yttrium Vanadate crystalline matrix (Nd:YVO_4). The triply ionized Nd act as an active medium for this four-level solid state pump laser, which has principle absorption bands in the red and near infra-red region. While excited with a diode laser, the strongest lasing form Nd:YVO_4 occurs at a wavelength ~1064 nm. The resulting 1064 nm emission is converted to a visible wavelength (532 nm) through frequency doubling (also known as second harmonic generation or SHG) in a nonlinear crystal. A 90º, non-critically phase-matched, temperature tuned, lithium triborate (LBO) nonlinear crystal is used as a frequency doubling (or SHG) medium inside Mai Tai one box oscillator. A dichroic output coupler allows the 532 nm light to exit from the pump cavity, but reflects the 1064 nm light back to the cavity. This 532 nm continues wave (CW) from a frequency doubled output of the Nd:YVO_4 pump laser is used to pump Ti-Sapphire laser, which in turn produces the Mai Tai output. Ti-Sapphire is a crystalline material produced by introducing Ti_2O_3 into a melt of Sapphire (Al_2O_3). The Ti^{3+} ion is responsible for the lasing action of Ti-Sapphire. Although the fluorescence band of Ti^{3+} extends from

wavelengths as short as 600 nm to wavelength greater than 1000 nm, the lasing action is possible at greater than 670 nm (most strong emission band ~800nm). Mai Tai uses an acousto-optic modulator (AOM) (constitutes a high quality optical material like quartz) to ensure the mode locked output from Ti-Sapphire. The Mai Tai reliability is maintained using the ultra-stable regenerative mode locking technique proven with the Spectra-Physics Tsunami® oscillator.

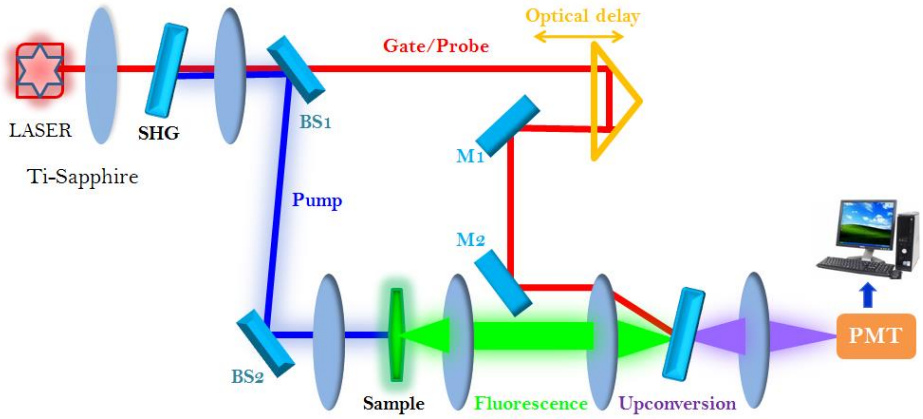

Figure 2.3. Schematic representation of upconversion set up.

Typical schematic diagram of a fluorescence upconversion set-up is represented in **Figure 2.3**. Gate beam is a fundamental laser beam of frequency (υ_1). The resulting fluorescence (υ_F) from the sample, is mixed with the gate beam (υ_2) arriving at time t = τ in nonlinear crystal (BBO) which generates sum frequency (υ_s) light satisfying the condition of phase matching that depends on the angle of BBO crystal (**Figure 2.4**).

$$\upsilon_F + \upsilon_1 = \upsilon_s \qquad (2.11)$$

Intensity of sum frequency light (I_{sum}) at a particular delay time τ is proportional to correlation function of fluorescence intensity (I_F) with gate light intensity (I_L) as shown below

$$I_{sum} = \int_{-\infty}^{\infty} I_F I_L(t-\tau) \qquad (2.12)$$

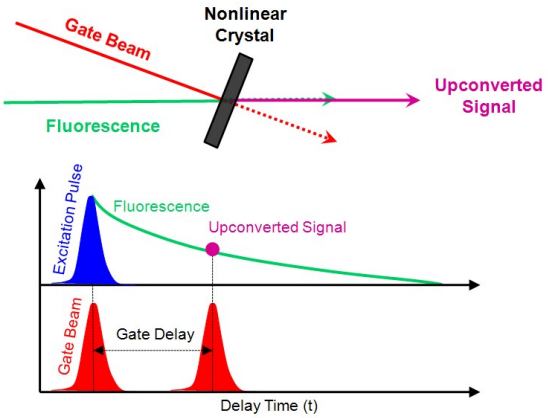

Figure 2.4. Schematic representation of upconversion phenomenon.

The copper nanocluster (CuNCs) samples were excited at 375, 405 and 420 nm using the second harmonic of a mode-locked Ti-sapphire laser. The fundamental output beams from the Ti-sapphire oscillator (750, 810 and 840 nm) were frequency doubled in a type-I BBO crystal (1 mm BBO, θ = 25°, φ = 90°) (**Figure 2.3)**. The frequency doubled blue pulses (375, 405 and 420 nm) are separated from the fundamental by a dichroic mirror (beam splitter) and focused onto a rotating cell containing the sample (**Figure 2.3)**. The residual fundamental beam is used as the gate to upconvert fluorescence emission. The time interval τ between fluorescence signal and gate pulse (υ_1) is regulated by changing the distance of travel of one of the pulses, using an optical delay line. Fluorescence emitted from the sample is collected by an achromatic lens. Fluorescence and gate beams are focused by a quartz lens (f = +80 mm) into a type-II nonlinear β-barium borate (BBO) crystal (0.5 mm BBO, θ = 38°, φ = 90°). The sum frequency of the fluorescence and gate pulse was detected as a function of the time delay between excitation and gate pulses. The angle between the polarization of the pump and gate pulses was maintained at the magic angle (54.7°) to eliminate effects from rotational diffusion. The upconverted signal was dispersed in a monochromator and detected using photon counting electronics. In the experiment, the delay time τ is scanned and intensity of sum frequency light (τ) is measured to obtain the fluorescence intensity versus time (**Figure 2.4**). A cross-correlation function obtained using the Raman scattering from ethanol provided a full-width at half-maximum (FWHM) of ~350 fs. Estimated uncertainties in the upconversion measurements are ~10-15%. The excitation average power was varied, but was a round 8±0.5 mW and an average collection time of 3 μs was used. The fluorescence decays were deconvoluted using a Gaussian shaped excitation pulse by Igor Pro 6.0 analysis software. During analysis of upconverted decay profiles, the long component lifetime obtained from TCSPC is kept fixed.

2.2.4. Circular Dichroism (CD)

Circularly polarized light travel through an optically active medium with different velocities due to the different refraction indices for right- and left-circularly polarized light called optical rotation or circular birefringence.[11] Optically active chiral molecules will preferentially absorb one direction of the circularly polarized light. circular dichroism (CD) is the difference in the absorption of left-handed circularly polarised light (A_L) and right-handed circularly polarised light (A_R) and occurs when a molecule contains one or more chiral chromophores (light-absorbing groups).[11]

$$Circular\ dichroism = \Delta A(\lambda) = A_L(\lambda) - A_R(\lambda) \qquad (2.13)$$

where λ is the wavelength.

Taking into account cell path length and compound concentration, we can arrive at a molar circular dichroism (Δε).

$$\Delta\varepsilon = \varepsilon_L - \varepsilon_R = \Delta A/(C \times l) \qquad (2.14)$$

Where ε_L and ε_R are the molar extinction coefficients for left and right circularly polarised light respectively, C = molar concentration, and l = path length in centimetres. The CD spectrum can also be expressed as degrees of ellipticity (θ), which is a measure of polarization, as given below,

$$tan\theta = \frac{E_L+E_R}{E_L-E_R} \qquad (2.15)$$

where, E_L and E_R is the magnitude of the electric field vector of the left-circularly and right-circularly polarized light, respectively.

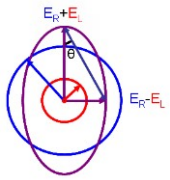

Figure 2.5. Elliptically polarized light (purple) is the superposition of LCP (red) and RCP (blue) light. θ is the angle between the magnitude of the electric field vector at its maximum and its minimum.
(Image has been taken from *https://en.wikipedia.org/wiki/Circular_dichroism*)

The measured ellipticity (θ) is related to the difference in absorbance by θ = 32.98 ΔA, where θ is in degrees. In the CD experiments, the reported unit is molar ellipticity [θ] with

units of deg.dl.mole^{-1}.dm^{-1}, which remove the concentration and path length dependence. The relationship between the measured and the molar ellipticity is given by[11d]

$$[\theta](\lambda) = \frac{100\,\theta(\lambda)}{lC} \qquad (2.16)$$

Where l is path length in centimetres, C is concentration of the sample in moles.lt^{-1}. The molar ellipticity is related to the difference in extinction coefficients by[11d]

$$[\theta] = 3298\Delta\varepsilon \qquad (2.17)$$

All CD spectra were recorded on a JASCO-800 automatic recording circular dichroism spectrophotometer (**Figure 2.6**). Quartz cuvette with 1.0 cm path length was used for measurements. CD spectra were recorded at 25 ºC in the wavelength range of 200-400 nm at a scan rate 100 nm/min. A fixed concentration of macromolecules (DNA/proteins) was titrated with increasing concentration of ligand, graphene oxide and MCM-41. Final CD spectrum was corrected by taking the blank of the individual ligand, graphene oxide and MCM-41 and buffer solution.

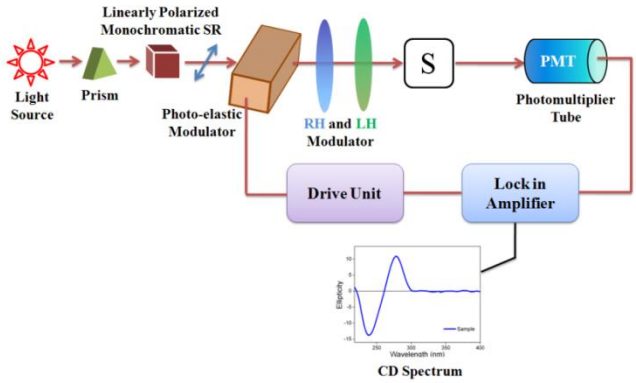

Figure 2.6. Schematic representation of circular dichroism (CD) spectrometer.

2.3. References

1. N. I. Kovtyukhova, P. J. Ollivier, B. R. Martin, T. E. Mallouk, S. A. Chizhik, E. V. Buzaneva and A. D. Gorchinskiy, *Chem. Mater.*, 1999, **11**, 771-778.
2. J. Völker, H. H. Klump and K. J. Breslauer, *Proc. Natl. Acad. Sci. U.S.A.*, 2001, **98**, 7694-7699.
3. E. Froehlich, J. S. Mandeville, C. J. Jennings, R. Sedaghat-Herati and H. A. Tajmir-Riahi, *J. Phys. Chem. B*, 2009, **113**, 6986-6993.
4. M. E. Reichmann, S. A. Rice, C. A. Thomas and P. Doty, *J. Am. Chem. Soc.*, 1954, **76**, 3047-3053.
5. S. Klitgaard, M. T. Neves-Petersen and S. B. Petersen, *J. Fluoresc.*, 2006, **16**, 595-609.
6. N. M. Correa, J. J. Silber, R. E. Riter and N. E. Levinger, *Chem. Rev.*, 2012, **112**, 4569-4602.

7. X. Yang, Y. Feng, S. Zhu, Y. Luo, Y. Zhuo and Y. Dou, *Anal. Chim. Acta*, 2014, **847**, 49-54.
8. (a) B. Valeur and M. N. Berberan-Santos, *Molecular Fluorescence: Principles and Applications*, Wiley-VCH, 2002; (b) J. R. Lakowicz, *Principles of fluorescence spectroscopy*, Springer, 2007.
9. G. R. Fleming, *Chemical Applications of Ultrafast Spectroscopy* Oxford University Press, New York, 1986.
10. (a) D. E. Moilanen, E. E. Fenn, D. Wong and M. D. Fayer, *J. Phys. Chem. B*, 2009, **113**, 8560-8568; (b) A. Patra, T. Q. Luong, R. K. Mitra and M. Havenith, *Physical Chemistry Chemical Physics*, 2014, **16**, 12875-12883; (c) A. Douhal, G. Angulo, M. Gil, J. Á. Organero, M. Sanz and L. Tormo, *J. Phys. Chem. B*, 2007, **111**, 5487-5493.
11. (a) D. S. Rodgers, *Circular Dichroism: Theory and Spectroscopy*, Nova Science Publishers, 2012; (b) B. Nordén, A. Rodger and T. Dafforn, *Linear Dichroism and Circular Dichroism: A Textbook on Polarized-Light Spectroscopy*, Royal Society of Chemistry, 2010; (c) N. Berova, K. Nakanishi and R. W. Woody, *Circular Dichroism: Principles and Applications*, John Wiley & Sons, 2000; (d) W. C. Johnson, in *Circular Dichroism and the Conformational Analysis of Biomolecules*, ed. G. D. Fasman, Springer US, Boston, MA, 1996, pp. 635-652.

Chapter 3

Loading of an Anticancer Drug into/on to the Material and Subsequent Release to Biomolecules

The present chapter deals with loading and subsequent release of an anticancer drug, ellipticine. Using the unique fluorescence switching properties of ellipticine, we have successfully monitored its loading in/on to materials such as graphene oxide (GO) and mesoporous silica nanochannels (MCM-41), and subsequent release to biomolecules. Detailed spectroscopic and other experimental investigations are done to unravel the reasons for the modulation of the optical properties of drug molecule in presence of materials. This chapter is divided in to two sub-sections, one is devoted for graphene oxide and second section deals with the MCM-41.

3a. Loading of an Anticancer Drug onto Graphene Oxide Surface and Subsequent Release by Biomolecules

3a.1. Introduction and Motivation of the Work

In chemotherapy, the targeted delivery and controlled release of anticancer drugs is an important concern.[1] In order to achieve this, various nano-materials are being explored that could serve the purpose of efficient drug carriers.[2] Recently, graphene its derivatives, namely, graphene oxide (GO) and reduced graphene oxides (RGO) are mostly considered as nano-carriers for certain anticancer drugs (the detail has been discussed in Chapter 1).[3] In view of nano-carrier activity, GO is much superior to RGO, primarily because of its unique surface functionality (presence of polar groups and π-conjugation), better water solubility and biocompatibility.[3a-f] However, one should also take into account some recent reports about the cytotoxicity of GO.[4] Although the drug loading and its subsequent release have been routinely monitored by usual absorption spectroscopic techniques,[5] intrinsic fluorescence property of the drug may prove to be very useful due to higher sensitivity of fluorescence over absorption[3g,6]. Moreover, instead of monitoring the fluorescence intensity, it would be very simple and effective, if the drug loading onto the carrier surface and subsequent release to specific biomolecules like DNA/RNA can be directly monitored by the change in the fluorescence colour. Herein, we have explored the distinctive interaction scenario, of GO and DNA/RNA/proteins/sugars with an important anticancer drug, ellipticine (EPT) (**Scheme 3.1**). Ellipticine and its derivatives intercalate in DNA base-pairs, and inhibit the DNA topoisomerase II enzyme activity, which ultimately restrict the DNA replication process and RNA transcription.[7] EPT mainly exists in two prototropic forms depending on the polarity and pH of the medium (**Scheme 3.1**). In non-polar and hydrophobic media, EPT predominantly exists as neutral form and exhibit emission maxima around 410-440 nm;[8] whereas in aqueous medium it exists as protonated form, showing emission maxima at 530 nm.[8] Thus, intrinsic dual fluorescence behaviour of EPT can be efficiently used to probe the loading and subsequent release to biomolecules with the help of fluorescence-switching of the drug, which would avoid the complexities associated with the standard techniques.

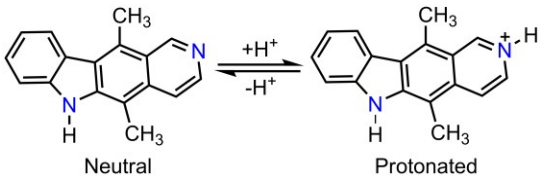

Scheme 3.1. Different prototropic forms of ellipticine.

Herein, we have probed the interaction scenario between ellipticine and graphene oxide (GO) and subsequent release to biomolecules like DNA/RNA with the help of fluorescence (both steady state and time-resolved), Raman, electron microscope, powder XRD measurements. Interestingly, intrinsic dual fluorescence behaviour of EPT can be efficiently used to probe the loading and subsequent release to biomolecules with the help of fluorescence-switching of the drug.

3a.2. Results and Discussion

3a.2a. Characterizations of Graphene Oxide (GO)

Results of GO charecterizations are presented in **Figure 3.1**. Overall, our results are in good agreements with those reported earlier.[9] Specifically, observation of the characteristics (i) stretching vibrations at 1056 cm^{-1} (epoxide or alkoxy-C–O), 1384 cm^{-1} (carboxyl C-O), 1630 cm^{-1} (graphene C=C), 1710 cm^{-1} (carbonyl moiety in –COOH) and 3444 cm^{-1} (-OH) in the FTIR spectrum (**Figure 3.1a**); (ii) D and G bands at 1336 cm^{-1} and 1596 cm^{-1} in the Raman spectrum[6,9a] (**Figure 3.1b**) altogether confirm the formation of GO. In Raman spectra,

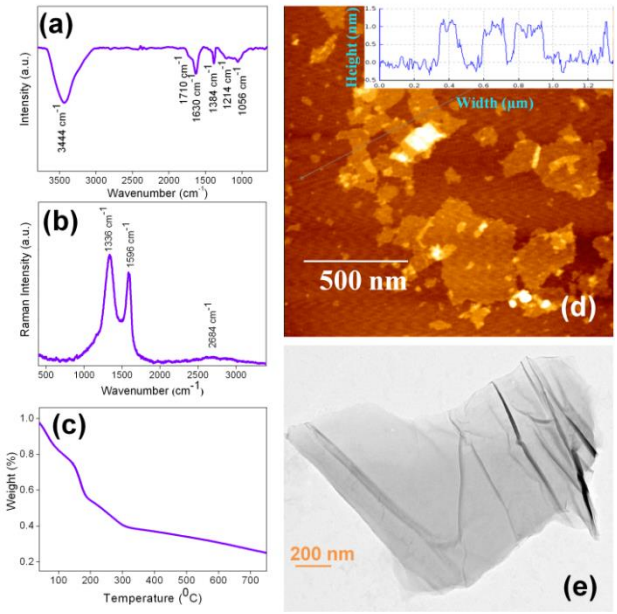

Figure 3.1. Graphene oxide characterizations (a) FTIR spectra (b) Raman spectra (c) Thermal gravimetric analysis (TGA) curve at heating rate of 10°C/minute in nitrogen (d) AFM image and depth profile of as prepared single layer GO and (e) HR-TEM image of GO.

compared to graphite, the intensity of the D band (I_D) increases while the intensity of the G band (I_G) decreases (I_D/I_G = 0.34 for graphite and I_D/I_G = 1.10833 for GO and both the bands are relatively broad in GO. The thermal stability of GO investigated by thermogravimetric analysis (TGA) (**Figure 3.1c**), shows weight loss of ~20% below 100 °C and is primarily

attributed to the trapped water molecules in between the π-stacked sheets.[9b] The further weight loss amounting to ~50% around 200 °C could be due to pyrolysis of labile hydroxyl, epoxy and carboxyl groups.[9b] Atomic force microscopy (AFM) image (**Figure 3.1d**) exhibits two-dimensional sheets of GO with lateral dimension in the range of tens to hundreds of nanometers and thickness of ~1 nm, which corroborates well with the previous report.[9c] Furthermore, HR-TEM image of GO (**Figure 3.1e**) clearly supports the AFM observations by showing a layered structure with a single layer resolution.

3a.2b. Steady State Fluorescence Spectroscopy Results

Ellipticine (EPT) in aqueous buffer medium predominantly exists in protonated form (**Scheme 3.1**) (as the pK_a of quinoline nitrogen is ~7.4[8a]) and shows green emission at 530 nm[8]. With progressive addition of GO, the peak at 530 nm gradually shifts towards lower wavelength and finally emits blue light at 450 nm (**Figure 3.2a**). Interestingly, we observe hike in the blue fluorescence intensity with the gradual addition of GO, and this observation differs from the previous findings, where GO acts as energy acceptor and quenches the fluorescence of drugs/fluorophore.[10] Notably, in all the prevoius cases where quenching is observed, no new species is generated in presence of GO. However, in our case neutral form of EPT generates at the cost of protonated form at the GO surface. Therefore, this counterintutive fluorescence behavior of EPT (**Figure 3.2a**) may be attributed to the increased population of neutral ellipticine molecules at the GO surface by the progressive addition of GO to the ellipticine containing buffer solution. Notably, similar kind of fluorescence enhancement was also observed for graphene bound -HPTS (8-hydroxy-1,3,6-pyrenetrisulfonic acid trisodium salt) and -DHPDS (6,8-dihydroxy-1,3-pyrenedisulfonic acid disodium salt), and it was attributed to shift of acid-base equilibrium in presence of graphene.[11] As blue emission corresponds to the neutral form of ellipticine (EPT_N) (**Scheme 3.1**),[8] it infers that EPT_N selectively binds to the GO surface mainly through π-π stacking interaction with a loading capacity of ~76% off its initial concentarion (**Note A2** in Appendix), indicating GO can be used as a potential carrier for EPT (detection limit is 1.33 μM/μg of GO).

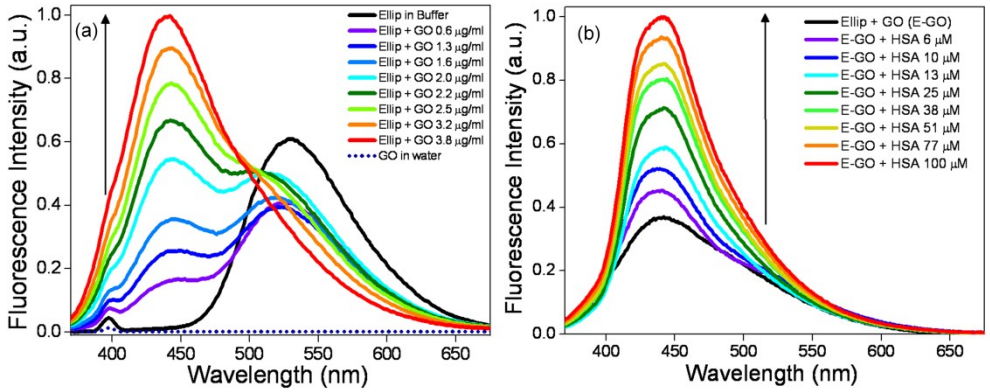

Figure 3.2. Fluorescence profiles (λ_{ex} = 355 nm) of (a) ellipticine with GO (0-3.8 μg/ml); (b) ellipticine-GO (E-GO) with increasing concentration of HSA (0-100 μM); The dotted spectrum in (a) represents the emission profile of GO in buffer at the same experimental conditions.

After that we were curious to know whether the drug interacts with serum albumin protein, which is rich in blood serum. With gradual addition of HSA to the Ellipticine-GO (E-GO) system (**Figure 3.2b**), the blue emission gets intensified, inferring EPT_N is interacting strongly with protein. Here it is pertinent to mention that EPT normally binds with protein in its neutral form (EPT_N) and hence, the intensification of blue emission might arise either from the binding of free EPT molecules with the protein and/or interaction of GO-bound EPT_N molecules with the protein. It is already evidenced from the previous reports that protein generally adsorbs on the surface of GO by hydrophobic, π-π stacking interactions with π-conjugated sub-domains, hydrogen bonding interactions (between the oxygen functional groups of GO and nitrogen and oxygen containing functional groups of protein) as well as electrostatic interactions between protein surface charges and oxygen functional groups over GO.[3b,12] GO exhibits two Raman bands (**Figure A1e** in Appendix) at 1336 cm^{-1} (D-band) and 1596 cm^{-1} (G-band) corresponding to sp^3 and sp^2 C-atoms, respectively.

Table 3.1. Intensity ratio of D, G bands and the crystalline size (L_c) of the graphene domains.

Sample	I_D/ I_G	$L_C = 4.4 (I_D/I_G)^{-1}$
Graphite	0.34	12.81
GO	1.10	3.97
GO + DNA	1.24	3.53
GO + RNA	1.15	3.80
GO + HSA	1.14	3.86
GO + HSA + DNA	1.17	3.75

In comparison to graphite, the observed alteration of intensity ratio between D and G-bands (I_D/I_G) provides information on the structural parameters, specifically the π-cunjugation.[6,9a] The crystalline size in the graphene layers is determined to be L_c = 4.4 (I_G/I_D)[13] (**Table 3.1**), which is three times lower than that of graphite. This L_c indicats that few domains of graphitic fraction exists over GO on which ellipticine and biomolecules can also bind via π-π interaction. Therefore, we believe that the enhancement of blue emission of EPT is an outcome of adsorbed protein on GO surface (in which EPT_N molecules experiences more hydrophobic environment in presence of protein), and it is supported by circular dichroism (CD) (**Note A3** in Appendix) and time-resolved spectroscopy results (discussed later). In view of drug delivery experiments, this observation has significant implication which assures during the journey through the blood stream ellipticine will not be easily released from the GO surface as it is further protected by serum protein.

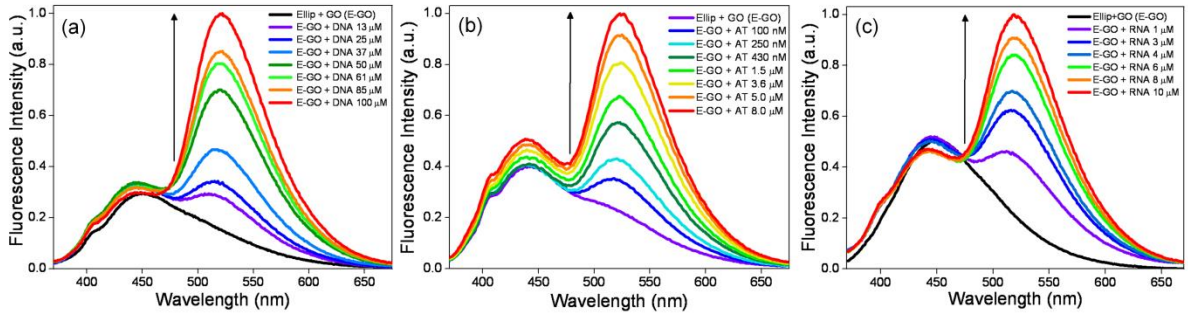

Figure 3.3. Fluorescence profiles (λ_{ex} = 355 nm) of (a) ellipticine-GO (E-GO) with increasing concentration of Salmon sperm DNA (0-100 μM); (b) E-GO with increasing concentration of $ds(AT)_{15}$ (0-8 μM); (c) E-GO with increasing concentration of TAR-RNA (0-10 μM).

As GO has the ability to penetrate the cell,[3b] which is enriched with DNA and RNA, next step is to check the interaction behavior of E-GO composite with the above mentioned biopolymers. To execute this experiment, we have taken salmon sperm DNA, $ds(AT)_{15}$ and TAR-RNA. In presence of DNA, GO bound EPT exhibits a new emission peak at 520 nm, in addition to 450 nm peak (**Figure 3.3a**, **3.3b**). With the progressive increase of DNA concentration, the peak at 520 nm dominates over 450 nm peak (**Figure 3.3a**, **3.3b**). At high DNA concentration, the 520 nm becomes major peak along with a small hump at 450 nm and it reflects a clear fluorescence-switch from blue to green colour. The binding constant (K_f) is estimated to be (6.18±0.6) × 10^5 M^{-1} from Scatchard plot (**Note A5** in Appendix), which is very close to the value obtained from chromatin-DNA bound ellipticine (EPT)[8a]. Almost similar observation is noticed in case of TAR-RNA (**Figure 3.2d**) and the binding constant (K_f = (1.014±0.1) × 10^5 M^{-1}) estimated from the Scatchard plot (**Note A5** in Appendix) is

lower than that of DNA. Raman results (discussed later) also indicate that composite formation of DNA and TAR-RNA with GO exhibits different modulation in the peak intensities of characteristic G and D-bands (I_D/I_G = 1.24 and I_D/I_G = 1.17 for DNA and RNA, respectively), which could be due to slightly different interaction scenario of DNA and TAR-RNA with GO. Here it is pertinent to mention that TAR-RNA (29 bases) consists of bulge, loop and a double stranded (arising from 20 complimentary bases) secondary structure[14] and it is known that protonated form of ellipticine (EPT_H^+) interacts with DNA/RNA through intercalative mode of binding[15]. Therefore, the lower affinity of ellipticine towards RNA may be attributed to the presence of bulge and loop secondary structures in case of TAR-RNA, which is absent in case of DNA. In our case, the selective detection of RNA/DNA by ellipticine is difficult, as the drug interacts with RNA/DNA with the protonated form, and leads to the enhancement of 520 nm peak in either of the cases. Therefore, unlike other probes,[16] selective detection of DNA/RNA is not possible in the present scenario. The sensitivity of the E-GO system is estimated by experiments with smaller dsDNA ($ds(AT)_{15}$), and we have verified that it can detect dsDNA concentration as small as 100 nM (**Figure 3.3b**).

The binding affinity of the drug towards DNA/RNA is also supported by steady state anisotropy measurement, where it has been observed that with the gradual addition of DNA, anisotropy value of EPT rises up and gets saturated at ~40 μM DNA. As the intensity at 450 nm does not vanish completely, we believe that there are few EPT molecules, which stick to GO surface, cannot be released even at higher concentration of DNA/RNA. The releasing capacities of GO bound EPT are 60% and 65% (**Note A2** in Appendix) for DNA and RNA, respectively. Fluorescence excitation spectra (**Note A2** in Appendix) further confirms the release of the drug from GO surface in presence of DNA/RNA, as a distinct peak is appeared at ~315 nm, which is attributed to DNA/RNA bound ellipticine molecules[17]. The interaction behavior between E-GO and DNA/RNA have also been probed with time-resolved fluorescence measurements.

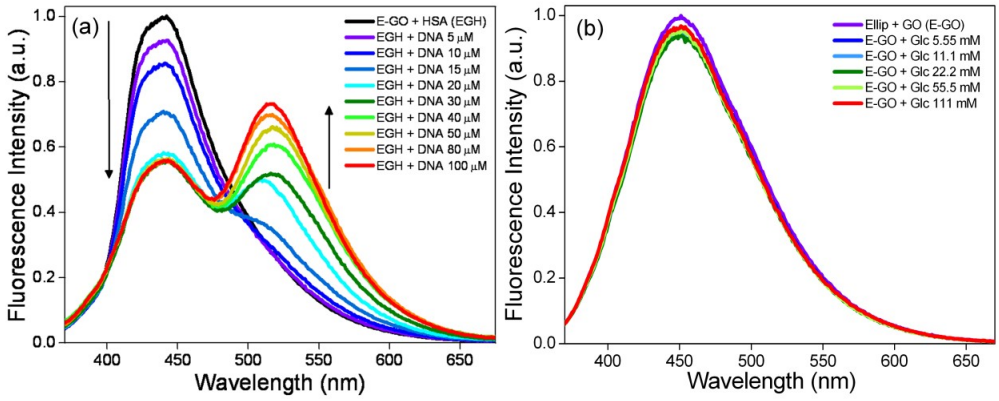

Figure 3.4. Fluorescence profiles (λ_{ex} = 355 nm) of (a) ellipticine-GO-HSA (EGH) with with increasing concentration of Salmon sperm DNA (0-100 μM); (b) E-GO in aqueous PBS with increasing concentration of Glucose (0-110 mM).

Note that the biological activity of EPT depends on the intercalation with DNA/RNA.[15] Therefore, it is important to demonstrate the interaction of GO bound EPT towards DNA/RNA and in order to do so, we have titrated E-GO-HSA (EGH) system with salmon sperm DNA (**Figure 3.4a**). It has been observed that DNA extracts EPT from protein-GO system, which is reflected through the appearance of a new peak at 520 nm in presence of DNA (**Figure 3.4a**). The peak at 520 nm becomes dominating at higher DNA concentration and it is reflected by the bluish green fluorescence of the solution. An important finding from this observation is that DNA has better binding affinity than HSA in a competing situation, which is essential for the functioning of ellipticine as a potential anticancer drug. To further demonstrate the specificity of E-GO system towards another important bio-molecule, namely, sugar, we have titrated E-GO system with various concentration of glucose (**Figure 3.4b**). Interestingly, neither increase in intensity likewise HSA nor fluorescence-switching likewise DNA/RNA is observed. Thus, our GO-based molecular switch for sensing important biomolecules resembles GO-based molecular beacon for detection of DNA-binding transcription factor, where GO played the role of a nanoquencher,[18] however, in the present study GO provided the platform of fluorescence switching.

3a.2c. Fluorescence Lifetime Measurements

Fluorescence lifetime measurements of ellipticine are performed in GO, GO-HSA, GO-DNA/RNA, and GO-HSA-DNA systems. We have monitored the decay profiles both at 450 nm as well as at 520 nm in order to probe the neutral (EPT_N) as well as protonated form (EPT_H^+) of the drug. Instead of emphasizing individual components, we have considered average lifetime to provide insight into the binding behaviour of EPT in the above mentioned

systems. The decay characteristics of neutral drug molecules (monitored at 450 nm) in presence of GO, GO-HSA, GO-DNA/RNA, and GO-HSA-DNA systems are displayed in **Figure 3.5a**, and corresponding fitting results are given in **Table 3.2a**. Neutral ellipticine (EPT_N) in buffer solution gives an average fluorescence lifetime of ~710 ps, which is enhanced to 2 ns in presence of GO. The increased lifetime may be attributed to π-π and hydrophobic interactions between neutral form of the drug and GO basal planes. When E-GO complex is titrated by bio-macromolecules like serum albumin (HSA), DNA and RNA, then significant changes are observed in the decay profiles of EPT (**Figure 3.5a**). In presence of HSA, fluorescence lifetime of E-GO increases from 2 ns to 6.2 ns, which indicates that the drug in E-GO complex are further getting stabilized when protein adsorbs on the GO surface, which is consistent with the intensity hike at 450 nm in presence of protein.

Table 3.2. Fluorescence decay (λ_{ex} = 375 nm) fitting parameters of ellipticine in presence of GO and E-GO complex in presence of various bio-macromolecules, decays are collected at (a) 450 nm and (b) 520 nm.

(a)

Sample	τ_1 (ns)	τ_2 (ns)	τ_3 (ns)	a_1	a_2	a_3	$\langle\tau\rangle^{\#}$ (ns)	χ^2
EPT in PBS	0.22	1.64	8.92	0.82	0.14	0.03	0.71	1.25
EPT + GO (3.8 μg/ml) (E-GO)	0.15	1.52	8.77	0.6	0.22	0.18	2.05	1.06
E-GO + DNA (100 μM)	0.12	1.57	9.42	0.54	0.22	0.24	2.53	1.06
E-GO + RNA (10 μM)	0.18	1.97	9.5	0.53	0.28	0.2	2.53	1.09
E-GO + HSA (100 μM)	0.49	4.57	20.3	0.47	0.3	0.23	6.2	1.08
EGH + DNA (100 μM)	0.24	2.62	12.9	0.62	0.27	0.11	2.26	1.14

(b)

Sample	τ_1 (ns)	τ_2 (ns)	τ_3 (ns)	a_1	a_2	a_3	$\langle\tau\rangle^{\#}$ (ns)	χ^2
EPT in PBS	-	1.95	6.46	-	0.87	0.13	2.52	1.08
EPT + GO (3.8 μg/ml) (E-GO)	0.22	1.89	9.12	0.51	0.37	0.12	1.88	1.04
E-GO + DNA (100 μM)	0.37	3.63	15.3	0.36	0.2	0.44	7.6	1.01
E-GO + RNA (10 μM)	0.31	3	15	0.3	0.46	0.25	7.71	0.99
E-GO + HSA (100 μM)	0.39	3.32	16.7	0.57	0.31	0.12	3.23	1.14
EGH + DNA (100 μM)	0.26	2.76	13.3	0.57	0.27	0.17	3.08	1.12

$^{\#}\langle\tau\rangle = \tau_1a_1 + \tau_2a_2 + \tau_3a_3$; whereas χ^2 is the measure of goodness of the fit. χ^2 close to 1 is considered as good fit.

In case of DNA/RNA, no such significant changes are observed inferring that neutral ellipticine (EPT_N) molecules in the GO surface are not interacting with DNA/RNA at all, which is also consistent with steady state observation, where we have seen the intensity at ~450 nm remains almost same in presence of DNA/RNA.

To verify the drug release behaviour inside the cell, we have gradually added DNA to the ellipticine-GO-HSA (EGH) complex. The average lifetime of EGH complex drastically drops from 6.2 ns to 2.26 ns in presence of DNA, inferring that EPT_N form of drug is destabilized when DNA/RNA interacts with EGH complex. This is because in presence of DNA/RNA, EPT_H^+ form of drug preferably interacts, and therefore, the equilibrium $EPT_N \rightleftharpoons EPT_H^+$ is shifted towards the latter side. So, the lifetime results also supports our claim based on the emission spectra that drug molecules are released from EGH complex in presence of DNA/RNA and binds to DNA/RNA.

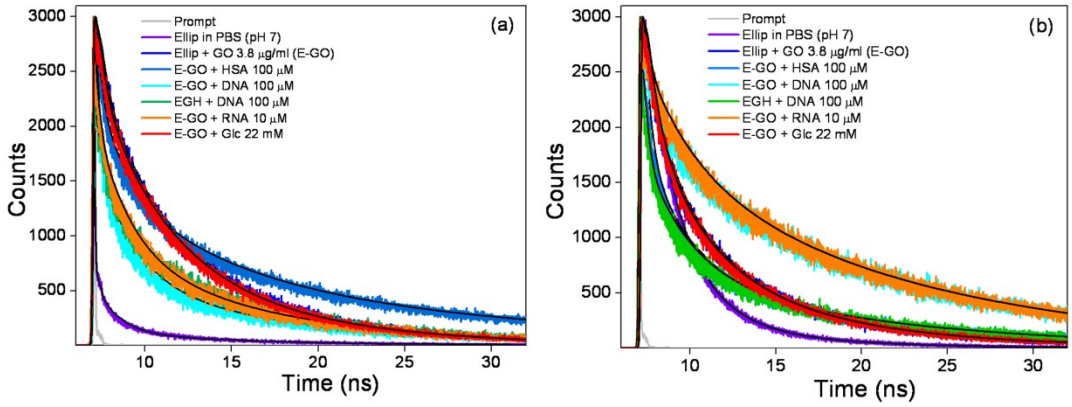

Figure 3.5. Fluorescence decay profiles (λ_{ex} = 375 nm) of ellipticine in presence of presence of GO and E-GO complex in presence of various bio-macromolecules, decays at (a) 450 nm and (b) 520 nm.

We have also probed the interaction behaviour between E-GO and glucose, and we found that glucose is not perturbing the decay profile of GO-bound EPT, suggesting that glucose is not at all interacting with drug, which corroborates well with our steady state observation where we found that glucose does not alter the emission profile of GO-bound EPT. Fluorescence lifetime profiles of protonated ellipticine (EPT_H^+) collected at 520 nm in presence of GO, GO-DNA, GO-HSA, GO-HSA-DNA, GO-RNA and GO-glucose are shown in **Figure 3.5b**, and the results are compiled in **Table 3.2b**. EPT_H^+ in aqueous buffer (pH 7) exhibits an average lifetime of 2.52 ns. In the presence of GO the average lifetime slightly decreases compared to EPT_H^+ in aqueous buffer, and it is attributed to the quenching effect by GO. However, when DNA/RNA is added to the GO-bound EPT, there is huge increment

of average lifetime of EPT_H^+, inferring that EPT is getting stabilized through interaction (probably through intercalation binding mode) with DNA/RNA in its protonated form.

The average lifetime of EPT_H^+ bound to E-GO-HSA complex increases when it was being titrated by DNA, and this suggests that EPT_H^+ is generating and getting stabilized in presence of DNA. This corroborates well with steady state results where we have observed that the peak at 520 starts appearing when E-GO-HSA complex is being titrated by DNA. Therefore, both steady state and time-resolved experiments confirm that DNA has higher binding affinity compared to E-GO as well as E-GO-HSA complex, which has important consequence in the context of drug release inside the cell. In presence of glucose there is no significant change in the average lifetime of EPT_H^+, indicating that EPT_H^+ in presence of glucose neither interacts nor release from surface of GO, and this observation is quite consistent with steady state emission results, where we have seen that emission spectra of EPT is unperturbed in presence of glucose.

3a.2d. Scanning and Transmission Electron Microscopy Results

The microstructures of GO, E-GO, EGH, EGH-DNA and E-GO- DNA/RNA were imaged by FE-SEM. From FE-SEM images, stacked-layers of GO platelets can be identified (**Figure 3.6a**), which is consistent with the AFM (**Figure 3.1d**) as well as HR-TEM (**Figure 3.1e**) observation of isolated GO platelets. Addition of ellipticine apparently did not change the morphology of GO (**Figure 3.6b**), which could be due to an easy intercalation of small EPT molecules in between the layers of GO mainly through π-π stacking interactions (see discussions in earlier section). Since GO has negligible fluorescence compared to EPT (**Figure 3.2a**), the fluorescence-switching from green to blue in presence of GO is attributed to the formation of EPT_N molecules inside the stacked layer of GO, primarily driving the equilibrium of $EPT_N \rightleftharpoons EPT_H^+$ towards the left.

Addition of DNA/RNA to E-GO system dramatically alters the morphology (**Figure 3.6c, 3.6d, 3.6h**) and this morphology is totally different from ellipticine-DNA/RNA morphology (**Note A1** in Appendix). We believe that π-π stacked E-GO layers were completely exfoliated in presence of DNA/RNA and an extended (hundreds of microns) networks of dsDNA-GO hybrid were formed involving similar interaction likewise the formation of DNA-carbon nanotube hybrids.[19] HR-TEM image (**Figure 3.6i**) also supports the FE-SEM observation and at the same time confirms the presence of the both GO and DNA in the GO-DNA hybrid composite likewise previously reported DNA-directed self-assembled structure of GO.[20] Once the exfoliation is achieved by DNA/RNA, EPT is left in

PBS solution with its protonated (EPT_H^+) form, which can be stabilized by the negative surface charge of DNA/RNA via electrostatic interactions. However, we cannot rule out the possibility that in presence of DNA/RNA, the drug desorbs and binds with DNA/RNA. Either of the case, the blue shift in the fluorescence peak (~530 nm in PBS to ~520 nm in DNA/RNA) reveals the interaction between EPT_H^+ and DNA/RNA. In case of ellipticine-GO-HSA (EGH) composite (**Figure 3.6e, 3.6f**), the distinctive assembly of HSA into leaf-like fashion is visible and GO platelets are aggregated at the leaf-edges. Interestingly, this kind of assembly structure is absent in case of ellipticine-HSA (**Figure A1a**). Therefore, this distinctive interaction feature of EGH composite system may be ascribed to the self-assembled structure of GO and HSA.

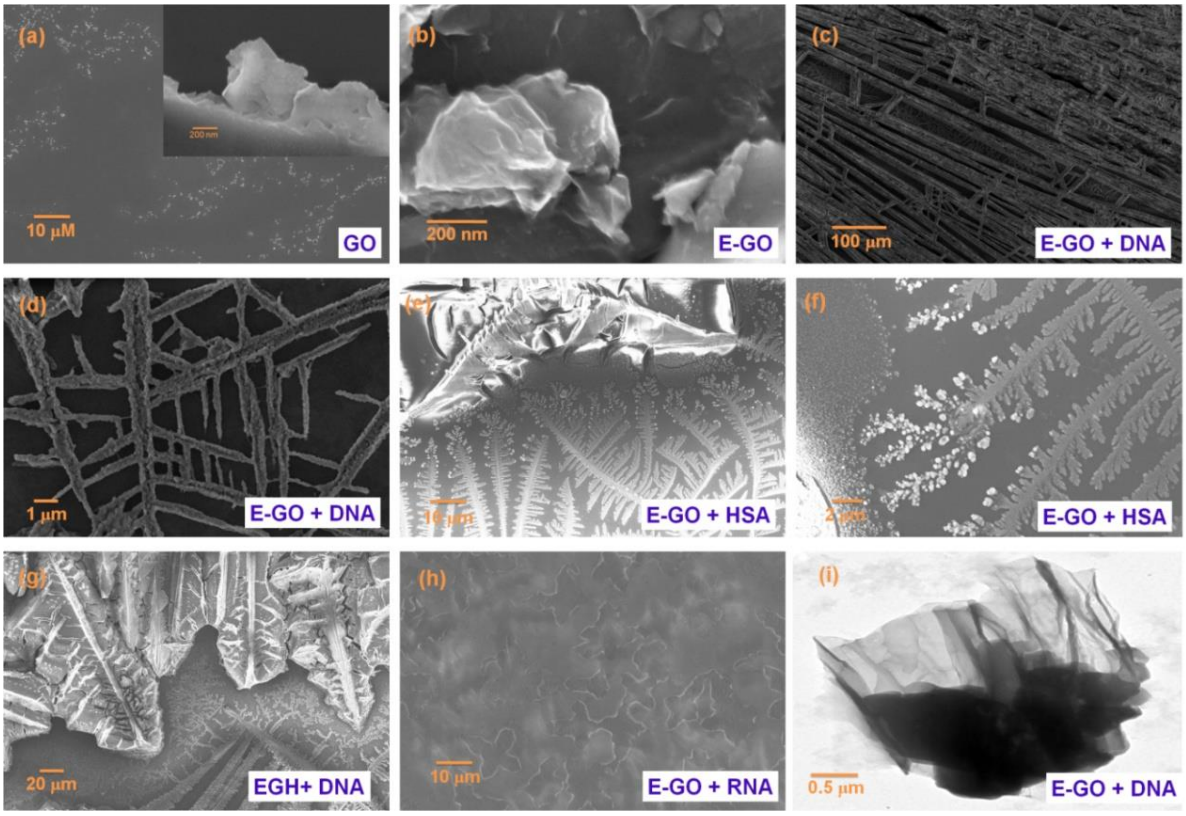

Figure 3.6. FE-SEM images of (a) GO (3.8 μg/ml) in aqueous PBS (inset is closed view); (b) ellipticine (7 μM) with GO (3.8 μg/ml) in PBS (E-GO complex); (c) E-GO complex with Salmon sperm DNA (100 μM); (d) closed view of (c); (e) E-GO complex with HSA (100 μM) (E-GO-HSA); (f) closed view of (e); (g) E-GO-HSA with DNA (100 μM); (h) E-GO complex with TAR-RNA (10 μM); (i) HR-TEM image of E-GO complex with Salmon sperm DNA.

The observed intensity enhancement in the blue-fluorescence of EGH composite could be due to insertion of additional EPT_N moieties into the hydrophobic cavities of HSA that overall shifts the equilibrium ($EPT_N \rightleftharpoons EPT_H^+$) more towards left. Astonishingly, upon

addition of DNA to the EGH composite (**Figure 3.6g**), the morphology changes significantly. The aggregated particle like features, (which are visible near leaf-edges of HSA in **Figure 3.6f**) no longer exist, rather it is extending into network and also, the leaf-like features of HSA assembly were somewhat modified (**Figure 3.6g**). Such edge-assembly of HSA-DNA supports the distinctive ternary complex formation as proposed during DNA-protein interactions study.[7d,21] Overall, the assembly driving the equilibrium towards protonated form of EPT (EPT_H^+) and thus switching of fluorescence from blue to bluish green occurred.

Interestingly, the E-GO-RNA composite exhibited entirely different morphology (**Figure 3.6h**) in comparison to the E-GO-DNA composite (compared to E-RNA in **Figure A1c** in Appendix), although the fluorescence features of both the above mentioned composites are same. This could be related to slightly different secondary structure of DNA and RNA, as we have already discussed in the previous section.

3a.2e. Powder X-Ray Diffraction and Raman Spectroscopy Results

Results from FE-SEM analysis are complemented by PXRD patterns presented in **Figure 3.7a**. The characteristic 2θ peak at ~9.36° corresponding to interlayer spacing of ~9.45 Å of GO is modulated upon interaction with EPT_N moieties (2θ ~10.5°). The reduction of the interlayer spacing to ~8.42 Å suggests an efficient intercalation of EPT_N predominantly through π-π interaction and thereby EPT acts as a gluing agent in sticking the GO sheets. Notably, in earlier reports on the 3D self-assembly of GO and ssDNA resulted in the formation of the composite materials for which no characteristics PXRD peak of GO was observed.[22] Similarly, in our composite systems (between GO and HSA/dsDNA/RNA), no such characteristic PXRD peaks of GO was detected and thus infers that complete exfoliation took place in the course of formation of various composite systems due to hydrogen bonding (between polar functional groups of GO and primary amines of DNA[22b]), van der Waals force and hydrophobic interactions between of GO and DNA/RNA.[23] To our knowledge, such morphological pattern specifically of GO with dsDNA originating from the three-dimensional self-assembly is very unusual and reported here for the first time. We believe this kind of GO-DNA network structures could find potential application in the fabrication of biomedical devices such GO based field effect transistors and bio-cellular devices.[24]

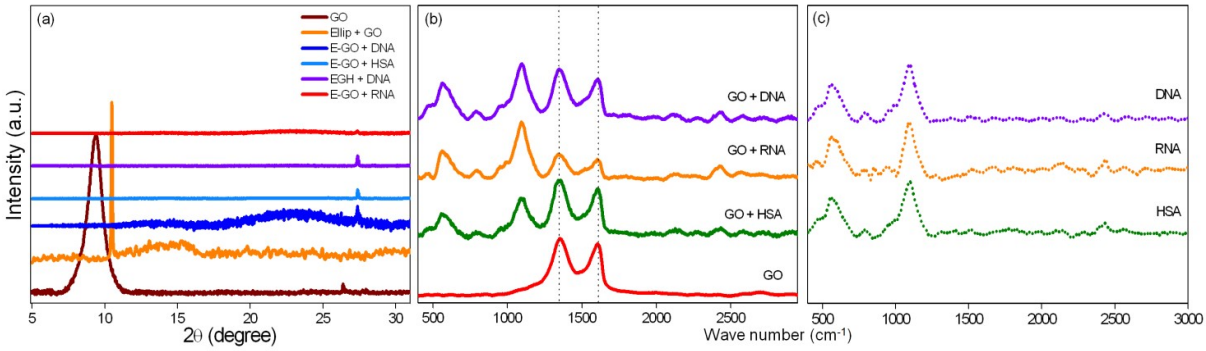

Figure 3.7. (a) Powder XRD pattern of GO, E-GO with various biomolecules; (b) Raman spectra of GO, GO with HSA, GO with RNA, GO with salmon sperm DNA; (c) Raman spectra of HSA, RNA and DNA.

Keeping in mind the fact that PXRD is not an ideal tool to conclusively prove or disprove the presence of GO in various composite systems prepared here, we have further carried out Raman spectroscopy and the spectra are shown in **Figure 3.7b and 3.7c**. Characteristic Raman signatures of both GO and different biomolecules can be easily identified in the spectra of various self-assembled composite systems like GO-DNA, GO-RNA, GO-HSA and GO-HSA-DNA.

It is also noteworthy to mention that E-GO, E-GO-DNA, EGH and EGH-DNA systems in PBS solution were stable even at ambient conditions for more than 64 hrs (**Note A6** in Appendix). Thus, the additional functionalization step of GO which has so far been routinely used in various drug delivery experiments[3a-e] is perhaps not necessary.

In summary, the green fluorescence of ellipticine (EPT) in phosphate buffer solution (PBS, pH ~7) switched to blue upon addition of GO and subsequently switched back to green upon addition of either DNA or RNA (**Scheme 3.2)**. Since in reality the ellipticine-GO (E-GO) complex is supposed to travel through blood stream before its targeted delivery to intracellular components like DNA or RNA, hence, we investigated the fluorescence property of E-GO complex in presence of HSA also, a major protein component presents in blood. Remarkably, the intensified blue fluorescence of the E-GO-HSA (EGH) complex switched to bluish green upon addition of DNA (**Scheme 3.2**), thereby directing towards potential use of GO for site-specific delivery of EPT without much change in pH which sometimes seemed to play a crucial role.[25] However, with addition of sugar to the E-GO complex, no such fluorescence-switching was observed. All the fluorescence-switching experiments are performed in this work are schematically presented in **Scheme 3.2**. We attribute the observed unique fluorescence-switching originating from the self-assembly of various components as

evidenced from the electron microscopy results and mediated by specific interactions with EPT.

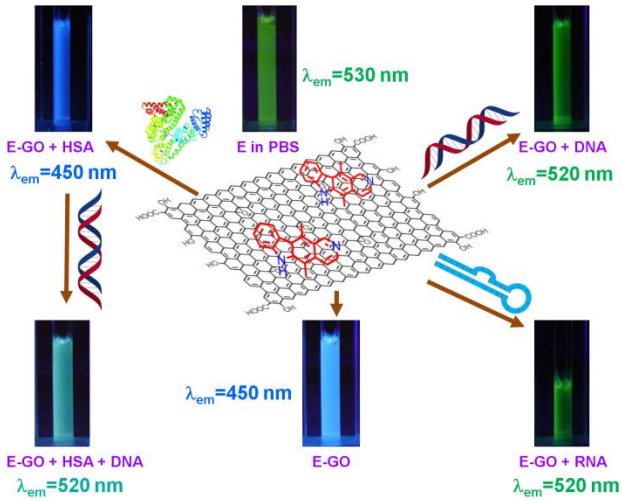

Scheme 3.2. Fluorescence-switching of ellipticine in presence of GO with various bio-macromolecules (HSA/dsDNA/RNA).

3a.3. Conclusion

We have demonstrated here GO-based fluorescence-switching of ellipticine (EPT), during its loading onto GO and subsequent release to specific biomolecules at physiological pH. Up to 76% of initial concentration of ellipticine (EPT) can be efficiently loaded onto GO, out of which 60-65% can be released to DNA/RNA but not to glucose. Finally, we have shown that ellipticine can also be released to DNA even from the E-GO-HSA composite. Electron microscopy (FE-SEM and HR-TEM), X-ray diffraction and Raman spectroscopy altogether suggest the formation of distinctive 3D assemblies involving GO and biomolecule(s) probably through non-covalent interactions and responsible for the biomolcule(s) assisted fluorescence-switching of ellipticine. Specifically, the GO-DNA assembly seems very unusual and needs further exploration. Here presented fluorescence-switching approach to monitor the drug loading and release through direct optical detection is very cheap and appealing for clinical trial experiments by, keeping the cytotoxicity of GO in minimal range. Moreover, our work is expected to stimulate future experiments across physical chemistry, biochemistry, computational chemistry and material science, for the development of various GO-based self-assembled structures with important biomolecules.

3a.4. References

1. Jeurgen Siepmann, Ronald A. Siegel and M. J. Rathbone, Springer, New York, U.S.A., 2012.
2. (a) R. A. Petros and J. M. DeSimone, *Nat. Rev. Drug Discov.*, 2010, 9, 615-627; (b) K. Cho, X. Wang, S. Nie, Z. Chen and D. M. Shin, *Clin. Cancer Res.*, 2008, 14, 1310-1316; (c) L. Yuan, Q. Tang, D. Yang, J. Z. Zhang, F. Zhang and J. Hu, *J. Phys. Chem. C*, 2011, 115, 9926-9932.
3. (a) C. Chung, Y.-K. Kim, D. Shin, S.-R. Ryoo, B. H. Hong and D.-H. Min, *Acc. Chem. Res.*, 2013; (b) H. Y. Mao, S. Laurent, W. Chen, O. Akhavan, M. Imani, A. A. Ashkarran and M. Mahmoudi, *Chem. Rev.*, 2013, 113, 3407-3424; (c) K. Yang, L. Feng, X. Shi and Z. Liu, *Chem. Soc. Rev.*, 2013, 42, 530-547; (d) Y. Zhang, T. R. Nayak, H. Hong and W. Cai, *Nanoscale*, 2012, 4, 3833-3842; (e) Y. Wang, Z. Li, J. Wang, J. Li and Y. Lin, *Trends biotechnol.*, 2011, 29, 205-212; (f) Y. Pan, N. G. Sahoo and L. Li, *Expert Opin. Drug Del.*, 2012, 9, 1365-1376; (g) Z. Liu, J. T. Robinson, X. Sun and H. Dai, *J. Am. Chem. Soc.*, 2008, 130, 10876-10877; (h) G. Wei, M. Yan, R. Dong, D. Wang, X. Zhou, J. Chen and J. Hao, *Chem. Eur. J.*, 2012, 18, 14708-14716.
4. (a) W. Hu, C. Peng, M. Lv, X. Li, Y. Zhang, N. Chen, C. Fan and Q. Huang, *ACS Nano*, 2011, 5, 3693-3700; (b) E. L. K. Chng and M. Pumera, *Chem. Eur. J.*, 2013, 19, 8227-8235.
5. (a) H. Bao, Y. Pan, Y. Ping, N. G. Sahoo, T. Wu, L. Li, J. Li and L. H. Gan, *Small*, 2011, 7, 1569-1578; (b) Y. Pan, H. Bao, N. G. Sahoo, T. Wu and L. Li, *Adv. Func. Mater.*, 2011, 21, 2754-2763; (c) G. Xin, H. Wang, N. Kim, W. Hwang, S. M. Cho and H. Chae, *Nanoscale*, 2012, 4, 405-407.
6. K. Liu, J.-J. Zhang, F.-F. Cheng, T.-T. Zheng, C. Wang and J.-J. Zhu, *J. Mater. Chem.*, 2011, 21, 12034-12040.
7. (a) J.-B. Le Pecq, Nguyen-Dat-Xuong, C. Gosse and C. Paoletti, *Proc. Natl. Acad. Sci. U.S.A.*, 1974, 71, 5078-5082; (b) M. Stiborová, C. A. Bieler, M. Wiessler and E. Frei, *Biochem. Pharmacol.*, 2001, 62, 1675-1684; (c) C. L. Arteaga, D. L. Kisner, A. Goodman and D. D. Von Hoff, *Eur. J. Cancer Clin. On.*, 1987, 23, 1621-1626; (d) S. J. Froelich-Ammon, M. W. Patchan, N. Osheroff and R. B. Thompson, *J. Biol. Chem.*, 1995, 270, 14998-15004.
8. (a) F. Sureau, F. Moreau, J. M. Millot, M. Manfait, B. Allard, J. Aubard and M. A. Schwaller, *Biophys. J.*, 1993, 65, 1767-1774; (b) S. Y. Fung, J. Duhamel and P. Chen, *J. Phys. Chem. A*, 2006, 110, 11446-11454; (c) Z. Miskolczy, L. Biczók and I. Jablonkai, *Chem. Phys. Lett.*, 2006, 427, 76-81.
9. (a) K. N. Kudin, B. Ozbas, H. C. Schniepp, R. K. Prud'homme, I. A. Aksay and R. Car, *Nano Letters*, 2007, 8, 36-41; (b) J. Shen, Y. Hu, C. Li, C. Qin and M. Ye, *Small*, 2009, 5, 82-85; (c) W. Hu, C. Peng, W. Luo, M. Lv, X. Li, D. Li, Q. Huang and C. Fan, *ACS Nano*, 2010, 4, 4317-4323.
10. (a) K. P. Loh, Q. Bao, G. Eda and M. Chhowalla, *Nat Chem*, 2010, 2, 1015-1024; (b) M. Zhang, H.-N. Le and B.-C. Ye, *ACS Appl. Mater. Interfaces*, 2013, 5, 8278-8282.
11. X. Pan, H. Li, K. T. Nguyen, G. Grüner and Y. Zhao, *J. Phys. Chem. C*, 2012, 116, 4175-4181.
12. (a) F. Yang, Y. Liu, L. Gao and J. Sun, *J. Phys. Chem. C*, 2010, 114, 22085-22091; (b) J. Liu, S. Fu, B. Yuan, Y. Li and Z. Deng, *J. Am. Chem. Soc.*, 2010, 132, 7279-7281; (c) V. Georgakilas, M. Otyepka, A. B. Bourlinos, V. Chandra, N. Kim, K. C. Kemp, P. Hobza, R. Zboril and K. S. Kim, *Chem. Rev.*, 2012, 112, 6156-6214.
13. T. Gokus, R. R. Nair, A. Bonetti, M. Böhmler, A. Lombardo, K. S. Novoselov, A. K. Geim, A. C. Ferrari and A. Hartschuh, *ACS Nano*, 2009, 3, 3963-3968.
14. S. G. Srivatsan and Y. Tor, *Tetrahedron*, 2007, 63, 3601-3607.

15. W. D. Wilson, L. Ratmeyer, M. Zhao, L. Strekowski and D. Boykin, *Biochemistry*, 1993, 32, 4098-4104.
16. B. Shirinfar, N. Ahmed, Y. S. Park, G.-S. Cho, I. S. Youn, J.-K. Han, H. G. Nam and K. S. Kim, *J. Am. Chem. Soc.*, 2012, 135, 90-93.
17. G. Dodin, M.-A. Schwaller, J. Aubard and C. Paoletti, *Eur. J. Biochem.*, 1988, 176, 371-376.
18. J.-J. Liu, X.-R. Song, Y.-W. Wang, G.-N. Chen and H.-H. Yang, *Nanoscale*, 2012, 4, 3655-3659.
19. (a) E. N. Primo, P. Cañete-Rosales, S. Bollo, M. D. Rubianes and G. A. Rivas, *Colloids and Surfaces B: Biointerfaces*, 2013, 108, 329-336; (b) M. Zheng, A. Jagota, M. S. Strano, A. P. Santos, P. Barone, S. G. Chou, B. A. Diner, M. S. Dresselhaus, R. S. McLean, G. B. Onoa, G. G. Samsonidze, E. D. Semke, M. Usrey and D. J. Walls, *Science*, 2003, 302, 1545-1548.
20. L. Tang, Y. Wang, Y. Liu and J. Li, *ACS Nano*, 2011, 5, 3817-3822.
21. H. Haruki, B. Gyurcsik, M. Okuwaki and K. Nagata, *FEBS Lett.*, 2003, 555, 521-527.
22. (a) Y. Xu, Q. Wu, Y. Sun, H. Bai and G. Shi, *ACS Nano*, 2010, 4, 7358-7362; (b) A. J. Patil, J. L. Vickery, T. B. Scott and S. Mann, *Adv. Mater.*, 2009, 21, 3159-3164.
23. (a) M. Wu, R. Kempaiah, P.-J. J. Huang, V. Maheshwari and J. Liu, *Langmuir*, 2011, 27, 2731-2738; (b) V. Kotikam, M. Fernandes and V. A. Kumar, *Phys. Chem. Chem. Phys.*, 2012, 14, 15003-15006.
24. (a) P. Nguyen and V. Berry, *J. Phys. Chem. Lett.*, 2012, 3, 1024-1029; (b) Q. He, H. G. Sudibya, Z. Yin, S. Wu, H. Li, F. Boey, W. Huang, P. Chen and H. Zhang, *ACS Nano*, 2010, 4, 3201-3208; (c) T. Cohen-Karni, Q. Qing, Q. Li, Y. Fang and C. M. Lieber, *Nano Lett.*, 2010, 10, 1098-1102.
25. T. Kavitha, S. I. Haider Abdi and S.-Y. Park, *Phys. Chem. Chem. Phys.*, 2013, 15, 5176-5185.

3a.5. APPENDIX

Note A1. FE-SEM Images and Raman Spectra

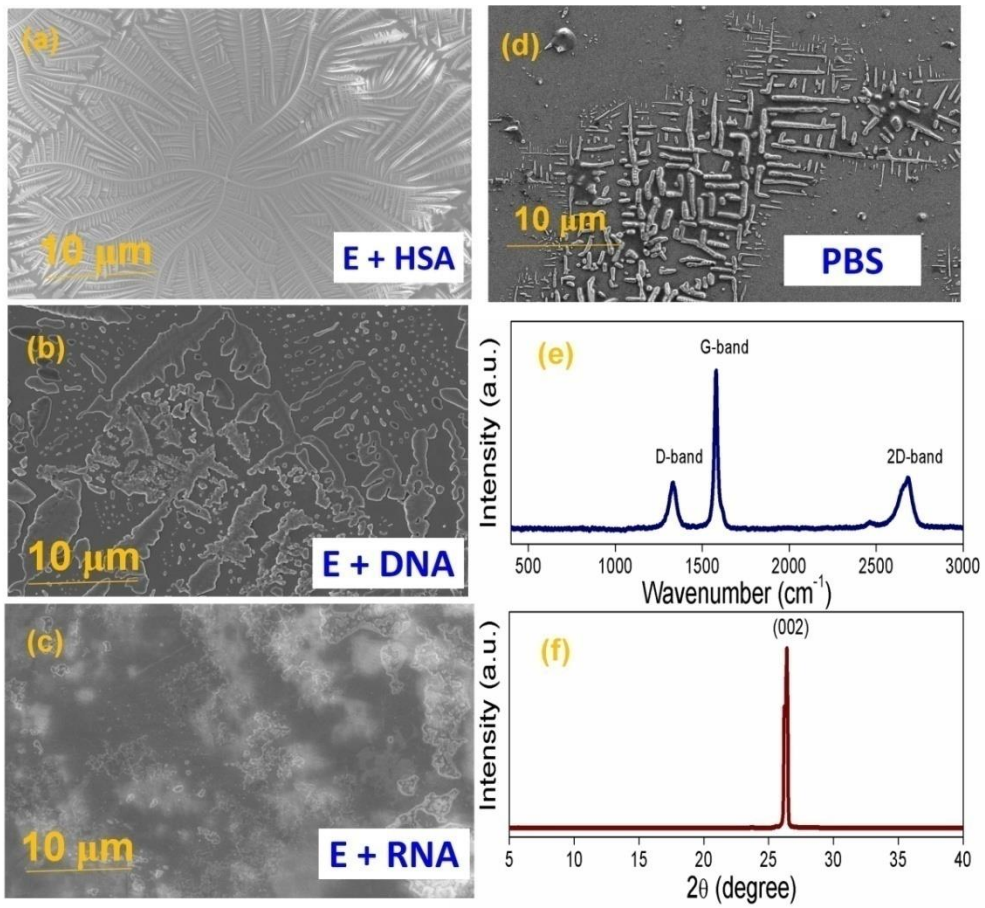

Figure A1. FE-SEM images of (a) ellipticine (7 µM) with HSA (100 µM), (b) ellipticine (7 µM) with DNA (100 µM), (c) ellipticine (7 µM) with TAR RNA (10 µM), (d) Phosphate buffer (PBS, pH 7); and (e) Raman Spectra of graphite; (f) Powder X-ray diffraction of graphite.

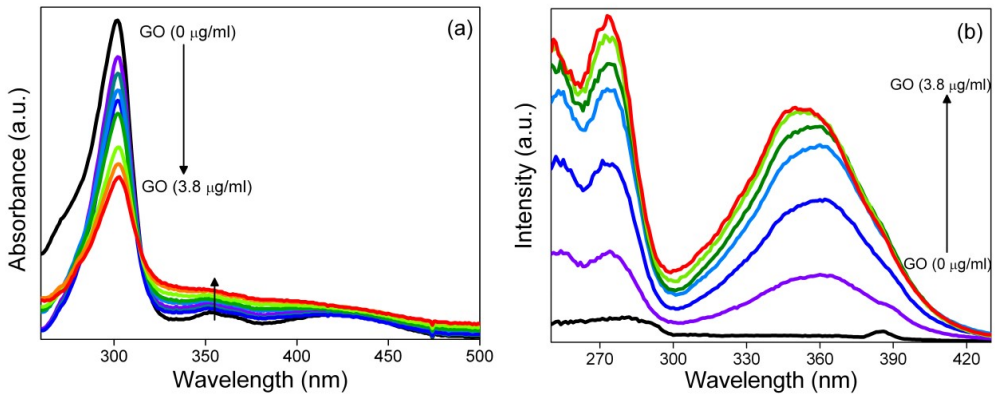

Figure A2. (a) Absorption spectra and (b) excitation spectra (λ_{em} = 450 nm) of ellipticine in aqueous PBS with increasing concentration of GO (0-3.8 µg/ml).

Note A2.

Loading Capacity of Drug On GO: The drug (ellipticine) loading on GO was monitored in phosphate buffer saline (PBS, pH ~7) at room temperature. As ellipticine (EPT) is sparingly soluble in water, hence, a small amount of concentrated DMSO stock solution of EPT was added into aqueous PBS buffer solution and strongly sonicated to make system homogeneous. After each addition of GO, the solution is strongly sonicated for 10-20 minutes. The loading capacity of drug was calculated by monitoring excitation spectra of the drug, rather than the conventional absorption spectra, as fluorescence excitation spectra is more sensitive than absorption spectra particularly when the concentration of the drug is in the range of nano-molar to micro-molar. The drug loading capacity was determined by monitoring its peak intensity at 300 nm (the peak at 300 nm arises due to the protonated form of EPT in PBS) (**Figure A3**) with the help of following equation:

$$W_{\text{loading capacity}} = 100 - \left\{ \left(\frac{\text{ellipticine final intensity in presence of GO}}{\text{ellipticine intenisty without GO}} \right) \times 100 \right\}$$

where, $W_{\text{loading capacity}}$ stands for loading capacity of EPT, and we found ~76% drug (from its initial concentration) was loaded on GO surface. The high loading capacity of EPT indicates that drug binds to both sides of single layer GO sheet predominantly by π-π stacking interactions.

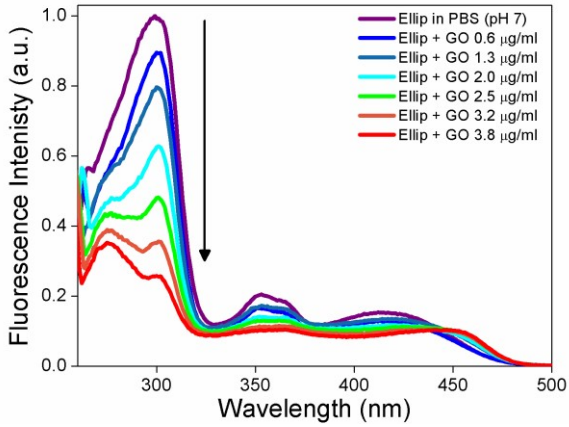

Figure A3. Excitation spectra of ellipticine in presence of GO (λ_{em} = 520 nm).

Unloading Capacity of Drug from GO: The progressive addition of DNA/RNA into ellipticine-GO (E-GO) composite, drug releasing from GO takes place, and it is evident from **Figure 3.2** that after coming out from GO surface the drug binds to DNA/RNA in its protonated form. The releasing capacity of the drug from GO was calculated monitoring the

intensity at 315 nm (as a new peak starts appearing at ~315 nm after addition of DNA, RNA)[1] in the excitation spectra (**Figure A4**) with the help of following equation,

$$W_{\text{unloading capacity}} = 100 - \left\{ \left(\frac{\text{ellipticine final intensity in presence of GO}}{\text{E-GO intenisty in presence of DNA or RNA}} \right) \times 100 \right\}$$

where, $W_{\text{unloading capacity}}$ stands for releasing capacity of drug, and finally we found ~ 60% of drug was released from GO.

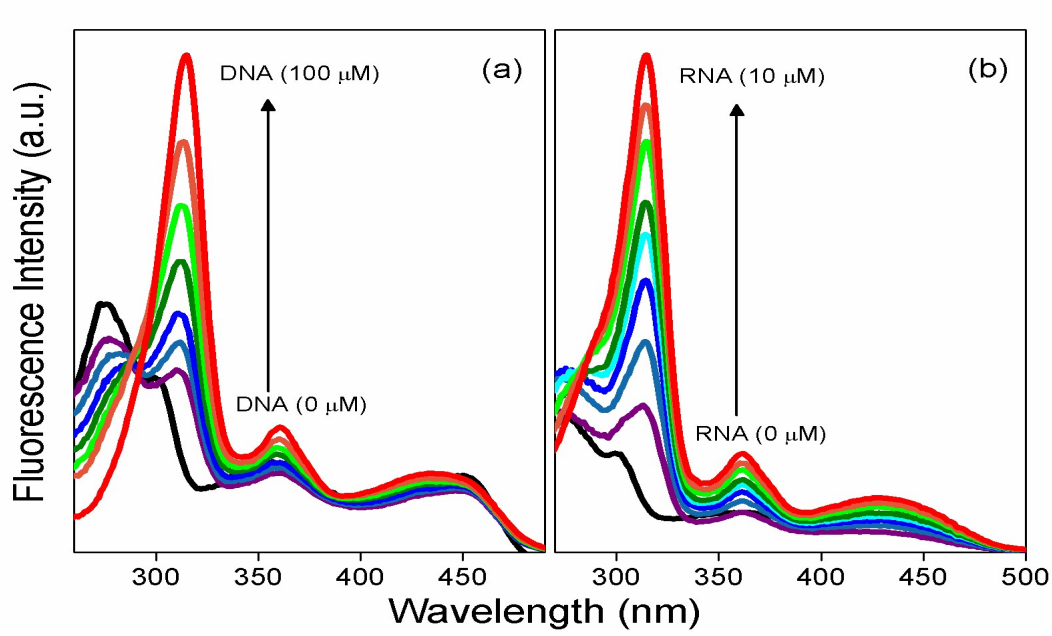

Figure A4. Excitation spectra of ellipticine-GO (E-GO) system in presence of (a) DNA and (b) RNA (λ_{em} = 520 nm).

Note A3. Circular Dichroism Measurements

Circular Dichroism (CD) spectra of HSA were monitored by the progressive increase concentration of the E-GO in the medium. HSA shows two distinct characteristic peaks at 208 nm and 222 nm, which appears from α-helices of the protein as HSA contains 65% of α-helix in its structure.[2] GO itself doesn't show any characteristic signal in CD. By the progressively increasing concentration of GO in the fixed concentration of HSA, a prominent decrease in CD signal at both of the dips is observed (**Figure A5**). The decreasing CD signal is surely an outcome of modulation in the secondary structure of protein in presence of GO. This ascribed to protein molecule adsorption over the GO surface by hydrophobic, π-π stacking interaction between aromatic moieties of protein and π-conjugate domains of GO.

Moreover electrostatic, H-bonding interactions also play crucial role in protein-GO complexation process.

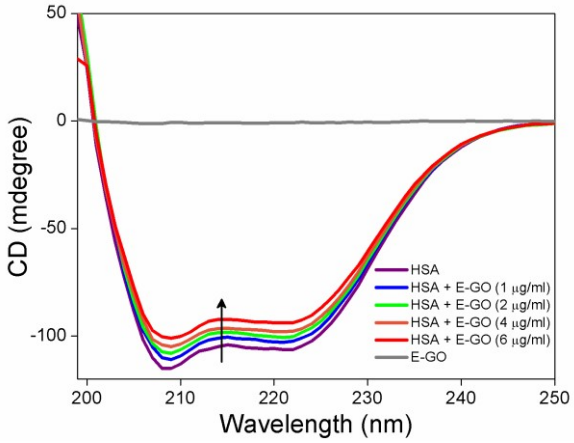

Figure A5. CD spectra of HSA in presence of E-GO solution.

Note A4. Time Resolved Fluorescence Anisotropy

To obtain further information about the microenvironments of the drug in presence of GO, GO-DNA, GO-RNA, GO-HSA-DNA, and GO-glucose systems, we have collected time-resolved anisotropy decays, which directly reflect the restriction over rotational motion imposed by the surrounding environment. The typical anisotropy decays are shown in **Figure A6**, and corresponding data are given **Table A1**. The average rotational correlation time of GO-bound EPT monitored at 450 nm is 110 ps. When GO-bound EPT is exposed to DNA/RNA, severe restriction of rotational motion of EPT_H^+ takes place (**Figure A6**), inferring that the drug molecules are interacting to DNA/RNA probably through intercalation binding mode. Interestingly, the decay profile consists of 'dip-rise' feature in case of E-GO-DNA composite system, and the decay exhibits some residual anisotropy, which does not fit within our experimental time window. This kind of not-so-common time-resolved anisotropy arises due to the presence of multiple species, each characterized by its own lifetime and anisotropy decay.[3] However, for the sake of relevance of the present work, we mainly focus on normal anisotropy decay features.

Further, we performed anisotropy measurements for ellipticine and EPT-GO in presence of serum protein (**Figure A6**) and the results are summarized in **Table A1**. Compared to ellipticine-HSA, E-GO-HSA system exhibits significantly slower rotational correlation time of ellipticine (**Table A1**), it attributes to the more confined environment of ellipticine molecules in E-GO-HSA composite than E-HSA system. This observation infers that protein adsorption takes place on the GO surface probably through hydrophobic, and π-π stacking

interactions with electron conjugated sub-domains, hydrogen bonding interactions (between the oxygen functional groups of GO and nitrogen and oxygen containing functional groups of protein) as well as electrostatic interactions between protein surface charges and oxygen functional groups over GO.[4]

Table A1. Time-resolved fluorescence anisotropy fitting parameters of ellipticine in presence of GO and various bio-macromolecules containing GO in aqueous buffer solution.

Sample	τ_{r1} (ns)	τ_{r2} (ns)	τ_{r3} (ns)	f_1	f_2	f_3	r_0	$\langle\tau_r\rangle^{\#}$ (ns)
EPT + GO (3.8 μg/ml) (E-GO)	0.15	-	-	0.37	-	-	0.37	0.15
E-GO + RNA (10 μM)	0.08	8.08	-	0.19	0.15	-	0.34	3.7
EPT + HSA (100 μM)	0.10	0.88	20.0	0.19	0.02	0.09	0.33	6.12
E-GO + HSA (100 μM)	0.082	0.86	32.0	0.19	0.09	0.10	0.38	9.03
EGH + DNA (100 μM)	0.12	2.92	35.0	0.14	0.06	0.08	0.39	11.03

$^{\#}\langle\tau_r\rangle = (\tau_1 f_1 + \tau_2 f_2 + \tau_3 f_3)/(f_1 + f_2 + f_3)$

In order to probe drug releasing behaviour from E-GO-HSA (EGH) in presence of DNA, anisotropy measurement was monitored (at 520 nm) in presence of DNA to the above mentioned system. It is clearly shown from the results (**Table A1** and **Figure A6**) that rotational motion of the drug is getting more restricted in EGH-DNA system. This observation leads us to conclude that DNA extracts the drug from EGH system by the formation of ternary complex with protein absorbed on GO surface, thereby; drug is experiencing slightly restricted motion compared to EGH system. When GO-bound EPT is exposed to glucose, the anisotropy decay profile remains same, indicating glucose is not interacting with E-GO, which is in agreement with steady state and lifetime results.

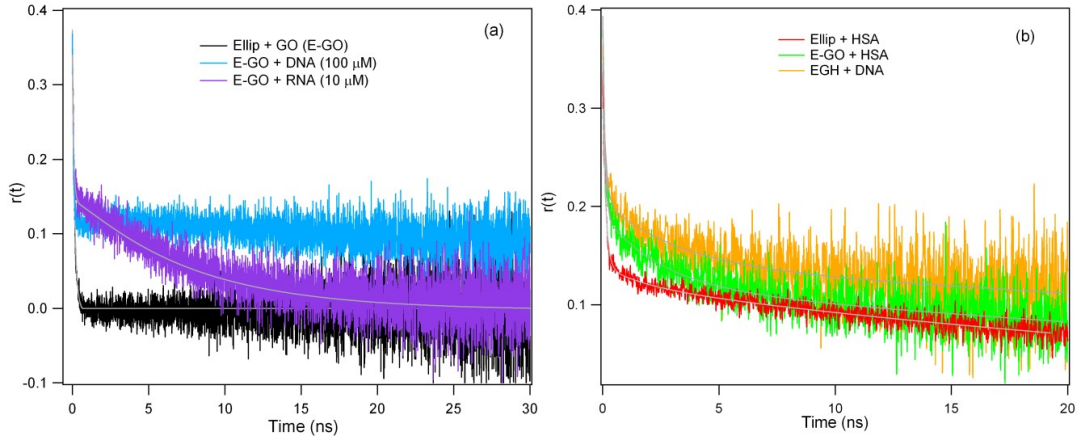

Figure A6. Time-resolved fluorescence anisotropy decay profiles of (a) E-GO (4 μg/ml), E-GO-DNA (100 μM) and E-GO-RNA (10 μM), (b) Ellip-HSA (100 μM), E-GO-HSA (100 μM) and EGH-DNA (100 μM).

Note A5. Binding Constants

The binding parameters of ellipticine (EPT) in presence of GO-HSA, GO-DNA, GO-RNA and GO-HSA-DNA were estimated from modified Scatchard plot,[5] which is described as follows

$$\frac{[M]_{total}}{f} = \frac{1}{NK_f(1-f)} + \frac{[L]_{toal}}{N} \qquad (1)$$

Where, $[M]_{total}$ is the final concentration of the macromolecule, $[L]_{total}$ is the total concentration of the drug, "N*"* is the number of sites in macromolecule and "f*"* represents the fraction of ligand bound to macromolecule. The value of "f*"* can be evaluated from the following equation

$$f = \frac{(I_{obs}-I_L)}{(I_{max}-I_L)} \qquad (2)$$

where I_{obs}, I_L, and I_{max} represents observed fluorescence intensity of the free drug and maximum intensity after saturation of all binding sites, respectively. A plot of $[M]_{total}$ /f vs. 1/(1-f) produces a straight line and one can calculate binding constant (K_f) from the slope. The Scatchard plot for neutral ellipticine (EPT_N) towards HSA was obtained by monitoring the peak intensity at 450 nm with the progressive addition of HSA into the E-GO complex (**Figure A7a**), and the binding constant of EPT_N towards HSA is determined to be K_f = (1.44±0.15) × 10^5 M^{-1}. The high binding constant along with the favourable free energy change (ΔG^0 = -29.43±2.96 kJ mol^{-1} indicates that HSA interacts with GO surface. It is evident from steady state spectra that when DNA/RNA interacts with E-GO complex, then protonated form (EPT_H^+) of the drug binds with those polynucleotides. The binding affinity of EPT_H^+ with DNA in presence of GO is estimated to be K_f = (6.18±0.6) × 10^5 M^{-1} from Scatchard plot (**Figure A7b**). The high binding constant and the favourable free energy change calculated (ΔG^0 = -33.03±3.3 kJ mol^{-1}) from the binding constant indicates that the EPT is released from GO surface and intercalates with DNA as protonated form of the drug. Very similar results are observed in presence of TAR-RNA (**Figure A7c**), where the association constant is estimated to be K_f = (1.014±0.1) × 10^5 M^{-1} which suggests the binding process is highly energy favoured (ΔG^0 = -28.56±2.84 kJ mol^{-1}) one. Drug release from EGO-HSA complex in presence of DNA and its binding affinity to DNA can be quantitatively determined from the binding constant estimated from the Scatchard plot (**Figure A7d**), and the estimated association constant is K_f = (2.21±0.22) × 10^5 M^{-1}. The high association constant and the favourable free energy (ΔG^0 = -30.5±3.0 kJ mol^{-1}) change

indicates that even though protein was giving further protection to drug on the surface of GO, drug releasing takes place even in presence of DNA, because of the higher binding affinity of protonated ellipticine (EPT_H^+) to DNA compared to protein.

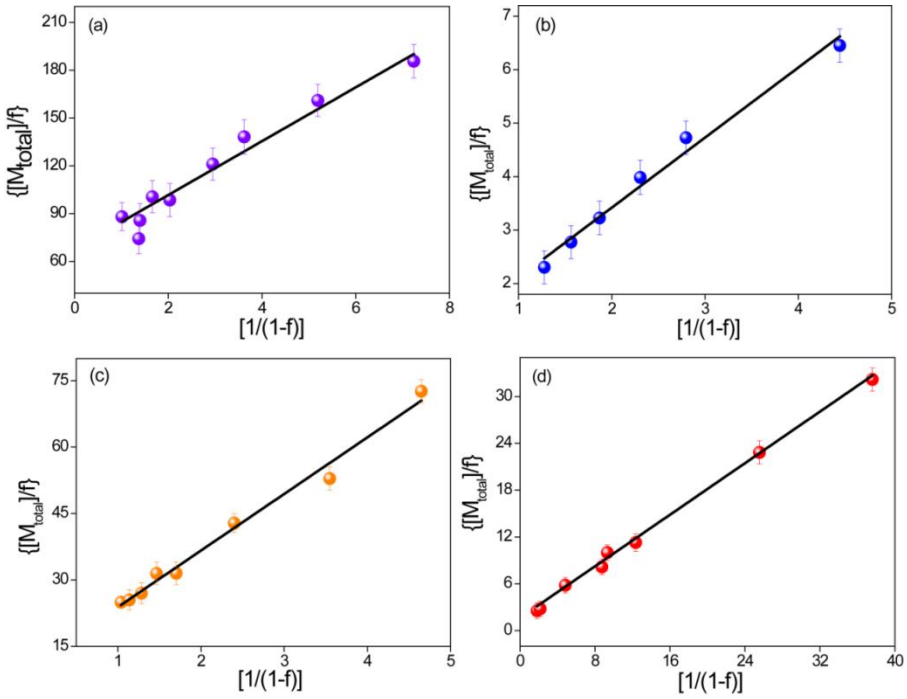

Figure A7. Scatchard binding plots constructed from emission intensities of ellipticine in presence of (a) GO-HSA, (b) GO-DNA, (c) GO-RNA and (d) GO-HSA-DNA.

Note A6.

Notably, the drug release in-vitro takes place within 72 hours.[6] Therefore, we have monitored the precipitation of E-GO, E-GO-DNA, E-GO-HSA and E-GO-HSA-DNA solution for 72 hours. Interestingly, all the solutions remains well dispersed even for 72 hours (**Figure A10**), which suggest that additional functionalization of GO, which has been routinely used in various drug delivery experiments, is not necessary.

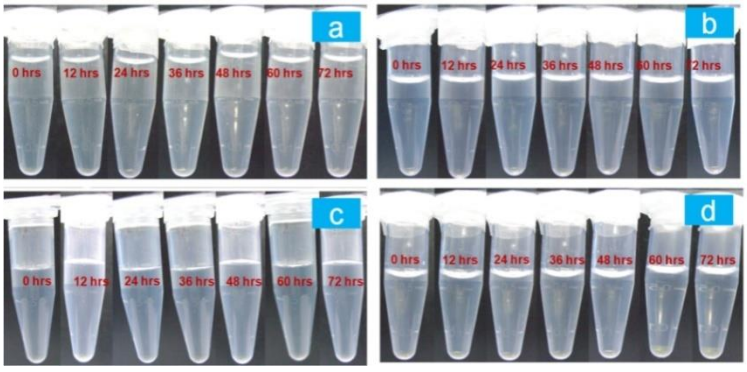

Figure A8. Pictures of (a) ellipticine-GO (E-GO) in aqueous PBS, (b) E-GO-HSA (EGH) in aqueous PBS (c) E-GO-DNA in aqueous PBS (d) EGH-DNA in aqueous PBS at different time intervals.

References

1. G. Dodin, M.-A. Schwaller, J. Aubard and C. Paoletti, *Eur. J. Biochem.*, 1988, **176**, 371-376.
2. Y. Moriyama and K. Takeda, *Langmuir*, 2005, **21**, 5524-5528.
3. T. Kanti Das and S. Mazumdar, *Biophys. Chem.*, 2000, **86**, 15-28.
4. (a) F. Yang, Y. Liu, L. Gao and J. Sun, *J. Phys. Chem. C*, 2010, **114**, 22085-22091; (b) J. Liu, S. Fu, B. Yuan, Y. Li and Z. Deng, *J. Am. Chem. Soc.*, 2010, **132**, 7279-7281; (c) V. Georgakilas, M. Otyepka, A. B. Bourlinos, V. Chandra, N. Kim, K. C. Kemp, P. Hobza, R. Zboril and K. S. Kim, *Chem. Rev.*, 2012, **112**, 6156-6214; (d) H. Y. Mao, S. Laurent, W. Chen, O. Akhavan, M. Imani, A. A. Ashkarran and M. Mahmoudi, *Chem. Rev.*, 2013, **113**, 3407-3424.
5. E. F. Healy, *J. Chem. Educ.*, 2007, **84**, 1304.
6. Y. Pan, H. Bao, N. G. Sahoo, T. Wu and L. Li, *Adv. Func. Mater.*, 2011, **21**, 2754-2763.

3b. Loading of an Anticancer Drug into Mesoporous Silica Nanochannel and Subsequent Release to Cellular DNA

3b.1. Introduction and Motivation of the Work

Recently, mesoporous silica nanomaterials (MSN) have attracted burgeoning interest due to its large surface area, pore volume, highly ordered pore structure, adjustable pore size (detail has been discussed in Chapter 1).[1] In addition to that, other unique properties of MSN, such as, water dispersibility, versatile surface modification, high drug binding affinity, low toxicity, cell penetrating ability and chemical stability, makes it suitable for biological and biomedical applications, including drug delivery, enzyme and protein immobilization, bio-separation.[1-2] Thus, the study of MCM-41with various drug molecules have been the subject of interest, and many research works have been devoted to understand the stability and physical properties of drugs encapsulated in MCM-41.[1a,1d,2-3] Few recent studies have shown the drug release from MCM-41 carrier by some external trigger, e.g. changing the medium pH and presence of bio-molecules.[1a,1d,2-3] However, it would be very simple and effective, if the drug loading into the carrier and subsequent release to specific biomolecule, like, DNA can be directly monitored by the change in fluorescence colour, without using any sophisticated and complex technique. In this regard, an anticancer drug, ellipticine (EPT), can be an ideal choice due to its interesting biological and photophysical properties. As already described in Chapter 3a, Ellipticine (EPT), a pyridocarbazole type of plant alkaloid,[4] exhibits its anticancer activity by means of intercalating in between the DNA base pairs, thereby inhibiting the topoisomerase-II enzyme activity, which eventually restricts the DNA replication process.[4b,4c,5] Herein we have probed the drug (EPT) loading in MCM-41 nanochannels and its subsequent release to intracellular biomolecule, like, DNA with the help of fluorescence colour switch. We have monitored the interaction scenario between MCM-41 and DNA through fluorescence and circular dichroism (CD) studies. Finally, the translocation of the drug from the EPT-lysozyme-MCM-41 composite system to DNA has been probed with the help of fluorescence colour switch and CD measurements. Electron microscopy (FE-SEM) results suggest the formation of distinctive 3D assemblies involving MCM-41 and the biomolecule(s) probably through non-covalent interactions.

3b.2. Results and Discussion

3b.2a. Steady State Fluorescence and Circular Dichroism Measurements

EPT in DCM exhibits a blue emission at 430 nm (**Figure 3.1**), corresponding to the neutral from of the drug. In presence of MCM-41, blue emission gradually disappears and a new green emission peak at ~505 nm starts appearing (**Figure 3.1**). At high concentration of MCM-41, the blue emission peak totally vanishes and the peak at ~505 nm becomes the sole peak. The newly generated green emission band is attributed to the protonated form of EPT. This switching in emission maximum confirms that EPT molecules are involved in strong interaction with MCM-41. Here it is necessary to mention that nano-pores of MCM-41 is occupied by the mild acidic silanol –OH groups (pK_a 3-4),[1a] which can easily donate proton to the surrounding basic molecule/moiety. Therefore, we believe that upon encapsulation in the nano-pores protonation of pyridine-N group takes place by accepting the proton from the surrounding –OH groups (silanol, -Si-OH), and consequently results in protonated form of EPT inside MCM-41.

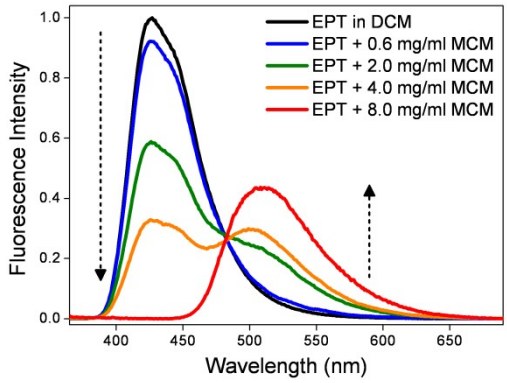

Figure 3.1. Emission spectra of EPT (λ_{ex} = 350 nm) in dichloromethane (DCM) solvent with gradual addition of MCM-41.

Loading of EPT into MCM-41 nanochannel further verified through powder X-ray diffraction (PXRD) measurements. PXRD patterns of the MCM-41 and EPT-MCM samples are shown in **Figure 3.2a**. Both the samples exhibit a very intense diffraction peak at 2θ values of 2.1º for 100 reflection plane and three weak intense peaks at 3.7º, 4.5º and 5.9º, for 110, 200 and 210 reflection planes, respectively.[6] Presence of 100 reflection pattern (at 2θ = 2.1º) indicates the presence of mesoporosity in both MCM-41 and EPT-MCM samples. Long range ordered hexagonal MCM-41 mesoporous phase is also confirmed by the PXRD. Characteristic PXRD diffraction peaks at 110, 200 and 210 confirms a 2-D hexagonal lattice structure for both the MCM-41 and

EPT-MCM.[6] Notably, the small angle XRD diffraction peaks of EPT-MCM sample isless intense than bare MCM-41. In general, the incorporation of organic molecules in MCM-41 nanochannels decreases the scattering intensity.[7] Hence, the decrement in the diffraction intensity peaks in small angle PXRD measurements reveals the encapsulation of EPT drug molecule inside the nano-pores of MCM-41. The wide angle PXRD measurements exhibits peaks in between 20º and 30º for both MCM-41 and EPT loaded MCM-41 (**Figure 3.2b**). However, the presence of sharp peak around 18º for EPT-MCM sample may be due to the crystalline EPT molecules bound to the MCM-41.

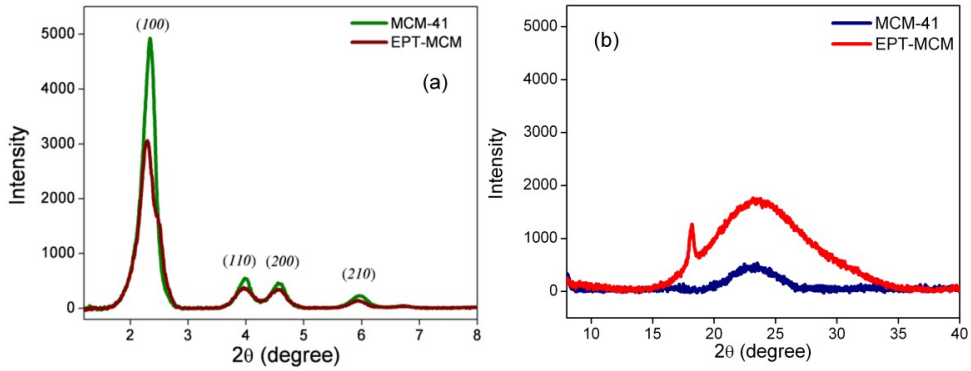

Figure 3.2. Powder X-ray diffraction (PXRD) pattern (a) small angle range (1-8°) and (b) wide angle range (8-40°) of MCM-41 and EPT-MCM.

Moreover, nitrogen gas adsorption measurements are carried out to confirm the drug loading inside the nano-pores. Nitrogen gas adsorption–desorption isotherms and pore-size distribution of MCM-41 before and after the loading of EPT (30 mmolg^{-1} of samples) have been shown in **Figure 3.3a**. Both the samples represent type-IV Brunauer-Emmett-Teller (BET) isotherms,[6] indicating the well defined mesoporous structure of MCM-41 before and after loading of drug. The reduced amount of adsorbed nitrogen in case of EPT containing MCM-41 sample confirms the encapsulation of drug molecules within the nano-pores, which results in lower space available for nitrogen gas adsorption. Moreover, pore size and pore volume of MCM-41 decrease after loading of EPT drug molecules from 32 to 28-30 Å and from 1.37 to 1.09 cm^3 g^{-1}, respectively (**Figure 3.3b**). Furthermore, surface area also reduced from 1520 to 1200 m^2 g^{-1} after being loaded with EPT. Diminished surface area and pore volume, along with shift in average pore size from 32 to 28-31 Å indicate that the drug molecules inside the nanochannels occupy the pore space. In summary, nitrogen gas

adsorption results provide evidence that the drug molecules are indeed adsorbed inside the nanochannels of MCM-41 samples.

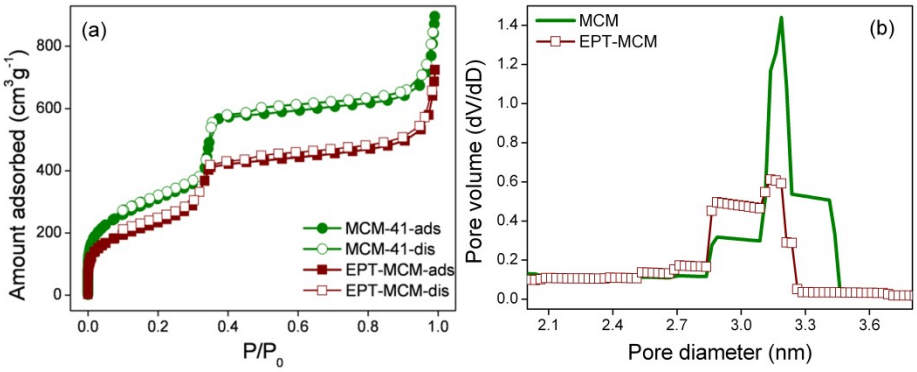

Figure 3.3. (a) Nitrogen gas adsorption and desorption of MCM-41 and EPT-MCM (Filled and open markers denote adsorption and desorption, respectively) (b) Pore-size distribution of MCM-41 and EPT-MCM.

Notably, for drug delivery/biological application, the MCM-41 needs to be dispersed in aqueous medium. Hence, EPT loaded MCM-41 (EPT-MCM) was extracted from DCM solvent (discussed in experimental section) and dried in ambient atmosphere. Unbound or weakly bound drug molecules are removed by repetitive washing with DCM solvent. Then, EPT loaded MCM-41 (EPT-MCM) has been dispersed in phosphate buffer saline (PBS) solution (pH 7), which shows a single emission peak at 515 nm (**Figure 3.4**). This is almost 15 nm blue shifted compared to EPT in PBS, which shows an emission maxima at 530 nm. The observed hypsochromic shift in emission maxima of EPT in presence of MCM-41 is attributed to the lower polarity inside nano-pores of MCM-41, which further supports the encapsulation of EPT molecules inside the nano-pores of MCM-41. We anticipate that the strong electrostatic interactions between protonated EPT and negatively charged Si-O$^-$ (pK_a 3-4) groups of MCM-41,[1a] may facilitate drug molecules residing inside the nano-pores.

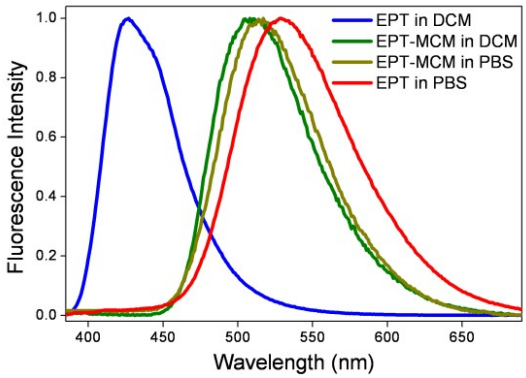

Figure 3.4. Emission spectra of EPT (λ_{ex} = 350 nm) in DCM, PBS before and after loading into MCM-41.

MCM-41 has penetration ability to the cell,[3a,8] which is enriched in DNA. Moreover, it has been proved that MCM-41 exerts less cytotoxic effect to the cell.[3a,8] Thus, the next step is to check the interaction behaviour between EPT loaded MCM-41 (EPT-MCM) and DNA (**Figure 3.5a**). Fluorescence intensity of protonated EPT gradually increases with the progressive addition of ct-DNA (**Figure 3.5a**) along with a significant (10 nm) red shift in emission maximum (insert in **Figure 3.5a**). This change in emission maximum is clearly reflected by alteration in the fluorescence colour from light green to intense green. Interestingly, emission results for EPT-MCM-DNA system exactly matches with the previous results of EPT-DNA system,[9] which suggests that EPT molecules are progressively releasing from MCM-41 nano-pores and bind to DNA. To confirm the interaction scenario between ct-DNA and EPT-MCM, we have also performed circular dichroism (CD) studies. The CD spectrum of ct-DNA in buffer solution (at pH 7) exhibits a positive peak at ~280 nm and a negative band at ~245 nm corresponding to a typical right handed B-form of DNA (**Figure 3.5b**).[10] Progressive addition of EPT-MCM to DNA solution gradually reduces the ellipticity of two bands (~245 and 280 nm) with an additional positive band appearing at ~320 nm. This newly observed band exactly matches (**Figure 3.6**) with the induced CD signal of EPT appeared during DNA intercalation mode of binding.[11] Thus, CD studies further supports DNA induced release of drug molecules from MCM-41 nano-pores. Due to high binding affinity of EPT towards DNA,[9] the drug molecules move from silica nanochannels to the segments of and it is believed to be major driving force for the release of EPT molecules from silica nanochannels. In addition to this, we cannot rule out the possibility of partial adsorption of DNA segment into/onto MCM-41. In fact there are reports, which suggest that Na^+ ions

present in the solution can cause a smaller amount of ct-DNA to be adsorbed inside/on the pores of silica nanochannels due to the intervention of the electrostatic repulsion between the negatively charged silica and the DNA molecule.[12]

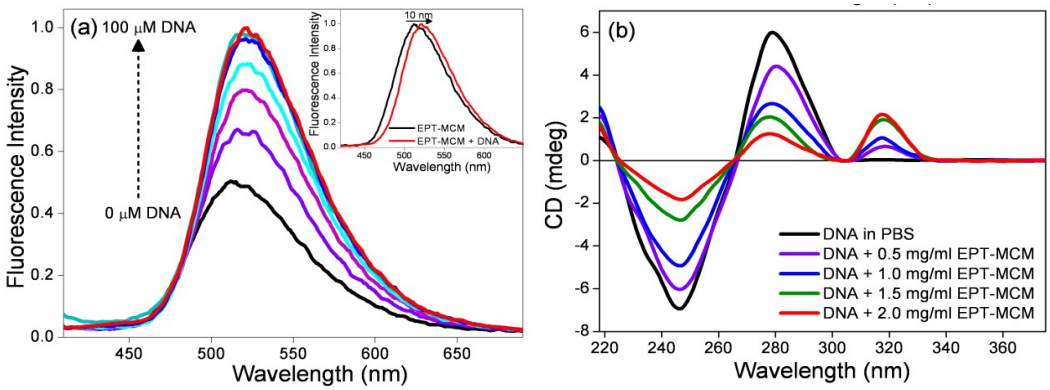

Figure 3.5. (a) Emission spectra of EPT-MCM (λ_{ex} = 350 nm) in PBS with gradual addition of DNA; (b) Circular dichroism spectra of DNA in PBS with gradual addition of EPT-MCM.

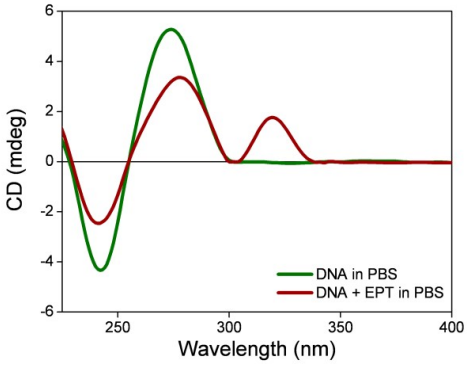

Figure 3.6. Circular dichroism (CD) spectra of DNA in PBS presence and absence of EPT.

In order to protect pre-mature drug release, various nano-particles (ZnO and CdS quantum dots etc.) were used as a pore blocker.[8,13] But efficient drug delivery applications, bio-compatible polymers might be useful to avoid cytotoxicity issues. We have chosen monomeric, globular lysozyme (Lyz) protein as a pore blocker. The emission intensity at 515 nm of EPT-MCM complex decreases progressively with increasing concentration of Lyz (**Figure 3.7a**). Here it is pertinent to mention that iso-electric point (pI) of Lyz is around 11;[14] so it is expected that the protein exists as positively charged entity at the physiological condition. On the other hand, MCM-41 mainly exists as negative charged entity at physiological pH condition (pH 7.2), because pK_a of hydroxyl groups present in MCM-41 is around 3-5.[15] As the size of the protein (35 Å) is slightly larger compared to pore diameter of MCM-41 (25-30 Å), it is expected that protein adsorbs at the surface or mouth of the nanochannels. Large

number of negatively charged Si-O$^-$ groups at the entrance of MCM-41 compared to external surface facilitate the adsorption of protein molecules close to the mouth of silica nano-pores. To get deep insight into the interaction between Lyz and EPT-MCM complex, the CD experiment was performed. The CD spectrum of lysozyme in PBS solution exhibits two negative bands in the ultraviolet (UV) region near 224 and 208 nm (**Figure 3.7b**) corresponding to the amount of α-helix in the secondary structure of the protein.[16] Addition of EPT-MCM to Lyz solution (**Figure 3.7b**), band intensity in the 208-330 nm range gradually decreases (similar results were observed by MCM-41 alone, shown in **Figure 3.8**). The result indicates that the amount of α-helix in the secondary structure of the protein decreases in presence of EPT-MCM, inferring the perturbation of secondary structure of protein by the MCM-41. We believe that MCM-41 causes conformational change in the native secondary structure of protein leading to decrease in helical content. Conformational change of Lyz upon adsorption on MCM-41 further supports our fluorescence results, where we have observed decrement of fluorescence intensity of EPT-MCM in presence of Lyz. We believe that the conformational change of Lyz leads to the exposure of some aromatic amino acids, which involve in electron transfer process with the drug molecule present at the close of the mouth or entrance. Furthermore, drug release kinetics (**Figure 3.9**) data shows that <7% of the EPT drug releases from EPT-MCM system into buffer solution, which is further reduced to <3% after lysozyme protection (i.e. for EPT-MCM-Lyz system). Thus, here Lyz acts as a pore blocker to prevent premature drug release form MCM-41.

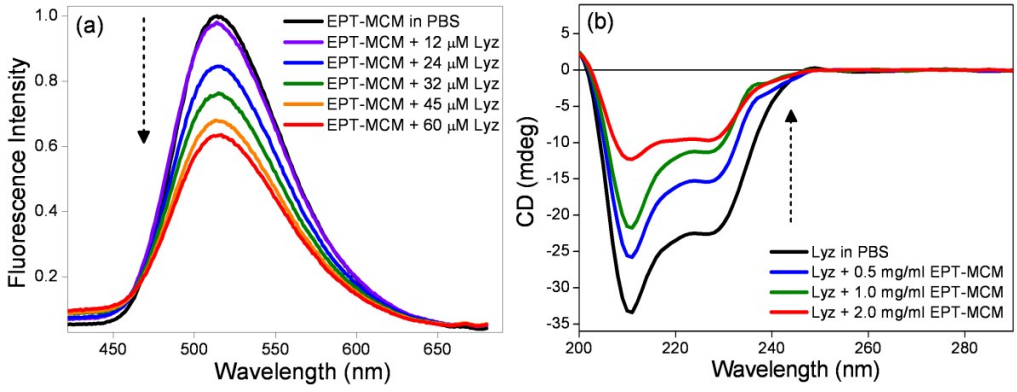

Figure 3.7. (a) Emission spectra of EPT-MCM (λ_{ex} = 350 nm) in PBS with gradual addition of lysozyme; (b) Circular dichroism spectra of lysozyme in PBS with gradual addition of EPT-MCM.

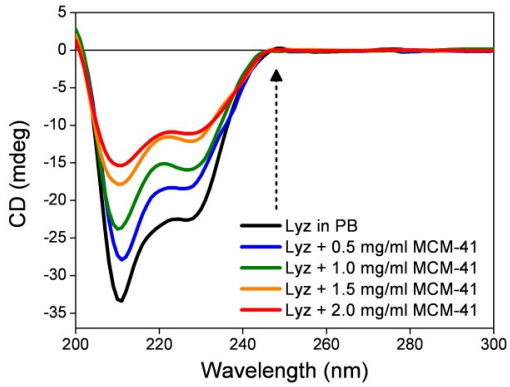

Figure 3.8. CD spectra of lysozyme in presence and absence of MCM-41 in PBS solution.

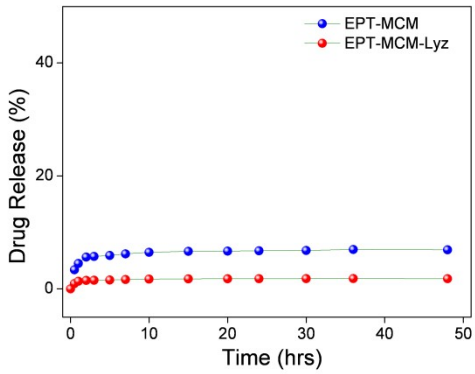

Figure 3.9. Release profile of drug from EPT-MCM and EPT-MCM-Lyz systems at pH 7.4.

Note that the biological role of EPT depends on its intercalation activity with DNA. Thus, it is important to demonstrate the interaction behaviour of protein blocked EPT-MCM towards DNA, and in order to do so, we have treated the EPT-MCM-Lyz system with ct-DNA (**Figure 3.10**). By progressive addition of DNA to EPT-MCM-Lyz (**Figure 3.10a**) system, intensity of emission maxima at 515 nm significantly increases along with 10 nm red shift in emission peak maxima (515 to 525 nm). Alteration in emission profile of EPT-MCM-Lyz in presence of DNA is clearly reflected by intensification of green emission. Interestingly, the peak maximum is closely matching with peak position of the drug in presence of DNA alone. Therefore, the above results indicate that DNA is capable of extracting EPT molecules from protein-MCM conjugate, which is reflected through the significant changes in the emission profile. Here it is necessary to mention that Lyz accumulates positive charge on its surface mainly due to the existence of positively charged amino acids (4 Lysine, 1 Histidine and 14 arginine).[17] As a result, positively charged lysozyme involves in electrostatic interaction with negatively charged phosphate backbone of DNA, and forms a protein-DNA complex. Because of this complex formation, the protein

molecules, which act as pore blockers to MCM-41 nanochannels, are removed from MCM-41, and subsequently, drug molecules can come out from MCM-41 nanochannels, and intercalates to DNA due to higher binding affinity of the EPT to DNA. Notably, the binding ratio of DNA to lysozyme is of about 20 base pairs per molecule of Lyz.[18] As ct-DNA has ~2000 base pairs, reasonable portion of DNA involves in complexation with Lyz, and remaining part will be available for the intercalation with EPT. As a result, translocation of the drug takes place from MCM-41 to ct-DNA. The CD studies also help us in understanding the interaction behaviour between EPT-MCM-Lyz composite and ct-DNA. On addition of ct-DNA to this EPT-MCM-Lyz system, CD spectrum is drastically modified (**Figure 3.10b**). Intensity of the negative peaks in the range of 210-230 nm systematically decreases and a new negative band at ~245 nm appears along with two positive bands at 280 and 320 nm. The negative band at ~245 nm corresponds to the helicity and a positive peak at ~280 nm due to base stacking of the added ct-DNA. Decrement of negative peaks in 210-230 nm in presence of DNA indicates the strong interaction between Lyz and DNA, which causes a major destabilization of native form of the protein. The appearance of a prominent positive band at 320 nm is due to induced CD signal of EPT bound DNA, confirming the translocation of EPT from the EPT-MCM-Lyz composite to the ct-DNA. Thus, our steady state fluorescence and circular dichroism results confirm DNA induced drug release from Lyz protected MCM-41 nano-pores.

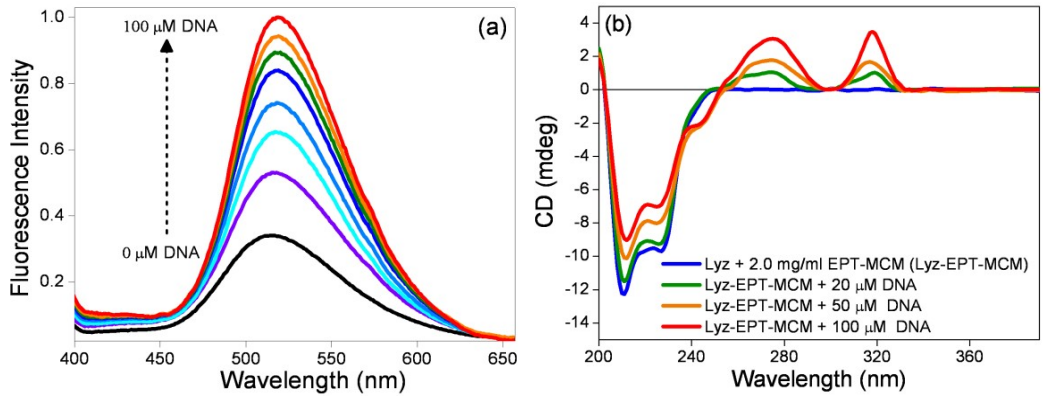

Figure 3.10. Emission spectra of EPT-MCM-Lyz (λ_{ex} = 350 nm) in PBS with gradual addition of DNA; (b) Circular dichroism spectra of Lyz-EPT-MCM in PBS with gradual addition of DNA.

3b.2b. Time Resolved Fluorescence Results

Fluorescence lifetime measurement is an excellent technique to explore the excited state environment around the fluorophore and it is highly sensitive to the excited-state interaction between the probe and guest molecule.[19] Thus, fluorescence lifetime data can significantly contribute in realizing the interaction behaviour between ellipticine and MCM-41, as well as translocation of EPT from MCM-41 to DNA. EPT in DCM exhibits bi-exponential decay (collected at 430 nm) profile having a major component of 16 ns (**Figure 3.11a** and **Table 3.1**). It is reported that ellipticine in non-polar solvents (like dioxane, cyclohexane, hexane etc.) exhibits a very long lifetime component.[20] Hence, 16 ns lifetime component is attributed to neutral form of EPT in DCM solvent. Addition of MCM-41 to the DCM solution exhibits a tri-exponential decay profile (collected at ~505 nm) consisting of a ~20 ns long major component (**Figure 3.11a** and **Table 3.1**). Increased lifetime in presence of MCM-41 indicates the encapsulation and stabilization of protonated form of EPT inside the silica nanochannels.

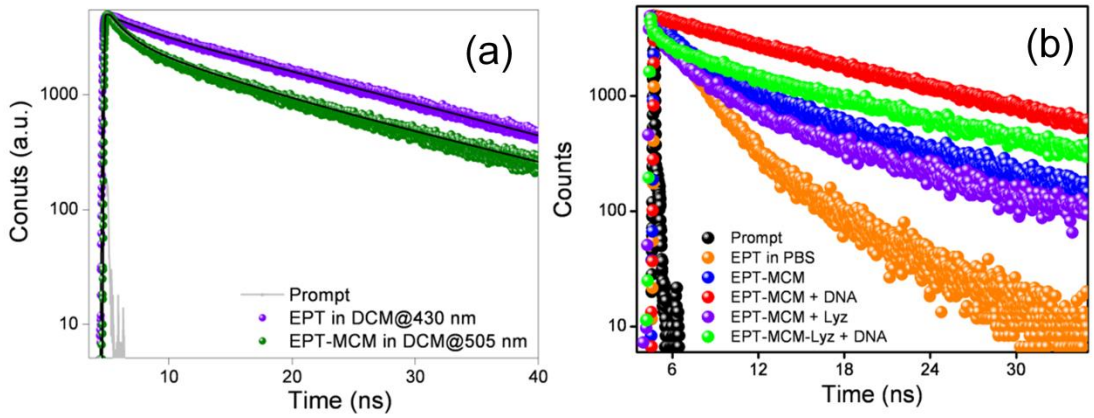

Figure 3.11. (a) Fluorescence transients of EPT (λ_{ex} = 375 nm) in DCM solvent decay collected at 430 nm (violate color decay) and fluorescence decay of EPT-MCM (λ_{ex} = 375 nm) in DCM solvent collected at 505 nm (green color decay); (b) Fluorescence transients (λ_{ex} = 375 nm) of EPT (λ_{col} = 530 nm), EPT-MCM (λ_{col} = 515 nm), EPT-MCM with addition of 100 µM DNA (λ_{col} = 525 nm), EPT-MCM with addition of 60 µM Lyz (EPT-MCM-Lyz) (λ_{col} = 515 nm) and EPT-MCM-Lyz with addition of 100 µM DNA in PBS (λ_{col} = 525 nm).

The decay profile of free drug in PBS buffer (pH 7) monitored at 530 nm (**Figure 3.11b** and **Table 3.1**) is found to exhibit bi-exponential feature having average lifetime of 2.5 ns, which is closely matching with literature reports.[9,21] However, lifetime (τ_{avg} = 4.75 ns) of EPT-MCM in dispersed solution is significantly different than that of EPT alone in PBS (τ_{avg} = 2.4 ns) (**Table 3.1**). The significant alterations in

Table 3.1. Fluorescence transient fittings of EPT (10 μM) in absence and presence of MCM-41 in DCM solvent, EPT (10 μM) in PBS; EPT-MCM in absence and presence of lysozyme (Lyz) and EPT-MCM-Lyz system in presence of DNA. All decays are excited at 375 nm and collected at respective emission maximum.

Sample	a_1	a_2	a_3	τ_1 (ns)	τ_2 (ns)	τ_3 (ns)	$^{\#}\tau_{avg}$(ns)
EPT in DCM at 430 nm	-	0.18	0.82	-	2.74	16.07	13.67
EPT-MCM in DCM at 505 nm	0.48	0.15	0.36	1.19	5.74	19.75	8.62
EPT in PBS at 530 nm	0.87	0.13	-	1.91	5.74	-	2.41
EPT-MCM in PBS at 515 nm	0.34	0.43	0.23	0.59	3.314	13.48	4.74
E-MCM + DNA at 525 nm	-	0.17	0.83	-	5.035	15.78	13.96
E-MCM + Lyz at 515 nm	0.49	0.39	0.12	0.550	3.10	14.87	3.22
E-MCM + Lyz + DNA at 525 nm	0.30	0.23	0.47	0.157	2.54	15.1	7.75

$^{\#}\tau_{avg} = (a_1\tau_1 + a_2\tau_2 + a_3\tau_3)$

the decay profile confirms the strong interaction between EPT and MCM-41 (**Figure 3.11b**). Moreover, the appearance of longer lifetime component of ~14 ns indicates the stability gained by drug molecule due to decreased non-radiative decay pathways of the drug inside the nano-pores of MCM-41. Similar kind of longer lifetime component was also noticed, when EPT molecules binds inside the protein nano-cavity,[9] DNA[9] and cucurbit[n]uril nano-cavity,[21] etc.

Lifetime transients of EPT-MCM in presence of Lyz (collected at 515 nm) are found to be tri-exponential (500 ps (49%), 3.1 ns (39%) and 15 ns (12%)) in nature having an average lifetime value of 3.22 ns (**Figure 3.11b** and **Table 3.1**). Decrease in the average lifetime of EPT-MCM in presence of Lyz clearly suggests some kinds of interaction between EPT and protein. We have already mentioned that Lyz acts as a pore blocker for MCM-41. Due to strong electrostatic interactions between MCM-41 and Lyz, some of the aromatic amino acids of protein come close contact to EPT molecules, and thereby, involves in electron transfer reaction with protonated form of

EPT, which results in generation of a fast 500 ps component. In consequence, intensity as well as lifetime of EPT-MCM decreases in presence of Lyz.

To verify the drug release behavior, we have gradually added DNA to the EPT-MCM-Lyz complex (**Figure 3.11b**). The average lifetime of EPT bound to EPT-MCM-Lyz complex increases (3.22 ns to 7.75 ns) with gradual addition of ct-DNA (**Table 3.1**). Interestingly, similar kind of lifetime feature also exists in EPT-DNA system. Therefore, the lifetime results suggest that protonated EPT molecules are translocating from MCM-Lyz and getting stabilized by DNA. Notably, when we compared the lifetime of EPT in presence of EPT-MCM-DNA and with EPT-MCM-Lyz-DNA systems, we have noticed a significant lifetime decrement in the latter case compared to former one. Importantly, in the latter case, we have observed a very short lifetime component of ~100 ps, which was absent in EPT-MCM-DNA and EPT-MCM-Lyz systems. This observation suggests that some of the EPT molecules are entrapped in between Lyz and ct-DNA due to electrostatic interaction between the positively charged Lyz and negatively charged DNA surface. Our CD results also supports this kind of complex formation, by which the secondary structure of protein is significantly perturbed in presence of ct-DNA. In this ternary complex consisting of Lyz-EPT-DNA, the protonated EPT molecules (stays in between the surface of DNA and protein), involves in strong electrostatic interaction with negatively charged phosphate backbone of DNA, by which electronic structure of protonated ellipticine is getting perturbed,[9] and as a result lifetime of EPT significantly reduces in this EPT-MCM-Lyz-DNA system. In summary, lifetime results corroborate our steady state fluorescence and CD results.

3b.2c. Confocal Microscopy and Field-emission Scanning Electron Microscopy (FE-SEM)

Confocal laser scanning microscopy (CLSM) images were recorded at 520 nm by the excitation at 380 nm. EPT-MCM sample was collected after 24 hrs incubation in PBS solution (**Figure 3.12a**). Green particles in the microscopy image clearly indicate that EPT molecules are residing inside MCM-41 nano-pores. The EPT-MCM-Lyz confocal image (**Figure 3.12b**) suggests that EPT molecules are not coming out from the MCM-nano-pores vindicating our claims that Lyz adsorbs and protects premature drug release.

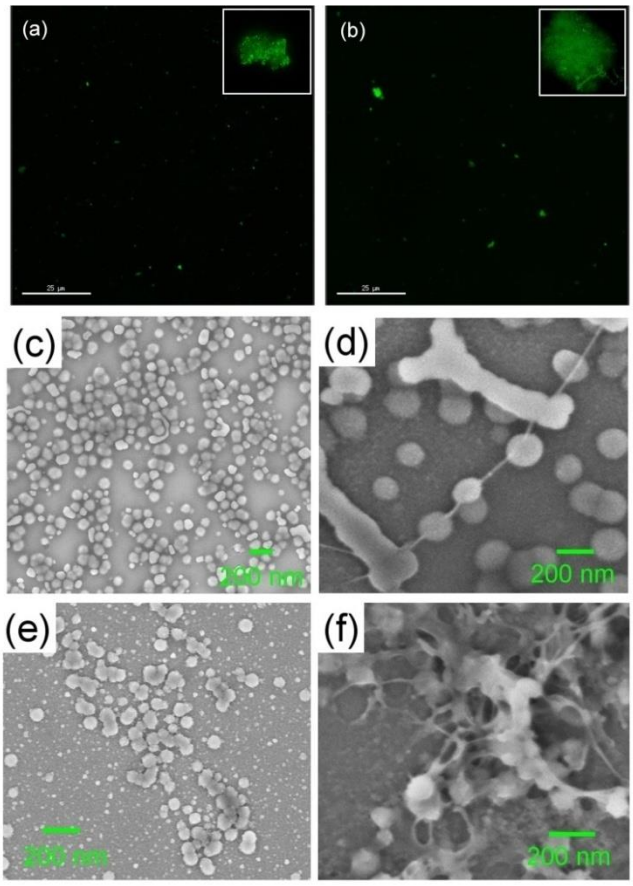

Figure 3.12. Fluorescence confocal laser scanning microscopy images of EPT-MCM (a); and EPT-MCM-Lyz (b) in PBS solution after incubating 12 hours at room temperature (λ_{ex} = 380 nm) (Insert shows zoomed portion of respective systems); FE-SEM images of MCM-41 (c), MCM-DNA (d), MCM-Lyz (e) and MCM-Lyz-DNA (f).

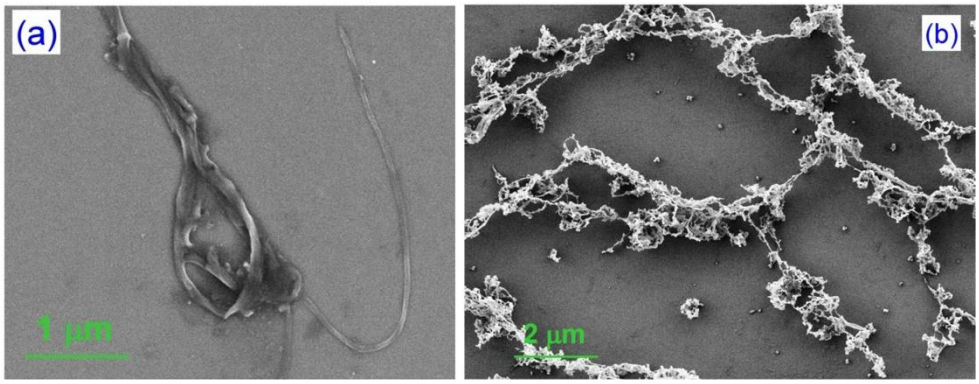

Figure 3.13. FE-SEM image of (a) DNA and (b) lysozyme.

To visualize the MCM-41 interactions with bio-molecules (DNA/Lyz), systems were subjected to field-emission scanning electron microscopy (FE-SEM) (**Figure 3.12c-f**). For relative comparison, we have also recorded the FE-SEM images of Lyz and DNA under identical experimental conditions (**Figure 3.13**). FE-SEM image of pure MCM-41 is shown in **Figure 3.12c** and exhibits mono-dispersed thin platelets

with an average particle size 200 nm. Addition of DNA to MCM-41 system dramatically alters the morphology (**Figure 3.12d**) and this morphology is totally different from the DNA alone system (**Figure 3.13a**). Interestingly, MCM-DNA system shows a garland kind of morphology, in which MCM-41 particles are connected by DNA, which acts as a thread here. To further confirm the morphological pattern we examined elemental EDAX measurements (**Figure 3.14**). Presence of C (10%), N (1.2%) and Si (80%) at the interface in the EDAX elemental analysis supports the existence of DNA in MCM-DNA composite (**Figure 3.14a**). In case of MCM-Lyz (**Figure 3.12e**) system, the composite morphology is not much different compared to MCM-41 alone. However, Lyz alone shows distinct structural morphology in the FE-SEM image (**Figure 3.13b**). Therefore, we anticipate that Lyz easily adsorbs at the mouth of MCM-41, thereby, the structural morphology of MCM-41 is not changing. EDAX analysis of MCM-Lyz system (**Figure 3.14b**) indicates the presence of N (1.5%), C (10%) and Si (80%). Existence of nitrogen in the elemental analysis comes from the amino acids of protein, which further confirms the presence of Lyz in MCM-Lyz composite. Interestingly, MCM-Lyz-DNA system (**Figure 3.12f**) shows very distinct structural morphology compared to individual systems. In this system (MCM-Lyz-DNA), spherical MCM-41 particles are connected with threads, which differ from MCM-DNA and MCM-Lyz morphological patterns. Moreover, the MCM particles are in close proximity and they are connected by thread. We believe that DNA here acts as glue due to formation of protein-DNA complex in between adjacent MCM-41 particles. Moreover, EDAX analysis of MCM-Lyz-DNA (**Figure 3.14c**) composite system infers the presence of nitrogen (1.2%), which confirms the presence of biomolecule(s) in the composite system.

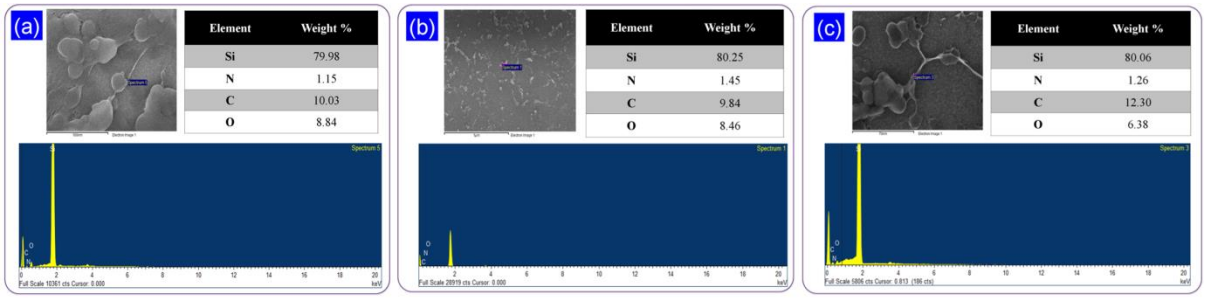

Figure 3.14. EDAX analysis of (a) MCM-DNA, (b) MCM-Lyz, and (c) MCM-Lyz-DNA.

3b.2d. *In vitro* assay

To evaluate the potential of EPT loaded MCM-41 in drug delivery; we have treated the HeLa cervical cancer cells with EPT-MCM in a time dependent manner. The nuclei of the cells were stained with blue fluorescent Hoechst 33342 dye and fixed cells were visualized under confocal microscopy. The gradual increase of green fluorescence in CLSM images (**Figure 3.15a**) from 1h to 12h clearly demonstrated that EPT-MCM slowly internalized inside the cells in a time dependent manner. Moreover, the merged images evidently confirmed that EPT-MCM localized temporally into the nucleus yielding increased amount of cyan colour after overlapping of green and blue fluorescence. These CLSM images revealed unequivocally that EPT-MCM internalized in the cancer cells and localized into the nucleus for targeting DNA.

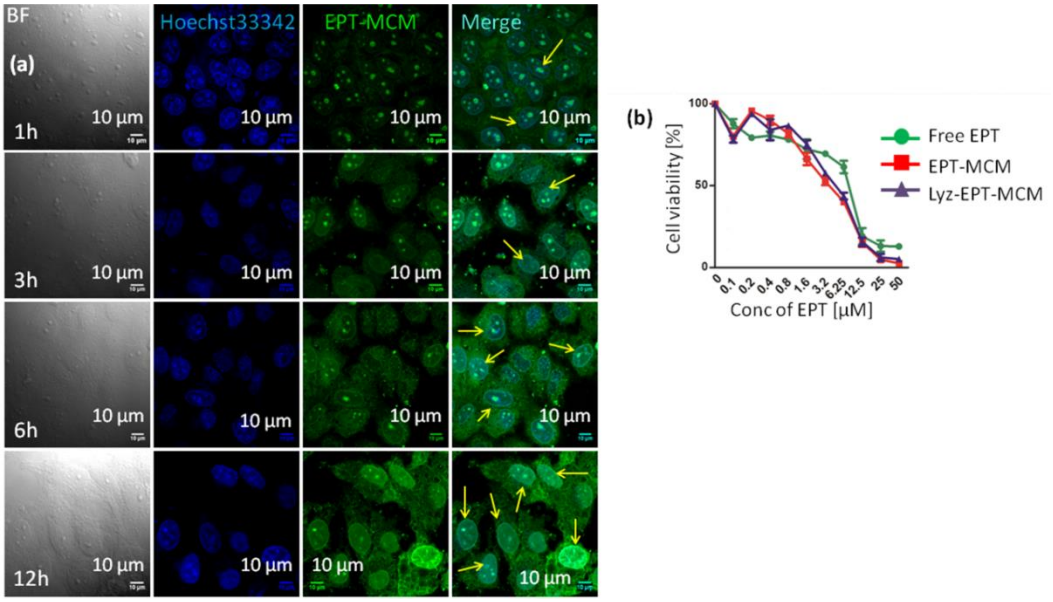

Figure 3.15. In vitro assay (a) CLSM images of HeLa cells at different time points after treatment with EPT-MCM. (b) Dose dependent cell viability assay of EPT-MCM, Lyz-EPT-MCM and free EPT in HeLa cells at 24h post-incubation.

We further assessed the efficacy of EPT-MCM and EPT-MCM-Lyz in HeLa cells. EPT-MCM and EPT-MCM-Lyz were incubated with HeLa cells for 24h in a dose dependent manner and cell viability was determined by MTT assay. HeLa cells were also treated with free EPT in the same concentrations as controls. Both EPT-MCM and EPT-MCM-Lyz showed much reduced IC_{50} value of 3.36±0.15 µM and 3.69±0.10 µM respectively compared to IC_{50} = 7.67±0.47 µM for free EPT (**Figure 3.15b**). Moreover, EPT-MCM and EPT-MCM-Lyz induced much increased HeLa cell death (cell viability = 2.58±0.35% and 5.13±1.76 % respectively) compared to free EPT

(cell viability = 12.8±0.64 %) at 50 μM concentration. This cell viability assay revealed that EPT-MCM and EPT-MCM-Lyz showed much improved efficacy in HeLa cancer cells compared to free ellipticine.

3b.3. Conclusion

We have demonstrated a MCM-41 based fluorescence switching of an anticancer drug, Ellipticine (EPT), during its loading into silica nanochannels and subsequent release to specific biomolecule, i.e. DNA (**Scheme 3.1**). Blue emission of EPT in DCM solvent completely switches to green in presence of MCM-41 (**Scheme 3.1**), due to the encapsulation and subsequent conversion of neutral to protonated form of EPT inside the MCM-41 nano-pores. Facile donation of proton form mildly acidic silanol (-Si-OH) groups of MCM-41 to neutral EPT is believed to facilitate this conversion process. Powder X-ray diffraction (PXRD), N_2 gas adsorption and confocal fluorescence microscopy results also confirm the adsorption of EPT inside the nano-pores of MCM-41. Interestingly, addition of DNA to the aqueous dispersion of EPT bound MCM-41 system results in drug release from MCM-41 and subsequent binding to DNA, which is reflected by the intensification of green fluorescence color (**Scheme 3.1**). We have used lysozyme (Lyz) protein as a pore blocker of MCM-41 in order to prevent premature drug release. Finally, we have shown that EPT can be released to DNA even from the EPT-MCM-Lyz composite system. Electron microscopy results reveal the formation of distinct morphologies involving MCM-41, DNA and Lyz probably through non-covalent interactions, and this is believed to facilitate the DNA assisted release of drug molecules from silica nanochannels. Furthermore, EPT-MCM was internalized into HeLa cancer cells temporally over 12h and localized into nucleus to induce improved efficacy compared to free drug. In summary, here we have presented fluorescence switching property of EPT to probe the loading to MCM-41 carrier and subsequent release to DNA, which is very cheap, straight forward and appealing for biomedical application of MCM-41.

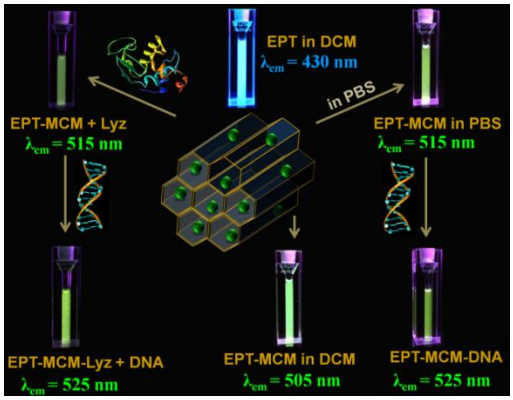

Scheme 3.1. Fluorescence switching of ellipticine (λ_{ex} = 350 nm) in presence of MCM-41 and various biomolecules (Lyz/DNA).

3b.4. References

1. (a) M. Colilla, A. Baeza and M. Vallet-Regí, in *The Sol-Gel Handbook*, Wiley-VCH Verlag GmbH & Co. KGaA, 2015, pp. 1309-1344; (b) Z. Li, J. C. Barnes, A. Bosoy, J. F. Stoddart and J. I. Zink, *Chem. Soc. Rev.*, 2012, 41, 2590-2605; (c) M. W. Ambrogio, C. R. Thomas, Y.-L. Zhao, J. I. Zink and J. F. Stoddart, *Acc. Chem. Res.*, 2011, 44, 903-913; (d) J. M. Rosenholm, C. Sahlgren and M. Linden, *Nanoscale*, 2010, 2, 1870-1883.
2. J. Salonen, L. Laitinen, A. M. Kaukonen, J. Tuura, M. Björkqvist, T. Heikkilä, K. Vähä-Heikkilä, J. Hirvonen and V. P. Lehto, *J. Control. Release*, 2005, 108, 362-374.
3. (a) I. I. Slowing, B. G. Trewyn, S. Giri and V. S. Y. Lin, *Adv. Funct. Mater.*, 2007, 17, 1225-1236; (b) B. G. Trewyn, I. I. Slowing, S. Giri, H.-T. Chen and V. S. Y. Lin, *Acc. Chem. Res.*, 2007, 40, 846-853; (c) C. Coll, A. Bernardos, R. Martínez-Máñez and F. Sancenón, *Acc. Chem. Res.*, 2013, 46, 339-349.
4. (a) L. Ding, J. Balzarini, D. Schols, B. Meunier and E. De Clercq, *Biochemical Pharmacol.*, 1992, 44, 1675-1679; (b) M. Ohashi and T. Oki, *Expert Opin. Ther. Pat.*, 1996, 6, 1285-1294; (c) C. L. Arteaga, D. L. Kisner, A. Goodman and D. D. Von Hoff, *Eur. J. Cancer Clin. On.*, 1987, 23, 1621-1626.
5. J.-B. Le Pecq, X. Nguyen Dat, C. Gosse and C. Paoletti, *Proc. Natl. Acad. Sci. U. S. A.*, 1974, 71, 5078-5082.
6. C. T. Kresge, M. E. Leonowicz, W. J. Roth, J. C. Vartuli and J. S. Beck, *Nature*, 1992, 359, 710-712.
7. F. Hoffmann, M. Cornelius, J. Morell and M. Fröba, *Angew. Chem. Int. Ed.*, 2006, 45, 3216-3251.
8. J. L. Vivero-Escoto, I. I. Slowing, B. G. Trewyn and V. S. Y. Lin, *Small*, 2010, 6, 1952-1967.
9. A. Sengupta, R. K. Koninti, K. Gavvala, N. Ballav and P. Hazra, *Phys. Chem. Chem. Phys.*, 2014, 16, 3914-3917.
10. J. Kypr, I. Kejnovská, D. Renčiuk and M. Vorlíčková, *Nucleic Acids Res.*, 2009, 37, 1713-1725.
11. K. Gavvala, S. Satpathi and P. Hazra, *RSC Adv.*, 2015, 5, 98080-98086.
12. (a) X. Li, J. Zhang and H. Gu, *Langmuir*, 2011, 27, 6099-6106; (b) S. M. Solberg and C. C. Landry, *J. Phys. Chem. B*, 2006, 110, 15261-15268.
13. (a) F. Muhammad, M. Guo, W. Qi, F. Sun, A. Wang, Y. Guo and G. Zhu, *J. Am. Chem. Soc.*, 2011, 133, 8778-8781; (b) C.-Y. Lai, B. G. Trewyn, D. M. Jeftinija, K. Jeftinija, S. Xu, S. Jeftinija and V. S. Y. Lin, *J. Am. Chem. Soc.*, 2003, 125, 4451-4459.
14. K. P. Wilson, B. A. Malcolm and B. W. Matthews, *J. Biol. Chem.*, 1992, 267, 10842-10849.
15. J. Deere, E. Magner, J. G. Wall and B. K. Hodnett, *J. Phys. Chem. B*, 2002, 106, 7340-7347.
16. F. Tanaka, L. S. Forster, P. K. Pal and J. A. Rupley, *J. Biol. Chem.*, 1975, 250, 6977-6982.
17. K.-C. Kao, T.-S. Lin and C.-Y. Mou, *J. Phys. Chem. C*, 2014, 118, 6734-6743.
18. L. K. Steinrauf, D. Shiuan, W.-j. Yang and M. Y. Chiang, *Biochem. Biophys. Res. Commun.*, 1999, 266, 366-370.
19. J. R. Lakowicz, *Principles of Fluorescence Spectroscopy*, 3 edn., Springer, New York, U.S.A., 2006.

20. (a) Z. Miskolczy, L. Biczók and I. Jablonkai, *Chem. Phys. Lett.*, 2006, 427, 76-81; (b) S. Y. Fung, J. Duhamel and P. Chen, *J. Phys. Chem. A*, 2006, 110, 11446-11454.
21. K. Gavvala, A. Sengupta, R. K. Koninti and P. Hazra, *J. Phys. Chem. B*, 2013, 117, 14099-14107.

Chapter 4

Excited State Proton Transfer Dynamics of Topotecan inside Bio-mimicking Nano-cavity

The present chapter deals with understanding an important excited state phenomenon, i.e., excited state proton transfer (ESPT) process, of a potentially important anticancer drug, Topotecan (TPT) in bio-mimicking nano-confined environment known as reverse micelles (RM). The ESPT dynamics of TPT has been explored in aqueous reverse micelle using steady state and time resolved fluorescence measurements.

4. Excited State Proton Transfer Dynamics of Topotecan inside Bio-mimicking Nano-cavity

4.1. Introduction

Topotecan (TPT) is a water soluble analogue of camptothecin (CPT), a pentacyclic alkaloid belonging to a class of antitumoral agents.[1] TPT is found to be a potential inhibitor for the growth of tumor cell through a unique mechanism by which it reduces the activity of the human topoisomerase I (Top1) enzyme through the formation of a Top1−DNA complex;[1b,1c,2] thereby, stabilizes the cleavable Top1−DNA complex that collides with the progression of the replication fork, producing lethal double strand DNA break and cell death.[1d,3] TPT consists of five rings, of which four (A, B, D, and E) are six membered and one (C) is five membered. The H-atoms on the 9- and 10-positions of the A-ring in CPT are replaced by dimethylaminomethylene and hydroxyl groups, respectively (**Scheme 4.1**). These extra functional groups on TPT enhance the solubility in physiological medium and reduce the cytotoxicity to human tissues.[1d,2b-d] Hence, TPT has been clinically approved anticancer drug for the treatment of several cancers.[1d,2b-d] The presence of 6-hydroxyquinoline (6HQ, A- and B-rings) subunit and the 9-dimethylaminomethylene group leads to the existence of different protolytic forms of TPT in ground state as well as excited state. Nunzio et al. reported elaborative pH dependent studies and solvent effect on the structural aspects of TPT, and it was found that TPT exists in different protolytic forms, such as enol (E), cationic (C) and zwitterionic (Z) forms depending on the pH as well as solvent.[4] Although in ground state the drug exists in different forms (E, C and Z) (**Scheme 4.2**), interestingly, TPT exhibits a single fluorescence peak (~530 nm) in aqueous solution (at physiological pH) responsible for the emission from Z^*, which is believed to be an outcome from the excited-state proton transfer (ESPT) from -OH group of TPT to water.[4-5] It was also found that the ESPT process in TPT is sensitive to polarity,[4b] and thus, the excited-state photophysics of TPT can be modulated inside the nano-cavities of a supramolecular host, such as cyclodextrin, calixarene, cucurbituril and so forth. In continuation of this effort, Gavvala et al. reported that the ESPT process of TPT is inhibited inside the cucurbit[7]uril (CB7) nano-cavity.[5a] Although it has been shown that the stability as well as photophysics of the drug can be modulated by encapsulating the drug into liposomes,[6] cyclodextrins,[5b,7] calixarene,[8] and cucurbituril,[5a] no focus has been made on modulating the ESPT process of TPT inside biological nano-cavities, where water often confined in a small pocket of a membrane.

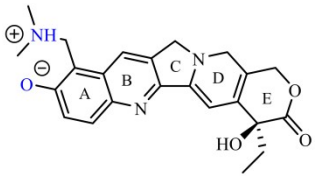

Scheme 4.1. Chemical structure of topotecan.

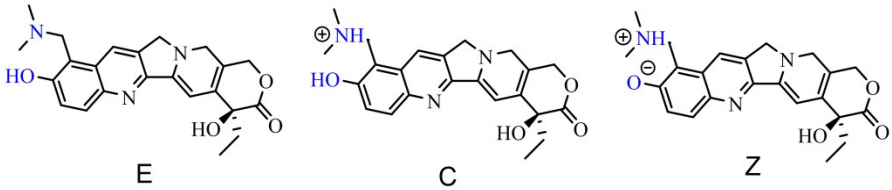

Scheme 4.2. Different prototropic forms of topotecan.

The reverse micelle (RM) is a nanometer-sized water droplet surrounded by a layer of surfactant molecules immersed in a non-polar solvent, and the concept of RM is well explored in Chapter 1. Recently, proton transfer attracts burgeoning interest to the researchers due to its key role in a variety of biological and chemical processes.[9] In continuation of this effort, fluorescence probes sensitive to H-bonding and proton transfer reactions are often probed in the reverse micellar environments due to the above mentioned unique features.[10] Herein, we report the encapsulation of TPT inside aqueous RMs, and the consequences of confinement on photophysical properties of TPT using steady state and time-resolved spectroscopic techniques. The prime focus of this work is to understand the effect of nano-confinement and polarity on excited state proton transfer (ESPT) dynamics of TPT. Interestingly, we have observed that ESPT dynamics is dramatically slowed down when the drug molecules are encapsulated inside the RMs compared to bulk water. The time-resolved emission spectrum (TRES) and time-resolved area normalized emission spectrum (TRANES) provide information about the existence of multiple emissive species in the excited state. We believe that our results might provide a new insight towards the understanding of fluorescence properties of TPT inside cell-like environment, and therefore, delivery of TPT inside the cell can be easily monitored by advanced imaging techniques.

4.2. Results and Discussion

4.2a. Steady State Measurements

The UV-visible absorption spectra of TPT with increasing water content of the RM are depicted in **Figure 4.1a**. Absorption spectra of TPT in water-RM exhibit three characteristic bands in the region of 250-410 nm, irrespective of the water content of RM. The absorption maximum at ~380 nm along with a shoulder at 368 nm is mainly attributed to the π-π* transition of quinoline moiety present in the TPT.[4b] With increasing water content of the RM,

although the bands positions are not changing, the absorbance is enhanced. The solubility of TPT in n-heptane is low, however, in presence of AOT and water the solubility enhances significantly. The increased absorbance may be an outcome of increased solubility of TPT in presence of AOT and water. Notably, a small shoulder at ~410 nm, which is believed to appear from the zwitterionic form of TPT,[4-5] is observed at higher w_0 values of the water-RM.

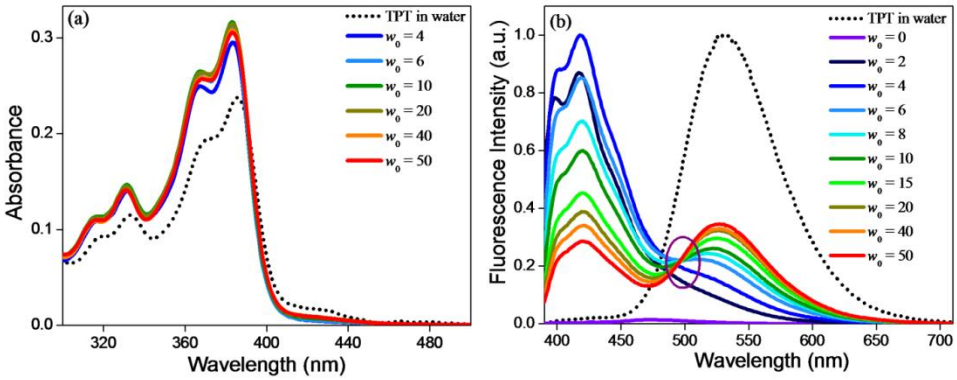

Figure 4.1. (a) Absorption spectra and (b) Steady state emission profiles of TPT in water (dotted line) and in AOT reverse micelles with progressively increasing water contents (w_0).

Figure 4.1b depicts the steady-state emission profiles of TPT with increasing water content of the RM upon excitation at 380 nm. Emission of TPT in n-heptane is negligibly small, as the solubility of drug in n-heptane is very low. However, in presence of AOT (w_0 = 0), a broad emission profile of TPT appears indicating that the solubility of TPT takes place in presence of surfactant. With the introduction of water to the system (w_0 = 2), an intense peak at 420 nm is observed. On further addition of water (w_0 = 4), a shoulder at 515 nm is clearly visible along with slight enhancement at 420 nm peak. The addition of water (w_0 > 4) results in prominent appearance of a peak at ~515 nm along with concomitant decrement in the intensity of higher energy peak. On further addition of water, the lower energy peak exhibits red shift along with the hike in intensity, whereas the intensity of high energy peak gradually decreases. As the emission property of TPT is highly dependent on the local hydrogen bonding network,[4a] the observed phenomena are attributed to the differential hydrogen bonding network inside RM. It is already reported that 420 nm emission band appears from excited state cationic form (C^*) of TPT.[4-5] Therefore, the initial increment in the emission intensity at 420 nm clearly suggests that reverse micellar environment facilitates the stabilization of cationic form of TPT (C-TPT). It is possible that C-TPT is involved in electrostatic interaction with the negatively charged polar head groups of AOT, and this interaction provides extra stabilization for cationic form of the drug inside the RM. As a result, cationic form is the dominant species inside RM at w_0 <5, and is reflected in the

emission profiles of TPT. It is well established that zwitterionic (Z^*) form of TPT emits around 520 nm.[4-5] Thus, the appearance of a peak at ~515 nm after a certain w_0 value indicates the formation of zwitterionic (Z^*) form of TPT. Notably, although we are selectively exciting the C-form (at 380 nm) of TPT, emission is detected from both zwitterionic as well as cationic forms. Therefore, Z^* form is generated at the cost of C^* as a result of excited state intermolecular proton transfer (ESPT) process from the –OH group of TPT to the surrounding water molecule.

Water plays pivotal role for the proton transfer reaction due to its H-bond accepting and conducting properties. Water is also recognized as an active participant in the transport mechanism of the proton as well as in the stabilization of an ion pair.[11] Initial addition of water to the AOT containing n-heptane solution causes all the water molecules to be trapped in the bound layers of AOT surfactant. The physical properties of these interfacial 'bound' water molecules are considerably different from the bulk water, as they are involved in strong H-bond interactions with the head groups of AOT and thereby, shows higher viscosity, lower mobility, lower polarity and diminished intra-solvent H-bonding network.[12] Moreover, the pH of the water molecules associated with the sulfonate groups in the nano-cavity is less than the bulk pH, as the hydronium ions of water are attracted towards the negatively charged sulfonate groups.[12e,13] Under the condition where the number of available water molecules are reduced and/or where the structure of water is partially broken, the probability of proton transfer is reduced.[11] Thus, the conversion from C^* to Z^*, which is accompanied by the excited state proton abstraction from the –OH group of the TPT by the water molecule, is restricted inside RM. Notably, it was found that the extent of ESPT process is not efficient at lower w_0 values. As for example, Spry et al. reported that the extent of ESPT of HPTS reduces significantly at lower w_0 value of the RM.[10a] Very recently, Sarkar and coworkers also found the intermolecular ESPT in water-RM begins at w_0 = 8 and increases with increasing w_0 value.[10g] Therefore, our observations are consistent with the literature reports. The fact that the quenching efficiency of the C^* emission grows monotonically and at the same time the emission of Z^* form increases (**Figure 4.1b**) with increasing w_0 suggesting that hydrogen bond plays an important role for the formation as well as stabilization of Z^*-TPT. When the size of the RM is small, the coupled core-shell hydrogen bond network has hydrogen bond dynamics that are substantially slower than those of bulk water[10a,14] and reduce the extent of excited state proton transfer rate. As w_0 value of the RM increases, the number of 'bound' water molecules, which are engaged in hydrogen bonding interaction with SO^{3-} of AOT, decreases, and at the same time the population of 'free' water molecules

enhances at the core of RM.[12a,12c-e,12h,15] Therefore, it is expected that the extent of proton activity (H-bonding interactions) accelerates with increasing percentage of 'free' water in RM, and thereby, facilitates the conversion of C^* to Z^*. The above observation is in good agreement with the literature report, where it was found that w_0 >5 onwards water molecules start forming 'water pool' inside the RM.[10d,10g,10h,16] The red shift in the emission peak of Z^*-TPT indicates the migration of TPT molecules from interfacial region towards the central region of the RM. Interestingly, unlike single emission from Z^* form in bulk water, we have observed emission from both C^* as well as Z^* forms of TPT even at highest w_0 value of the RM. This suggests that some TPT molecules are still residing near the AOT group of the RM, where proton activity is not sufficient for the transformation of C^* to Z^*. Notably, the appearance of an iso-emissive point at ~495 nm in the emission profiles suggests the existence of equilibrium between C and Z forms of TPT in the excited state. Interestingly, at highest water content of the RM, the emission spectra is not matching with that of pure water spectrum, indicating the photopyrolytic reaction of the drug is getting modulated inside the RM.

4.2b. Fluorescence Lifetime Measurements

The time-resolved fluorescence decays of TPT in dry AOT and after addition of water were collected at the corresponding emission maxima of cationic and zwitterionic forms exciting at 375 nm. The fluorescence transients of C^*-TPT in water-RMs at their corresponding emission maxima are depicted in **Figure 4.2a** and the results are tabulated in **Table 4.1**. The decay profile of C^*-TPT at any w_0 value consists of two lifetime components. For example, fluorescence transient at w_0 = 4 exhibits two lifetime components, 720 ps (22%) and 2 ns (78%). The bi-exponential nature of decay profile indicates that the drug molecules experience heterogeneous environment inside the RM. With raising water content of the RM, percentage contribution of short lifetime component (~700 ps) continuously enhances, whereas percentage contribution of long lifetime component (~2 ns) gradually reduces. Notably, increasing water content of the RM, the percentage of 'free' water molecules responsible for the formation of 'water pool' also increases.[12a-e,12h,16a] The results indicate that 2 ns component, whose contribution diminishes as w_0 value increases, corresponds to the lifetime of C^*-TPT residing near head groups of RM, whereas the short lifetime component may be attributed to the C^*-TPT near the central 'water pool' of RM. Strong electrostatic interaction between the negatively charged AOT head groups and the positively charged drug molecule may be responsible for the long lifetime of cationic species residing at the interface

of RM. Decrease in average lifetime of C^*-TPT suggests that the cationic species gradually move towards the central pool of RM, and, thereby, cationic species start photoprotolytic reaction. The location of the probe will be confirmed by the time-resolved anisotropy measurement discussed in later part.

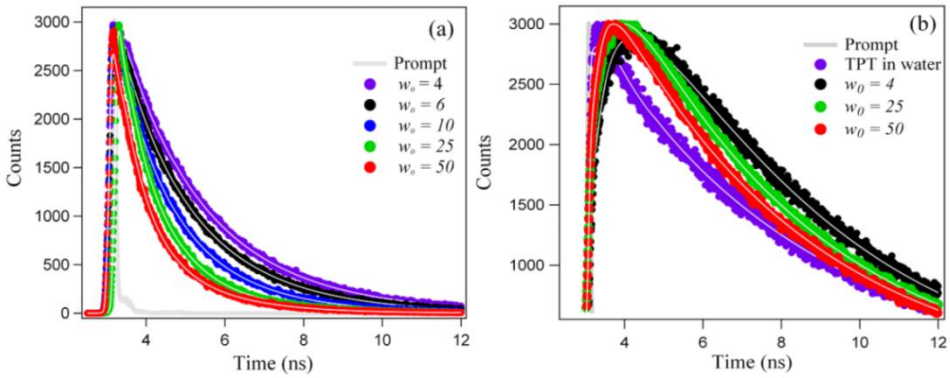

Figure 4.2. Fluorescence transients of TPT (excited at 375 nm) in reverse micelles with progressively increasing water contents (w_0); (a) λ_{col} = 420 nm (b) λ_{col} = 570 nm.

In order to avoid a minimal overlap from the emission of C^*-TPT, the time-resolved fluorescence signals from Z^*-TPT in water-RMs were collected at 570 nm (**Figure 4.2b**) A completely different and novel characteristic features come out when the time-resolved fluorescence signals from Z^*-TPT in water-RMs were collected at 570 nm (**Figure 4.2b**). The decay profiles consist of two components (**Table 4.1**); one long nano-second component (~5 ns) and another rise component (0.25-1 ns). The ~5 ns component is assigned to be the lifetime of Z^*-TPT.[4-5] Surprisingly, the shorter component (0.25-1 ns) has a negative pre-exponential factor (**Table 4.1**). The negative amplitudes (or pre-exponential factor) indicate that there exists an excited-state process which generates a new emitting state that is different from the initially excited cationic species.[17] Notably, although we are selectively exciting (λ_{ex} = 375 nm) the cationic species, we are observing the emission from the zwitterionic species, and it is attributing to the excited state proton transfer (ESPT) from –OH group of TPT to the water molecule.[4] Thus, the negative pre-exponential factor appeared in the decay profile provides the direct support for the conversion of C^* to Z^*. The increment in the percentage of long lifetime component (~5.0 ns) with the increase in water content of the RM suggests that population of Z^* species hikes inside the RM. The slightly increased lifetime of Z^*-TPT (**Table 4.1**) indicates that Z^*-TPT is gaining stability inside the RM. It is well known that extent of proton activity increases as water content inside the RM increases;[10a,10i,10j,14b] hence, facilitates the conversion of cationic form (C^*) to zwitterions (Z^*) via ESPT process. Generally, the rise time appeared in the decay profile indicates the existence of excited state

dynamics which is coming out from previously excited state. Therefore, the growth component appeared in the decay profile indicates the dynamics of ESPT process by which C^* is converted to Z^* species. Notably, the decay profile of TPT in bulk water is devoid of any growth component (**Figure 4.2b**), indicating that the ESPT dynamics is too fast to be detected by our TCSPC set-up. Here it is relevant to mention that Douhal group reported a slow proton transfer dynamics even in bulk water, although the contribution is very less (5%). The different observations by us and Douhal groups may be attributed to the different instrument response of TCSPC set-up. A closer look of time-resolved results indicate that the lifetime of growth component reduces (**Table 4.1**), inferring that the rate of ESPT dynamics becomes faster as the water content of the RM increases. Notably, the dynamics of proton transfer is dramatically affected by the ability of the solvent to reorganize.[10a,18] The observed dynamics also depends on the proton mobility, that is, the ability of the hydronium ion to move away from the resulting anion. These properties make excited state proton transfer (ESPT) a suitable probe for monitoring the local water environment. It was reported that, for small water pool of RMs, the orientational relaxation of water is much slower than in bulk water, and becomes increasingly fast as the size of RM increases.[12f,12k,15,19] The slow rates of water orientational relaxation in nanoscopic water environments demonstrate that the time scale for hydrogen bond network rearrangement is slowed down substantially. In consequence, ESPT dynamics, which depends on the dynamics of H-bonded network, becomes sluggish at lower water content of the RMs, and it gradually accelerates as the behaviour of water approaches towards the bulk. The presence of positively charged counter ions (Na^+ ions) inside the RM may also have significant role on the observed slow ESPT dynamics. In the absence of any ions in bulk water, proton transfer takes place directly to the water molecule without any intervention, as water molecules do not involve in electrostatic/hydrogen bond interactions with the counter ions. Thus, we believe that the ESPT dynamics inside RM is slowed down possibly also due to the screening effect of the sodium ions presented at the interface of the RM. In fact there are reports, where it has been observed that ESPT dynamics of HPTS gets affected by the presence of salt.[20] The variation of polarity inside RM with respect to water content may also play crucial role in slowing down of proton transfer dynamics, as it is known that PT dynamics of TPT is also dependent on the polarity of the surrounding environments.[4-5] In order to further elucidate this ESPT process, we have performed kinetic isotope effect (KIE) experiment, and found considerable (1.7 times) KIE effect when H_2O is replaced by D_2O inside RM (**Table 4.2**).

Table 4.1. Fluorescence decay parameters of TPT in water reverse micelles (λ_{ex} = 375 nm).

w_0	λ_{col}	τ_1 (ns)	τ_2 (ns)	τ_3 (ns)	a_1	a_2	a_3	$\tau_{avg}^{\#}$ (ns)	χ^2
Water	570 nm	0.63		5.93	0.13		0.87	5.24	1.01
w_0 = 0	570 nm	1.24	-	4.47	0.26	-	0.74	3.63	1.02
w_0 = 4	420 nm	0.85	2.51	-	0.19	0.81	-	2.19	0.86
	520 nm	0.65	3.30	5.05	-0.10	0.28	0.62	4.10	0.98
	570 nm	1.01	-	5.07	-0.35	-	0.65	3.64	1.15
w_0 = 10	420 nm	0.69	1.94	-	0.34	0.66	-	1.52	1.02
	520 nm	0.62	3.07	5.16	-0.17	0.29	0.54	3.78	1.01
	570 nm	0.63	-	5.03	-0.35	-	0.65	3.51	1.08
w_0 = 15	420 nm	0.57	1.60	-	0.46	0.54	-	1.12	1.04
	570 nm	0.49	-	5.19	-0.32	-	0.68	3.66	1.04
w_0 = 25	420 nm	0.51	1.47	-	0.52	0.48	-	0.97	1.12
	520 nm	0.49	3.04	5.37	-0.19	0.22	0.59	3.94	1.00
	570 nm	0.42	-	5.26	-0.31	-	0.69	3.77	1.04
w_0 = 50	420 nm	0.50	1.42	-	0.57	0.43	-	0.89	1.19
	520 nm	0.32	2.42	5.47	-0.16	0.19	0.65	4.08	1.02
	570 nm	0.30	-	5.28	-0.30	-	0.70	3.76	1.06
w_0 = 70	420 nm	0.42	1.30	-	0.58	0.42	-	0.79	1.25
	570 nm	0.25	-	5.27	-0.30	-	0.70	3.76	1.07

$^{\#}\tau_{avg} = a_1\tau_1 + a_2\tau_2 + a_3\tau_3$

To get insight into the geminate recombination process, which is opposite of reversible or irreversible recombination of proton to the zwitterionic form of the drug, we have analyzed the time-resolved data around 520 nm (**Table 4.1**) for verifying the presence of any extra component, which we might have missed in the decay profiles collected at red end side of the emission spectra. Here, the time-resolved data consists of three components, among which two components are very much similar to that of obtained in the decay profiles monitored at 570 nm. The third ~3 ns component is coming out from the cationic species of the drug,[5a] as the emission of cationic species also contributes toward the 520 nm peak. Thus, we confirm that geminate recombination process is not present in our system possibly because of the presence of sodium ions in nearby vicinity of the drug, which can prevent diffusion of proton

towards the zwitterionic form of the drug. The other possibility is that geminate recombination is too fast to be detected by our set-up.

Table 4.2. Fluorescence decay parameters of TPT in D_2O reverse micelles (λ_{ex} = 375 nm).

w_0	λ_{col}	τ_1 (ns)	τ_2 (ns)	a_1	a_2	$\tau_{avg}^{\#}$ (ns)	χ^2
w_0 = 15	570 nm	0.86	5.40	-0.37	0.63	3.74	1.15
w_0 = 25	570 nm	0.72	5.54	-0.35	0.65	3.84	1.07
w_0 = 50	570 nm	0.55	5.60	-0.35	0.65	3.86	1.18

$^{\#}\tau_{avg} = a_1\tau_1 + a_2\tau_2$

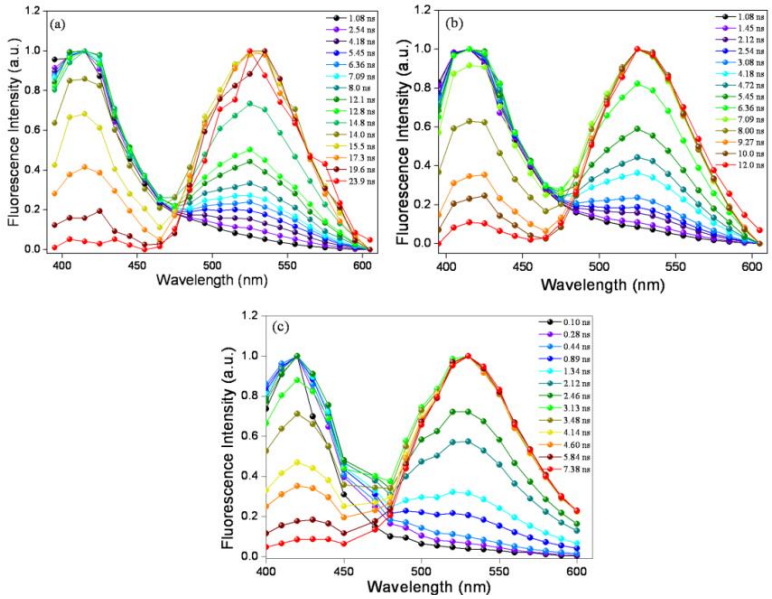

Figure 4.3. Time resolved emission spectra (TRES) of TPT in reverse micelle (λ_{ex} = 375 nm) at (a) w_0 = 4, (b) w_0 = 10, and (c) w_0 = 50.

To confirm the presence of two different types of species in the excited state, we have constructed time resolved area normalized emission spectrum (TRANES), an advanced technique to explore excited state components. TRANES method is a one-step extension of the commonly used time resolved emission spectrum (TRES) analysis.[21] TRES and TRANES and of TPT inside the water-RM are depicted in **Figure 4.3** and **Figure 4.4**, respectively. It is clear from the figures that the emission intensity of C^*-TPT progressively decreases with time, whereas the intensity of Z^*-TPT gradually rises up. This observation reinforces our claim that Z^* form of the drug is generated at the cost of C^* form. The timescales at which Z^* form appeared are ~1.02 ns, ~700 ps and 280 ps for w_0 = 4, w_0 = 10 and w_0 = 50, respectively.

These time-scales are in good agreement with the respective growth component obtained in the decay profiles collected at 570 nm (**Table 4.1**). Moreover, a clear iso-emissive point at ~480 nm in all above mentioned w_0 values suggests that two different types of emissive species (C^* and Z^* form) are present in the excited state.

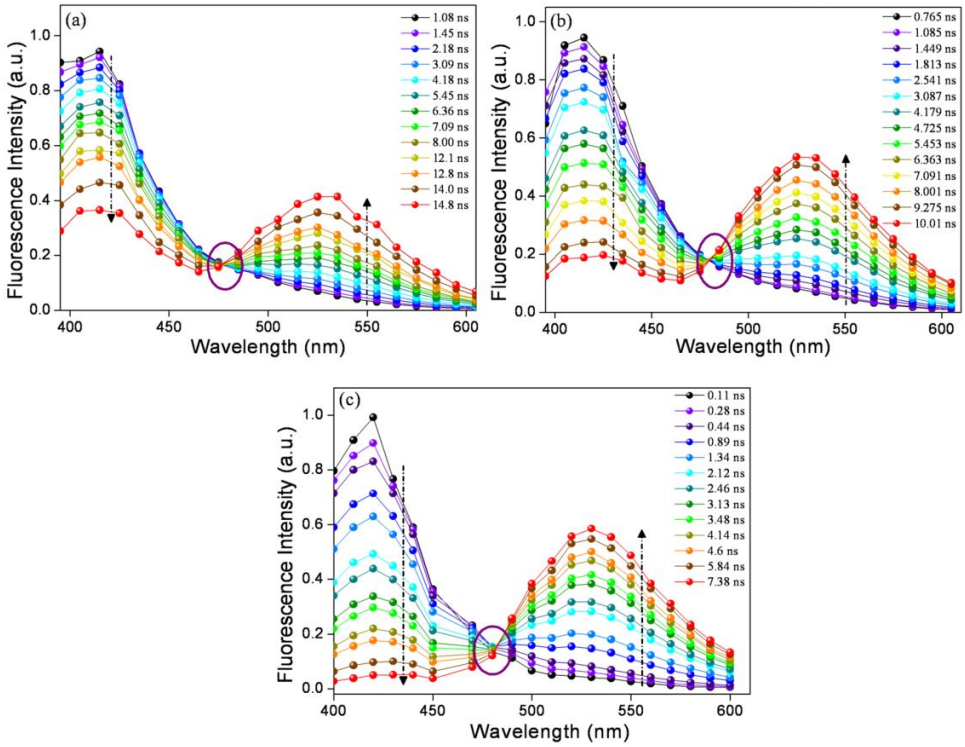

Figure 4.4. Time-resolved area normalized emission spectra (TRANES) of TPT in reverse micelle (λ_{ex} = 375 nm) at (a) w_0 = 4, (b) w_0 = 10, (c) w_0 = 50.

4.2c. Time Resolved Fluorescence Anisotropy Measurements

It is well established that time-resolved anisotropy measurements can provide important information about the rotational motion of fluorophore, which directly reflects the extent of restriction imposed by the surrounding environment.[22] Thus, time resolved anisotropy measurements have been employed to probe the encapsulation process of TPT inside the RMs. The information regarding the rotational relaxation of TPT in bulk water and water containing RMs are gathered by probing time-resolved fluorescence anisotropy of zwitterionic form of TPT at 525 nm. The decay profiles are shown in **Figure 4.5** and corresponding results are summarized in **Table 4.3**. The rotational relaxation time (τ_r) of drug molecule in bulk water is 216 ps and single exponential in nature. However, the decays are bi-exponential in nature in RMs. The bi-exponential decay is fitted by the eqn. 4.1,

$$r(t) = r_0\left[\mathrm{f}_1\exp\left(\frac{-\mathrm{t}}{\tau_{1r}}\right) + \mathrm{f}_2\exp\left(\frac{-\mathrm{t}}{\tau_{2r}}\right)\right] \qquad (4.1)$$

where r_0 is the limiting anisotropy to represent the inherent depolarization of the probe molecule, τ_{1r} and τ_{2r} are the fast and slow rotational relaxation components of the probe molecule inside RM, respectively, and f_1 and f_2 are the relative amplitudes of two components, respectively. To get overall idea, the average rotational relaxation time has been calculated, it becomes 2.4 ns, 2.1 ns and 1.8 ns for w_0 = 4, 25 and 50, respectively. The significant increment in rotational relaxation time in RMs compared to water infers that the drug molecules reside in highly restricted milieu. The faster rotational motion of TPT with increasing w_0 value indicates that drug molecules are experiencing slightly less restricted environments, as the size of the RM increases.

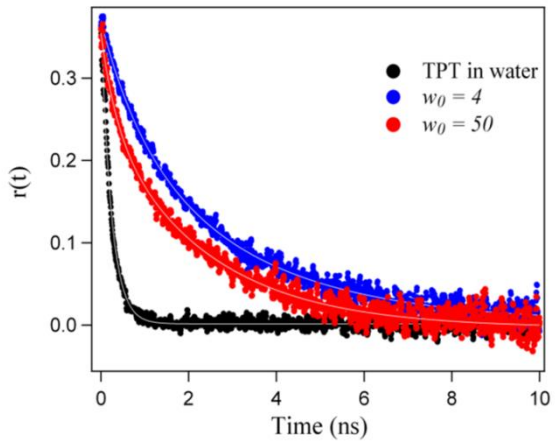

Figure 4.5. Fluorescence anisotropy transients of TPT (λ_{ex} = 375 nm and λ_{col} = 520 nm) in reverse micelles and in bulk water.

Table 4.3. Time-resolved fluorescence anisotropy fitting parameters of TPT in reverse micelles (λ_{ex} = 375 nm, λ_{col} = 520 nm).

Sample	τ_{r1} (ns)	τ_{r2} (ns)	f_1	f_2	r_0	S	θ°	$\langle\tau_r\rangle^{\#}$(ns)
Water	-	0.22	-	1.00	0.39	-	-	0.22
w_0 = 4	0.91	3.05	0.31	0.69	0.38	0.83	28.05	2.40
w_0 = 25	0.38	2.80	0.29	0.71	0.36	0.84	26.98	2.09
w_0 = 50	0.36	2.42	0.30	0.70	0.37	0.84	27.52	1.79

$^{\#}\langle\tau_r\rangle = f_1\tau_{r1} + f_2\tau_{r2}$

For detailed understanding of the bi-exponential behaviour of anisotropy decays, we have used wobbling-in-a-cone mode[10n,23] discussed in chapter 2. In this model, the order parameter (S^2) can be used for understanding the location of the probe inside the RM. The order parameter describes the equilibrium orientational distribution of the probe inside the

RM. S = 0 indicates that the motion is completely free, whereas S = 1 corresponds to the completely restricted environment. Here in our systems, the estimated S value varies from 0.831 at w_0 = 4 to 0.837 at w_0 = 50 (**Table 4.3**). Moreover, the cone angle θ° calculated (**Table 4.3**) from the order parameter varies from 28.05° (at w_0 = 4) and 27.52° (at w_0 = 50) and the values are in accordance with the previous findings.[23] As the order parameters and cone angles are not changing significantly with the w_0 values, we believe that TPT is not located at the central 'water pool' but closer to the interface (even at higher water content of the RM), and still feels the effect of both bound water and sodium counter ions.

Even though few organic probes (HPTS,[10a,10i,10j] D-luciferin,[10g]7 HQ,[10c-e] 2N68DS,[10h] 2PBI,[10b] 7H4MC[18] and MFOH[10o] etc.) are used to understand the role of water inside RMs by excited state intermolecular proton transfer (ESPT) process, ESPT dynamics of a potential anticancer drug, TPT, is being probed for the first time inside nano-cavity of RM. The significant essence of the present work is that we could able to directly monitor the ESPT process of TPT from the conversion dynamics of excited state cationic (C^*) to zwitterionic form (Z^*) of the drug. Notably, the ESPT dynamics of TPT is ultrafast in bulk water; however, the ESPT dynamics is slowed down drastically when TPT is entrapped inside the RM. The sluggish ESPT dynamics of TPT is an outcome of several impacts. The combined effects of nano-confinement and slow solvation dynamics of water are believed to be responsible for the observed slow ESPT dynamics inside RM. The screening effects of counter ions present at the interface of RM also have some role towards the ESPT dynamics. We believe that the present findings are important to elucidate the role of water in many biological functions and to understand small and fast structural changes in the water network, which are essential factors in proton transfer reactions. Moreover, the study of photophysical properties inside the RMs and its switchover from C^* to Z^* form might helpful to understand the proton transfer dynamics of TPT inside biological membrane and its function as photo-sensitizer trigger anticancer activity inside the tumor cell.

4.3. Conclusion

The photophysical properties of TPT have been studied in aqueous AOT reverse micelle (RM) by steady-state and time-resolved fluorescence measurements. In bulk water, TPT exhibits single emission, which is believed to be originated from zwitterionic (Z^*) form of the drug, as an outcome of excited state proton transfer (ESPT) process from excited state cationic form (C^*) of TPT to the nearby water molecule. In AOT/n-heptane RM, the drug shows dual emission attributed to the simultaneous existence of both C^* and Z^* forms of the

drug. The presence of single iso-emissive point in time-resolved area normalized emission spectrum (TRANES) further confirms the co-existence of two species (C^* and Z^*) in the excited state. Interestingly, ESPT dynamics was found to be severely retarded within the polar nano-cavity of RM, exhibiting time constant of ~250 ps to ~1 ns, which is slower than the dynamics obtained for TPT in bulk water (30 ps). The retardation of EPST dynamics in RM compared to bulk water might be due to cumulative effects of nano-confinement, disrupted hydrogen bonding network of water molecules and the screening of the sodium ions present at the interface.

4.4. References

1. (a) M. E. Wall, M. C. Wani, C. E. Cook, K. H. Palmer, A. T. McPhail and G. A. Sim, *J. Am. Chem. Soc.*, 1966, **88**, 3888-3890; (b) Y. Pommier, *Nat. Rev. Cancer*, 2006, **6**, 789-802; (c) R. Garcia-Carbonero and J. G. Supko, *Clin. Cancer Res.*, 2002, **8**, 641-661; (d) D. Hartwell, J. Jones, E. Loveman, P. Harris, A. Clegg and A. Bird, *Cancer Treat. Rev.*, **37**, 242-249.
2. (a) F.-M. Siu and C.-M. Che, *J. Am. Chem. Soc.*, 2008, **130**, 17928-17937; (b) C. Kollmannsberger, K. Mross, A. Jakob, L. Kanz and C. Bokemeyer, *Oncology*, 1999, **56**, 1-12; (c) J. E. Kurtz, G. Freyer, F. Joly, L. Gladieff, M. C. Kaminski, M. Fabbro, A. Floquet, A. C. Hardy-Bessard, N. Raban, I. Ray-Coquard, E. Pujade-Lauraine and F. On Behalf Of The Gineco Group, *Anticancer Res.*, 2012, **32**, 1045-1049; (d) D. Mirchandani, H. Hochster, A. Hamilton, L. Liebes, H. Yee, J. P. Curtin, S. Lee, J. Sorich, C. Dellenbaugh and F. M. Muggia, *Clin. Cancer Res.*, 2005, **11**, 5912-5919.
3. (a) A. Lalloo, P. Chao, P. Hu, S. Stein and P. J. Sinko, *J. Controlled Release*, 2006, **112**, 333-342; (b) J. Leppard and J. Champoux, *Chromosoma*, 2005, **114**, 75-85.
4. (a) M. R. di Nunzio, Y. Wang and A. Douhal, *J. Phys. Chem. B*, 2012, **116**, 8182-8190; (b) M. R. di Nunzio, Y. Wang and A. Douhal, *J. Phys. Chem. B*, 2012, **116**, 7522-7530.
5. (a) K. Gavvala, A. Sengupta, R. K. Koninti and P. Hazra, *ChemPhysChem*, 2013, **14**, 3375-3383; (b) M. R. di Nunzio, Y. Wang and A. Douhal, *J. Photo. Chem. Photobiol. A*, 2013, **266**, 12-21.
6. P. Tardi, E. Choice, D. Masin, T. Redelmeier, M. Bally and T. D. Madden, *Cancer Res.*, 2000, **60**, 3389-3393.
7. C. Foulon, J. Tedou, T. Queruau Lamerie, C. Vaccher, J. P. Bonte and J. F. Goossens, *Tetrahedron: Asymmetry*, 2009, **20**, 2482-2489.
8. G.-S. Wang, H.-Y. Zhang, F. Ding and Y. Liu, *J Incl. Phenom. Macrocycl. Chem.*, 2011, **69**, 85-89.
9. (a) M. Rini, B.-Z. Magnes, E. Pines and E. T. J. Nibbering, *Science*, 2003, **301**, 349-352; (b) G. Mathias and D. Marx, *Proc. Natl. Acad. Sci. U.S.A.*, 2007, **104**, 6980-6985.
10. (a) D. B. Spry, A. Goun, K. Glusac, D. E. Moilanen and M. D. Fayer, *J. Am. Chem. Soc.*, 2007, **129**, 8122-8130; (b) T. K. Mukherjee, D. Panda and A. Datta, *J. Phys. Chem. B*, 2005, **109**, 18895-18901; (c) O.-H. Kwon, T. G. Kim, Y.-S. Lee and D.-J. Jang, *J. Phys. Chem. B*, 2006, **110**, 11997-12004; (d) G. Angulo, J. A. Organero, M. A. Carranza and A. Douhal, *J. Phys. Chem. B*, 2006, **110**, 24231-24237; (e) S.-Y. Park, O.-H. Kwon, T. G. Kim and D.-J. Jang, *J. Phys. Chem. C*, 2009, **113**, 16110-16115; (f) M. K. Sarangi, A. K. Mitra, C. Sengupta, S. Ghosh, S. Chakraborty, C. Saha and S. Basu, *J. Phys. Chem. C*, 2013, **117**, 2166-2174; (g) J. Kuchlyan, D. Banik, N. Kundu, S. Ghosh, C. Banerjee and N. Sarkar, *J. Phys. Chem. B*, 2014, **118**, 3401-3408; (h) B. Cohen, D. Huppert, K. M.

Solntsev, Y. Tsfadia, E. Nachliel and M. Gutman, *J. Am. Chem. Soc.*, 2002, **124**, 7539-7547; (i) K. J. Tielrooij, M. J. Cox and H. J. Bakker, *ChemPhysChem*, 2009, **10**, 245-251; (j) M. Sedgwick, R. L. Cole, C. D. Rithner, D. C. Crans and N. E. Levinger, *J. Am. Chem. Soc.*, 2012, **134**, 11904-11907; (k) S. D. Choudhury and H. Pal, *J. Phys. Chem. B*, 2009, **113**, 6736-6744; (l) A. Orte, M. J. Ruedas-Rama, J. M. Paredes, L. Crovetto and J. M. Alvarez-Pez, *Langmuir*, 2011, **27**, 12792-12799; (m) O.-H. Kwon and D.-J. Jang, *J. Phys. Chem. B*, 2005, **109**, 20479-20484; (n) A. Douhal, G. Angulo, M. Gil, J. Á. Organero, M. Sanz and L. Tormo, *J. Phys. Chem. B*, 2007, **111**, 5487-5493; (o) M. Mukhopadhyay, A. Mandal, R. Misra, D. Banerjee, S. P. Bhattacharyya and S. Mukherjee, *J. Phys. Chem. B*, 2008, **113**, 567-573.

11. W. H. Thompson, *Annu. Rev. Phys. Chem.*, 2011, **62**, 599-619.
12. (a) B. E. S. P. L. Luisi, *Reverse Micelles: Bilogical and Technological Relevance of Amphiphilic Structure in Apolar Media*, 1 edn., Springer, New York, USA, 1999; (b) N. M. Correa, J. J. Silber, R. E. Riter and N. E. Levinger, *Chem. Rev.*, 2012, **112**, 4569-4602; (c) N. Nandi, K. Bhattacharyya and B. Bagchi, *Chem. Rev.*, 2000, **100**, 2013-2046; (d) K. Bhattacharyya, *Acc. Chem. Res.*, 2002, **36**, 95-101; (e) D. C. Crans and N. E. Levinger, *Acc. Chem. Res.*, 2012, **45**, 1637-1645; (f) M. D. Fayer, *Acc. Chem. Res.*, 2011, **45**, 3-14; (g) H.-S. Tan, I. R. Piletic and M. D. Fayer, *J. Chem. Phys.*, 2005, **122**, 174501-174509; (h) K. Kalyanasundaram, in *Photochemistry in Microheterogeneous Systems*, ed. K. Kalyanasundaram, Academic Press, 1987, pp. 143-172; (i) S. Rafiq, R. Yadav and P. Sen, *J. Phys. Chem. B*, 2010, **114**, 13988-13994; (j) N. E. Levinger and L. A. Swafford, *Annu. Rev. Phys. Chem.*, 2009, **60**, 385-406; (k) R. Biswas, J. Furtado and B. Bagchi, *J. Chem. Phys.*, 2013, **139**, -.
13. B. S. Marques, N. V. Nucci, I. Dodevski, K. W. C. Wang, E. A. Athanasoula, C. Jorge and A. J. Wand, *J. Phys. Chem. B*, 2014, **118**, 2020-2031.
14. (a) I. R. Piletic, H.-S. Tan and M. D. Fayer, *J. Phys. Chem. B*, 2005, **109**, 21273-21284; (b) I. R. Piletic, D. E. Moilanen, D. B. Spry, N. E. Levinger and M. D. Fayer, *J. Phys. Chem. A*, 2006, **110**, 4985-4999; (c) H.-S. Tan, I. R. Piletic, R. E. Riter, N. E. Levinger and M. D. Fayer, *Phys. Rev. Lett.*, 2005, **94**, 057405.
15. N. E. Levinger, *Science*, 2002, **298**, 1722-1723.
16. (a) J. Chowdhary and B. M. Ladanyi, *J. Phys. Chem. B*, 2009, **113**, 15029-15039; (b) A. M. Durantini, R. Darío Falcone, J. J. Silber and N. Mariano Correa, *J. Phys. Chem. B*, 2013, **117**, 3818-3828.
17. M. Novaira, M. A. Biasutti, J. J. Silber and N. M. Correa, *J. Phys. Chem. B*, 2007, **111**, 748-759.
18. S. D. Choudhury, S. Nath and H. Pal, *J. Phys. Chem. B*, 2008, **112**, 7748-7753.
19. (a) A. Patra, T. Q. Luong, R. K. Mitra and M. Havenith, *Phys. Chem. Chem. Phys.*, 2014, **16**, 12875-12883; (b) B. Baruah, J. M. Roden, M. Sedgwick, N. M. Correa, D. C. Crans and N. E. Levinger, *J. Am. Chem. Soc.*, 2006, **128**, 12758-12765.
20. P. Leiderman, R. Gepshtein, A. Uritski, L. Genosar and D. Huppert, *J. Phys. Chem. A*, 2006, **110**, 5573-5584.
21. (a) A. S. R. Koti and N. Periasamy, *J. Chem. Phys.*, 2001, **115**, 7094-7099; (b) A. S. R. Koti, M. M. G. Krishna and N. Periasamy, *J. Phys. Chem. A*, 2001, **105**, 1767-1771.
22. J. R. Lackowicz, *Principles of Fluorescence Spectroscopy*, 3 edn., Springer, New York, U.S.A., 2006.
23. (a) D. E. Moilanen, E. E. Fenn, D. Wong and M. D. Fayer, *J. Phys. Chem. B*, 2009, **113**, 8560-8568; (b) A. Chatterjee, B. Maity and D. Seth, *Phys. Chem. Chem. Phys.*, 2013, **15**, 1894-1906.

Chapter 5

Excited State Fluorescence Dynamics of Highly Stable Copper Nanoclusters Synthesized inside the Aqueous Nanopool of Reverse Micelles

In this chapter, we have reported a new strategy for the synthesis of highly stable and ultrabright fluorescent copper nanoclusters (CuNCs) within the water nanopool of reverse micelles (RMs). The origin and mechanism behind the multi-fluorescence and spectral broadening behaviors of CuNCs has been reported using TCSPC and femtosecond fluorescence upconversion techniques.

5. Excited State Fluorescence Dynamics of Highly Stable Copper Nanoclusters Synthesized inside the Aqueous Nanopool of Reverse Micelles

5.1. Introduction and Motivation of the Work

Here, the introduction about the nanoclusters has been avoided, as concept of nanocluster has already been introduced in detail in chapter 1. As already mentioned in Chapter 1, the syntheses and stabilities of these noble metal (Au, Ag and Cu) NCs remain as one of the primary challenges due to their aggregation phenomenon, which results in non-fluorescent nanoparticles.[1] Among noble metal nanoclusters, gold (AuNCs) and silver (AgNCs) are significantly explored in terms of synthesis,[1b,2] stabilization[3] and physical properties[2b,3b,4] compared to copper (CuNCs) due low oxidation potential of copper ($E^0_{Cu(II)/Cu(0)}$ = 0.34 V, $E^0_{Ag(I)/Ag(0)}$ = 0.80 V and $E^0_{Au(III)/Au(0)}$ = 1.50 V).[5] Recently, dendrimers,[6] polymers[7] and various bio-molecules such as DNA oligomers,[8] and protein[5a,9] have been efficiently utilized as scaffolds for the synthesis CuNCs emitting from blue to near-infrared region. However, most of these methods generate low quantum yield CuNCs. Moreover, the syntheses involve toxic reducing agents, multiple steps and high cost scaffolds such as protein/DNA. Thus, a new strategy for the synthesis of stable and highly fluorescent CuNCs under ambient conditions remains one of the primary challenges.

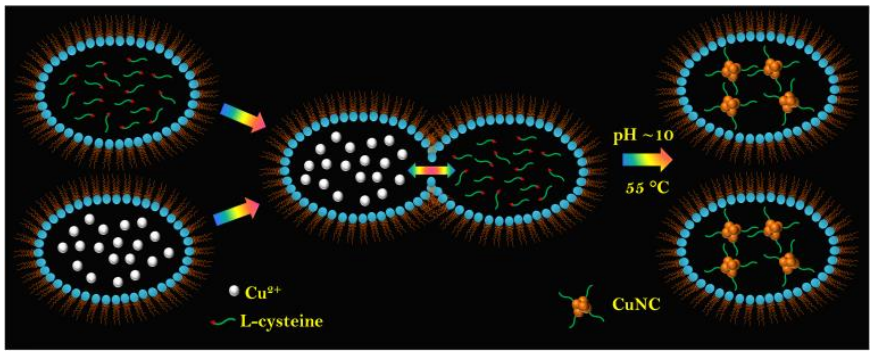

Scheme 5.1. Schematic representation of CuNCs synthesis inside the reverse micelles.

Keeping these aspects in mind, we have designed a simple and effective strategy for the synthesis of highly stable and ultrabright fluorescent CuNCs with L-cysteine (Cys) as a protecting ligand within the water nanopool of reverse micelles (RMs) (**Scheme 5.1**) without using any toxic reducing agents. Here it is necessary to mention that the nano meter-sized aqueous core of reverse micelle can act as a "nano reactor" for controlled reactions, which leads to the formation of a wide variety of nanostructures.[10] The significant advantage of this approach is that the nanostructures are homogeneous and mono-dispersed, and one can precisely tailor the size and morphology of nanostructures by controlling the structure of

reverse micelles.[10] Notably, CuNCs obtained (in our study) from this method exhibits intense fluorescence in blue-green regions and displays multi-fluorescence (excitation dependent emission) behaviour. Moreover, we have observed that CuNCs synthesized inside the RMs are extremely stable even after 180 days (stored at room temperature), because of the inhibition of aerial oxidation of Cu(0) inside the reverse micellar core.

Understanding the origin and mechanism behind the multi-fluorescence and spectral broadening behaviors of CuNCs are fundamentally important for their applications in bioimaging and photonics. We elucidate that the broad fluorescence from CuNCs in RM consists of two spectrally overlapped bands, corresponding to the metal-core and surface states of CuNCs, respectively. The excited state dynamic properties of NCs have been experimentally explored in the past decade by various techniques, such as ultrafast pump-probe[11] and ultrafast upconversion fluorescence,[11a,12] but are mostly focused on AuNCs and AgNCs. Dynamics studies of CuNCs are not available in the literature and its fundamental understanding of the fluorescence mechanism is still lacking. In the present study, efforts are also made on studying the relaxation dynamics of CuNCs using both TCSPC and ultrafast fluorescence upconversion techniques. Here it is necessary to mention that fluorescence upconversion is unique in its ability to preferentially monitor the exciton dynamics, intra-band transition and fast solvation without interference from other processes such as excited state absorption, or ground state bleaching or stimulated emission. The study of ultrafast fluorescence dynamics in CuNCs allows for a deeper understanding of their fundamental properties. Femto-second fluorescence upconversion and TCPSC decays of CuNCs in RMs comprise of multitude of lifetime components spanning from <1 ps to few nano-second time scale. The dynamics have been explained on the basis of several competing deactivation pathways and a broad distribution of radiative electron-hole recombination dynamics originating from core and surface states. We anticipate that our study will provide a deep insight towards fundamental understanding of optical properties of CuNCs.

5.2. Results and Discussion

5.2a. Characterizations

Synthesized CuNCs are characterized with Fourier transform infrared spectroscopy (FTIR) and matrix-assisted laser-desorption ionization time of flight (MALDI-TOF) mass spectrum. As shown in the FTIR spectra (**Figure 5.1**), the stretching vibrations of –SH group (2550 cm^{-1}) disappears in case of CuNCs suggesting the attachment of L-cysteine on nanocluster surface through Cu-S bond formation. For determining the number of Cu atoms in the cluster,

we have recorded the mass spectra in positive-ion mode MALDI-TOF instrument. The dominant m/z peaks at 580, 624, 646, 705, 735, and 911 (**Figure 5.2)** indicates a chemical composition of $Cu_{4-6}(Cys)_{3-4}$ in all reverse micelles. This result demonstrates that synthesized CuNCs are composed of four to six copper atoms in all water content of three different reverse micelles. UV-Vis absorption spectra of CuNCs in three different reverse micelles exhibit broad absorption features and don't show any characteristic absorption band above 550 nm (**Figure 5.3**), which mainly arises due to plasmonic nature of nanoparticles, indicating that synthesized nanoclusters are stable and not forming bigger size nanoparticles.

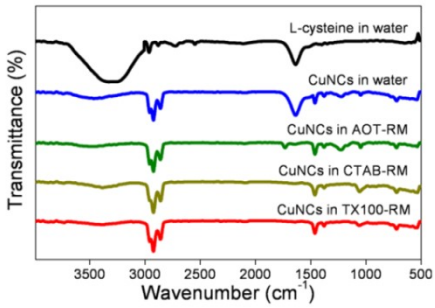

Figure 5.1. FTIR spectra of L-cysteine and CuNCs in water and different reverse micelles.

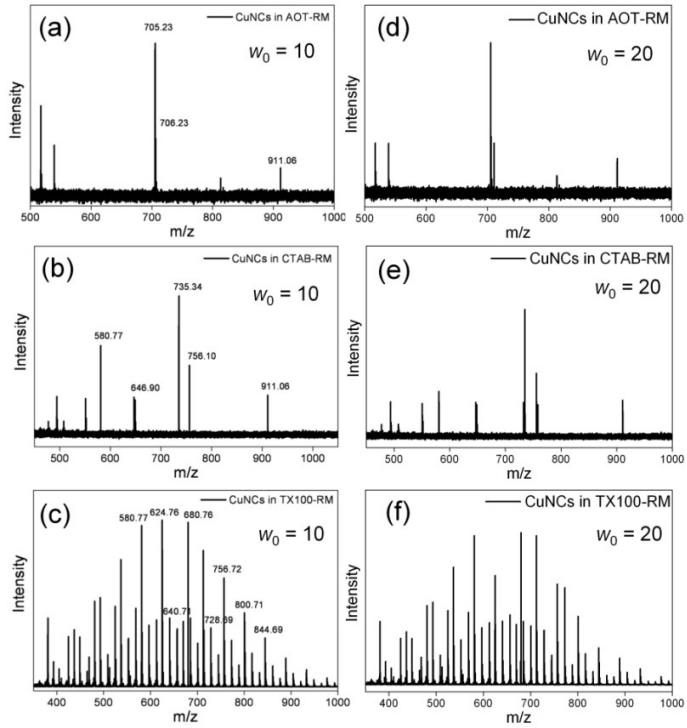

Figure 5.2. Positive mode MALDI-TOF mass spectra of CuNCs in (a) AOT, (b) CTAB and (c) TX-100 reverse micelles (w_0 = 10). The estimated composition of CuNCs in all reverse micelles are as follows: $[Cu_4L_3+Na^+]$ = 640.71 (m/z), $[Cu_5L_2+Na^+]$ = 580.71 (m/z), $[Cu_5L_3]$ = 680.13, $[Cu_5L_3+2Na^++2H^+]$ = 728.69 (m/z), $[Cu_4L_4+Na^++H^+]$ = 756.10 (m/z), $[Cu_4L_4-3H^+]$ = 734.34 (m/z), $[Cu_5L_3+Na^++2H^+]$ = 705.23 (m/z), $[Cu_5L_4-H^+]$ = 800.71 (m/z), $[Cu_5L_4+2Na^+-3H^+]$ = 844.69 (m/z), $[Cu_6L_2+H^+]$ = 624.76 (m/z), $[Cu_6L_4+2Na^+]$ = 911.06 (m/z); (d-f) MALDI-TOF mass spectra of CuNCs in various reverse micelles (w_0 = 20).

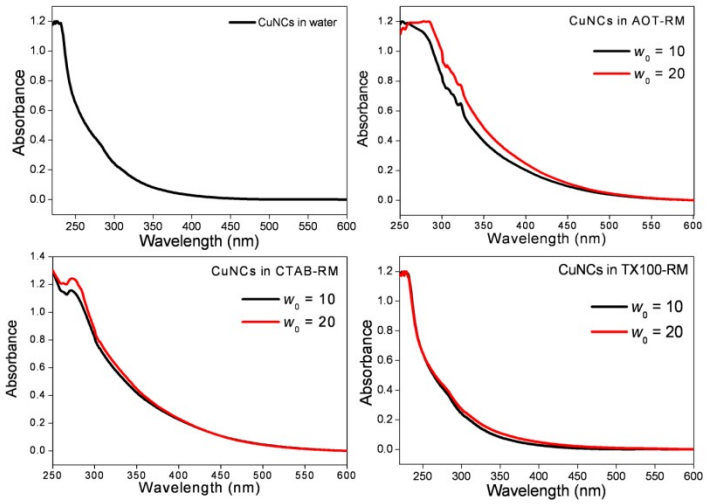

Figure 5.3. UV–Vis absorption spectra of CuNCs in water, AOT, CTAB and TX-100 RMs.

5.2b. Steady State Emission Results

Optical properties of CuNCs inside the reverse micelles have been investigated by fluorescence studies. The emission spectra (λ_{ex} = 375 nm; **Figure 5.4a**) are found to be dependent on the water content of AOT-RM, i.e. w_0 values. Enhancement in emission intensity is observed in going from $w_0 = 5$ to $w_0 = 10$ along with a significant blue shift in the emission maximum. However, the decrement in intensity takes place after $w_0 = 10$ although the trend in spectral shift remains same. In order to understand the effect of surface charge on optical properties of CuNCs, the measurements are carried out in other two RMs, namely, CTAB and TX-100 reverse micelles having positively charged and neutral surfactant, respectively. Almost Similar observation was noticed in case of CTAB and TX-100 RMs, however, the trends in intensity increment and shift are slightly different (**Figure 5.4b-c**).

One notable observation in all the reverse micelle is the 4-5 times increment in emission intensity of CuNCs inside the RM nano-cavity compared to bulk water. The enhancement in the emission intensity of CuNCs inside the RM may be attributed to the enhanced rigidity of the capping ligand (L-cysteine) generating from the restricted environment inside the reverse micelle. The improved compactness inside the reverse micelle facilitates the cuprophilic Cu(I)···Cu(I) interaction[13], which in term reinforces the formation of ordered nanoclusters (NCs) self-assembly. The formation of NCs self-assembly inside the RM induces the emission enhancement of CuNCs in two different ways. Firstly, the enhanced inter- and intra-NCs cuprophilic interactions greatly facilitate the excited state relaxation dynamics via radiative pathway. Secondly, the restriction of intramolecular vibration and rotation of capping ligands reduce the non-radiative relaxation of excited states. These two combined effects greatly enhance the emission intensity of NCs self-assembly inside RM nano-cavity.

The above observation is also supported by the literature report, where it has been mentioned that improved rigidity of the organic capping ligands of gold nanoclusters enhances the luminescent yield of the material to a larger extent.[3b,14]

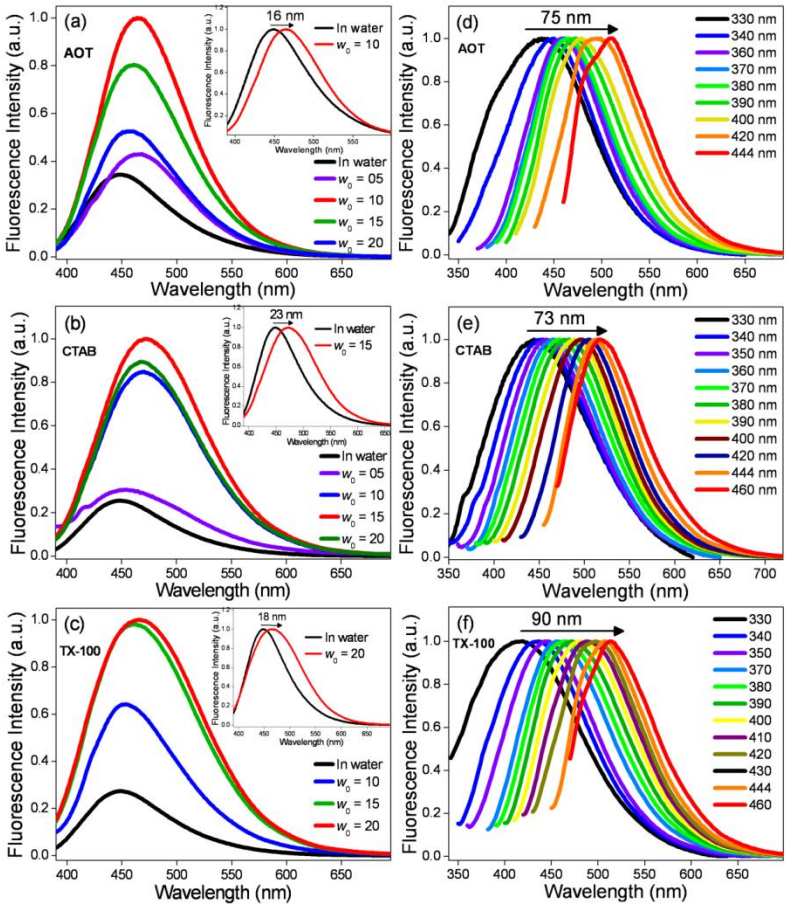

Figure 5.4. Emission spectra of CuNCs synthesized inside the 'water pool' of (a) AOT and (b) CTAB and (c) TX-100 reverse micelles by varying the w_0 values. Inset represents the normalized emission spectra of CuNCs. Excitation dependent emission spectra of CuNCs in (d) AOT, (e) CTAB and (f) TX-100 reverse micelles at $w_0 = 15$. The numbers in the legends indicate the excitation wavelengths.

Here it is necessary to mention that the presence of oxygen can significantly reduce the emission quantum yield of CuNCs.[5b,13c] This is because oxygen can easily oxidize Cu(0)/Cu(I) to Cu(II), and breaks the bond between the ligand and Cu(0)/Cu(I), thereby destabilizing the CuNCs.[5b,13c] Use of non-aqueous solvent (n-heptane) as the bulk media for synthesizing the copper nanoclusters, minimizes the oxidation possibility of Cu(0)/Cu(I) by aerial or dissolved oxygen. Thus, the absence of oxygen inside the RM is also responsible for the emission enhancement inside the RM compared to bulk water. Another intriguing observation is the stability of CuNCs inside the RMs. Our synthesized CuNCs inside the RMs are stable even after 180 days storing at room temperature (**Figure 5.5a**), whereas CuNCs

synthesized in bulk water, shows gradual decrement in emission intensity after 30th day storage even at 4 °C (**Figure 5.5a**). Moreover, photo bleaching experiments have been carried out to explore the stability of CuNCs, and it shows unchanged emission intensity even after 10 hr irradiation of UV light (λ_{exc} ~365 nm; **Figure 5.5b**), indicating the good photo-bleaching resistance of the synthesized CuNCs clusters within the reverse micelles. Thus, our strategy to synthesis CuNCs in reverse micelles paves away for long time storing of CuNCs. Another important observation of our results is the red shift in emission maxima in going from water to RM (even at highest water content). CuNCs are experiencing the different micro-environment within the water 'nanopool' of RMs compared to bulk water, causing a red shift in emission maxima compared to bulk water.

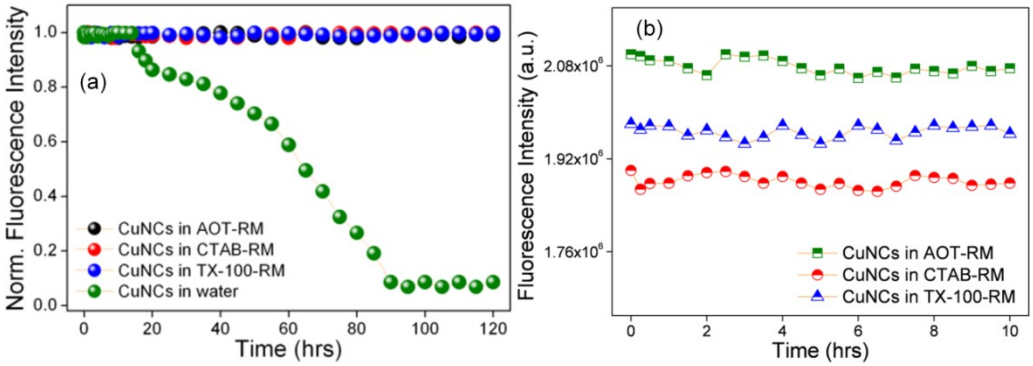

Figure 5.5. (a) The variation of emission intensity of CuNCs synthesized in bulk water and within 'water pool' of AOT, CTAB and TX-100 reverse micelles (at w_0 = 15) over time;(b) The variation of emission intensity of CuNCs synthesized within water pool of reverse micelles at w_0 = 15 under the UV-lamp (λ_{exc} ~365 nm) exposure.

The intensity variation of CuNCs with w_0 value can be correlated to the number of fluorescent CuNCs inside the RM. The weak intensity at w_0 = 5 is attributed to the less number of available water molecules (as 'water pool' does not form properly at this water content) and this results in the generation of less number of fluorescent CuNCs. While at higher w_0 value (where sufficient number of water molecules presents), the presence of higher number of fluorescent CuNCs in the water pool of AOT-RM is responsible for the significant emission enhancement compared to w_0 = 5. The decrement in emission intensity after a certain w_0 may be attributed to the reduced compactness arising due to the increased volume of the 'water pool' inside RM.

5.2c. Excitation Dependent Emission and Emission Dependent Excitation Spectra

In order to understand the heterogeneity in optical properties, the emission (**Figure 5.4d-f**) and excitation spectra (**Figure 5.6**) of CuNCs are collected at various

wavelengths. The fluorescence spectra of CuNCs in RMs exhibit gradual red shift and spectral broadening with increasing excitation wavelengths (**Figure 5.4d-f**). This observation suggests the existence of spectroscopic heterogeneity in solution of CuNCs in RMs, and this kind of spectroscopic heterogeneity was also reported by other noble metal NCs, such as, Silver and gold.[4,12a,15] For small Au and Ag clusters, the surface states are believed to be responsible for broad and excitation dependent fluorescence.[4,12a,15] This kind of excitation wavelength dependent emission spectra of CuNCs may originate from a combination of quantum confinement effects and distribution of different emissive states.[12a,13a,13c,16] In order to verify the above two possibilities, we have recorded the excitation spectra of CuNCs in RMs at various collections wavelengths (**Figure 5.6a-c**). Interestingly, the excitation spectra are found to be varied with the emission wavelengths (range of 440-560 nm). The excitation spectrum appears as single excitation band when the collection wavelength is ≤470 nm (**Figure 5.7**). On the other hand, the excitation spectra collected at >470 nm are composed of two spectral overlapped bands, which can be fitted by two Gaussian functions (**Figure 5.6d-f** and **Figure 5.7**). These two excitation bands are centered at 375 and ~430 nm, and labeled as excitation band-1 (B-I) and band-2 (B-II), respectively (**Figure 5.6d-f** and **Figure 5.7**). Out of these two excitation bands, the band centered at 375 nm (B-I) hardly shifts with monitoring emission wavelengths; on other hand, excitation band centered at ~430 nm (B-II) progressively shifts with monitoring wavelengths (**Figure 5.6g-i**). As shown in **Figure 5.6g**, shift in excitation maximum of B-II band is almost 30 nm, but the same in the case of B-I, is only ~8 nm. Large spectral shift in B-II band generally associates with more heterogeneity comprising of multi-emissive states in comparison to B-I band. Thus, we assign that the B-I corresponds to metal core states and B-II is originated from the surface states. We are assuming that, metal core states are exclusively arising from copper atoms only, whereas, surface states may arise due to metal atoms bonded with protecting ligands. During the excitation at B-I, the electrons are generated in the higher excited core states, and then electrons quickly relax into the lower core states of CuNC through the non-radiative pathway. Finally, the molecules come back to the ground from core states state by radiative transition. Hence, the short wavelength excitation leads to the fluorescence mostly originating from the core state. In contrast, during the excitation at longer wavelength, the electrons move to the lower excited states, and from there electrons mostly relax to the nearby surface states, which are close in

energy to the core state. As a result, the fluorescence coming from the surface states is of lower in energy compared to the core state. Therefore, the observed excitation dependent emission spectral feature is believed to appear because of distribution of different emissive states (core states and surface states), rather than the quantum confinement effect. The spectral broadening (in both emission and excitation spectra) arises due to broadening from surface localized states and the intrinsic broadening from the core states of CuNC. The electron–electron (e-e) scattering in the core states of CuNCs may be responsible for intrinsic broadening. After irradiation, exited electrons in the excited states rapidly relax by thermalization process via e-e scattering process.

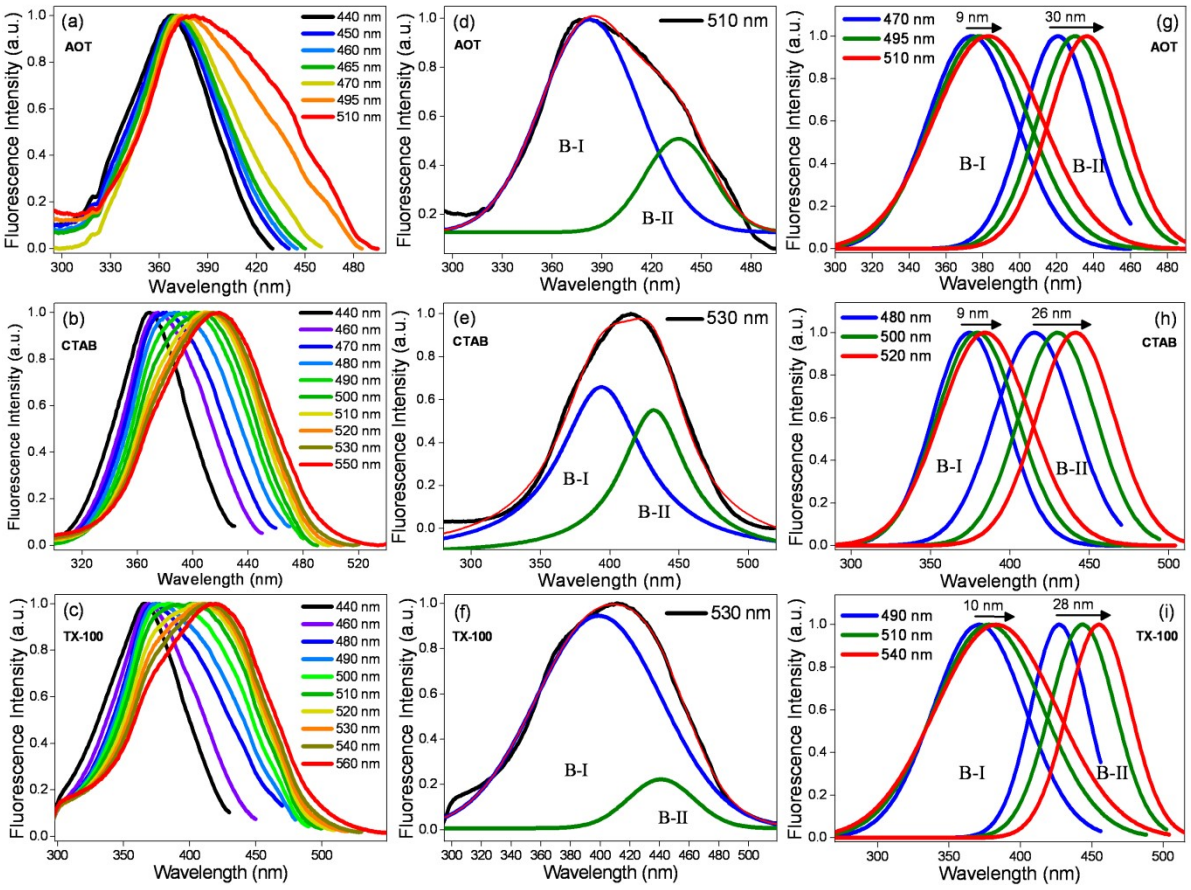

Figure 5.6. Excitation spectra of CuNCs synthesized within the 'water pool' of (a) AOT, (b) CTAB and (c) TX-100 reverse micelles (at w_0 = 15) by varying the emission wavelengths. (d), (e), and (f) are the deconvoluted excitation spectra collected at emission maxima; (g), (h), and (i) are the overlays of deconvoluted excitation spectra.

In order to give a better understanding about the optical properties of CuNCs inside the three different reverse micelles, we have provided the 2D fluorescence topographical map. The emission maxima (λ_{exc} ~320-460 nm) of CuNCs in the negatively charged AOT reverse

micelles are mainly distributed in the 430-470 nm range (**Figure 5.8a**), exhibiting an intense blue emission under the UV-light irradiation (365 nm, **Scheme 5.2**). Whereas emission maxima of CuNCs inside the positively charged CTAB reverse micelles, (λ_{exc} ~320-460 nm) are majorly distributed around 500 nm (**Figure 5.8b**), producing cyan-green colour fluorescence under the UV-light irradiation (**Scheme 5.2**). Inside the TX-100 reverse micelles (neutral), the emission maxima of CuNCs (λ_{exc} ~320-460 nm) are distributed in the range of 430-480 nm (**Figure 5.8c**) which shows a blue-cyan fluorescence colour under the UV-light (**Scheme 5.2**).

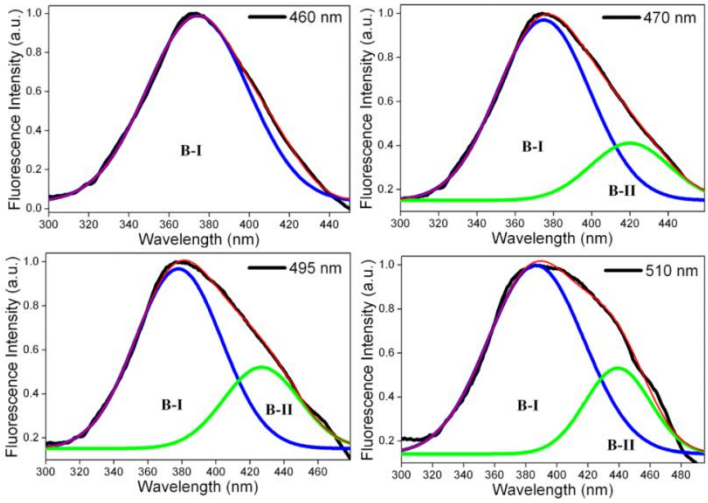

Figure 5.7. Deconvoluted excitation spectra of CuNCs in AOT reverse micellar nanopool (w_0 = 15) at emission maxima of 460, 470, 495 and 510 nm, respectively.

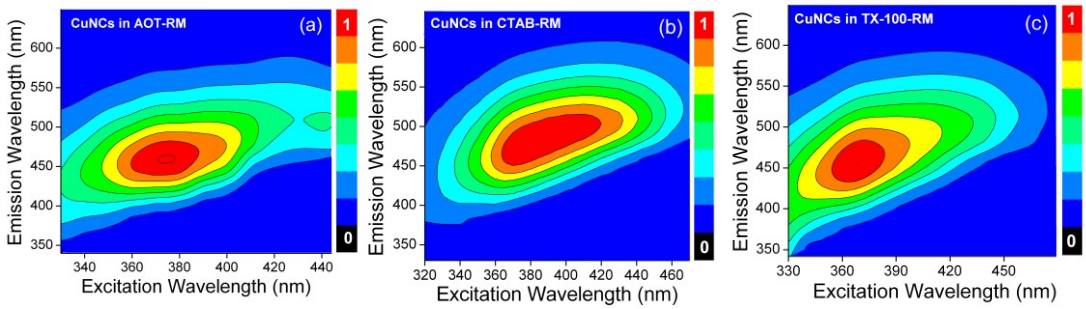

Figure 5.8. 2D fluorescence topographical map of CuNCs synthesized within the RM of (a) AOT, (b) CTAB and (c) TX-100 reverse micelles at w_0 = 15.

Spectral shift in emission maximum of CuNCs is majorly governed by the size, composition and average Cu(I)···Cu(I) distance associated with cuprophilic interactions.[1a,13c,15] Due to their similar composition of NCs (as discussed earlier), we anticipate the spectral shift in the emission maxima of CuNCs in different RMs is attributed to the alteration of average Cu(I)···Cu(I) distance. Generally, increase in average

Cu(I)···Cu(I) distance arises the compactness of NCs leading to the blue shift in emission maxima, while the decrement of the same causes red shift.[13c] This average Cu(I)···Cu(I) distance in the CuNCs are majorly influenced by two kinds of cuprophilic interactions, intra- (occurs within NCs) and inter-NCs (between neighboring NCs in the compact situation or self-assembly).[13c] Electrostatic repulsion between negative charged AOT surfactants and carboxylate groups of Cys in CuNCs localizes the clusters towards the central 'water pool' in AOT reverse micelles (**Scheme 5.2**). This increases the average Cu(I)···Cu(I) distance by inducing inter-NCs cuprophilic interaction in addition to the intra- interactions within the NCs. However, this kind of inter-NCs cuprophilic interaction is absent in case of CTAB reverse micelles due to electrostatic interactions between carboxylate group of Cys (capping ligand) and positively charged $-N(CH_3)_3^+$ moiety of CTAB surfactant (**Scheme 5.2**), and NCs are distributed near interfacial region (away from the central water pool). This causes the decrement of average Cu(I)···Cu(I) distance for CTAB-RMs in comparison to that of AOT-RMs, which results in a blue shifted emission maximum for AOT-RMs (blue emission i.e. 430-470 nm) compared to CTAB-RMs (cyan-green emission around 500 nm). CuNCs inside TX-100 RMs are distributed in both near interfacial as well as in the central 'water pool' due to the absence of any charge in the surfactant chain which results in a random Cu(I)···Cu(I) distance coming in between the average distances of AOT and CTAB-RMs. Thus, the emission maximum of CuNCs inside TX-100 RMs (around 480 nm) appears in between the emission maximums of AOT and CTAB-RMs exhibiting a mix blue-cyan emission (**Scheme 5.2**).

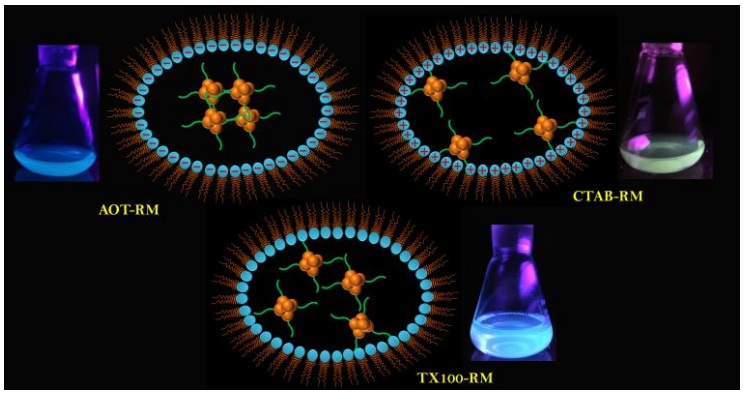

Scheme 5.2. Schematic representation of CuNCs arrangement within the 'water pool' of the reverse micelles of AOT (negative charged), CTAB (positive charged) and TX-100 (neutral).

5.2d. Fluorescence Dynamics

Both time-correlated single photon counting (TCSPC) and fluorescence upconversion techniques have been used to explore the ultrafast relaxation dynamics of CuNCs in different water content of various reverse micelles. A comparative investigation of the CuNCs dynamics in all the RMs (w_0 = 10) are tabulated in **Table 5.1** and the representative fluorescence time resolved decay traces are shown in **Figure 5.9-5.14** and **Table 5.1-5.3**. Multitudes of lifetime components are observed spanning from picosecond to several nanoseconds. These components are categorized in various timescales, such as, <1 ps, 10-15 ps, 200-300 ps, 1.5-2 ns and 5-7 ns. This results infers that either several competing deactivation pathways or broad distribution of recombination rate exist in excited CuNCs. Notably, the last three components are obtained from TCSPC technique and fixed during the fitting of upconversion decay profiles. At first, we will focus on the observed last three long relaxation dynamics, which takes place from several hundred of picosecond to several nanosecond time scales, and could be attributed to the fluorescence lifetime of the molecular like states of CuNCs originating from the quantum confinement effect. As already discussed, the

Table 5.1. Fluorescence dynamics of CuNCs in reverse micelles (w_0 = 10).

System	λ_{exc} (nm)	λ_{em} (nm)	τ_1	τ_2	τ_3	τ_4	τ_5
AOT-RM	375	460	780 fs (48.0%)	9.5 ps (37.0%)	226 ps (9.0%)	1.57 ns (4.0%)	5.53 ns (2.0%)
CTAB-RM	375	460	750 fs (47.0%)	11.5 ps (31.0%)	203 ps (15.0%)	1.49 ns (5.0%)	5.47 ns (2.0%)
TX-100-RM	375	460	800 fs (50.0%)	15.0 ps (30.0%)	185 ps (14.0%)	1.96 ns (4.0%)	6.80 ns (2.0%)
AOT-RM	420	500	800 fs (41.0%)	11.0 ps (39.0%)	180 ps (8.0%)	1.76 ns (9.0%)	6.23 ns (3.0%)
CTAB-RM	420	500	700 fs (50.0%)	14.0 ps (24.0%)	244 ps (12.0%)	1.93 ns (10.0%)	5.57 ns (4.0%)
TX-100-RM	420	500	770 fs (50.0%)	16.0 ps (25.0%)	220 ps (12.0%)	1.92 ns (9.0%)	5.87 ns (4.0%)
Water	375	440	580 fs (60.0%)	17.0 ps (32.0%)	250 ps (5.5%)	2.00 ns (3.0%)	5.62 ns (1.5%)

fluorescence from CuNCs is appearing from the electron-hole recombination process originating from the core states and/or the surface states. Initially, photo-excited carriers are generated in the higher excited LUMO (of the core state), and carrier reaches to the lowest

LUMO through non-radiative relaxation process. In absence of any surface state, carrier would reach to the ground state through radiative recombination process; thereby, the fluorescence kinetic evolution by TCSPC would exhibit single exponential decay feature. This kind of single exponential decay feature is observed in high quantum yield quantum dots, in which the surface is well passivated.[12a] However, CuNCs inside reverse micelle exhibits multi-exponential long decay features in TCSPC. The presence of this multi-exponential decay feature also confirms the presence of surface states in addition to the core states. Three long components detected in the fluorescence decay profile are attributed to the radiative electron-hole recombination dynamics either through the core state or from various surface states. We anticipate that 200-300 ps component is originated due to the radiative recombination process of carrier present in the core state; whereas the other two long nano-second components are associated to the radiative recombination process from the two different surface states. The origin of these two different surface states presently unclear but may be originating from different cuprophilic interactions or the interaction of CuNCs with capping ligands. The presence of 1.5-2 ns component may be attributed from the intrinsic cuprophilic interaction within CuNCs through which surface state gets modified. Another type of cuprophilic interaction is in between the neighboring NCs inside the compact environment of RMs, which stabilizes the surface states compared to previous case, and thereby enhances emission intensity and fluorescence lifetime. To confirm our assignments, we have examined the changes of these components when the excitation wavelength was turned away from 375 nm to 444 nm, where the surface states are preferentially excited. Fluorescence decay traces of CuNCs obtained by the excitation at ≥420 nm (λ_{ex} = 420 nm in upconversion and λ_{ex} = 444 nm in TCSPC) and collected at corresponding emission maxima (500 nm) are shown in **Figure 5.9b, 5.10b, 5.11b, 5.12b, 5.13b, 5.14b** and the results are summarized in **Table 5.1-5.3**. Interestingly, for all the systems (CuNCs in AOT, CTAB and TX-100 reverse micelles), the relative contribution of 1.5-2 ns and 5-7 ns component increases, whereas the relative contribution of 200 ps component decreases as the excitation wavelength is shifted from 375 nm to 444 nm. Significant increment of the relative contribution of slow lifetime components (1.5-2 ns and 5-7 ns) and simultaneous decrement in the relative contribution from 200 ps lifetime component, suggests that the electron-hole recombination dynamics from the surface states dominate at higher excitation wavelengths (>420).

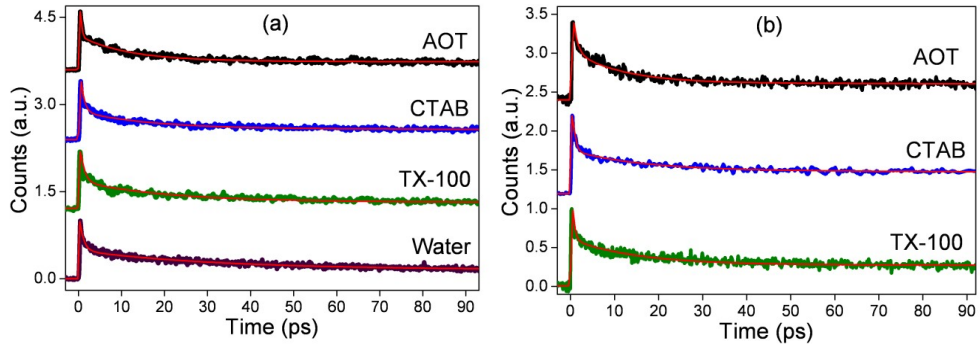

Figure 5.9. Fluorescence upconversion decay profiles of CuNCs in water and various RMs ($w_0 = 10$) excited at (a) 375 nm, collected at 460 nm, and (b) 420 nm, collected at 500 nm.

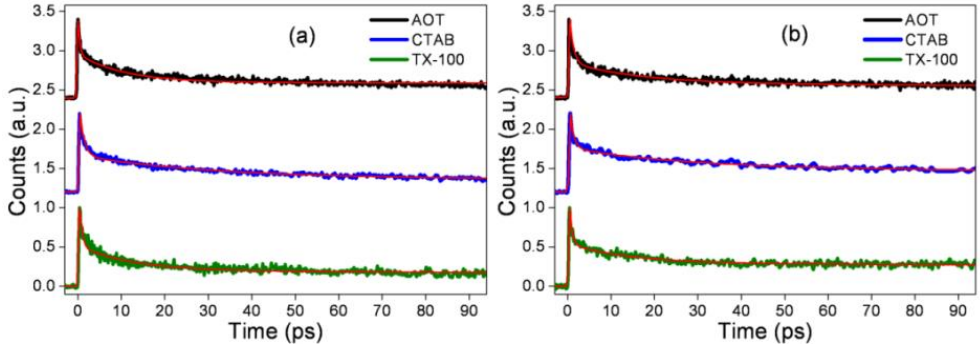

Figure 5.10. Fluorescence upconversion decay profiles of CuNCs in various RMs ($w_0 = 15$) excited at (a) 375 nm and collected at 460 nm (b) 420 nm and collected at 500 nm.

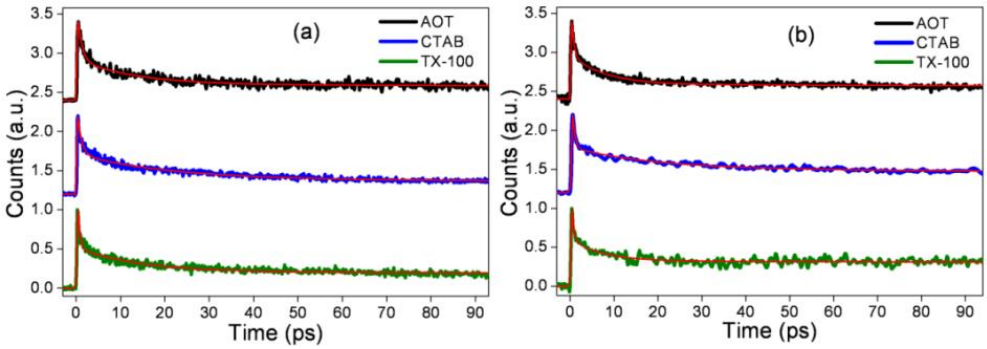

Figure 5.11. Fluorescence upconversion decays profiles CuNCs in various RMs ($w_0 = 20$) excited at (a) 375 nm and collected at 460 nm (b) 420 nm and collected at 500 nm.

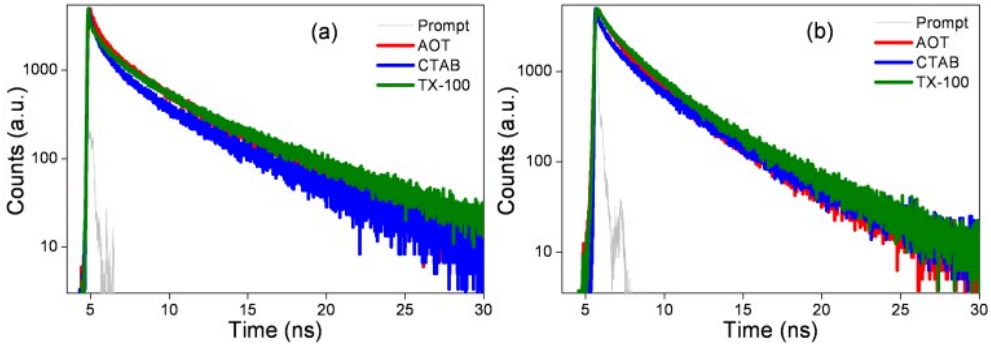

Figure 5.12. Pico- to nanoseconds fluorescence decays of CuNCs in various reverse micelles ($w_0 = 10$), excited at (a) 375 nm and collected at 460 nm (b) 444 nm and collected at 500 nm.

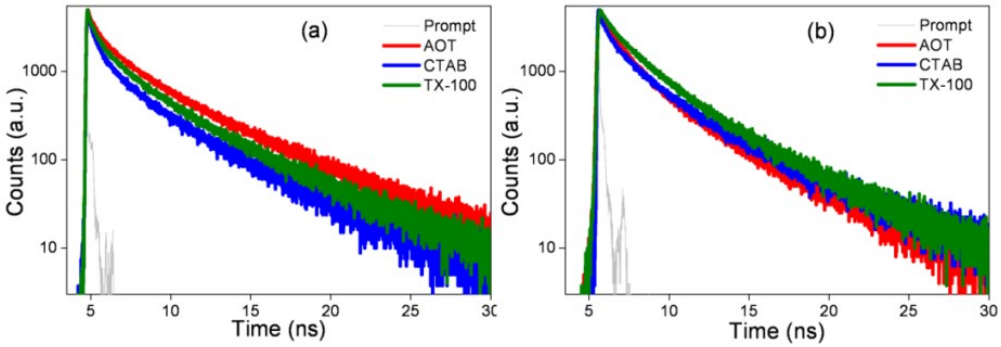

Figure 5.13. Pico- to nanoseconds fluorescence decays of CuNCs in various reverse micelles ($w_0 = 15$) excited at (a) 375 nm and collected at 460 nm (b) 444 nm and collected at 500 nm.

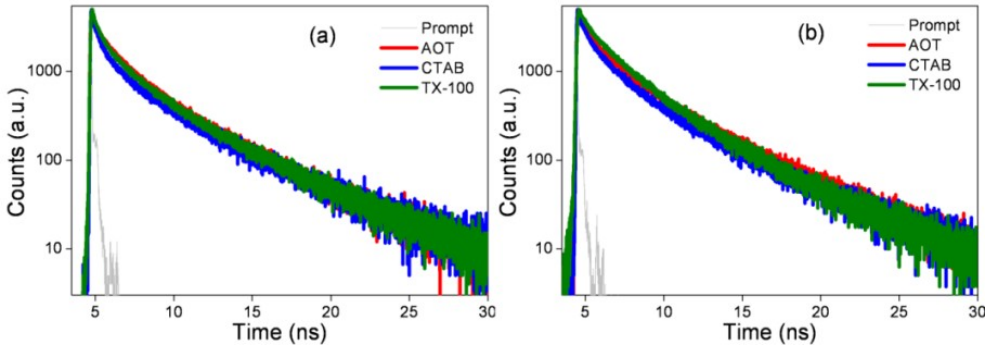

Figure 5.14. Pico- to nanoseconds fluorescence decays of CuNCs in various reverse micelles ($w_0 = 20$) excited at (a)375 nm and collected at 460 nm (b) 444 nm and collected at 500 nm.

Table 5.2. Fluorescence dynamics of CuNCs in reverse micelles ($w_0 = 15$).

Sample	λ_{exc} (nm)	λ_{em} (nm)	τ_1	τ_2	τ_3	τ_4	τ_5
AOT-RM	375	460	750 fs (51.0%)	15.5 ps (30.0%)	280 ps (10.0%)	1.60 ns (6.0%)	6.02 ns (3.0%)
CTAB-RM	375	460	800 fs (51.5%)	16.0 ps (26.0%)	220 ps (16.0%)	1.50 ns (4.5%)	5.56 ns (2.0%)
TX-100-RM	375	460	780 fs (52.0%)	16.0 ps (29.0%)	250 ps (11.5%)	1.80 ns (5.5%)	5.58 ns (2.0%)
AOT-RM	420	500	760 fs (50.0%)	15.8 ps (28.0%)	300 ps (7.5%)	1.50 ns (10.0%)	4.60 ns (4.5%)
CTAB-RM	420	500	850 fs (47.0%)	15.5 ps (26.0%)	250 ps (12.5 %)	1.85 ns (11.0%)	5.77 ns (3.5%)
TX-100-RM	420	500	820 fs (48.0%)	14.0 ps (27.0%)	250 ps (10.0%)	1.80 ns (11.0%)	5.76 ns (4.0%)

Table 5.3. Fluorescence dynamics of CuNCs in reverse micelles ($w_0 = 20$).

Sample	λ_{exc} (nm)	λ_{em} (nm)	τ_1	τ_2	τ_3	τ_4	τ_5
AOT-RM	375	460	760 fs (51.0%)	12.0 ps (30.0%)	230 ps (10.5%)	1.68 ns (6.0%)	5.30 ns (2.5%)
CTAB-RM	375	460	850 fs (49.0%)	15.0 ps (31.5%)	250 ps (13.0%)	1.43 ns (4.5%)	5.52 ns (2.0%)
TX-100-RM	375	460	800 fs (50.0%)	16.0 ps (28.0%)	280 ps (13.5%)	1.90 ns (6.0%)	5.60 ns (2.5%)
AOT-RM	420	500	750 fs (49.0%)	11.0 ps (29.5%)	260 ps (9.0%)	1.64 ns (9.0%)	5.29 ns (3.5%)
CTAB-RM	420	500	780 fs (50.0%)	13.0 ps (26.0%)	250 ps (11.0%)	1.74 ns (9.5%)	5.78 ns (3.5%)
TX-100-RM	420	500	800 fs (48.0%)	9.5 ps (26.0%)	300 ps (11.0%)	1.97 ns (11.0%)	5.80 ns (4.0%)

Time-resolved emission spectra (TRES) of CuNCs in reverse micelle were collected to further explore multi-emissive states and to understand the interplay between the core and surface states (**Figure 5.15**). Representative TRES spectra in all the reverse micelles (**Figure 5.15-5.17**) clearly depict that the emission peak maximum gradually shifts towards higher wavelength regions with increasing time delay from 0 to 20 ns without showing any iso-emissive point. In general, the red-shifted fluorescence spectra in TRES are reported to be due to the excited-state relaxation process and/or multiple emissive species or states.[17] Upon excitation at 375 nm, the fluorescence maximum were found to shift from ~430 nm to ~480 nm depending upon the systems, when the delay time is extended from 0 ns to 20 ns. The peak around ~430 nm is originated from the core state and the peak in the range of 480-500 nm is arising from surface states. Interestingly, when the excitation wavelength is shifted to 405 nm, the emission peak is transferred towards the lower energy sides. Thus, we conclude that the spectral shift of CuNCs in TRES is attributed to the contribution of excited electron relaxation from the core to surface states.

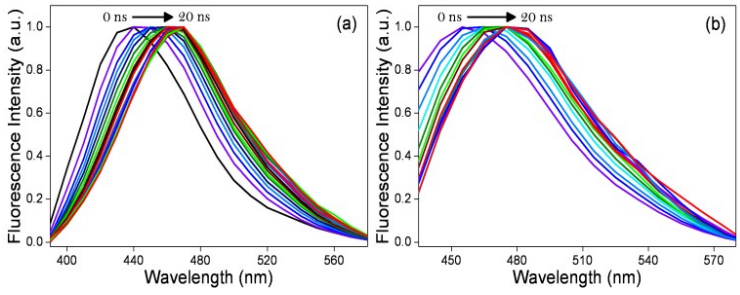

Figure 5.15. Time resolved emission spectra (TRES) of CuNCs in AOT reverse micelle ($w_0 = 10$) excited at (a) 375 nm and (b) 405 nm.

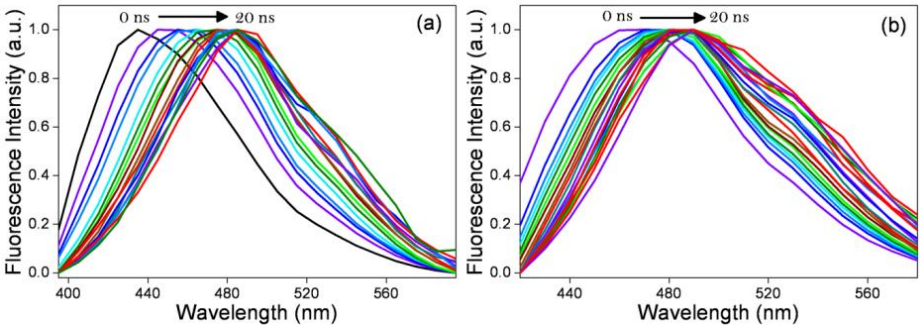

Figure 5.16. Time resolved emission spectra (TRES) of CuNCs in CTAB ($w_0 = 10$) reverse micelles excited at (a) 375 nm and (b) 405 nm.

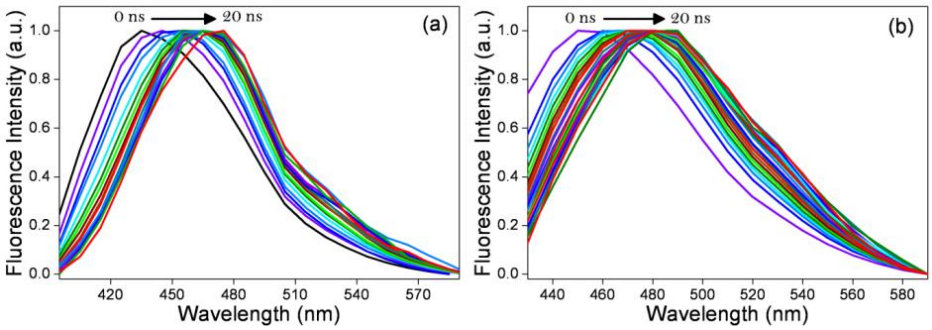

Figure 5.17. Time resolved emission spectra (TRES) of CuNCs in TX-100 ($w_0 = 10$) reverse micelles excited at (a) 375 nm and (b) 405 nm.

Now, we focus on fast dynamics that have been detected by fluorescence upconversion set-up. Some possible processes resulting in fast dynamics of 0.5-1 ps in CuNCs (**Table 5.1**) include intra-band transition, Auger recombination and ultrafast hydration dynamics. In our experiment, we have also collected decay profiles at different excitation laser powers (**Figure 5.18**). Decay profiles are almost similar or unchanged with the laser fluence; hence, Auger recombination dynamics could be ruled out. Thus, the observed 0.5-1 ps dynamics is assigned to the intra-band transition and/or inertial part of solvent response arising due to the charge character of Cu cluster (**Scheme 5.3**). Such solvation component may arise due to the adsorbed solvent molecules around the excited state CuNCs. The excited state non-radiative relaxation of electron from core to surface states is also an important process in this whole excited state dynamics events of CuNCs. Although upconversion observes only the radiative dynamics, but the non-radiative processes depletes the radiative rate, thereby, affecting the radiative decay kinetics. Hence, the non-radiative decay dynamics can be indirectly detected in upconversion decay profile. We assign the 10-15 ps component to the non-radiative relaxation dynamics from core to surface states (**Scheme 5.3**). Notably, other non-radiative process, such as electron-phonon scattering event may

appear in this time-scale. However, the electron-phonon scattering is very weak in this type of small quantum-sized nanoclusters.[12a,15]

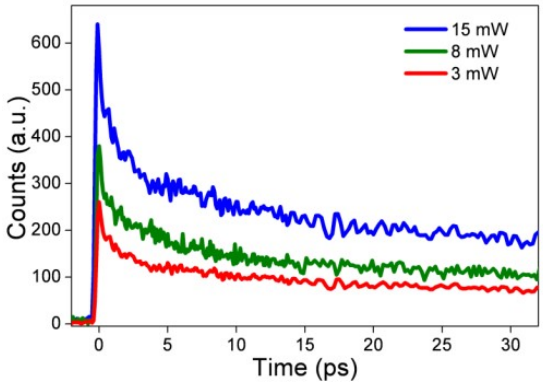

Figure 5.18. Excitation laser power dependent femto-second fluorescence decay profiles of CuNCs in CTAB reverse micelles ($w_0 = 15$). ($\lambda_{exc} = 375$ nm and $\lambda_{em} = 460$ nm).

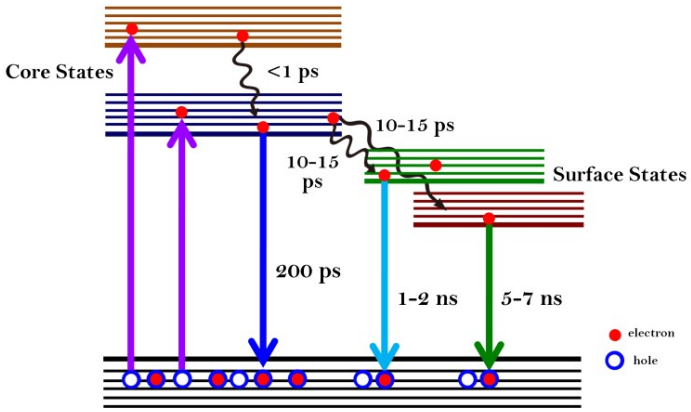

Scheme 5.3. Schematic illustration showing all the excited state relaxation dynamics of CuNCs.

In summary, the broad fluorescence and excitation dependent emission spectra of CuNCs inside RMs arise due to the radiative e-h recombination processes from the core and surface states. As shown in **Scheme 5.3**, after photo-excitation, excited electrons involve in intra-band non-radiative transition in sub-picosecond time scale, and trapping of excited electrons to the various surface states from core states takes place in 9-15 ps time-scale (**Scheme 5.3**). Excited electrons, which stay in the core states, come back to the ground state through radiative pathway, and this radiative electron-hole recombination dynamics from the core state takes place in ~200 ps time scale (**Scheme 5.3**). Whereas electrons trapped in various surface states recombine with holes in the ground state in nanosecond time-scales (**Scheme 5.3**). We believe that unraveling the excited state carrier dynamics of CuNCs through our study

provides a new perception towards the fundamental understanding of the optical properties of CuNCs.

5.3. Conclusion

Here, we have presented new synthetic strategy for the fluorescent copper nanoclusters (CuNCs). Interestingly, CuNCs synthesized inside the water pool of reverse micelles are stable even for ~180 days, whereas CuNCs synthesized in bulk water is stable only for 40 days. Steady state and time-resolved fluorescence spectroscopic techniques have been used to investigate the mysterious origins of excitation-dependent fluorescence spectral shift of CuNCs and its excited state carrier dynamics. We elucidate that the broad fluorescence from CuNCs in RM consists of two spectrally overlapped bands corresponding to the metal-core and surface states. The intrinsic emission of CuNCs distributed in shorter wavelength regions mainly originates from metal-core, and the extrinsic fluorescence band is caused by surface states. The extrinsic emission band has a much broader emission due to the presence of numerous surface states. The trapping of excited electrons in the various surface states leads to emission in the longer wavelength regions as well as excitation dependent emission of CuNCs in RM. Femto-second fluorescence upconversion and TCSPC decay profiles of CuNCs in RMs comprise of an ultrafast sub-pico second (~500-800 fs), a fast pico second (10-15 ps), a slow sub-nanosecond (~200 ps) and two slow nano-second (1.5-2 ns and 5-7 ns) components. The two fast components of ~800 fs and 10-15 ps are attributed to the intra-bands non-radiative transition of excited state electron and the relaxation of carrier from core to surface/trapped states of CuNCs, respectively. Slow sub-nanosecond component is appearing due to the radiative electron-hole recombination from the core states, whereas slowest components (1.5-2 ns and 5-7 ns) are originated due to radiative electron-hole recombination from two different types of surface states.

5.4. References

1. (a) J. Zheng, P. R. Nicovich and R. M. Dickson, *Annu. Rev. Phys. Chem.*, 2007, **58**, 409-431; (b) J. Li, J.-J. Zhu and K. Xu, *TrAC, Trends Anal. Chem.*, 2014, **58**, 90-98.
2. (a) T. Udayabhaskararao and T. Pradeep, *J. Phys. Chem. Lett.*, 2013, **4**, 1553-1564; (b) J. Xie, Y. Zheng and J. Y. Ying, *J. Am. Chem. Soc.*, 2009, **131**, 888-889; (c) C.-A. J. Lin, T.-Y. Yang, C.-H. Lee, S. H. Huang, R. A. Sperling, M. Zanella, J. K. Li, J.-L. Shen, H.-H. Wang, H.-I. Yeh, W. J. Parak and W. H. Chang, *ACS Nano*, 2009, **3**, 395-401.
3. (a) C. I. Richards, S. Choi, J.-C. Hsiang, Y. Antoku, T. Vosch, A. Bongiorno, Y.-L. Tzeng and R. M. Dickson, *J. Am. Chem. Soc.*, 2008, **130**, 5038-5039; (b) K. Pyo, V. D. Thanthirige, K. Kwak, P. Pandurangan, G. Ramakrishna and D. Lee, *J. Am. Chem. Soc.*,

2015, **137**, 8244-8250; (c) H. Yamamoto, H. Yano, H. Kouchi, Y. Obora, R. Arakawa and H. Kawasaki, *Nanoscale*, 2012, **4**, 4148-4154; (d) J. Yoshimoto, A. Sangsuwan, I. Osaka, K. Yamashita, Y. Iwasaki, M. Inada, R. Arakawa and H. Kawasaki, *J. Phys. Chem. C*, 2015, **119**, 14319-14325.

4. (a) I. Diez, R. H. A. Ras, M. I. Kanyuk and A. P. Demchenko, *Phys. Chem. Chem. Phys.*, 2013, **15**, 979-985; (b) M. Zhou, S. Long, X. Wan, Y. Li, Y. Niu, Q. Guo, Q.-M. Wang and A. Xia, *Phys. Chem. Chem. Phys.*, 2014, **16**, 18288-18293.
5. (a) R. Ghosh, A. K. Sahoo, S. S. Ghosh, A. Paul and A. Chattopadhyay, *ACS Appl. Mater. Interfaces*, 2014, **6**, 3822-3828; (b) W. Wei, Y. Lu, W. Chen and S. Chen, *J. Am. Chem. Soc.*, 2011, **133**, 2060-2063; (c) S. Ghosh, N. K. Das, U. Anand and S. Mukherjee, *J. Phys. Chem. Lett.*, 2015, **6**, 1293-1298.
6. M. Zhao, L. Sun and R. M. Crooks, *J. Am. Chem. Soc.*, 1998, **120**, 4877-4878.
7. Z. Qing, X. He, D. He, K. Wang, F. Xu, T. Qing and X. Yang, *Angew. Chem. Int. Ed.*, 2013, **52**, 9719-9722.
8. (a) A. Rotaru, S. Dutta, E. Jentzsch, K. Gothelf and A. Mokhir, *Angew. Chem. Int. Ed.*, 2010, **49**, 5665-5667; (b) Z. Zhou, Y. Du and S. Dong, *Anal. Chem.*, 2011, **83**, 5122-5127.
9. N. Goswami, A. Giri, M. S. Bootharaju, P. L. Xavier, T. Pradeep and S. K. Pal, *Anal. Chem.*, 2011, **83**, 9676-9680.
10. (a) M.-P. Pileni, *Nat. Mater.*, 2003, **2**, 145-150; (b) A. K. Ganguli, A. Ganguly and S. Vaidya, *Chem. Soc. Rev.*, 2010, **39**, 474-485; (c) S. Sharma and A. K. Ganguli, *J. Phys. Chem. B*, 2014, **118**, 4122-4131; (d) R. Ranjan, S. Vaidya, P. Thaplyal, M. Qamar, J. Ahmed and A. K. Ganguli, *Langmuir*, 2009, **25**, 6469-6475.
11. (a) S. H. Yau, O. Varnavski and T. Goodson, *Acc. Chem. Res.*, 2013, **46**, 1506-1516; (b) X. Wen, P. Yu, Y.-R. Toh, A.-C. Hsu, Y.-C. Lee and J. Tang, *J. Phys. Chem. C*, 2012, **116**, 19032-19038; (c) M. S. Devadas, J. Kim, E. Sinn, D. Lee, T. Goodson and G. Ramakrishna, *J. Phys. Chem. C*, 2010, **114**, 22417-22423.
12. (a) X. Wen, P. Yu, Y.-R. Toh, X. Ma, S. Huang and J. Tang, *Nanoscale*, 2013, **5**, 10251-10257; (b) S. H. Yau, N. Abeyasinghe, M. Orr, L. Upton, O. Varnavski, J. H. Werner, H.-C. Yeh, J. Sharma, A. P. Shreve, J. S. Martinez and T. Goodson Iii, *Nanoscale*, 2012, **4**, 4247-4254.
13. (a) X. Jia, J. Li and E. Wang, *Small*, 2013, **9**, 3873-3879; (b) X. Jia, X. Yang, J. Li, D. Li and E. Wang, *Chem. Commun.*, 2014, **50**, 237-239; (c) Z. Wu, J. Liu, Y. Gao, H. Liu, T. Li, H. Zou, Z. Wang, K. Zhang, Y. Wang, H. Zhang and B. Yang, *J. Am. Chem. Soc.*, 2015, **137**, 12906-12913.
14. K. Pyo, V. D. Thanthirige, S. Y. Yoon, G. Ramakrishna and D. Lee, *Nanoscale*, 2016, **8**, 20008-20016.
15. P. Yu, X. Wen, Y.-R. Toh, X. Ma and J. Tang, *Part. Part. Syst. Charact.*, 2015, **32**, 142-163.
16. Y. Choi, B. Kang, J. Lee, S. Kim, G. T. Kim, H. Kang, B. R. Lee, H. Kim, S.-H. Shim, G. Lee, O.-H. Kwon and B.-S. Kim, *Chem. Mater.*, 2016, **28**, 6840-6847.
17. N. Dhenadhayalan, K.-C. Lin, R. Suresh and P. Ramamurthy, *J. Phys. Chem. C*, 2016, **120**, 1252-1261.

********* THE END *********

SPRINGER NATURE LICENSE TERMS AND CONDITIONS

May 14, 2018

This Agreement between Mr. Raj Kumar Koninti ("You") and Springer Nature ("Springer Nature") consists of your license details and the terms and conditions provided by Springer Nature and Copyright Clearance Center.

License Number	4264650675072
License date	Jan 09, 2018
Licensed Content Publisher	Springer Nature
Licensed Content Publication	Nature Materials
Licensed Content Title	The rise of graphene
Licensed Content Author	A. K. Geim, K. S. Novoselov
Licensed Content Date	Mar 1, 2007
Licensed Content Volume	6
Licensed Content Issue	3
Type of Use	Thesis/Dissertation
Requestor type	academic/university or research institute
Format	electronic
Portion	figures/tables/illustrations
Number of figures/tables/illustrations	1
High-res required	no
Will you be translating?	no
Circulation/distribution	<501
Author of this Springer Nature content	no
Title	Exploring the Optical Properties of Anticancer Drugs/Metal Nanoclusters inside the Confined Environments and on the Graphene Oxide Surface
Instructor name	Dr. Partha Hazra
Institution name	Indian Institute of Science Education and Research (IISER), Pune
Expected presentation date	Jan 2018
Portions	Scheme 1.1.
Requestor Location	Mr. Raj Kumar Koninti Department of Chemistry IISER-Pune Pune, Maharashtra 411008 India Attn: Mr. Raj Kumar Koninti
Billing Type	Invoice

Billing Address	Mr. Raj Kumar Koninti Department of Chemistry IISER-Pune Pune, India 411008 Attn: Mr. Raj Kumar Koninti
Total	0.00 USD

Terms and Conditions

Springer Nature Terms and Conditions for RightsLink Permissions

Springer Customer Service Centre GmbH (the Licensor) hereby grants you a non-exclusive, world-wide licence to reproduce the material and for the purpose and requirements specified in the attached copy of your order form, and for no other use, subject to the conditions below:

1. The Licensor warrants that it has, to the best of its knowledge, the rights to license reuse of this material. However, you should ensure that the material you are requesting is original to the Licensor and does not carry the copyright of another entity (as credited in the published version).

   If the credit line on any part of the material you have requested indicates that it was reprinted or adapted with permission from another source, then you should also seek permission from that source to reuse the material.

2. Where **print only** permission has been granted for a fee, separate permission must be obtained for any additional electronic re-use.

3. Permission granted **free of charge** for material in print is also usually granted for any electronic version of that work, provided that the material is incidental to your work as a whole and that the electronic version is essentially equivalent to, or substitutes for, the print version.

4. A licence for 'post on a website' is valid for 12 months from the licence date. This licence does not cover use of full text articles on websites.

5. Where **'reuse in a dissertation/thesis'** has been selected the following terms apply: Print rights for up to 100 copies, electronic rights for use only on a personal website or institutional repository as defined by the Sherpa guideline (www.sherpa.ac.uk/romeo/).

6. Permission granted for books and journals is granted for the lifetime of the first edition and does not apply to second and subsequent editions (except where the first edition permission was granted free of charge or for signatories to the STM Permissions Guidelines http://www.stm-assoc.org/copyright-legal-affairs/permissions/permissions-guidelines/), and does not apply for editions in other languages unless additional translation rights have been granted separately in the licence.

7. Rights for additional components such as custom editions and derivatives require additional permission and may be subject to an additional fee. Please apply to Journalpermissions@springernature.com/bookpermissions@springernature.com for these rights.

8. The Licensor's permission must be acknowledged next to the licensed material in print. In electronic form, this acknowledgement must be visible at the same time as the figures/tables/illustrations or abstract, and must be hyperlinked to the journal/book's homepage. Our required acknowledgement format is in the Appendix below.

9. Use of the material for incidental promotional use, minor editing privileges (this does not include cropping, adapting, omitting material or any other changes that affect the meaning, intention or moral rights of the author) and copies for the disabled are permitted under this licence.

10. Minor adaptations of single figures (changes of format, colour and style) do not require the Licensor's approval. However, the adaptation should be credited as shown in

Appendix below.

Appendix — Acknowledgements:

For Journal Content:
Reprinted by permission from [**the Licensor**]: [**Journal Publisher** (e.g. Nature/Springer/Palgrave)] [**JOURNAL NAME**] [**REFERENCE CITATION** (Article name, Author(s) Name), [**COPYRIGHT**] (year of publication)

For **Advance Online Publication papers:**
Reprinted by permission from [**the Licensor**]: [**Journal Publisher** (e.g. Nature/Springer/Palgrave)] [**JOURNAL NAME**] [**REFERENCE CITATION** (Article name, Author(s) Name), [**COPYRIGHT**] (year of publication), advance online publication, day month year (doi: 10.1038/sj.[JOURNAL ACRONYM].)

For Adaptations/Translations:
Adapted/Translated by permission from [**the Licensor**]: [**Journal Publisher** (e.g. Nature/Springer/Palgrave)] [**JOURNAL NAME**] [**REFERENCE CITATION** (Article name, Author(s) Name), [**COPYRIGHT**] (year of publication)

Note: For any republication from the British Journal of Cancer, the following credit line style applies:

Reprinted/adapted/translated by permission from [**the Licensor**]: on behalf of Cancer Research UK: : [**Journal Publisher** (e.g. Nature/Springer/Palgrave)] [**JOURNAL NAME**] [**REFERENCE CITATION** (Article name, Author(s) Name), [**COPYRIGHT**] (year of publication)

For **Advance Online Publication** papers:
Reprinted by permission from The [**the Licensor**]: on behalf of Cancer Research UK: [**Journal Publisher** (e.g. Nature/Springer/Palgrave)] [**JOURNAL NAME**] [**REFERENCE CITATION** (Article name, Author(s) Name), [**COPYRIGHT**] (year of publication), advance online publication, day month year (doi: 10.1038/sj.[JOURNAL ACRONYM])

For Book content:
Reprinted/adapted by permission from [**the Licensor**]: [**Book Publisher** (e.g. Palgrave Macmillan, Springer etc) [**Book Title**] by [**Book author**(s)] [**COPYRIGHT**] (year of publication)

Other Conditions:

Version 1.0

JOHN WILEY AND SONS LICENSE TERMS AND CONDITIONS

May 14, 2018

This Agreement between Mr. Raj Kumar Koninti ("You") and John Wiley and Sons ("John Wiley and Sons") consists of your license details and the terms and conditions provided by John Wiley and Sons and Copyright Clearance Center.

License Number	4264700284168
License date	Jan 09, 2018
Licensed Content Publisher	John Wiley and Sons
Licensed Content Publication	Angewandte Chemie International Edition
Licensed Content Title	Silica-Based Mesoporous Organic–Inorganic Hybrid Materials
Licensed Content Author	Frank Hoffmann,Maximilian Cornelius,Jürgen Morell,Michael Fröba
Licensed Content Date	May 5, 2006
Licensed Content Pages	36
Type of use	Dissertation/Thesis
Requestor type	University/Academic
Format	Print and electronic
Portion	Figure/table
Number of figures/tables	1
Original Wiley figure/table number(s)	Figure 2.
Will you be translating?	No
Title of your thesis / dissertation	Exploring the Optical Properties of Anticancer Drugs/Metal Nanoclusters inside the Confined Environments and on the Graphene Oxide Surface
Expected completion date	Jan 2018
Expected size (number of pages)	1
Requestor Location	Mr. Raj Kumar Koninti Department of Chemistry IISER-Pune Pune, Maharashtra 411008 India Attn: Mr. Raj Kumar Koninti
Publisher Tax ID	EU826007151
Total	0.00 USD
Terms and Conditions	

TERMS AND CONDITIONS

This copyrighted material is owned by or exclusively licensed to John Wiley & Sons, Inc. or one of its group companies (each a"Wiley Company") or handled on behalf of a society with which a

Wiley Company has exclusive publishing rights in relation to a particular work (collectively "WILEY"). By clicking "accept" in connection with completing this licensing transaction, you agree that the following terms and conditions apply to this transaction (along with the billing and payment terms and conditions established by the Copyright Clearance Center Inc., ("CCC's Billing and Payment terms and conditions"), at the time that you opened your RightsLink account (these are available at any time at http://myaccount.copyright.com).

Terms and Conditions

- The materials you have requested permission to reproduce or reuse (the "Wiley Materials") are protected by copyright.

- You are hereby granted a personal, non-exclusive, non-sub licensable (on a stand-alone basis), non-transferable, worldwide, limited license to reproduce the Wiley Materials for the purpose specified in the licensing process. This license, **and any CONTENT (PDF or image file) purchased as part of your order,** is for a one-time use only and limited to any maximum distribution number specified in the license. The first instance of republication or reuse granted by this license must be completed within two years of the date of the grant of this license (although copies prepared before the end date may be distributed thereafter). The Wiley Materials shall not be used in any other manner or for any other purpose, beyond what is granted in the license. Permission is granted subject to an appropriate acknowledgement given to the author, title of the material/book/journal and the publisher. You shall also duplicate the copyright notice that appears in the Wiley publication in your use of the Wiley Material. Permission is also granted on the understanding that nowhere in the text is a previously published source acknowledged for all or part of this Wiley Material. Any third party content is expressly excluded from this permission.

- With respect to the Wiley Materials, all rights are reserved. Except as expressly granted by the terms of the license, no part of the Wiley Materials may be copied, modified, adapted (except for minor reformatting required by the new Publication), translated, reproduced, transferred or distributed, in any form or by any means, and no derivative works may be made based on the Wiley Materials without the prior permission of the respective copyright owner.**For STM Signatory Publishers clearing permission under the terms of the STM Permissions Guidelines only, the terms of the license are extended to include subsequent editions and for editions in other languages, provided such editions are for the work as a whole in situ and does not involve the separate exploitation of the permitted figures or extracts,** You may not alter, remove or suppress in any manner any copyright, trademark or other notices displayed by the Wiley Materials. You may not license, rent, sell, loan, lease, pledge, offer as security, transfer or assign the Wiley Materials on a stand-alone basis, or any of the rights granted to you hereunder to any other person.

- The Wiley Materials and all of the intellectual property rights therein shall at all times remain the exclusive property of John Wiley & Sons Inc, the Wiley Companies, or their respective licensors, and your interest therein is only that of having possession of and the right to reproduce the Wiley Materials pursuant to Section 2 herein during the continuance of this Agreement. You agree that you own no right, title or interest in or to the Wiley Materials or

any of the intellectual property rights therein. You shall have no rights hereunder other than the license as provided for above in Section 2. No right, license or interest to any trademark, trade name, service mark or other branding ("Marks") of WILEY or its licensors is granted hereunder, and you agree that you shall not assert any such right, license or interest with respect thereto

- NEITHER WILEY NOR ITS LICENSORS MAKES ANY WARRANTY OR REPRESENTATION OF ANY KIND TO YOU OR ANY THIRD PARTY, EXPRESS, IMPLIED OR STATUTORY, WITH RESPECT TO THE MATERIALS OR THE ACCURACY OF ANY INFORMATION CONTAINED IN THE MATERIALS, INCLUDING, WITHOUT LIMITATION, ANY IMPLIED WARRANTY OF MERCHANTABILITY, ACCURACY, SATISFACTORY QUALITY, FITNESS FOR A PARTICULAR PURPOSE, USABILITY, INTEGRATION OR NON-INFRINGEMENT AND ALL SUCH WARRANTIES ARE HEREBY EXCLUDED BY WILEY AND ITS LICENSORS AND WAIVED BY YOU.

- WILEY shall have the right to terminate this Agreement immediately upon breach of this Agreement by you.

- You shall indemnify, defend and hold harmless WILEY, its Licensors and their respective directors, officers, agents and employees, from and against any actual or threatened claims, demands, causes of action or proceedings arising from any breach of this Agreement by you.

- IN NO EVENT SHALL WILEY OR ITS LICENSORS BE LIABLE TO YOU OR ANY OTHER PARTY OR ANY OTHER PERSON OR ENTITY FOR ANY SPECIAL, CONSEQUENTIAL, INCIDENTAL, INDIRECT, EXEMPLARY OR PUNITIVE DAMAGES, HOWEVER CAUSED, ARISING OUT OF OR IN CONNECTION WITH THE DOWNLOADING, PROVISIONING, VIEWING OR USE OF THE MATERIALS REGARDLESS OF THE FORM OF ACTION, WHETHER FOR BREACH OF CONTRACT, BREACH OF WARRANTY, TORT, NEGLIGENCE, INFRINGEMENT OR OTHERWISE (INCLUDING, WITHOUT LIMITATION, DAMAGES BASED ON LOSS OF PROFITS, DATA, FILES, USE, BUSINESS OPPORTUNITY OR CLAIMS OF THIRD PARTIES), AND WHETHER OR NOT THE PARTY HAS BEEN ADVISED OF THE POSSIBILITY OF SUCH DAMAGES. THIS LIMITATION SHALL APPLY NOTWITHSTANDING ANY FAILURE OF ESSENTIAL PURPOSE OF ANY LIMITED REMEDY PROVIDED HEREIN.

- Should any provision of this Agreement be held by a court of competent jurisdiction to be illegal, invalid, or unenforceable, that provision shall be deemed amended to achieve as nearly as possible the same economic effect as the original provision, and the legality, validity and enforceability of the remaining provisions of this Agreement shall not be affected or impaired thereby.

- The failure of either party to enforce any term or condition of this Agreement shall not constitute a waiver of either party's right to enforce each and every term and condition of this

Agreement. No breach under this agreement shall be deemed waived or excused by either party unless such waiver or consent is in writing signed by the party granting such waiver or consent. The waiver by or consent of a party to a breach of any provision of this Agreement shall not operate or be construed as a waiver of or consent to any other or subsequent breach by such other party.

- This Agreement may not be assigned (including by operation of law or otherwise) by you without WILEY's prior written consent.

- Any fee required for this permission shall be non-refundable after thirty (30) days from receipt by the CCC.

- These terms and conditions together with CCC's Billing and Payment terms and conditions (which are incorporated herein) form the entire agreement between you and WILEY concerning this licensing transaction and (in the absence of fraud) supersedes all prior agreements and representations of the parties, oral or written. This Agreement may not be amended except in writing signed by both parties. This Agreement shall be binding upon and inure to the benefit of the parties' successors, legal representatives, and authorized assigns.

- In the event of any conflict between your obligations established by these terms and conditions and those established by CCC's Billing and Payment terms and conditions, these terms and conditions shall prevail.

- WILEY expressly reserves all rights not specifically granted in the combination of (i) the license details provided by you and accepted in the course of this licensing transaction, (ii) these terms and conditions and (iii) CCC's Billing and Payment terms and conditions.

- This Agreement will be void if the Type of Use, Format, Circulation, or Requestor Type was misrepresented during the licensing process.

- This Agreement shall be governed by and construed in accordance with the laws of the State of New York, USA, without regards to such state's conflict of law rules. Any legal action, suit or proceeding arising out of or relating to these Terms and Conditions or the breach thereof shall be instituted in a court of competent jurisdiction in New York County in the State of New York in the United States of America and each party hereby consents and submits to the personal jurisdiction of such court, waives any objection to venue in such court and consents to service of process by registered or certified mail, return receipt requested, at the last known address of such party.

WILEY OPEN ACCESS TERMS AND CONDITIONS

Wiley Publishes Open Access Articles in fully Open Access Journals and in Subscription journals offering Online Open. Although most of the fully Open Access journals publish open access articles under the terms of the Creative Commons Attribution (CC BY) License only, the subscription journals and a few of the Open Access Journals offer a choice of Creative Commons Licenses. The license type is clearly identified on the article.

The Creative Commons Attribution License

The Creative Commons Attribution License (CC-BY) allows users to copy, distribute and transmit an article, adapt the article and make commercial use of the article. The CC-BY license permits commercial and non-

Creative Commons Attribution Non-Commercial License

The Creative Commons Attribution Non-Commercial (CC-BY-NC)License permits use, distribution and reproduction in any medium, provided the original work is properly cited and is not used for commercial purposes.(see below)

Creative Commons Attribution-Non-Commercial-NoDerivs License

The Creative Commons Attribution Non-Commercial-NoDerivs License (CC-BY-NC-ND) permits use, distribution and reproduction in any medium, provided the original work is properly cited, is not used for commercial purposes and no modifications or adaptations are made. (see below)

Use by commercial "for-profit" organizations

Use of Wiley Open Access articles for commercial, promotional, or marketing purposes requires further explicit permission from Wiley and will be subject to a fee.

Further details can be found on Wiley Online Library

http://olabout.wiley.com/WileyCDA/Section/id-410895.html

Other Terms and Conditions:

v1.10 Last updated September 2015

Questions? customercare@copyright.com or +1-855-239-3415 (toll free in the US) or +1-978-646-2777.

ROYAL SOCIETY OF CHEMISTRY LICENSE TERMS AND CONDITIONS

May 14, 2018

This Agreement between Mr. Raj Kumar Koninti ("You") and Royal Society of Chemistry ("Royal Society of Chemistry") consists of your license details and the terms and conditions provided by Royal Society of Chemistry and Copyright Clearance Center.

License Number	4264671147159
License date	Jan 09, 2018
Licensed Content Publisher	Royal Society of Chemistry
Licensed Content Publication	RSC Advances
Licensed Content Title	Removal of Pb(ii) from aqueous solution by mesoporous silica MCM-41 modified by ZnCl2: kinetics, thermodynamics, and isotherms
Licensed Content Author	Foad Raji,Alireza Saraeian,Majid Pakizeh,Faridreza Attarzadeh
Licensed Content Date	Apr 17, 2015
Licensed Content Volume	5
Licensed Content Issue	46
Type of Use	Thesis/Dissertation
Requestor type	non-commercial (non-profit)
Portion	figures/tables/images
Number of figures/tables/images	1
Format	print and electronic
Distribution quantity	500
Will you be translating?	no
Order reference number	
Title of the thesis/dissertation	Exploring the Optical Properties of Anticancer Drugs/Metal Nanoclusters inside the Confined Environments and on the Graphene Oxide Surface
Expected completion date	Jan 2018
Estimated size	1
Requestor Location	Mr. Raj Kumar Koninti Department of Chemistry IISER-Pune Pune, Maharashtra 411008 India Attn: Mr. Raj Kumar Koninti
Billing Type	Invoice
Billing Address	Mr. Raj Kumar Koninti Department of Chemistry IISER-Pune

Pune, India 411008
Attn: Mr. Raj Kumar Koninti

Total 0.00 USD

Terms and Conditions

This License Agreement is between {Requestor Name} ("You") and The Royal Society of Chemistry ("RSC") provided by the Copyright Clearance Center ("CCC"). The license consists of your order details, the terms and conditions provided by the Royal Society of Chemistry, and the payment terms and conditions.

RSC / TERMS AND CONDITIONS

INTRODUCTION

The publisher for this copyrighted material is The Royal Society of Chemistry. By clicking "accept" in connection with completing this licensing transaction, you agree that the following terms and conditions apply to this transaction (along with the Billing and Payment terms and conditions established by CCC, at the time that you opened your RightsLink account and that are available at any time at .

LICENSE GRANTED

The RSC hereby grants you a non-exclusive license to use the aforementioned material anywhere in the world subject to the terms and conditions indicated herein. Reproduction of the material is confined to the purpose and/or media for which permission is hereby given.

RESERVATION OF RIGHTS

The RSC reserves all rights not specifically granted in the combination of (i) the license details provided by your and accepted in the course of this licensing transaction; (ii) these terms and conditions; and (iii) CCC's Billing and Payment terms and conditions.

REVOCATION

The RSC reserves the right to revoke this license for any reason, including, but not limited to, advertising and promotional uses of RSC content, third party usage, and incorrect source figure attribution.

THIRD-PARTY MATERIAL DISCLAIMER

If part of the material to be used (for example, a figure) has appeared in the RSC publication with credit to another source, permission must also be sought from that source. If the other source is another RSC publication these details should be included in your RightsLink request. If the other source is a third party, permission must be obtained from the third party. The RSC disclaims any responsibility for the reproduction you make of items owned by a third party.

PAYMENT OF FEE

If the permission fee for the requested material is waived in this instance, please be advised that any future requests for the reproduction of RSC materials may attract a fee.

ACKNOWLEDGEMENT

The reproduction of the licensed material must be accompanied by the following acknowledgement: Reproduced ("Adapted" or "in part") from {Reference Citation} (or Ref XX) with permission of The Royal Society of Chemistry.

If the licensed material is being reproduced from New Journal of Chemistry (NJC), Photochemical & Photobiological Sciences (PPS) or Physical Chemistry Chemical Physics (PCCP) you must include one of the following acknowledgements:

For figures originally published in NJC:

Reproduced ("Adapted" or "in part") from {Reference Citation} (or Ref XX) with permission of The Royal Society of Chemistry (RSC) on behalf of the European Society for Photobiology, the

European Photochemistry Association and the RSC.
For figures originally published in PPS:
Reproduced ("Adapted" or "in part") from {Reference Citation} (or Ref XX) with permission of The Royal Society of Chemistry (RSC) on behalf of the Centre National de la Recherche Scientifique (CNRS) and the RSC.
For figures originally published in PCCP:
Reproduced ("Adapted" or "in part") from {Reference Citation} (or Ref XX) with permission of the PCCP Owner Societies.

HYPERTEXT LINKS

With any material which is being reproduced in electronic form, you must include a hypertext link to the original RSC article on the RSC's website. The recommended form for the hyperlink is http://dx.doi.org/10.1039/DOI suffix, for example in the link http://dx.doi.org/10.1039/b110420a the DOI suffix is 'b110420a'. To find the relevant DOI suffix for the RSC article in question, go to the Journals section of the website and locate the article in the list of papers for the volume and issue of your specific journal. You will find the DOI suffix quoted there.

LICENSE CONTINGENT ON PAYMENT

While you may exercise the rights licensed immediately upon issuance of the license at the end of the licensing process for the transaction, provided that you have disclosed complete and accurate details of your proposed use, no license is finally effective unless and until full payment is received from you (by CCC) as provided in CCC's Billing and Payment terms and conditions. If full payment is not received on a timely basis, then any license preliminarily granted shall be deemed automatically revoked and shall be void as if never granted. Further, in the event that you breach any of these terms and conditions or any of CCC's Billing and Payment terms and conditions, the license is automatically revoked and shall be void as if never granted. Use of materials as described in a revoked license, as well as any use of the materials beyond the scope of an unrevoked license, may constitute copyright infringement and the RSC reserves the right to take any and all action to protect its copyright in the materials.

WARRANTIES

The RSC makes no representations or warranties with respect to the licensed material.

INDEMNITY

You hereby indemnify and agree to hold harmless the RSC and the CCC, and their respective officers, directors, trustees, employees and agents, from and against any and all claims arising out of your use of the licensed material other than as specifically authorized pursuant to this licence.

NO TRANSFER OF LICENSE

This license is personal to you or your publisher and may not be sublicensed, assigned, or transferred by you to any other person without the RSC's written permission.

NO AMENDMENT EXCEPT IN WRITING

This license may not be amended except in a writing signed by both parties (or, in the case of "Other Conditions, v1.2", by CCC on the RSC's behalf).

OBJECTION TO CONTRARY TERMS

You hereby acknowledge and agree that these terms and conditions, together with CCC's Billing and Payment terms and conditions (which are incorporated herein), comprise the entire agreement between you and the RSC (and CCC) concerning this licensing transaction, to the exclusion of all other terms and conditions, written or verbal, express or implied (including any terms contained in any purchase order, acknowledgment, check endorsement or other writing prepared by you). In

the event of any conflict between your obligations established by these terms and conditions and those established by CCC's Billing and Payment terms and conditions, these terms and conditions shall control.

JURISDICTION

This license transaction shall be governed by and construed in accordance with the laws of the District of Columbia. You hereby agree to submit to the jurisdiction of the courts located in the District of Columbia for purposes of resolving any disputes that may arise in connection with this licensing transaction.

LIMITED LICENSE

The following terms and conditions apply to specific license types:

Translation

This permission is granted for non-exclusive world English rights only unless your license was granted for translation rights. If you licensed translation rights you may only translate this content into the languages you requested. A professional translator must perform all translations and reproduce the content word for word preserving the integrity of the article.

Intranet

If the licensed material is being posted on an Intranet, the Intranet is to be password-protected and made available only to bona fide students or employees only. All content posted to the Intranet must maintain the copyright information line on the bottom of each image. You must also fully reference the material and include a hypertext link as specified above.

Copies of Whole Articles

All copies of whole articles must maintain, if available, the copyright information line on the bottom of each page.

Other Conditions

v1.2

Gratis licenses (referencing $0 in the Total field) are free. Please retain this printable license for your reference. No payment is required.

If you would like to pay for this license now, please remit this license along with yourpayment made payable to "COPYRIGHT CLEARANCE CENTER" otherwise you will be invoiced within 48 hours of the license date. Payment should be in the form of a check or money order referencing your account number and this invoice number {Invoice Number}.

Once you receive your invoice for this order, you may pay your invoice by credit card.

Please follow instructions provided at that time.

Make Payment To:

Copyright Clearance Center

29118 Network Place

Chicago, IL 60673-1291

For suggestions or comments regarding this order, contact Rightslink Customer Support: customercare@copyright.com or +1-855-239-3415 (toll free in the US) or +1-978-646-2777.

Questions? customercare@copyright.com or +1-855-239-3415 (toll free in the US) or +1-978-646-2777.

RightsLink®

Home | Account Info | Help

Title:	Visible to Infrared Luminescence from a 28-Atom Gold Cluster
Author:	Stephan Link, Andrew Beeby, Simon FitzGerald, et al
Publication:	The Journal of Physical Chemistry B
Publisher:	American Chemical Society
Date:	Apr 1, 2002

Logged in as:
Raj Kumar Koninti
Account #:
3001235722

LOGOUT

PERMISSION/LICENSE IS GRANTED FOR YOUR ORDER AT NO CHARGE

This type of permission/license, instead of the standard Terms & Conditions, is sent to you because no fee is being charged for your order. Please note the following:

- Permission is granted for your request in both print and electronic formats, and translations.
- If figures and/or tables were requested, they may be adapted or used in part.
- Please print this page for your records and send a copy of it to your publisher/graduate school.
- Appropriate credit for the requested material should be given as follows: "Reprinted (adapted) with permission from (COMPLETE REFERENCE CITATION). Copyright (YEAR) American Chemical Society." Insert appropriate information in place of the capitalized words.
- One-time permission is granted only for the use specified in your request. No additional uses are granted (such as derivative works or other editions). For any other uses, please submit a new request.

If credit is given to another source for the material you requested, permission must be obtained from that source.

BACK | CLOSE WINDOW

Title: Excited State Proton Transfer Dynamics of Topotecan Inside Biomimicking Nanocavity

Author: Raj Kumar Koninti, Krishna Gavvala, Abhigyan Sengupta, et al

Publication: The Journal of Physical Chemistry B

Publisher: American Chemical Society

Date: Feb 1, 2015

PERMISSION/LICENSE IS GRANTED FOR YOUR ORDER AT NO CHARGE

This type of permission/license, instead of the standard Terms & Conditions, is sent to you because no fee is being charged for your order. Please note the following:

- Permission is granted for your request in both print and electronic formats, and translations.
- If figures and/or tables were requested, they may be adapted or used in part.
- Please print this page for your records and send a copy of it to your publisher/graduate school.
- Appropriate credit for the requested material should be given as follows: "Reprinted (adapted) with permission from (COMPLETE REFERENCE CITATION). Copyright (YEAR) American Chemical Society." Insert appropriate information in place of the capitalized words.
- One-time permission is granted only for the use specified in your request. No additional uses are granted (such as derivative works or other editions). For any other uses, please submit a new request.

Title:	Ultrafast Fluorescence Dynamics of Highly Stable Copper Nanoclusters Synthesized inside the Aqueous Nanopool of Reverse Micelles
Author:	Raj Kumar Koninti, Sagar Satpathi, Partha Hazra
Publication:	The Journal of Physical Chemistry C
Publisher:	American Chemical Society
Date:	Mar 1, 2018

PERMISSION/LICENSE IS GRANTED FOR YOUR ORDER AT NO CHARGE

This type of permission/license, instead of the standard Terms & Conditions, is sent to you because no fee is being charged for your order. Please note the following:

- Permission is granted for your request in both print and electronic formats, and translations.
- If figures and/or tables were requested, they may be adapted or used in part.
- Please print this page for your records and send a copy of it to your publisher/graduate school.
- Appropriate credit for the requested material should be given as follows: "Reprinted (adapted) with permission from (COMPLETE REFERENCE CITATION). Copyright (YEAR) American Chemical Society." Insert appropriate information in place of the capitalized words.
- One-time permission is granted only for the use specified in your request. No additional uses are granted (such as derivative works or other editions). For any other uses, please submit a new request.